The Production and Use of Proton-Induced Ultrasoft X-rays

Jones, Elizabeth Anne

The Production and Use of Proton-Induced Ultrasoft X-rays

by

Elizabeth Anne Jones, B.Sc., A.R.C.S.

A thesis submitted for the degree of Doctor of Philosophy
of the University of London.

Dept. of Medical Electronics and Physics
The Medical College of St. Bartholomew's Hospital
Charterhouse Square
London EC1

June 1988

ABSTRACT

A 700 keV Van de Graaff accelerator was used to accelerate protons onto solid targets of different light elements to produce ultrasoft, characteristic X-rays ($\lesssim$ 5 keV). The proton energies were calibrated using the (p,γ) resonances at 633 keV in Aluminium and at 340 and 483 keV in Fluorine.

The X-ray emission characteristics of Aluminium, Carbon, Gold, Silicon/Carbon, Silicon/Nitrogen and Titanium/Boron were studied as a function of incident proton energy, angle of inclination of the target (30° - 60° to the proton beam) and angle of detection of the X-rays (40° - 130° to the beam). Detection of the X-rays was achieved using a gas-flow proportional counter directly coupled to a low-noise pre-amplifier. The resulting spectra, recorded on a multichannel analyser, were well fitted by linear combinations of single Gaussian curves to give peak position (X-ray energy), width and area (X-ray intensity).

Carbon contamination of the target surface was studied in detail for the Aluminium target. A number of low beam currents onto the target (10 - 70 nA) were used for total irradiation times of up to 17 hours in order to establish the degree of overall X-ray energy mixing.

The information gained from the study of both the Carbon contamination and the X-ray emission characteristics was used to propose practical optimum conditions for the production of ultrasoft X-rays by proton bombardment in their application to biological and biochemical irradiations.

A computer code, capable of following the electron track histories resulting from ultrasoft X-ray interactions has been used to compare the details of such energy deposition with the results of mammalian cell irradiations made at the M.R.C. Radiobiology Unit for a number of different ultrasoft X-ray energies. Such a comparison has been used to try to identify the mechanisms of radiation action. Included in this work is the application of the computer code to a variety of characteristic X-ray photon energies, thus extending the available, calculated data.

ACKNOWLEDGEMENTS

I am deeply indebted to many people for their help towards the completion of this work. Foremost among these is my supervisor, Dr. F.A. Smith, who has patiently steered me throughout the duration of this study and has been a constant source of inspiration, encouragement and advice. Sincere thanks are also due to Dr. D.T. Goodhead at the M.R.C. Radiobiology Unit (Chilton, Didcot) who was always available for discussion and guidance on all aspects of the work.

My thanks are also due to Prof. N.F. Kember for making the facilities at the Physics Department of the Medical College of St. Bartholomew's Hospital available, and I am grateful for the comradeship afforded to me by him and all the members of the department during my three years there. Special thanks must go to Len Eastgate for constructing various parts of the equipment and James Oriel for his constant advice and help with the electronic equipment (and breakdowns!). I am also grateful to Peter Browne and his colleagues for their assistance with the computing side of the work.

During the duration of this study I made several visits to the M.R.C. Radiobiology Unit and I am grateful to all those who made these visits possible. I am especially grateful for being allowed access to the computing facilities at the Unit and appreciate the help given by members of the Computer Services Division. I also appreciate the friendship and advice given by members of the Cell and Molecular Biology Division. In particular, I would like to mention Dave Charlton (now at Concordia University, Montreal, Canada) and Hooshang Nikjoo - who was an invaluable source of advice and information concerning the use of the Monte-Carlo track structure codes. They, along with Dr. Goodhead, also provided me with unpublished data, for which I am very grateful.

I am indebted to the Science and Engineering Research Council for the award of a research studentship and to the Medical Research Council for covering the cost of the visits to the Radiobiology Unit. I am also grateful to Mrs. D. Boyle for deciphering my writing and typing the thesis.

Finally, I would like to thank my family. My brother, Hefin has always been ready with his support and helpful advice, and submitted himself willingly (?) to reading the final versions of this work. My parents have given continual encouragement, support and devotion over the years and this was reiterated by their willingness to help check the data presented in Appendix 2. It is as a token of my appreciation that I dedicate this work to my parents and brother.

Diolch o galon i bob un ohonoch!

TABLE OF CONTENTS

		Page
Abstract		2
Acknowledgements		3
Table of Contents		5
List of Figures		7
List of Tables		10
Chapter 1	Introduction	11
Chapter 2	Experimental Apparatus	22
2.1	The Van de Graaff accelerator	22
2.1.1	The Generator	22
2.1.2	The Accelerator	24
2.1.3	The Pressurised Tank	25
2.2	The Beam Line	26
2.2.1	Accelerator tube extension	26
2.2.2	Collimators	29
2.2.3	The Scattering Chamber	29
2.3	The Target System	30
2.4	The Detection System	34
2.4.1	The Proportional Counter	34
2.4.2	Associated Electronics	43
Chapter 3	Calibration of the Van de Graaff machine	45
Chapter 4	Data Analysis	55
4.1	Subroutine SIMPLX	56
4.2	Subroutine FCN	58
Chapter 5	Experimental Section	61
5.1	Experimental Procedures	61
5.1.1	Surface contamination study	61
5.1.2	Angular distribution study	62
5.1.3	Proton energy dependence of X-ray emission	62
5.2	Results	62
5.2.1	Surface contamination study	79
5.2.2	Angular distribution study	85
5.2.3	Proton energy dependence of X-ray emission	92

		Page
Chapter 6	Theoretical Treatment of Results	96
	6.1 Compensation for target surface contamination	96
	6.1.1 Example of surface contamination calculations	101
	6.2 Calculation of theoretical angular distribution	103
	6.2.1 Example of the theoretical angular distribution calculation	108
Chapter 7	Application of Monte-Carlo Track Structure Codes	115
	7.1 Introduction	115
	7.2 Local Energy Deposition of Radiation Tracks	116
	7.3 Calculations using a Monte-Carlo structure code	118
	7.3.1 Track Structure and Scoring Programme	119
	7.3.2 Results	120
Chapter 8	Discussion	141
	8.1 Comparison of the observed angular dependence of proton-induced ultrasoft X-rays with theoretical calculation	141
	8.2 A practical beam line for proton-induced ultrasoft X-rays	143
	8.3 Monte-Carlo electron track structure data	150
Bibliography		154
Appendices:		
Appendix 1	Subroutine FCN	165
Appendix 2	The absolute frequency of energy depositions greater than a given amount in each elemental cylinder per Gray of absorbed dose to the medium	169

LIST OF FIGURES

Figure		Page
1.1	Frequencies of dicentric exchange aberrations in human lymphocytes after irradiation with high and low L.E.T. radiations.	12
1.2	Dominant mode of absorption of Aluminium K X-rays by an Oxygen atom.	14
1.3	Energy deposited locally by electrons from low L.E.T. radiations.	15
1.4	Typical X-ray energy spectrum from a hot-filament X-ray tube.	18
2.1	Simplified drawing of the AN700 Van de Graaff accelerator.	23
2.2	Schematic diagram of the beam line.	27
2.3	Schematic drawing of the target system.	31
2.4	The effect of applying a positive bias voltage to the electron suppression shield.	32
2.5	The angular dependence of the target charge collection time.	33
2.6	The Manson Gas-flow Proportional Counter.	35
2.7	The transmission of ultrasoft X-rays through the VYNS window.	36
2.8	The effect of adding Polypropylene filters above the detector window.	38
2.9	Magnetic deflection of scattered protons.	39
2.10	Calculation of the magnetic field required to deflect the scattered protons away from the hole in the steel shield.	40
2.11	The correction to the required magnetic field due to the limited extent of the available field.	42
2.12	Schematic drawing of the ultrasoft X-ray detection system with the associated electronics.	44
3.1	Proton capture.	46
3.2	Schematic diagram of the beam line as used during the calibration of the Van de Graaff.	48
3.3	An example of the energy spectrum from the CaF_2 target.	50
3.4	Thick target γ-ray yield curve for $^{19}F\ (p,\gamma)\ ^{20}Ne$.	51
3.5	Thick target γ-ray yield curve for $^{27}Al\ (p,\gamma)\ ^{28}Si$.	52

Figure		Page
3.6	Calibration graph for the proton energy as a function of the generating voltmeter reading.	54
4.1	A two dimensional simplex.	57
5.1	Examples of the spectra obtained for each of the targets when bombarded with 500keV protons.	65
5.2	Derivation of the B_K X-ray intensity.	73
5.3	The transmission characteristics of 6 μm Polypropylene at low energies.	74
5.4	Energy calibration graph for the proportional counter and MCA system.	76
5.5	The variation of the C_K X-ray yield with collected charge on the target.	82
5.6	The variation of the Al_K X-ray yield with collected charge on the target.	83
5.7	The Al_K : C_K X-ray intensity ratio as a function of the charge collected on the target.	84
5.8	The build-up of Carbon contamination X-ray intensity with the total amount of charge collected on an Al target.	86
5.9	The rate of Carbon contamination build-up as a function of the proton beam current.	87
5.10	The relative X-ray intensity as a function of the detector angle.	89
5.11	The mass attenuation coefficient of low energy X-rays in Carbon, Silicon and Gold targets.	93
5.12	The measured X-ray intensities of C_K and Al_K X-rays.	94
5.13	The ratio of the measured Carbon-to-Aluminium K-shell X-ray intensity as a function of proton energy.	95
6.1	The mass attenuation coefficient of low-energy photons in Carbon.	97
6.2	Calculation of the depth of Carbon contaminant on the target surface.	100
6.3	Simplifying assumptions used for the calculation of the theoretical angular dependence of the emitted X-rays from a thick target.	104
6.4	The variation of proton energy with depth into the target.	105
6.5	The K-shell X-ray production cross-section for proton bombardment of various low Z targets.	106

Figure		Page
7.1	Diagram illustrating the virtual sphere enclosing the simulated electron track(s) and crossed by the scoring cylinders arranged at random.	122
7.2	The frequency of energy depositions obtained when considering the interaction of C_K X-rays with soft tissue.	124
7.3	The frequency of energy depositions obtained when considering the interaction of Al_K X-rays with soft tissue.	128
7.4	The frequency of energy depositions in a 2 nm x 2 nm cylinder by simulated electron tracks from various low Z characteristic X-rays.	133
7.5	The frequency of energy depositions in a 10 nm x 5 nm cylinder by simulated electron tracks from various low Z characteristic X-rays.	134
7.6	The frequency of energy depositions in a 25 nm x 25 nm cylinder by simulated electron tracks from various low Z characteristic X-rays.	135
7.7	An inter-elemental comparison for the frequency of energy deposition in a 2 nm x 2 nm cylinder.	137
7.8	An inter-elemental comparison for the frequency of energy deposition in a 10 nm x 5 nm cylinder.	138
7.9	An inter-elemental comparison for the frequency of energy deposition in a 25 nm x 25 nm cylinder.	139
8.1	The sin θ dependence of the difference in the distance travelled within the target at either end of each μm increment.	142
8.2	A schematic diagram summarising some of the properties of a practical beam line for biological irradiation by proton-induced ultrasoft X-rays.	149

LIST OF TABLES

Table		Page
5.1	The energies of the characteristic X-rays studied.	64
5.2	The average parameter values for the various targets.	71
5.3	The observed yield of X-rays.	78
5.4	Comparison between the observed and documented yields of proton-induced ultrasoft X-rays.	80
6.1	The linear attenuation coefficient of ultra-soft X-rays in Carbon.	98
6.2	The Al_K intensity - correcting for surface contamination.	102
6.3	The energy loss experienced by a 500 keV proton in an Al target.	109
6.4	The Al_K production cross-section.	110
6.5	The distance travelled by the X-ray within the target.	111
6.6	The product of the Al_K X-ray production cross-section and the attenuation of the X-ray in the target.	112
6.7	The contribution of the Al_K X-rays produced in the first μm of the target.	114
7.1	Input parameters for the electron generating code, MOCA7.	121
8.1	The mass attenuation coefficients of low energy X-rays in Oxygen.	152

CHAPTER 1

INTRODUCTION

In 1938 K. Sax published the results of a study of chromosome aberrations induced in cells by ionising radiations. These results, together with further studies (for example : Sax,1940,1957; Evans, 1962; Revell,1974; Savage,1975), showed that ionising radiations were capable of inducing the exchange of chromosome material and it was suggested that an aberration arose as a consequence of two radiation damaged chromosomes undergoing an exchange. Radiations of different ionisation density or linear energy transfer, L.E.T., (L.E.T. is a measure of the energy imparted to a medium along the path of a charged particle [ICRU,1970]) were observed to have varying degrees of effect on the irradiated cells (Figure 1.1). Combining this information with the size of the chromosome structures involved led to the suggestion that the required distances between pairs of damaged chromosomes for aberration induction (termed the interaction distances) were of the order of 0.1 to 1 μm (Lea and Catcheside,1942; Lea,1955; Wolff,1959; Heddle and Wolff,1966; Neary, Preston and Savage,1967). In comparison, the diameter of cell nuclei is typically of the order of 10 μm and the diameter of a DNA double helix is approximately 2 nm.

During the same time period, developments in experimental physics, particularly with the introduction in the late 1950s of the low-pressure (Rossi) proportional counter (Rossi and Rosenzweig,1955), enabledddirect measurements to be made of the energy deposited by radiation within a small simulated tissue volume. Such measurements, and their analyses, became known as microdosimetry - the study of the properties of radiation in small tissue volumes usually smaller than the nuclei of mammalian cells.

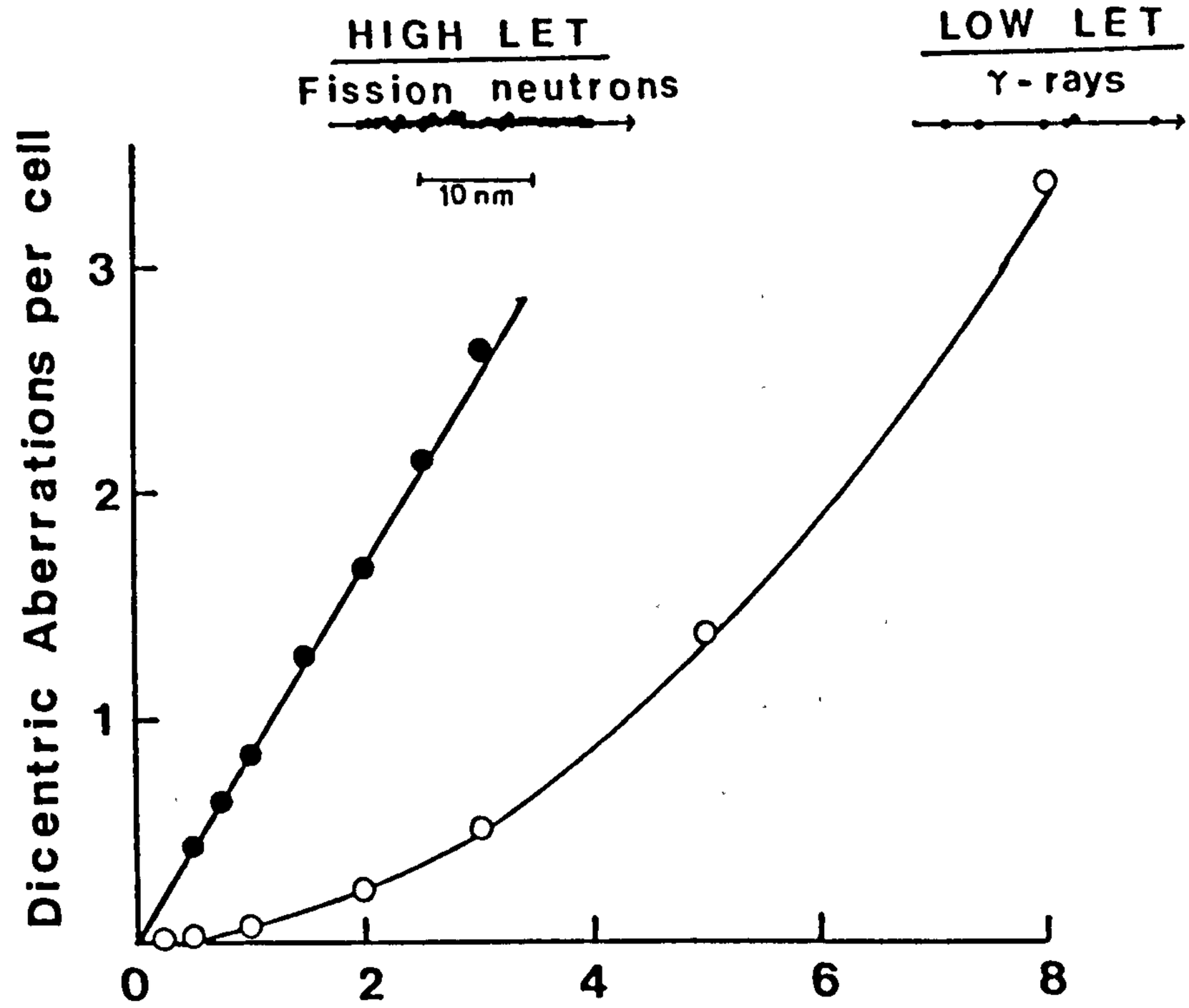

Figure 1.1 Frequencies of dicentric exchange aberrations in human lymphocytes after irradiation with radiations of high L.E.T. (Lloyd *et al.*, 1976) and low L.E.T (Lloyd *et al.*, 1975). Above each curve is a diagrammatical representation of the track of ionisation produced by a typical secondary charged particle from each radiation (*from Goodhead, 1982 with permission, copyright by Academic Press, Inc.*).

By using microdosimetric techniques attempts could be made to measure some physical properties of ionising radiations that corresponded to the properties of radiation resulting in chromosome aberrations and other biological effects in cells. Such studies might then elucidate the mechanisms of radiation action, enabling the radiological risks to human beings to be better understood and quantified.

As mentioned earlier, L.E.T. is often varied within studies of radiation mechanisms. The radiations used frequently deposit energy along tracks which are long in comparison with sub-cellular dimensions, thus making it difficult to pinpoint the cause of any specific damage. Radiations which produce tracks of short, defined lengths have been available, but practical limitations such as their attenuation coefficient have limited their use.

However, ultrasoft X-rays of less than ~ 5 keV, although having very large attenuation coefficients and a limited availability, have been used intermittently since the late 1920s (Goodhead and Thacker, 1977). The interaction of ultrasoft X-rays with matter takes place almost entirely by photoelectric absorption (Figure 1.2) leading to the production of photo- and Auger- electrons of low, well defined energies, capable of producing only very short tracks ($\lesssim$ 0.1 μm). Recent studies on mammalian cells have shown that ultrasoft X-rays are highly effective in inducing biological damage (Cox *et al.*,1977; Goodhead *et al.*,1979,1981a; Virisk *et al.*,1980; Thacker *et al.*,1983; Brenner *et al.*,1987; Raju *et al.*,1987) and have been found, in general, to be more effective per unit dose than hard X-rays and gamma (γ) rays. Although other ionising radiations, such as hard X-rays and γ-rays, produce a large number of low energy electrons (Figure 1.3), the effect

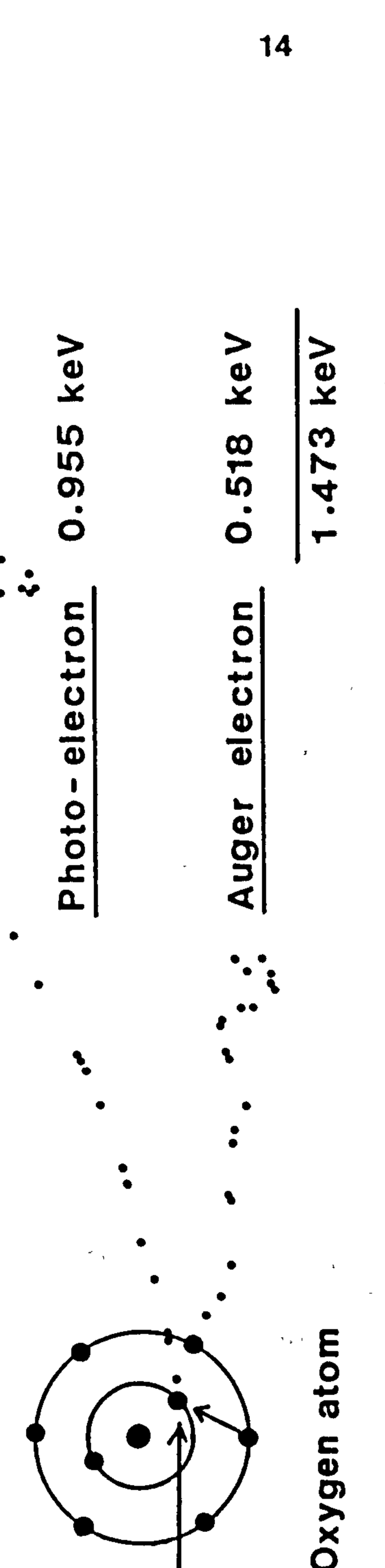

Figure 1.2 Dominant mode of absorption of Aluminium K X-rays (of 1.487 keV) by an Oxygen atom, showing the ionisation tracks of the photo- and Auger-electrons. The electron ranges are 0.05 and 0.02 μm respectively (ICRU, 1970) (*from Goodhead and Thacker, 1977 with permission.*).

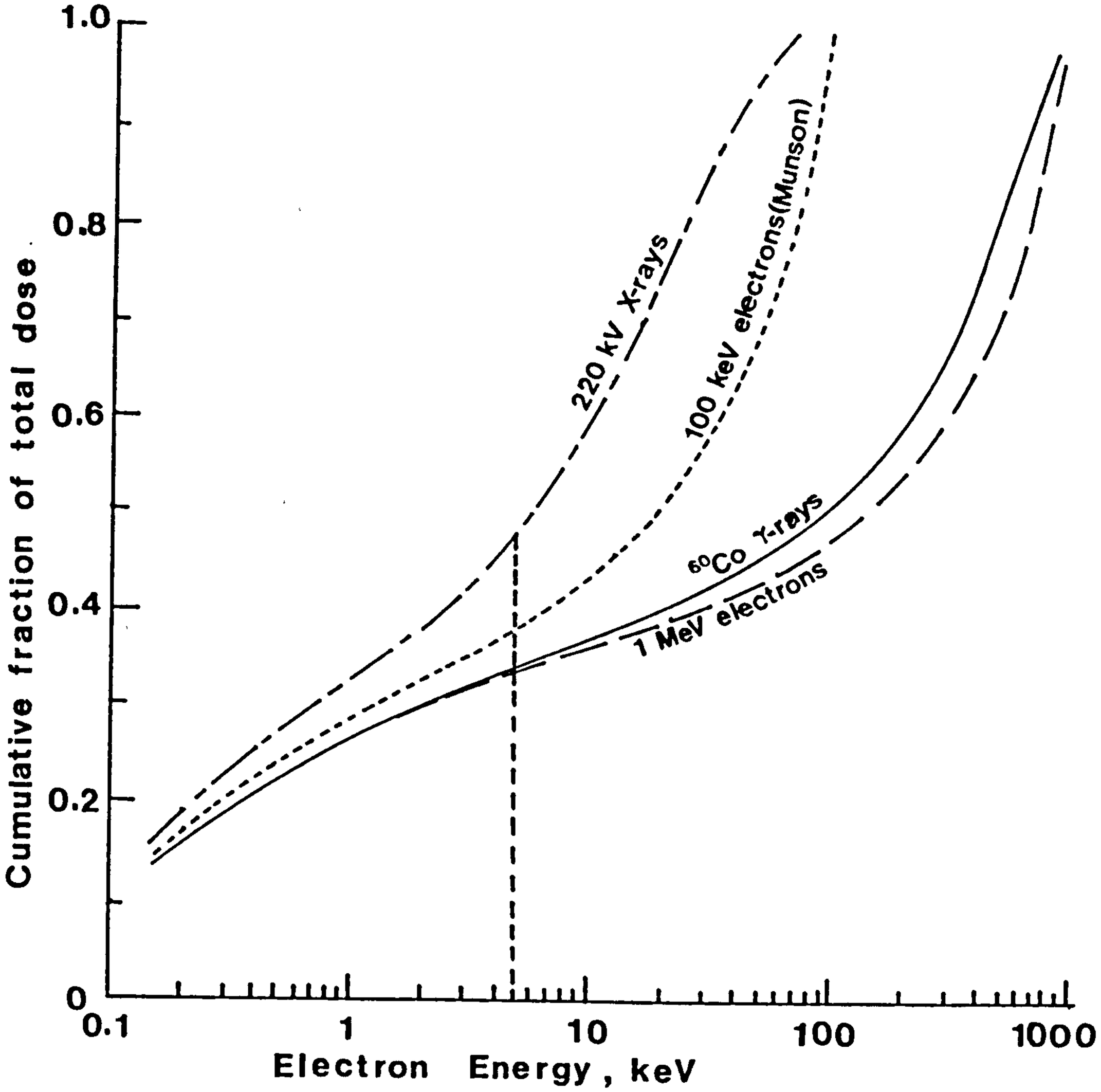

Figure 1.3 Energy deposited locally by electrons from low L.E.T. radiations (D.T. Goodhead and H. Nikjoo, (*pers.comm.*) based on data by Burch (1957) and R.J. Munson (*unpublished data*) using the method of Burch). 35 - 45 % of the energy is deposited by electrons of 5 keV energy or less.

of the low energy electrons cannot be studied in isolation from the effect of the higher energy electrons (Raju *et al.*,1987). The effectiveness of ultrasoft X-rays was also observed to increase with decreasing photon energy.

Numerous models and concepts attempt to explain radiation-induced biological damage (Goodhead,1987a,1987b) and, consequently, studies involving short track length radiations have become increasingly appropriate. The observation that small, highly localised energy depositions are effective in inducing biological damage is not only important to the understanding of the mechanisms of radiation action but also sets tight constraints on any proposed model of radiation action (Goodhead,1977,1982; Goodhead, Thacker and Cox,1978; Goodhead *et al.*,1981b; Thacker, Goodhead and Wilkinson,1983).

The full potential of ultrasoft X-rays as a fine probe of the energy and the spatial requirements of mechanisms of radiation damage in biological systems can only be realised with a wide, versatile range of sources. A variety of sources have, and are being used to produce ultrasoft X-rays including cold-cathode discharge tubes, hot-filament electron tubes, hard X-ray induced fluorescent characteristic ultrasoft X-rays from secondary targets, laser induced X-rays and synchrotron radiation sources (First International Ultrasoft X-Ray Workshop,1987). All these techniques have their advantages and disadvantages (Goodhead and Bance,1984).

A further method of producing ultrasoft, characteristic X-rays is by the use of heavy ion bombardment of solid targets. When a target is bombarded by a heavy particle (proton, deuteron, alpha particle), electrons are ejected from the electron shells surrounding the target nuclei. If an impact removes an electron from an inner shell, the

subsequent filling of the vacancy by an electron from an outer shell leads to the emission of X-rays characteristic of the element bombarded.

The production of characteristic X-rays by electron impact is a familiar phenomenon and gives rise to characteristic peaks super-imposed on the continuous *bremsstrahlung* background (Figure 1.4). The ionisation of an atom by the impact of a heavy particle on the other hand, and the subsequent emission of an X-ray, has received only sporadic attention since Chadwick and others first observed and identified the characteristic X-rays of several elements (ranging from Aluminium to Uranium) which were bombarded by alpha (α) particles (Chadwick,1912,1913; Chadwick and Russell,1913,1914; Thomson,1914; Slater,1921). A more comprehensive investigation of inner-shell ionisation in various elements by α-particles was published in 1928 by Bothe and Fränz who used a Polonium source for the production of α-particles. They studied both the K-shell ionisation for targets of atomic number, Z, greater than 12 and L-shell ionisation for targets with Z > 34, as well as the M-shell ionisation of Bismuth (Z = 83).

In 1941, Cork used deuterons of energies up to 10 MeV and examined the blackening of photographic plates by X-rays from 38 chemical elements. Cork found that for K-shell ionisation by deuterons, the yield of the emitted X-rays maximised in the region of Z = 28 whilst for L-shell ionisation, the yield maximised at Z = 64. Although Barton (1930) had unsuccessfully searched for X-rays from a Copper target by low energy (15-25 keV) proton bombardment, it was Gerthsen and Reusse (1933) who performed the first successful experiments with protons as the incident particles. Protons in the energy range 30 - 150 keV were used and the K-shell radiation emitted from Aluminium and Magnesium as well as the L-shell radiation from Selenium were observed. Further work was carried out by Livingston, Genevese and Konopinski (1937)

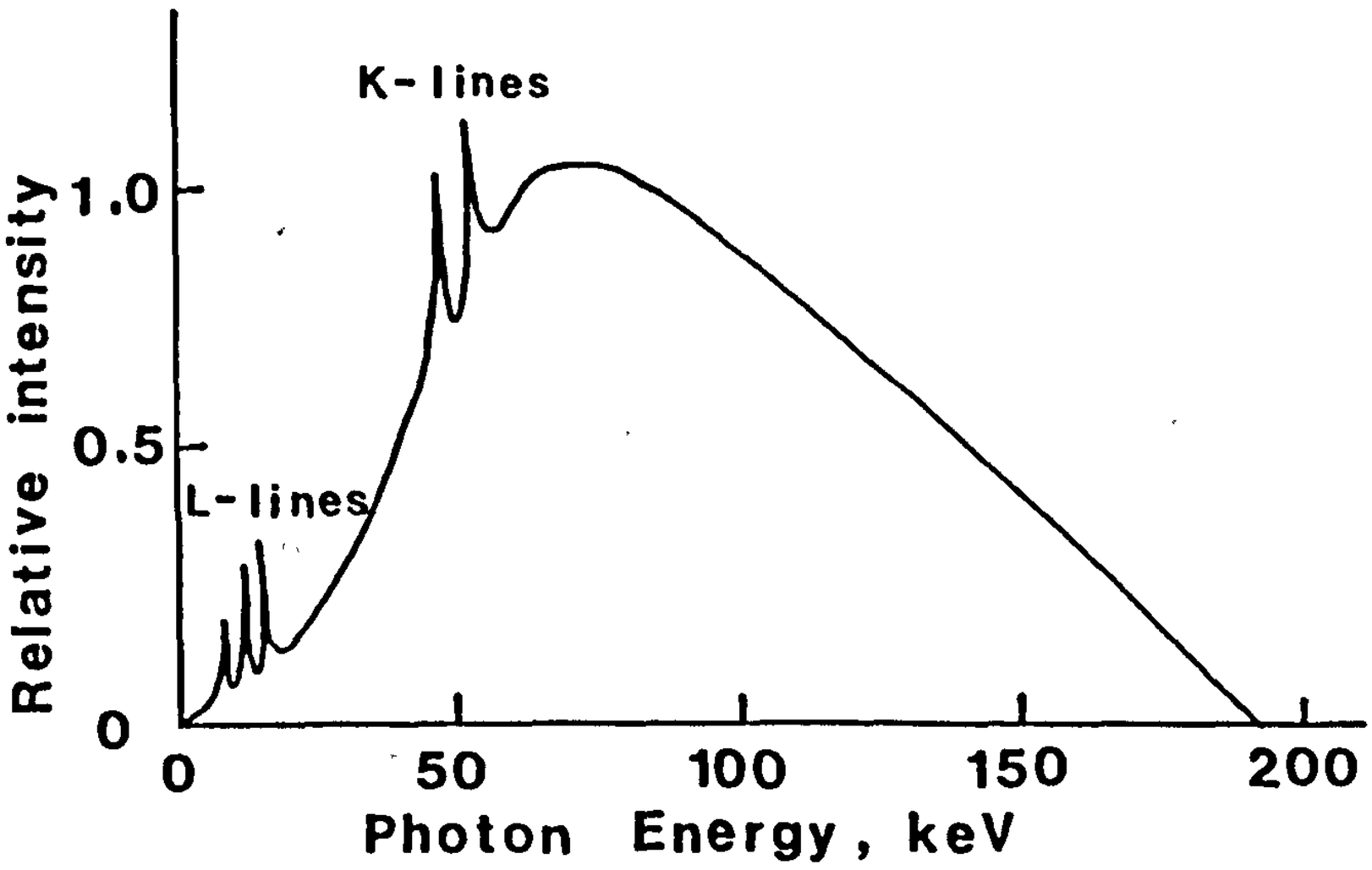

Figure 1.4 Typical X-ray energy spectrum from a hot-filament X-ray tube with a Tungsten (Z = 74) target.

using protons up to 1·72 MeV. They measured the intensity of the emitted X-rays as a function of the atomic number and estimated the order of magnitude of the cross-section for proton-induced X-ray production.

Numerous experiments have since been carried out with protons of energies less than a few MeV. These have been primarily in the field of particle-induced X-ray emission (P.I.X.E.) for analytical purposes (Rutledge and Watson,1973; Johansson and Johansson,1976). Protons, as opposed to α-particles and other heavy ions, have been favoured as the bombarding particle mainly as a result of the availability of small proton accelerators in many laboratories. Furthermore protons have been shown to give the best sensitivity in most practical applications. There is also a greater problem with target heating and deterioration when α-particles are used and because of their large energy loss it is necessary to limit the beam intensity.

Measurements presented by Goodhead and Bance (1984) indicated that proton bombardment is also a favoured method of producing characteristic ultrasoft X-rays with greater, and more widely variable, intensities than are available from sources such as the cold-cathode discharge tube. The main advantage of proton-induced ultrasoft X-rays, especially when compared to hot-filament electron-induced sources, may however be considered to be the relatively low level of background contamination (which is dominated by secondary electron *bremsstrahlung* emission). Goodhead (1987c), for example, has found that for a proton energy of 600 keV, the *bremsstrahlung* contamination contribution in air, in a practical irradiation configuration, in the detected photon beam is less than 0.2% when using a Carbon target and approximately an order of magnitude less using an Aluminium target. Comparable values for electron-induced sources are in the region of 1 to 5% (Goodhead and Bance,1984; Raju *et al.*,1987).

To date virtually all proton-induced ultrasoft X-ray radiobiological information has been obtained with Carbon or Aluminium targets (First International Ultrasoft X-Ray Workshop, 1987) producing the corresponding K-shell characteristic X-rays (C_K X-rays at 0.28 keV and Al_K X-rays at 1.49 keV). However, the application of ultrasoft X-rays in radiobiology and radiation chemistry would benefit greatly from the availability of other X-ray energies thereby producing different electron energies and varying ratios of photo- and Auger-electrons.

Using a 700 keV Van de Graaff accelerator at St. Bartholomew's Hospital Medical College the study reported here set out to investigate the possibility of using proton bombardment of other solid target materials and to look in greater detail at the angular distribution of the emitted photons. The study was limited to the characterisation of the ultrasoft X-rays and no biological irradiations were undertaken. From the information gained, certain practical optimum conditions for the production of proton-induced ultrasoft X-rays for biological and biochemical irradiations are proposed.

As previously mentioned, radiobiological studies involving ultrasoft X-rays are important in furthering our understanding of radiation damage mechanisms. Their effectiveness in producing complete biological effects, even though their energy deposition is small and highly localised, increases the need for further understanding of the physical properties of radiation interactions, particularly those which may be correlated with the biological effect of practical radiations.

The biological features of ionising radiations should be contained within the details of their track structure. Hence, the critical characteristics of radiation action may possibly be identified by using computed Monte-Carlo track structure codes to simulate

the radiation tracks. By recording all the spatial and energy transfer information (Paretzke, 1980) these can then be compared with the observed relative biological effectiveness (R.B.E.) of the different radiations. The M.R.C. Radiobiology Unit, Chilton, Didcot possess one of the codes which is capable of full simulation of electron track histories, interaction by interaction. In addition to the experimental work on the beam line characteristics, the work reported here also applied this code to a variety of characteristic X-ray energies, thus extending the available, calculated data.

CHAPTER 2

EXPERIMENTAL APPARATUS

2.1 The Van de Graaff accelerator

The proton beam was produced using a 700 keV Van de Graaff positive ion accelerator (Model AN700, High Voltage Ltd.). The Van de Graaff machine produces high voltages by driving charges along a conveyor belt into a conducting terminal, and consists of three main parts: the generator (drive motor, power supply, moving belt, high-voltage electrode), the accelerator proper (the ion source and the accelerator tube) and the pressurised tank.

2.1.1 The Generator

A simplified drawing of the AN700 Van de Graaff accelerator is shown in Figure 2.1. The charging belt transports electrons electrostatically from the high voltage terminal to ground potential by revolving around a system of two cylindrical pulleys, the drive pulley situated at the base of the accelerator at ground potential and a pulley alternator at the high voltage terminal end. The belt charge is provided by a fine-mesh, stainless steel screen which is insulated from the generator base plate and positioned such that the corona points face the outer surface of the belt at the drive pulley. The drive pulley, on the inner surface of the belt, is grounded through a Carbon-brush contact, and the charging screen is maintained at a positive potential by a power supply located on the generator base. A similar (collector) screen is connected directly onto the high voltage terminal plate, with the fine stainless steel mesh trimmed to present a series of sharp corona points to the positively charged belt. Electrons from the terminal are attracted to the belt through the collector screen, electrostatically held by the belt and transported to the base plate

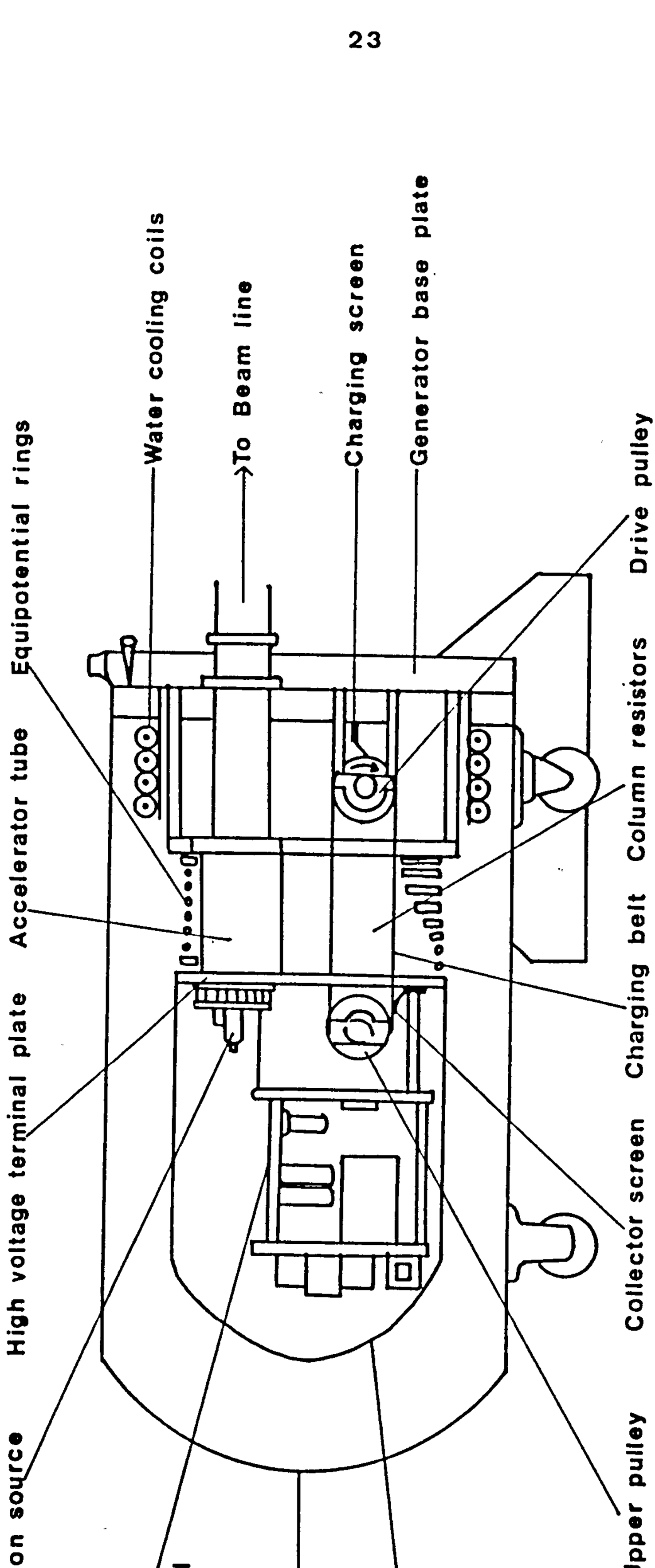

Figure 2.1 Simplified drawing of the AN700 Van de Graaff accelerator.

where they are removed by the positive potential at the charging screen, leaving behind them a positively charged belt.

The high voltage terminal is mounted at the top of the accelerator column and houses the oscillator which supplies the radio frequency (r.f.) power for ionising the source gas. Also situated on the high voltage terminal plate are the power supply units for providing voltages to the terminal plate, collector screen and the probe of the ion source bottle. The high voltage terminal is insulated from the generator base by a column made up from a number of circular equipotential planes separated from one another by porcelain insulators. Appropriately shaped holes in the equipotential planes allow access for the accelerator tube, the charging belt and the various control rods.

The equipotential planes are electrically connected through series resistors. These form a voltage divider network and maintain a constant voltage gradient between the terminal and ground. Each plane is provided with an Aluminium gradient bar placed such that it faces the upcharge side of the belt, thus decreasing the possiblity of discharge between the belt and the plane.

2.1.2 The Accelerator

Hydrogen gas is introduced into the ion source bottle through a Palladium (Pd) leak assembly. This consists of a Pd thimble surrounded by a quartz sleeve which serves to insulate the thimble from the spiral heating element wound closely around it. Power is supplied to the heater by a 5 to 10 Volt transformer secondary winding which warms the Pd, thus making it porous to Hydrogen and its isotopes. The gas passes through the Pd and flows through a gas line connected to the thimble into the ion source.

Within the ion source bottle the gas is ionised by r.f. energy with the resulting plasma being magnetically concentrated at the exit canal of the source bottle. Positive ions are initially expelled through the exit canal into the acceleration path by a potential applied to the probe of the source bottle. Further acceleration is provided by the voltage gradient developed along the column. Focusing of the beam can be achieved by applying a negative potential to the focus electrode situated at the ion source end of the accelerator tube.

The accelerator tube is evacuated to 10^{-6} torr (1.33×10^{-4} Pa) and provides a long mean-free path for the accelerated particles. The tube is mounted on the generator base and extends up through the column of equipotential planes to the high voltage terminal. It consists of a number of ring-shaped insulators cemented between dished Aluminium electrodes, the number of electrodes in the tube being equal to the number of equipotential planes in the column, each tube electrode being electrically connected to a column plane by a spring connector.

2.1.3 The pressurised tank

The generator is housed within a cylindrical tank containing a high pressure gas mixture in order to prevent the continuous discharge from the high voltage terminal to ground. As the pressure of a gas increases the distance between the molecules becomes correspondingly shorter as does the mean-free path of an ion with the effect that any gaseous discharge will appear at higher electrical fields and thus enable stable operation up to a higher voltage limit.

The AN700 Van de Graaff accelerator was operated at gas pressures $\gtrsim 115$ lb.in^{-2} (7.9×10^{5} Pa) with a mixture of Freon (CCl_2F_2), Carbon dioxide (CO_2) and Nitrogen (N_2). Initially these gases were used in the proportion 15% Freon, 35% CO_2 and 50% N_2. However, a reduction

in the percentage of CO_2 proved to give a more stable mode of operation. As a result the accelerator was operated in the later stages of the work with 30% Freon and 70% N_2 in the tank, the Freon being introduced first to bring the evacuated tank up to about 30 $lb.in^{-2}$ (~2.1 x 10^5 Pa). Whilst the tank was filled to a total pressure of 115 $lb.in^{-2}$ (7.9 x 10^5 Pa) the subsequent warming up of both the Freon and the Nitrogen meant that the accelerator was invariably operated at gas pressures of 120 - 130 $lb.in^{-2}$ (8.2 x 10^5 - 9.0 x 10^5 Pa).

2.2 The Beam Line (Figure 2.2)

2.2.1 Accelerator tube extensions

On leaving the accelerator, the proton beam travelled through an assembly of different tube extensions that provided an evacuated channel between the accelerator and the scattering chamber. Included in the tube extension assembly were:

(a) Penning ionisation gauge. The vacuum in the accelerator tube system was monitored by a Penning ionisation gauge (C.V.C. Products Inc.) capable of measuring vacuum pressures in the range 1 x 10^{-6} to 1 x 10^{-3} torr (1.33 x 10^{-4} - 1.33 x 10^{-1} Pa). The vacuum pressure, as measured by the gauge, was monitored on the accelerator control panel.

(b) Main gate valve. The main gate valve was used to isolate the accelerator tube from the tube extensions.

(c) The Associated Vacuum System. The accelerator-tube system could only be operated under a high vacuum (low pressure) to minimise collisions between the accelerated particles and gas molecules in the tube. This was achieved using an Edwards Speedivac Oil Vapour Diffusion Pump (Model 203B). The pump was water cooled, had a pumping capacity of 250 - 300 m^3/hour and contained 60 cm^3 of Diffusion Pump Fluid 704 (Dow Corning). A mechanical backing-pump (Edwards E2M2 Double-stage

Figure 2.2 Schematic diagram of the beam line :

1. Scattering chamber
2. Electron suppression shield
3. Insulator
4. Thick target
5. 6 μm Polypropylene filter
6. 1 mm diameter Cd collimator
7. Gas-flow proportional counter
8. +300 V biased 1 mm diameter collimator
9. 7 mm diameter collimator
10. Auxillary gate valve
11. Diffusion pump and liquid Nitrogen trap
12. Main gate valve
13. Penning ionisation gauge
14. AN700 Van de Graaff accelerator
15. Charge integrator

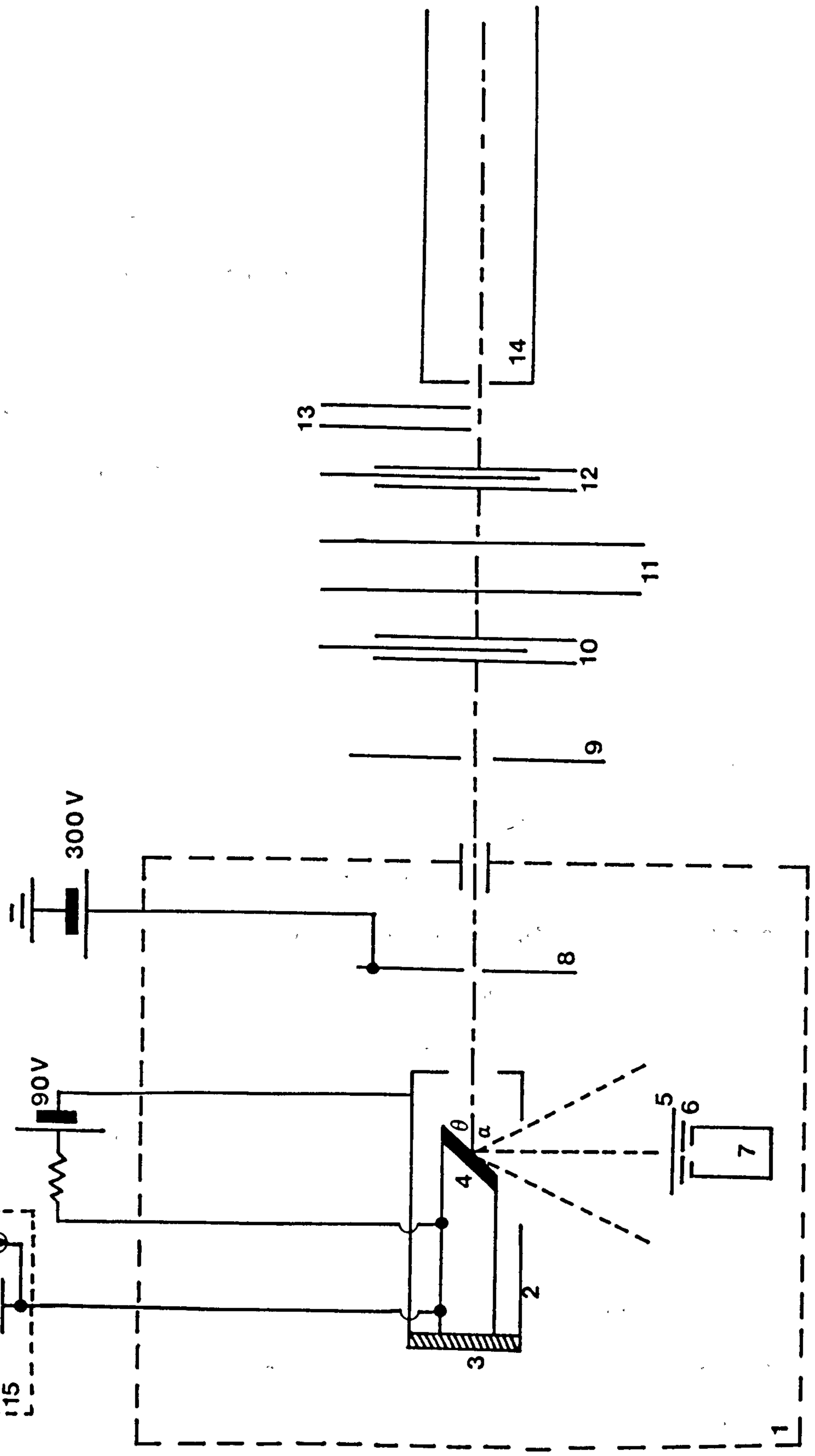
14
13
12
11
10
9
300 V
8
90V
5
6
7
θ
α
4
2
3
2μF
15
1

Rotary Vacuum Pump) was used as a secondary system to remove the exhaust from the main oil-diffusion pump to the atmosphere. Situated between the oil-diffusion pump and the proton beam line was a double walled, liquid-Nitrogen cooled cold trap to serve as a hydrocarbon condenser.

(d) Auxillary gate valve. This gate valve was used to isolate the scattering chamber from the tube extensions. Work could therefore be carried out on the chamber without interrupting the evacuated state of the accelerator tube.

2.2.2 Collimators

Prior to entering the scattering chamber, the proton beam encountered an Aluminium (Al) collimator with a 7mm diameter central hole. Once within the scattering chamber the beam passed through another Al collimator (1 mm diameter hole). Previous work (Khan and Potter, 1964) has established that electrons produced by collisions of imperfectly focused protons on the tube walls pass down the accelerating tube with the protons. Secondary electrons are also produced at the edge of the collimating discs so the collimator within the scattering chamber was held at 300 V positive potential (supplied from a Harwell 2000 Series E.H.T. Unit, Type 2147 - 2) to reduce backstreaming of the electrons from the collimator to the accelerator.

2.2.3 The Scattering Chamber

The scattering chamber consisted of a 43 cm diameter, 23 cm wide cylinder, orientated with the cylinder axis horizontal, with both circular ends forming removable, vertical lids. The target and detection systems entered the chamber through opposite lids through 'O' ring seals and the required electrical connections were made using B.N.C. pressurised bulkhead adaptors (including one high voltage version) and insulated glass-metal seal 'feed-throughs' on the chamber walls. Separate pumping systems were used for the scattering chamber and the accelerator, the

scattering chamber being evacuated with an Edwards Speedivac Oil Vapour Diffusion Pump (Model F203) with a Welch Duo-Seal (Sargent-Welch Scientific Company) backing pump. A double walled, liquid-Nitrogen cooled cold trap was mounted onto the scattering chamber. The vacuum pressure in the chamber was monitored by an Edwards Penning Gauge Head (Model 6) positioned on the cylinder wall, and was generally at $\sim 10^{-5}$ torr (1.33×10^{-3} Pa) at the start of an experiment.

2.3 The Target System (Figure 2.3)

Thick (6 mm) solid targets of Aluminium (Al), Carbon (C), Gold (Au), Silicon/Carbon (SiC), Silicon/Nitrogen (Si/N) and Titanium/Boron (TiB_2) were clamped onto an insulated, semi-cylindrical brass holder which entered the scattering chamber through one of the removable lids (Section 2.2.3). The TiB_2 (Borax Consolidated) SiC and Si/N (Morganite Special Carbons Ltd.) targets were hot compressed, the Si/N target believed to be predominantly Si_3N_4 ($\sim$ 90%) and the remainder consisting of an unknown ratio of Si to N atoms. The target holder could accommodate all six targets together, each target being sufficiently wide ($\gtrsim$ 1 cm) to allow the proton beam to strike at least two positions. Movement from one target position to another was possible without breaking the vacuum in the scattering chamber as was varying the target orientation with respect to the beam. This latter facility permitted a complete 360° rotation about the target holder's axis although in practice, the need for electrical connections restricted it to < 180°. The angle which the target made to the beam could be monitored from outside the scattering chamber.

The target holder was surrounded by an electron suppressor shield which was insulated from the target holder and the scattering chamber. Using a similar design to that used by Sterk, Marks and Saylor (1967),

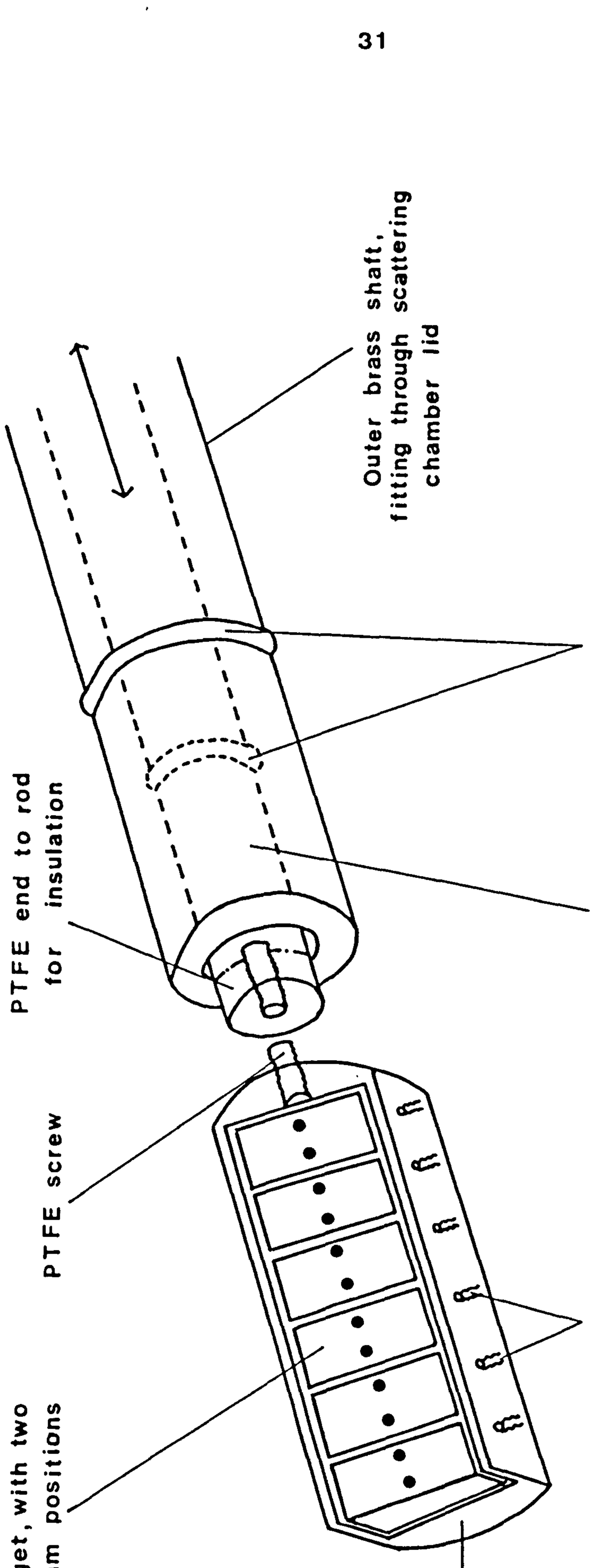

Figure 2.3 Schematic drawing of the target system.

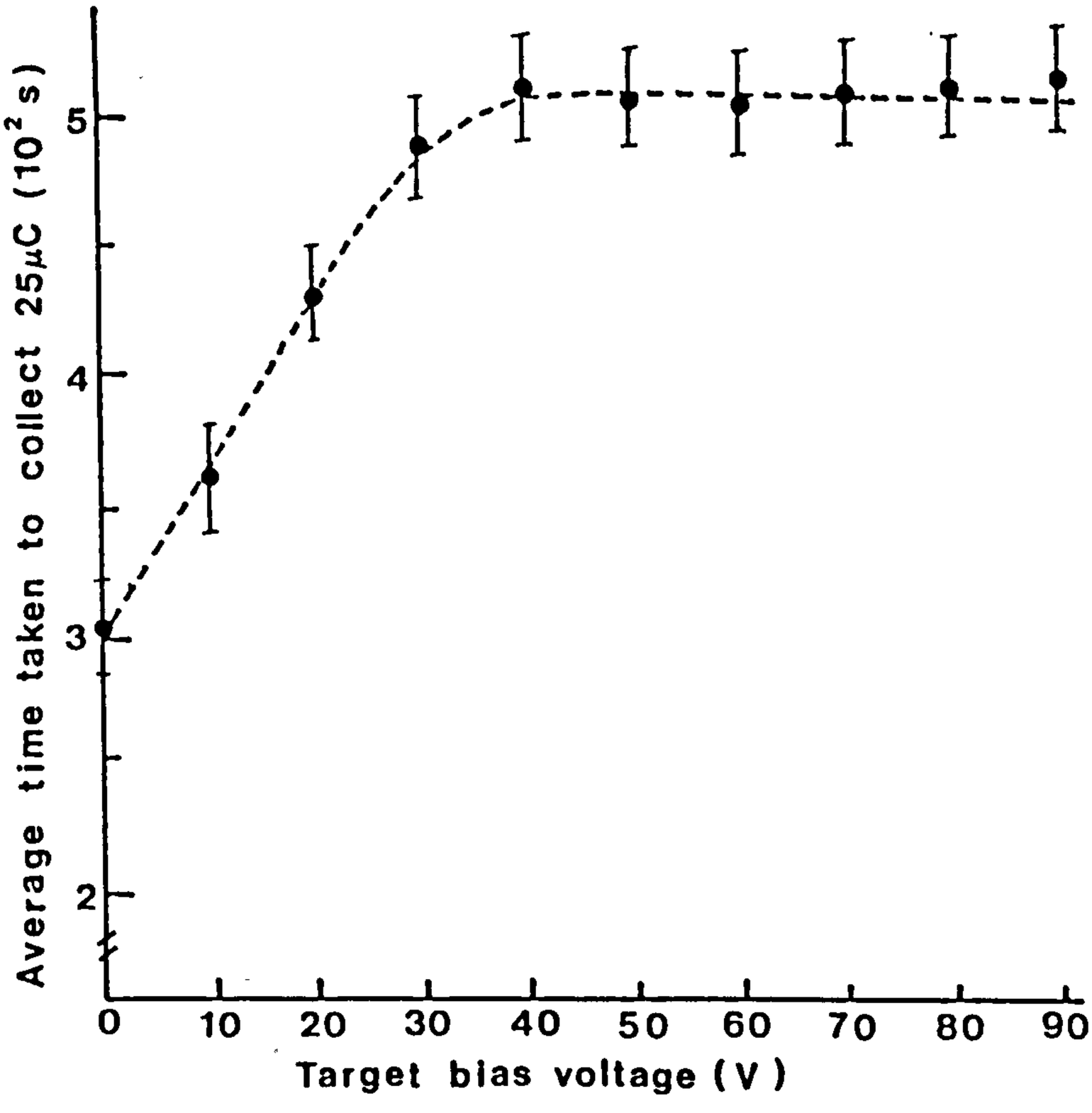

Figure 2.4 The effect of applying a negative bias voltage to the electron suppression shield with the target at 45° to the beam. The points shown are the average values (± *s.d.*), over five readings, for the time taken to collect a charge of 25 μC on the target.

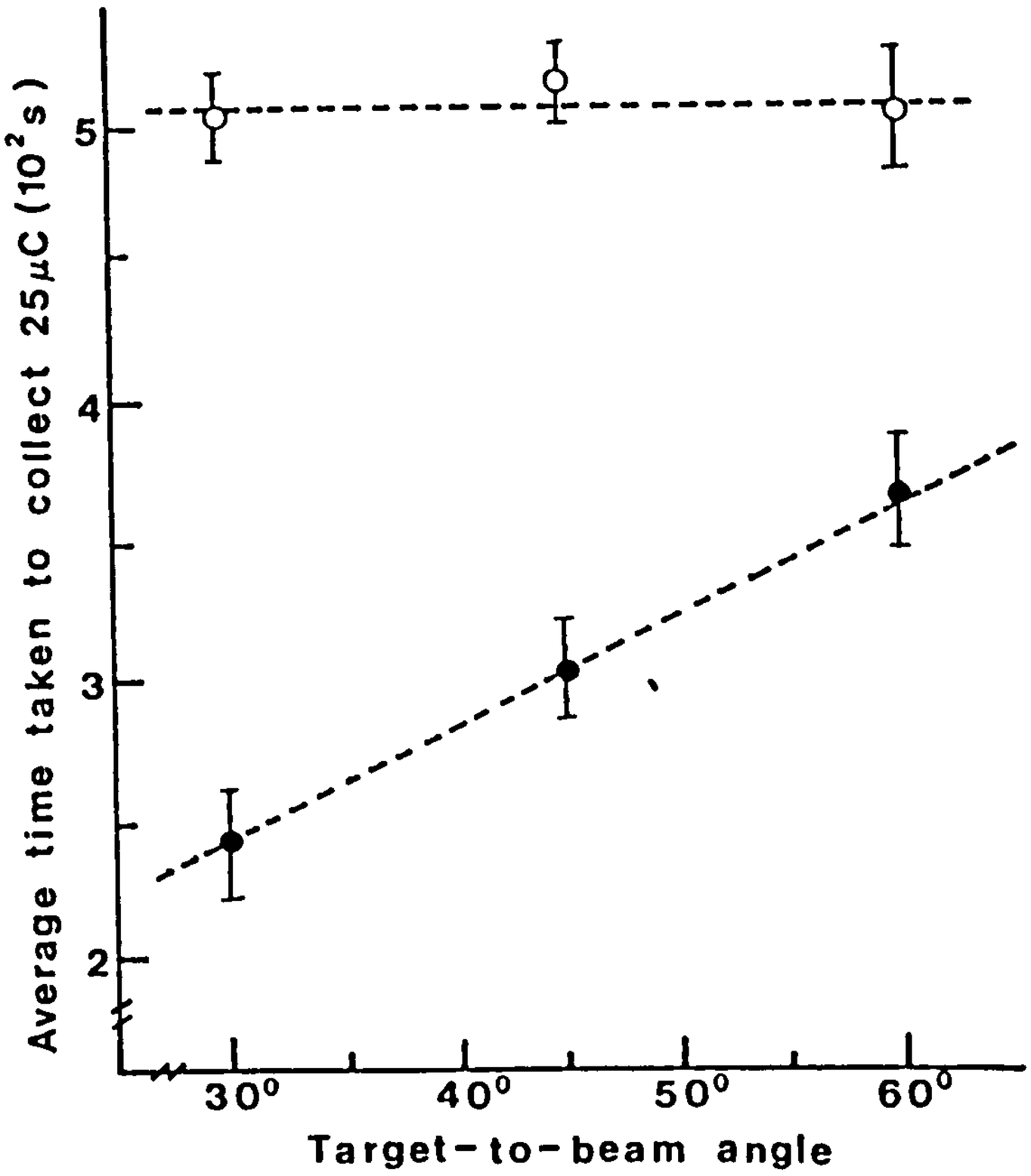

Figure 2.5 The angular dependence of the target charge collection time for an unbiased electron suppression shield (●) and with a -90 V bias voltage on the shield (○). The points shown are the average values (± *s.d.*) taken over five readings.

the target was biased at +90 V relative to the electron shield using a power supply operated with its output floating (but referenced to the shield). This was found to be sufficient to prevent secondary electrons from escaping (Figure 2.4) thereby causing a false indication of beam current - an effect which was observed to be target-angle dependent (Figure 2.5).

The current onto the target was monitored using a charge integrator (Figure 2.2) constructed in the Physics Department of St. Bartholomew's Hospital Medical College. The current onto the target was transferred, through a coaxial cable, to the integrator where a 2 μF capacitor was charged. The voltage across the capacitor was measured and monitored on a 25 V full scale deflection (f.s.d.) meter, thus giving a charge measurement of 50 μC f.s.d. The integrator had a number of different capacitors (1 nF to 2 μF) in its circuitry such that a suitable value could be chosen for the particular current being measured.

2.4 The Detection System

2.4.1 The Proportional Counter (Figure 2.6)

The emitted X-rays were detected using a gas-flow proportional counter (Model 04, J.E. Manson Co., Inc.) directly coupled to a low noise pre-amplifier (Manson Model PAL-01). The counter had a Nickel plated brass body with cylindrical internal symmetry of 1.95 cm diameter and length 7.3 cm. The 3 mm x 10 mm slotted window consisted of a VYNS (a copolymer of 90% Vinyl chloride and 10% Vinyl acetate: $C_{22}H_{23}O_2Cl_9$) window of 28μg.cm^{-2} nominal thickness ($\simeq$ 0.1 μm) on a 60% open 400 lines per inch ($\sim$ 160 lines per cm) Nickel mesh. The transmission characteristics of the window at low photon energies (Manson literature) are shown in Figure 2.7. The X-rays transmitted through the window were absorbed in the cylindrical cavity (maximum diametric gas path

A.

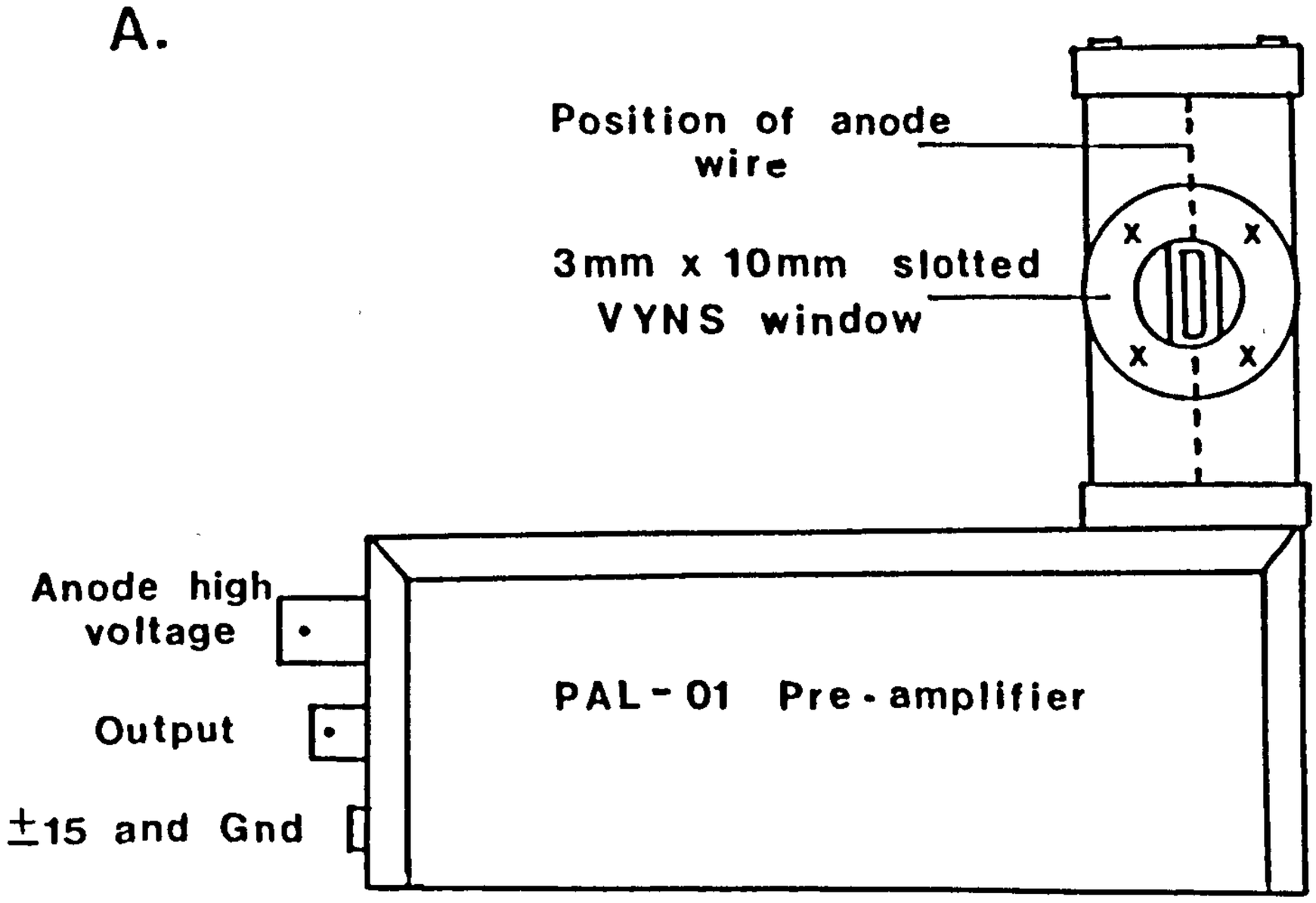

B.

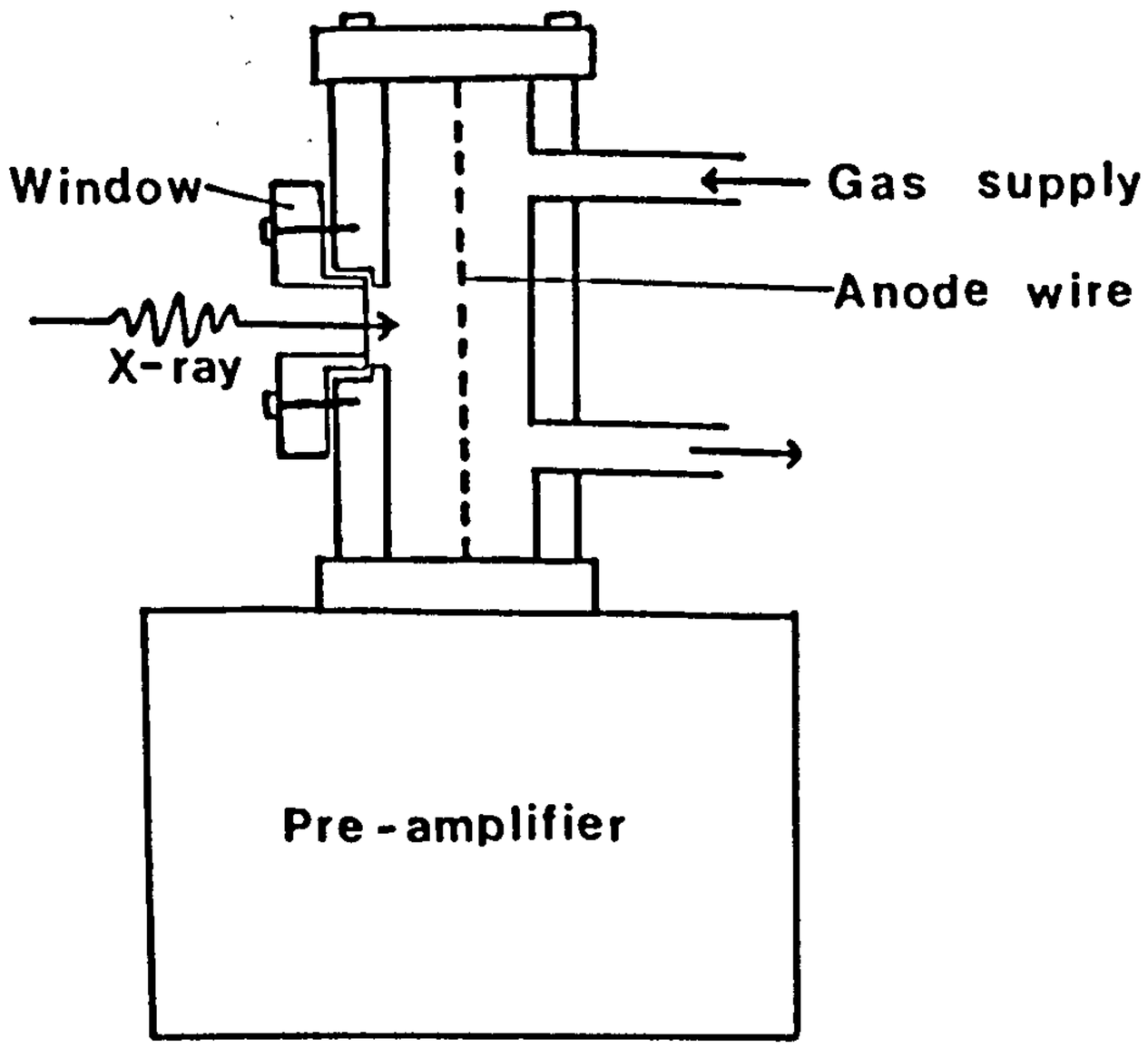

Figure 2.6 The Manson Gas-flow Proportional Counter :
A. Showing the 3 mm x 10 mm slotted VYNS window.
B. Cross-section through the centre of the counter, showing the window, anode wire and gas path.

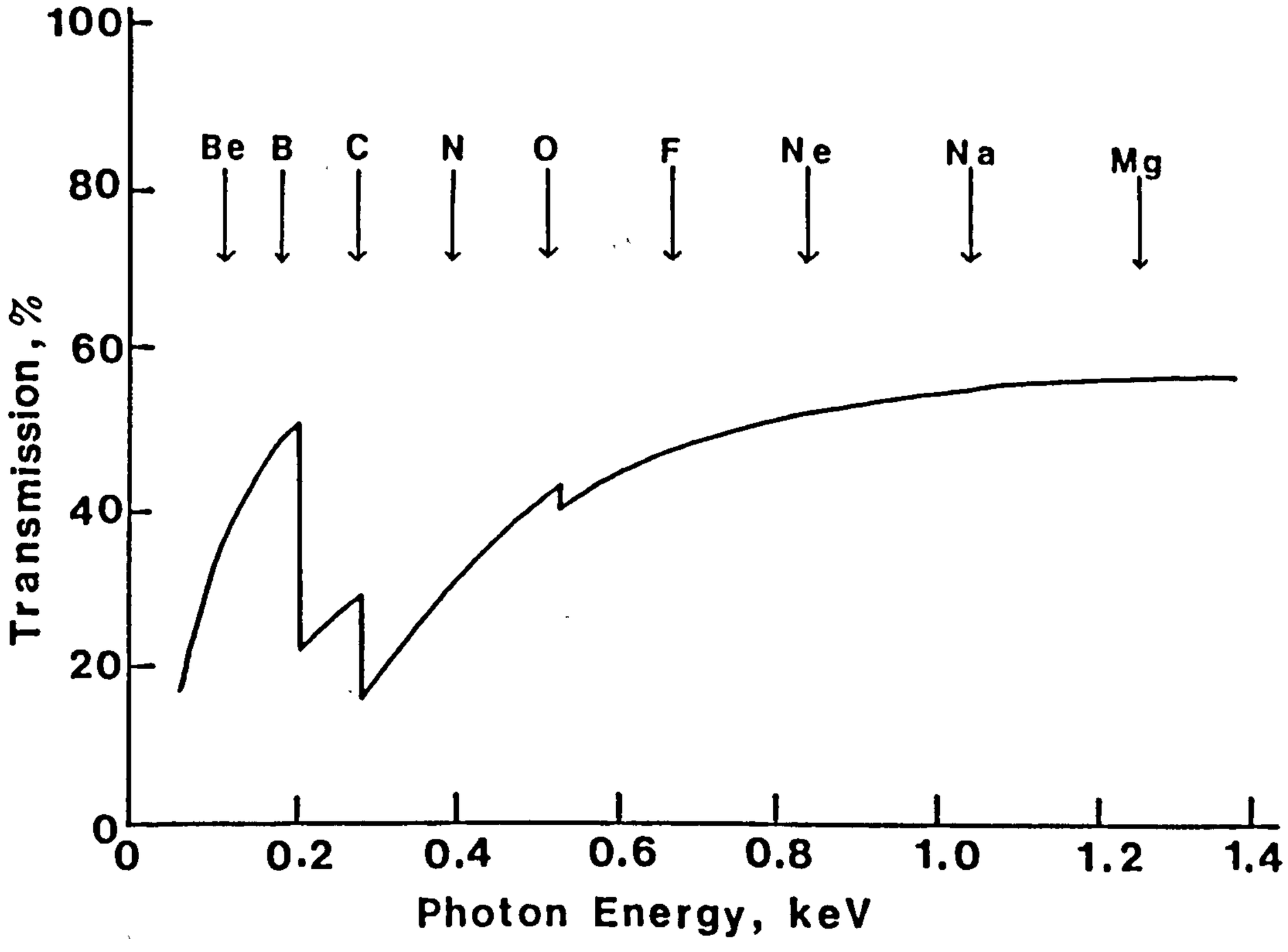

Figure 2.7 The transmission of ultrasoft X-rays through the VYNS window (28 $\mu g.cm^{-2}$ film on a 60 % open mesh). The position of some light element K-lines are indicated.

length of 2.05 cm) by P10 (90% Argon and 10% Methane) gas at a flow rate of 12.5 $cm^3.min^{-1}$. A bias voltage of +1700 V was used on the central 50 μm diameter stainless steel anode for all the X-rays except Titanium K-shell (Ti_K) X-rays, for which, because of their higher energy (4.5 keV), a bias voltage of +1600 V was used to produce less amplification. The collecting area was defined by a 1 mm diameter hole in a Cadmium disc placed in front of the counter window. This also reduced the X-ray intensity and hence the counting rate, avoiding pile-up.

Directly above the counter window was placed 6 μm of Polypropylene ($CH_2 = CHCH_3$) which, when combined with the counter window, was found to be sufficient to prevent backscattered protons entering the counter. The thickness of Polypropylene used was determined experimentally by observing the X-ray emission spectra from a Carbon target, when bombarded with 500keV protons, for varying thicknesses of 'filter' above the detector window. The optimum condition was taken to be the point at which additional layers of filter served only to attenuate the X-rays being produced with no effect on the background (Figure 2.8). An alternative, magnetic method was used in the earlier stages of the work (Figure 2.9). Using the expression for the magnetic field, B, required to deflect charged particles of rest energy W_o and kinetic energy T, through an arc of a circle with radius r (Rosenblatt,1968):

$$B = \frac{[T\ (T + 2\ W_o)]^{\frac{1}{2}}}{300\ r} \qquad 2.1$$

where T and W_o are in MeV, it was possible to estimate the field strength required to deflect any scattered protons away from the window. A simplified drawing is shown in Figure 2.10 (A). With the magnet pole pieces 7 mm apart (Figure 2.9 (A)) and the steel shielding (present to prevent the magnetic field affecting the operation of the pre-amplifier) having a 3 mm aperture, the maximum value of 'x' was

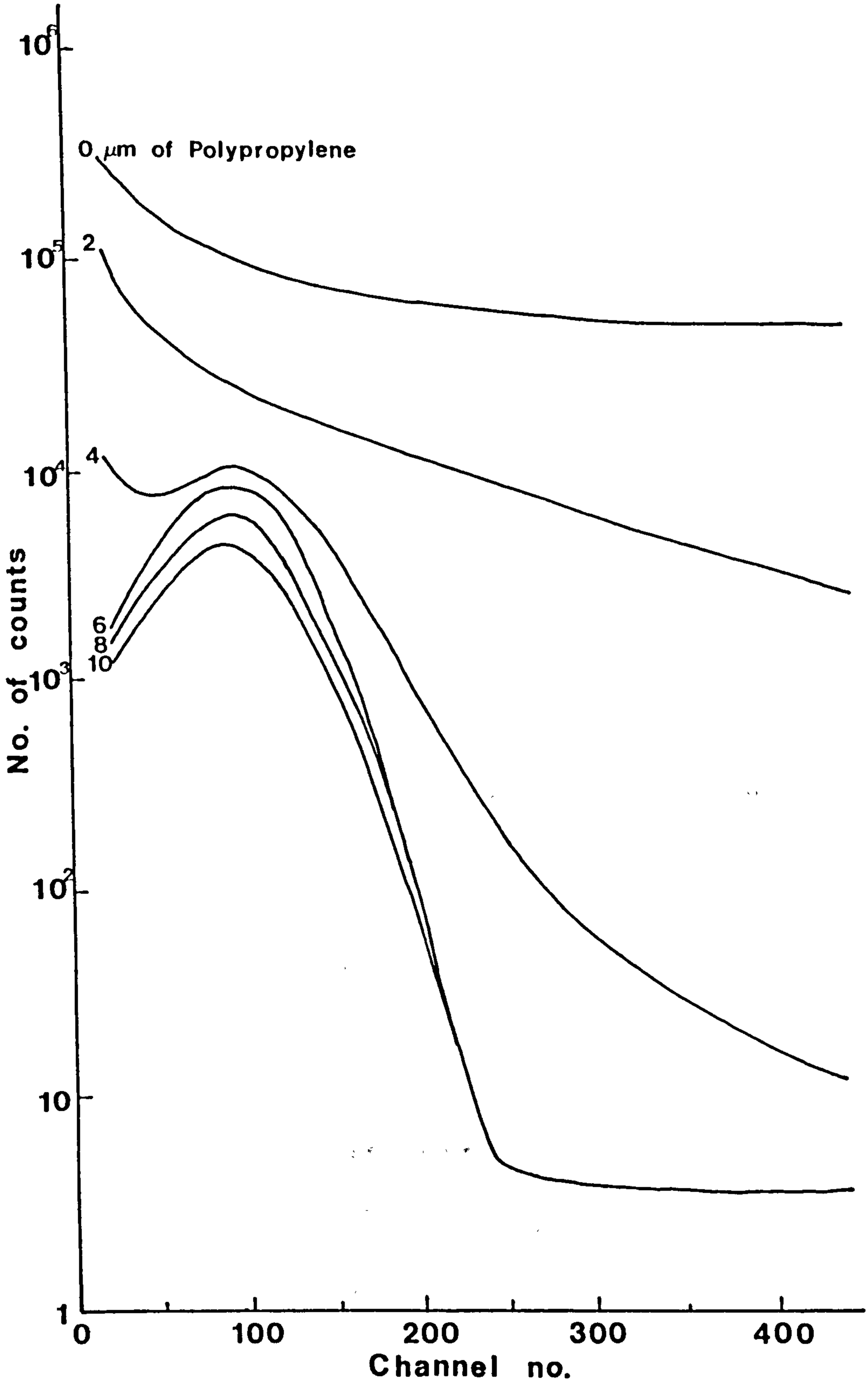

Figure 2.8 The effect of adding Polypropylene filters above the detector window. The spectrum from a Carbon target bombarded with 500 keV protons is shown with filters added in 2 μm increments from 0 to 10 μm of Polypropylene.

A.

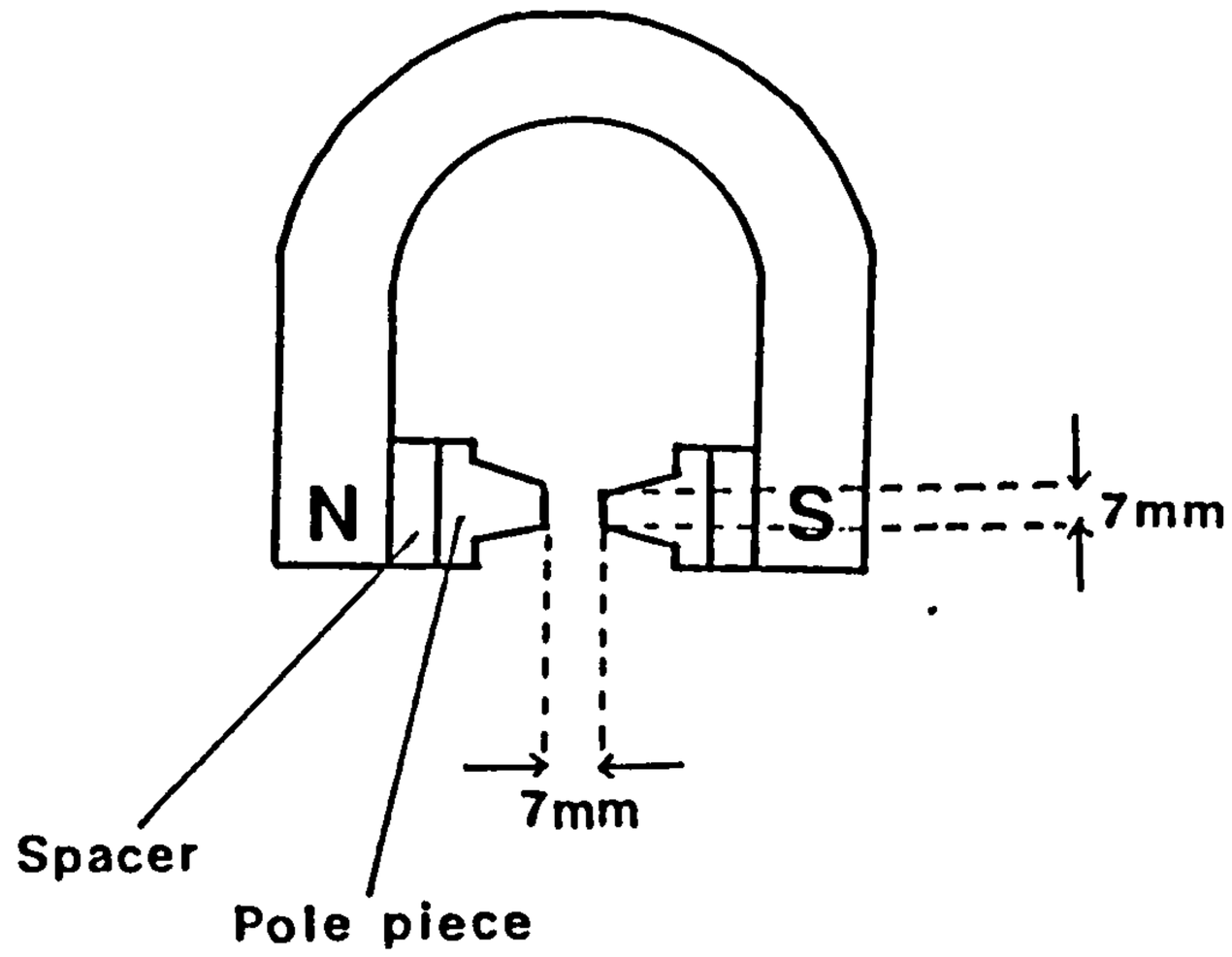

B.

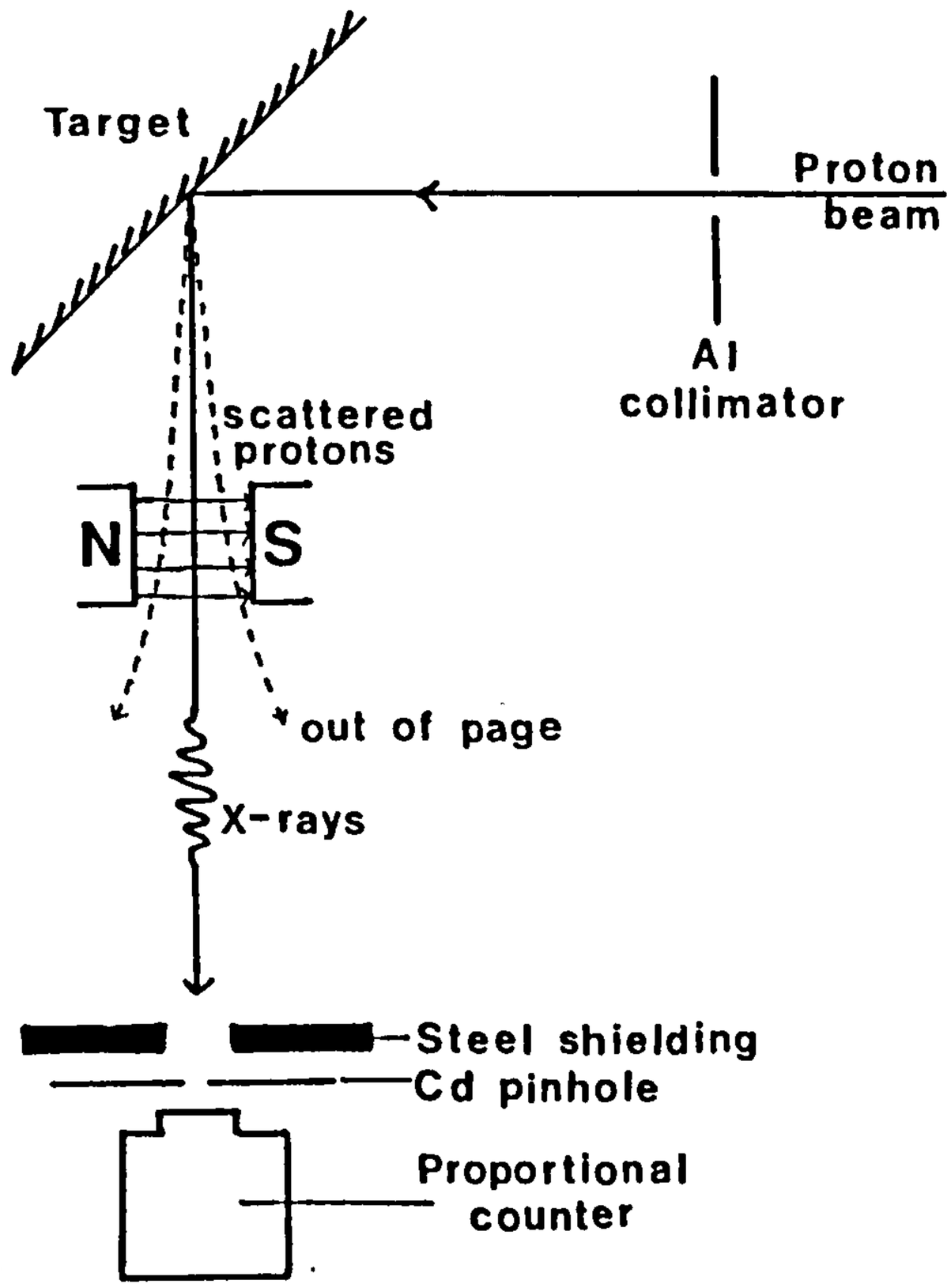

Figure 2.9 Magnetic deflection of scattered protons :
A. Schematic diagram of the magnet (with a magnetic field of ≈ 0.3 T between the pole pieces).
B. The experimental arrangement used.

A.

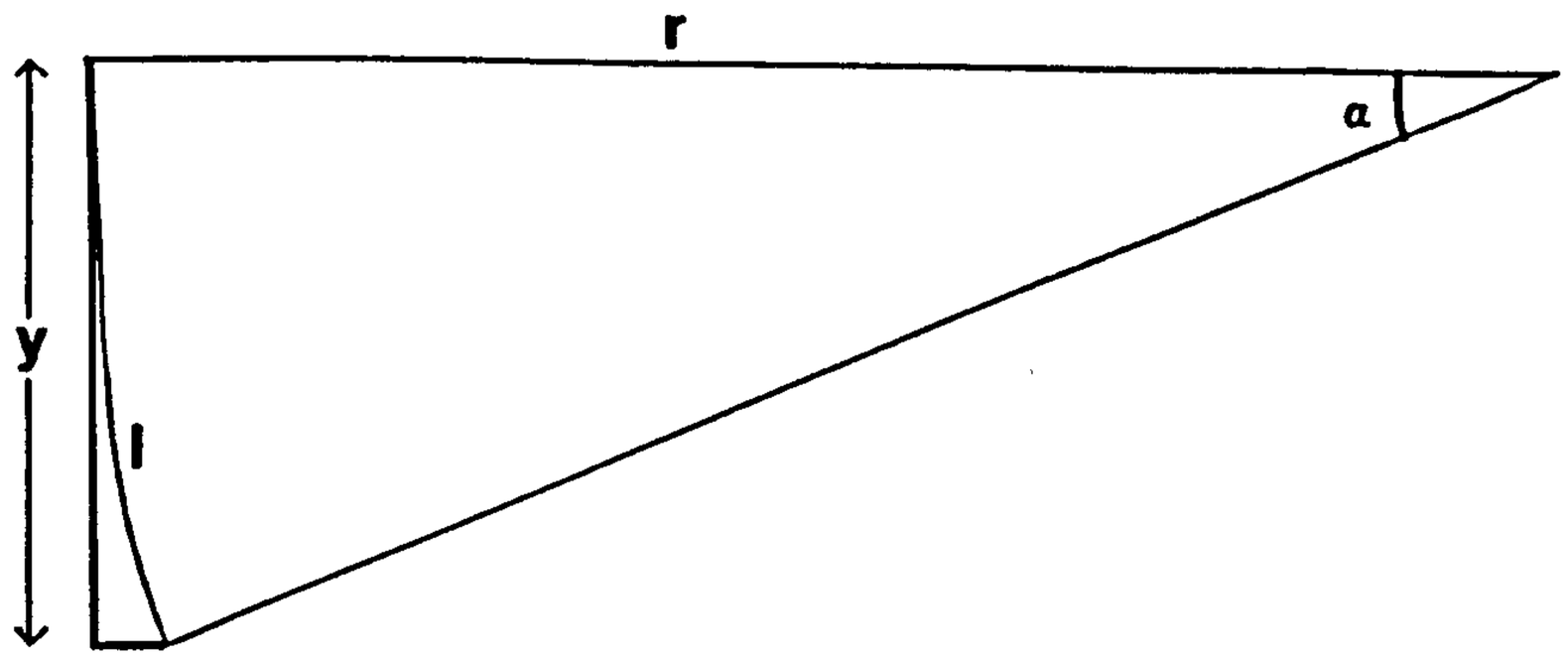

For $y \gg x$, $y \simeq l$ and $\alpha \simeq \tan^{-1}\left(\frac{x}{y}\right)$

$$r = \frac{180}{\pi} \cdot \frac{l}{\alpha} \qquad 2.2$$

B.

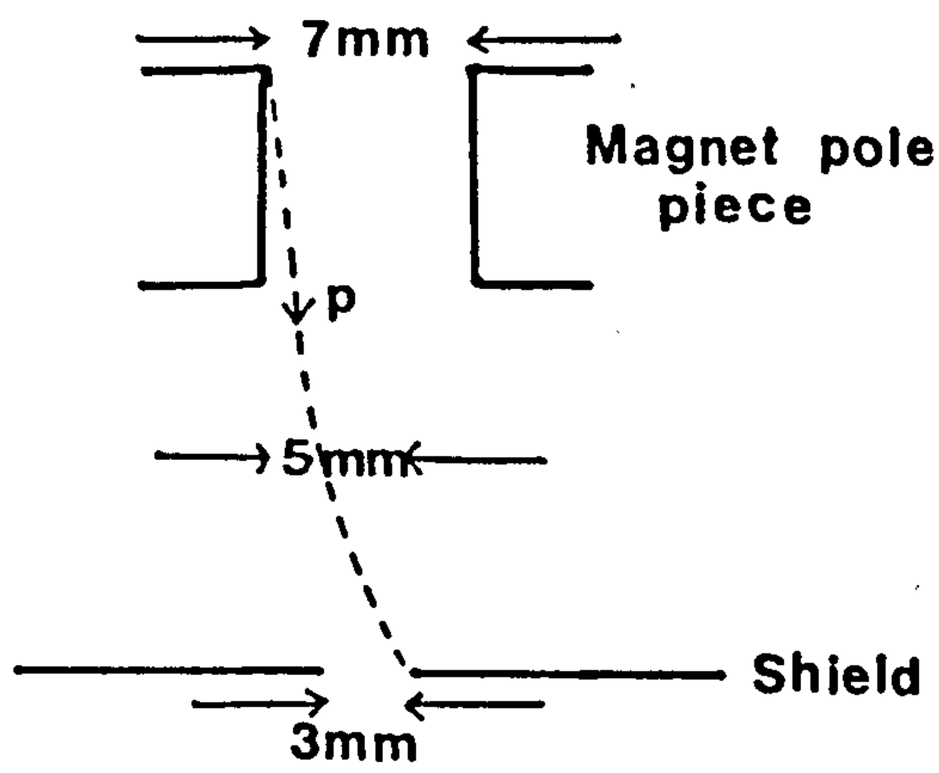

Figure 2.10 Calculation of the magnetic field required to deflect the scattered protons away from the hole in the steel shield.

A. The simplifying assumptions used for the calculation of the radius of the arc of the circle through which the protons are deflected.

B. The maximum distance over which the protons are deflected (x).

taken as 5 mm, where a proton at the edge of the field just avoids the edge of the aperture (Figure 2.10(B)). The distance between the magnet and the shielding was 6 cm (=y). Using the approximations that the arc length, $l \approx y$, and $\alpha \approx \tan^{-1}(x/y)$ in Equation 2.2 gave a value of r = 0.7 m. When used in Equation 2.1 for 500 keV protons this then gave a required magnetic field of 0.15 T.

Since the magnetic field used was 0.3 T, it should have been more than sufficient to deflect even the most energetic backscattered protons. This was not, however, found to be the case. The presence of the magnet between the target and the detector proved to be largely ineffective in reducing the amount of backscattered projectiles entering the counter. There are three possible reasons for this:

(i) It is possible that the protons reached the magnet pole pieces at an angle other than parallel to the axis, and that therefore some protons which were originally well off-course from the 3 mm aperture were curved back to it.

(ii) In the preceding calculation it was assumed that the proton was subjected to the field B throughout the distance y. In practice however, the field only extends for the 7 mm within the pole pieces, after which the proton will continue on a tangential path to the curve it was following. As a result the field required would be higher if the same eventual deflection was to be achieved (Figure 2.11).

(iii) Buck, Wheatley and Feldman (1973) showed that for proton energies $\sim$ 100 keV, a large fraction of the backscattered projectiles were neutralised. Consequently any attempt to remove the recoil particles from the X-ray flux by electrostatic (or magnetic) deflection techniques would be expected to be only partially successful.

It was therefore concluded that an absorbing filter was necessary to prevent back-scattered protons and Hydrogen atoms from entering the proportional counter.

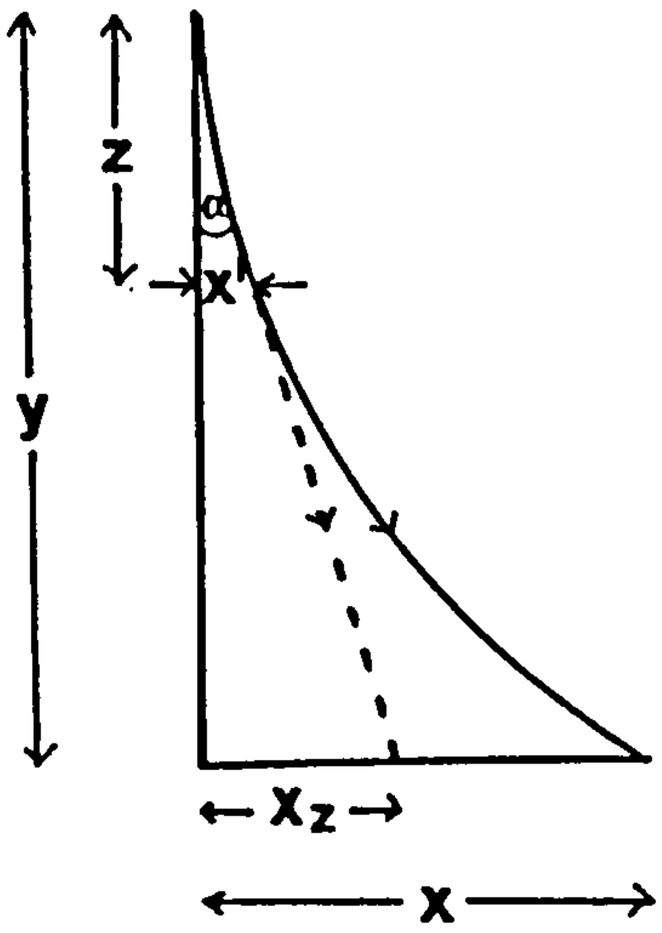

Path of a proton subjected to a magnetic field over a distance: (a) —→— y

(b) --→--- z

Figure 2.11 The correction to the magnitude of the required magnetic field due to the limited extent of the available field (z = 7 mm).

$$\tan \alpha = \frac{x'}{z} = \frac{x_z}{y}$$

$$For\ x_z = 5 \text{ mm} \quad (i.e.\ x_z = x)$$

$$x' = \frac{z.x_z}{y} = 0.6 \text{ mm}$$

Assuming $l \approx z$ (Figure 5.10(A)) and using Equation 2.2, r = 8.5 cm which, when substituted into Equation 2.1, gives $B \approx 1.2$ T.

2.4.2 Associated Electronics (Figure 2.12)

The bias voltage to the counter anode was provided using a Harwell 2000 Series E.H.T. Unit, Type 2147-2 with a variable output from 0 to 3 kV. The Manson PAL-01 pre-amplifier required a + 15 V and a - 15 V input which was obtained from a Harwell 2000 Power Supply Unit, Type 2015-4.

The input stage of the pre-amplifier was a junction field-effect transistor followed by quasi-Gaussian double differentiating and integrating filters with time constants of 0.75 μs. The output pulse was bipolar with the positive lobe leading. The output from the pre-amplifier was fed into the input of a Norland IT-5300 Multichannel Analyser (MCA) (Norland Instruments/Ino-Tech. Inc.). Using the pulse height analysis mode of the MCA the energy distribution of the output from the pre-amplifier was obtained and recorded onto the GOULD PN6000 mini-computer.

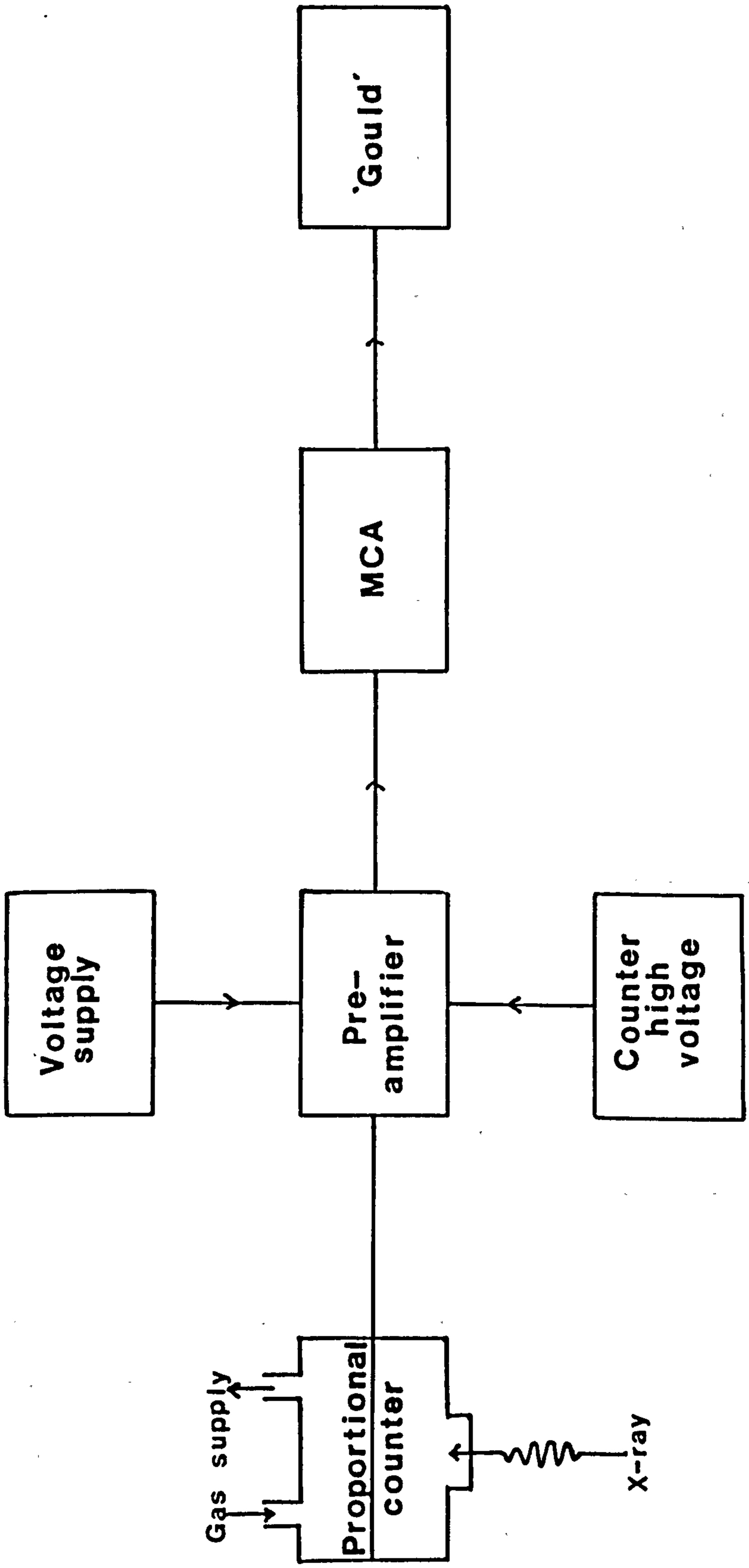

Figure 2.12 Schematic drawing of the ultrasoft X-ray detection system with the associated electronics.

CHAPTER 3

CALIBRATION OF THE VAN DE GRAAFF MACHINE

The potential at the high-voltage terminal of the Van de Graaff accelerator was monitored using an in-built generating voltmeter. The voltmeter assembly consisted of a motor-driven rotor, with four equally spaced, 45° sectors cut out of it and a stator plate divided into eight insulated 45° sectors. As the rotor rotates, it alternately exposes the high voltage terminal to the stator and shields from it each sector. Triangular wave alternating current (a.c.) voltages are thus electrostatically induced between adjacent sectors of the stator, the voltages being directly proportional to the terminal voltage. Four alternate stator sectors of the voltmeter are connected in parallel to the a.c. terminal of a bridge-rectifier circuit, located on the voltmeter housing, which is connected to the generator voltage meter on the control console of the accelerator.

The generating voltmeter was calibrated using the (p, γ) resonances method (Hunt and Jones, 1953). A low-energy proton may be captured by a nucleus which is thereby transformed into a residual nucleus in a highly excited state (Figure 3.1). Instead of expelling the incident particle again (scattering), the residual nucleus may decay to the ground state and rid itself of the binding energy of the particle by the emission of one or more gamma (γ) rays. The capture of a proton depends upon the energy being of the correct amount needed to enable the residual nucleus to be formed in one of its excited states, and is thus resonant in nature.

For the calibration of the Van de Graaff accelerator, resonant proton energies were looked for in Fluorine and Aluminium. Strong

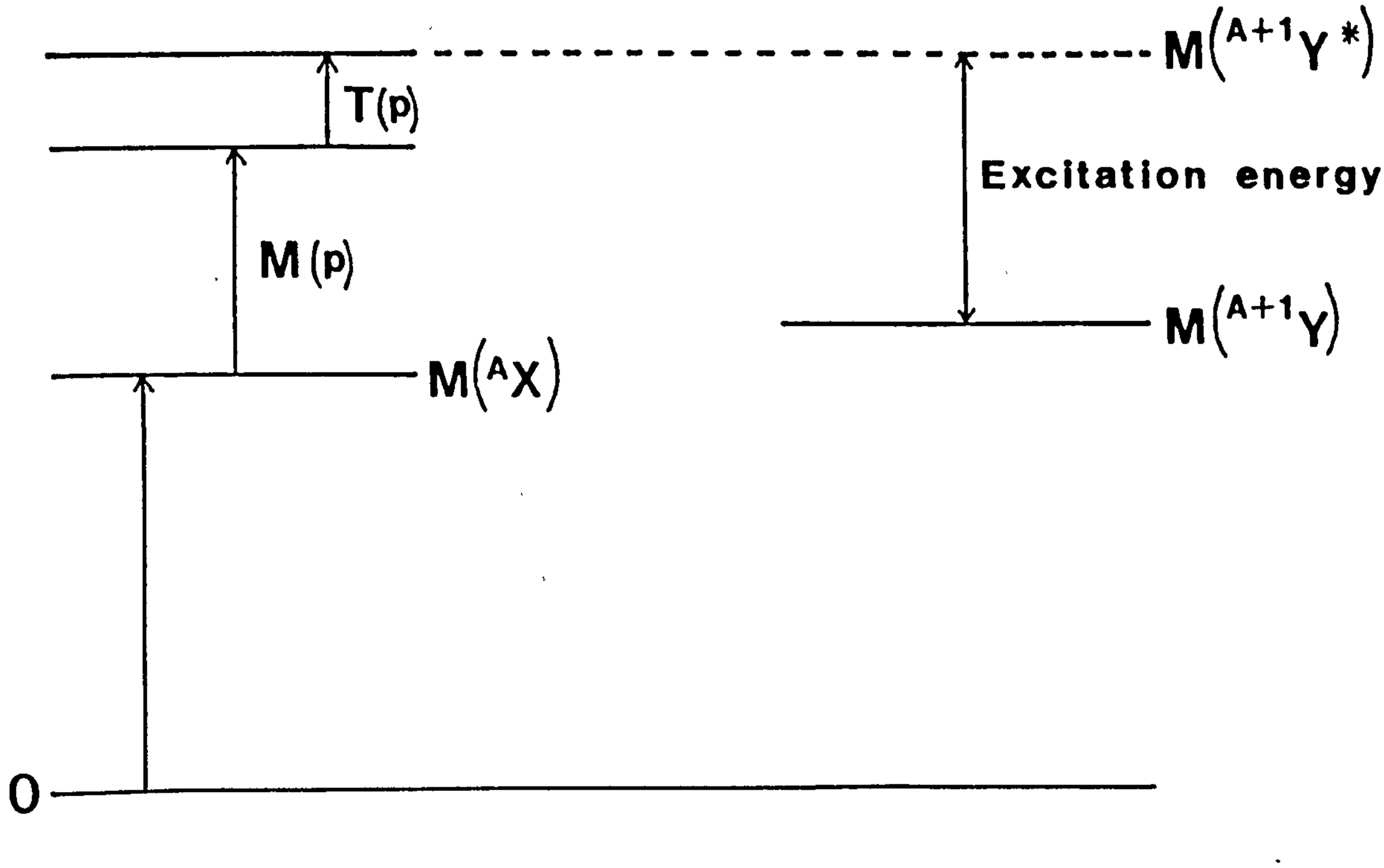

Figure 3.1 Proton capture : the target nucleus (^{A}X) captures a proton (rest-mass, M(p), kinetic energy, T(p)) to form a residual nucleus in an excited state, $^{A+1}Y^{*}$.

resonances have been observed at 340.4 keV and 483.1 keV in Fluorine (Hornyak *et al.*, 1950) and at 633 keV in Aluminium (Meyer, Venter and Reitmann, 1975). For these cases the expected reactions are as given below, with the available excitation energy, E, being calculated from:

$$E = M\ (^{A}X) + M\ (p) + T\ (p) - M\ (^{A+1}Y) \qquad 3.1$$

where M, the rest mass, was obtained from the Table of Isotopes, 1978, and T (p) was the kinetic energy of the proton.

For Fluorine, the resonance reaction is given by

$$^{19}F\ (p, \gamma)\ ^{20}Ne \qquad 3.2$$

with M (^{19}F) = 17697.032 MeV, M (^{20}Ne) = 18622.977 MeV and M (p) = 938.280 MeV. Thus for a proton of energy T (p) = 340.4 keV, the excitation energy was calculated to be 12.675 MeV, and for T (p) = 483.1 keV, E = 12.818 MeV. For Aluminium, the reaction is given by

$$^{27}Al\ (p, \gamma)\ ^{28}Si \qquad 3.3$$

with M (^{27}Al) = 25133.333 MeV and M (^{28}Si) = 26060.537 MeV giving an excitation energy of 11.709 MeV for a 633 keV proton.

For both Fluorine and Aluminium the calculated excitation energies are such that the energy levels of the residual nucleus are very close together. For example, for the ^{20}Ne nucleus there are over 125 energy levels in the region of E = 11 to 23.5 MeV. As a result, an increase of only 0.14 MeV in the energy of the protons interacting with the Fluorine nuclei is sufficient to give rise to a second resonance position.

The emission of γ-rays from thick ($\gtrsim$6 mm) targets of Aluminium and Fluorine (in the form of a Calcium fluoride, CaF_2 target) was studied using a 3" diameter x 3" length (75 mm x 75 mm) cylindrical Thallium activated Sodium iodide (NaI(Tl)) crystal detector in conjunction with a Norland IT-5300 MCA. As is shown in Figure 3.2 the

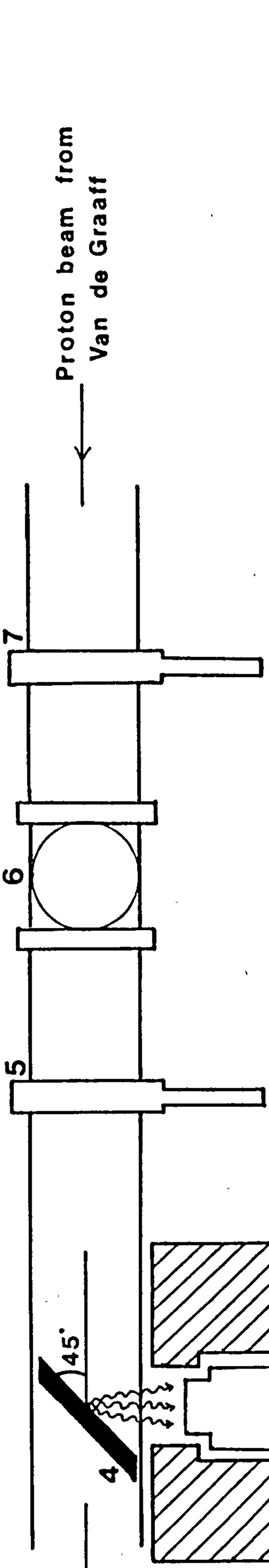

Figure 3.2 Schematic diagram of the beam line as used during the calibration of the Van de Graaff (viewed from above).

1. Lead shielding
2. Pre-amplifier
3. 3" x 3" NaI(Tl) detector
4. Target (Al or CaF_2)
5. Main gate valve
6. Vacuum pumping system
7. Auxillary gate valve

target was positioned at 45° to the proton beam with the detector at 90°. In order to eliminate most of the background counts the NaI(Tl) detector was encased in ≳ 5 cm Lead shielding. The accelerator terminal voltage was varied in 10 kV increments around the expected resonance positions (340.4 ± 0.5 and 483.1 ± 0.5 keV for ^{19}F, 633 ± 1 keV for ^{27}Al). The energy spectrum from the NaI(Tl) detector was collected and, using the integrating facility on the MCA, the number of emitted γ-ray counts measured (Figure 3.3) as a function of the accelerating voltage. As shown in Figure 3.3, for the Fluorine resonances it was possible to integrate a specific γ-ray peak which, using the two γ-rays from a ^{60}Co source for calibration, was found at a photon energy $E_\gamma \sim 7$ MeV. However, for the Aluminium target, no such peak was observed - the γ-ray energy believed to be ≳ 10 MeV (High Voltage Ltd. literature) thus extending beyond the range of the 1024 channels of the MCA. However, for a 75 mm x 75 mm cylindrical NaI(Tl) crystal a large proportion of the photon interactions would be expected to be of the Compton effect kind, where only a portion of the energy of the photon is deposited in the crystal thus giving rise to a range of reduced height pulses which would appear on the MCA scale. The resonance position for the Al target was therefore deduced by integrating the total energy spectrum above channel 100 (thus eliminating most of the low energy, accelerator voltage independent noise).

Having normalised all the measurements to the proton beam current, thick target γ-ray yield curves were obtained (Figures 3.4 and 3.5). The resonance positions were identified at the point of maximum gradient of the thick target yield curves versus accelerating voltage (Khan and Potter, 1964):

$^{19}F(p, \gamma)\ ^{20}Ne$ - 340 ± 10 kV
480 ± 10 kV

$^{27}Al(p, \gamma)\ ^{28}Si$ - 640 ± 10 kV.

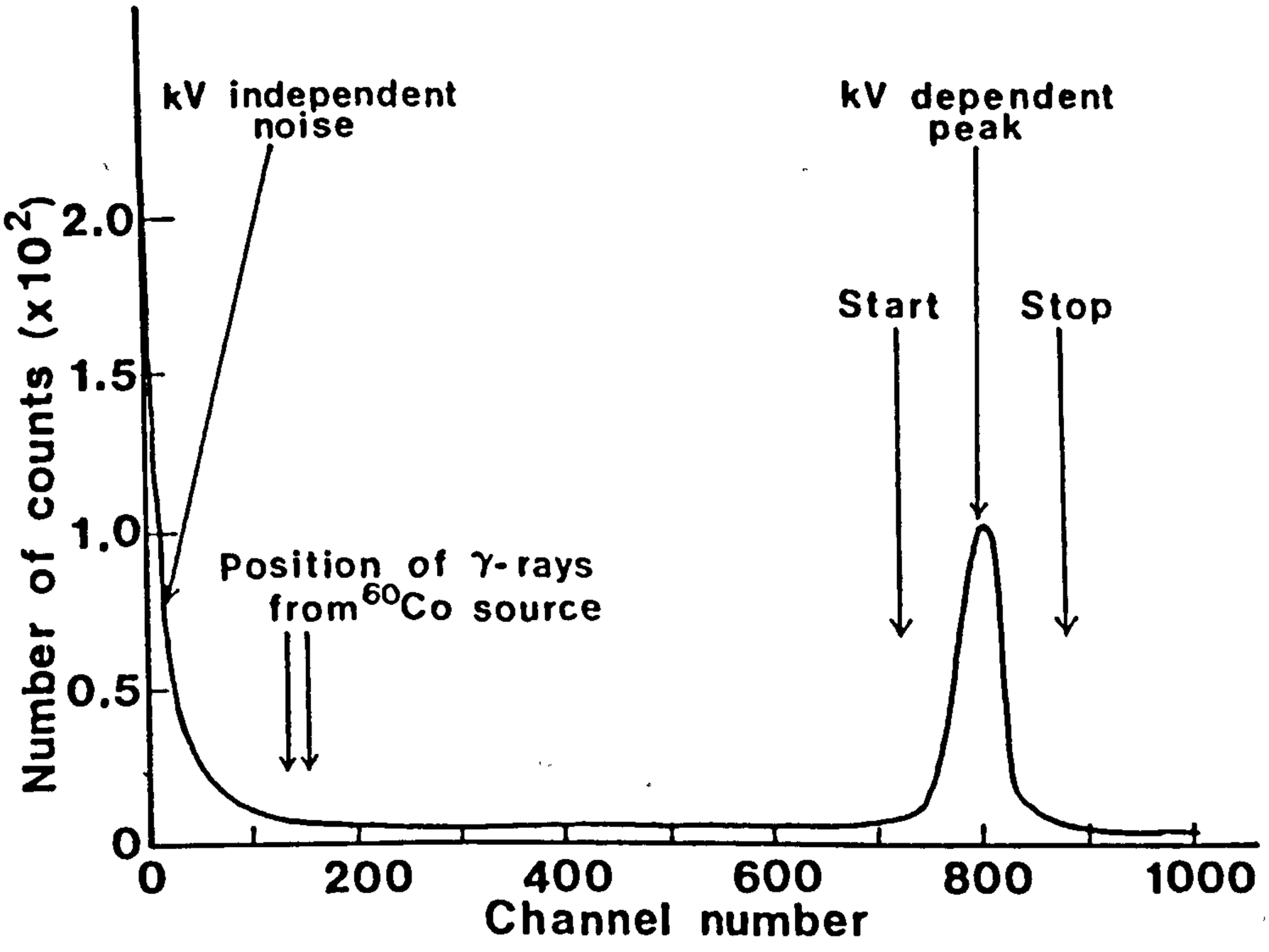

Figure 3.3 An example of the energy spectrum obtained from the CaF_2 target with an accelerating voltage of 350 kV. The γ-ray counts were obtained by integrating the peak between the *'Start'* and *'Stop'* positions. An energy calibration based on the γ-rays from a ^{60}Co source (at 1.17 and 1.33 MeV) gave the energy at channel 800 as ≈ 7 MeV (assuming a linear energy scale through the origin).

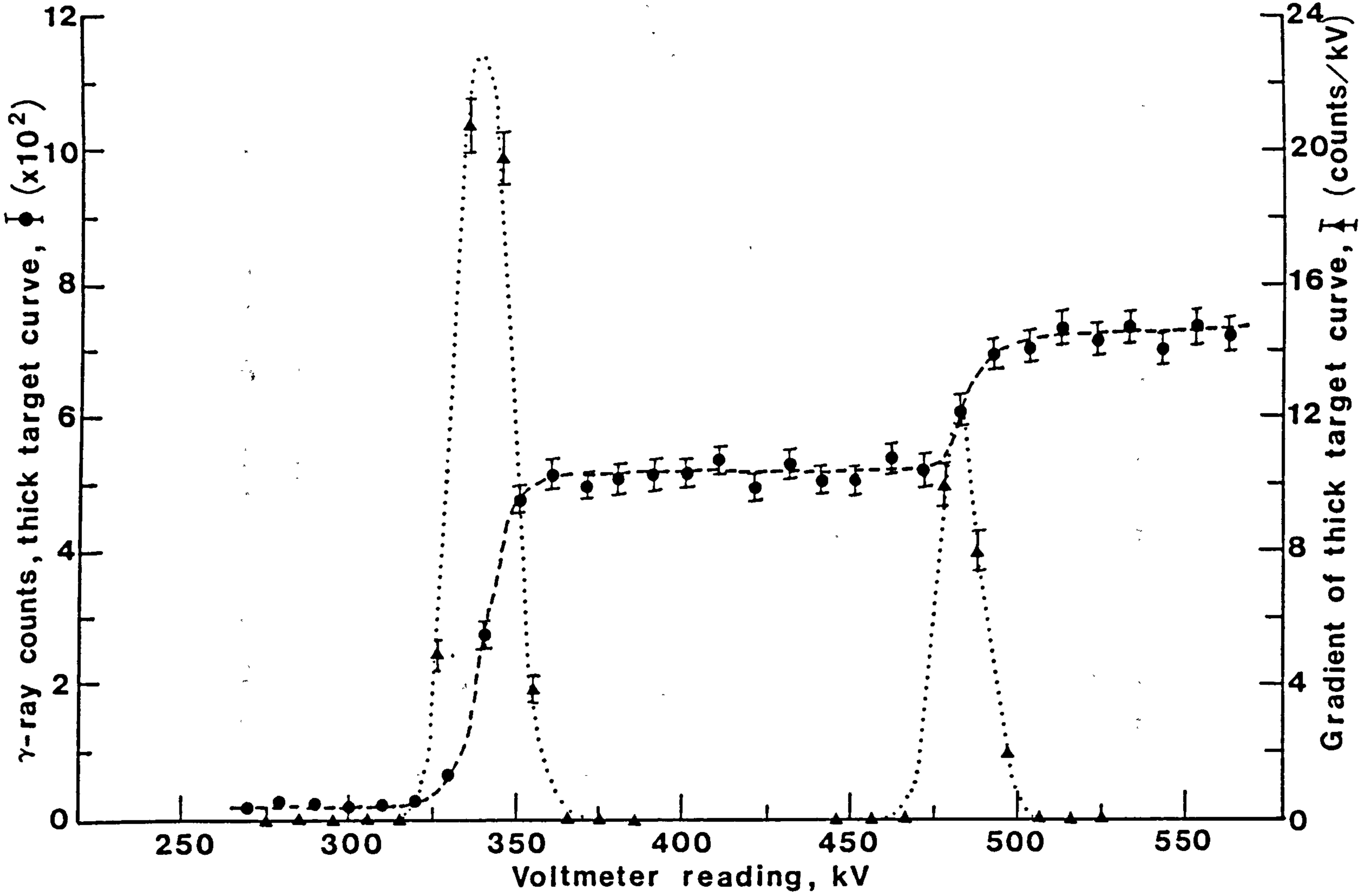

Figure 3.4 Thick target γ-ray yield curve for $^{19}F(p,\gamma)^{20}Ne$ with calculated gradient to give resonance positions. Error bars were assumed to be given by $(counts)^{\frac{1}{2}}$.

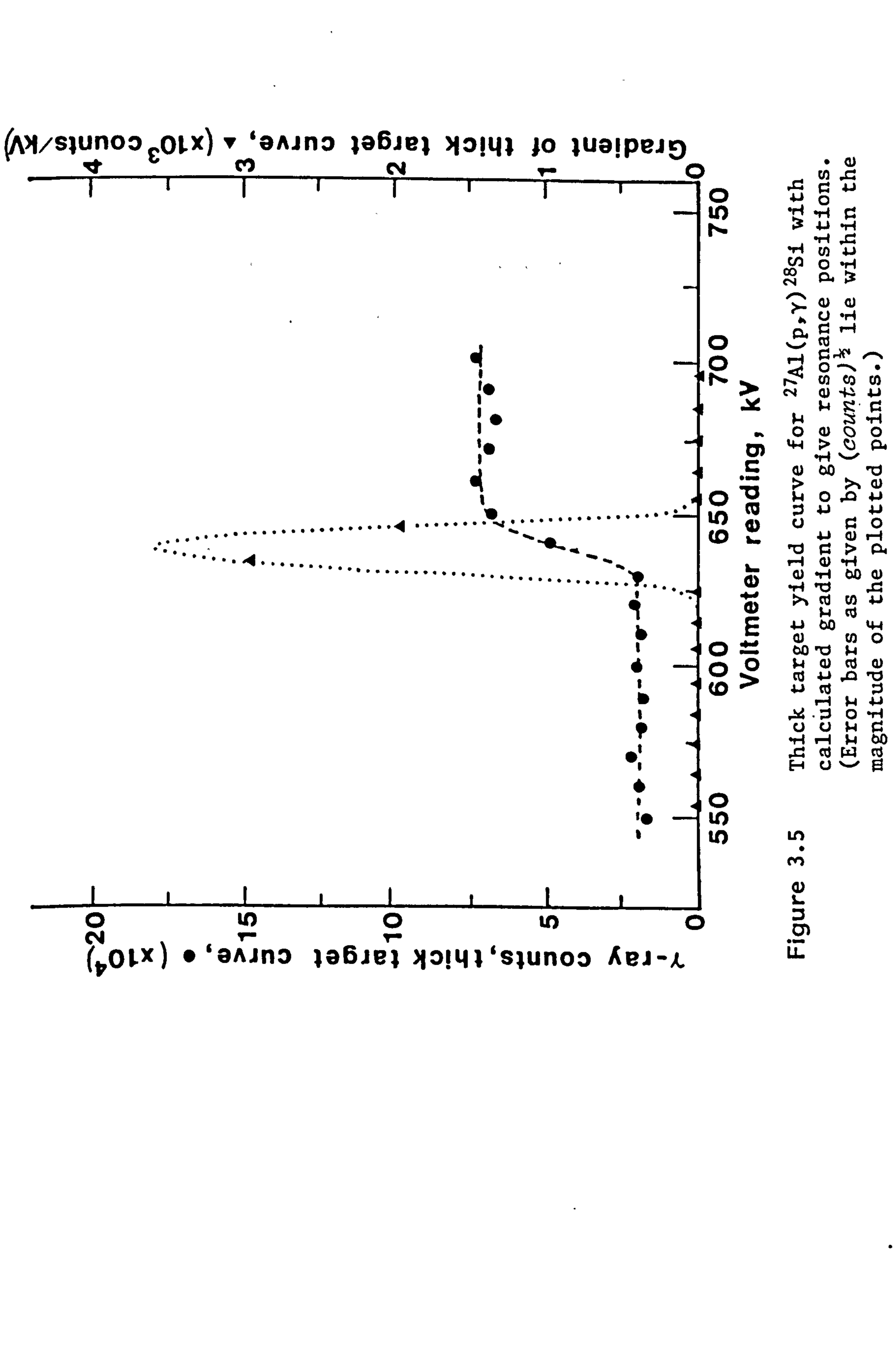

Figure 3.5 Thick target yield curve for $^{27}Al(p,\gamma)^{28}Si$ with calculated gradient to give resonance positions. (Error bars as given by $(counts)^{\frac{1}{2}}$ lie within the magnitude of the plotted points.)

In order to calibrate the proton beam energy against the accelerating voltage, as monitored by the generating voltmeter, the observed resonance positions were compared with the known resonance energies as given by Hornyak *et al.*, 1950 and Meyer, Venter and Reitmann, 1975. This information was then used to produce a calibration graph for the actual proton beam energy in terms of the generating voltmeter reading (Figure 3.6). The vertical error bars were smaller in magnitude than the size of the plotted points.

From the three resonance positions observed it was seen that the terminal voltage as measured by the generating voltmeter was within ± 5 kV of the proton beam energy, thus lying within the experimental accuracy of ± 10 kV under which the major part of this work was undertaken (Chapter 5).

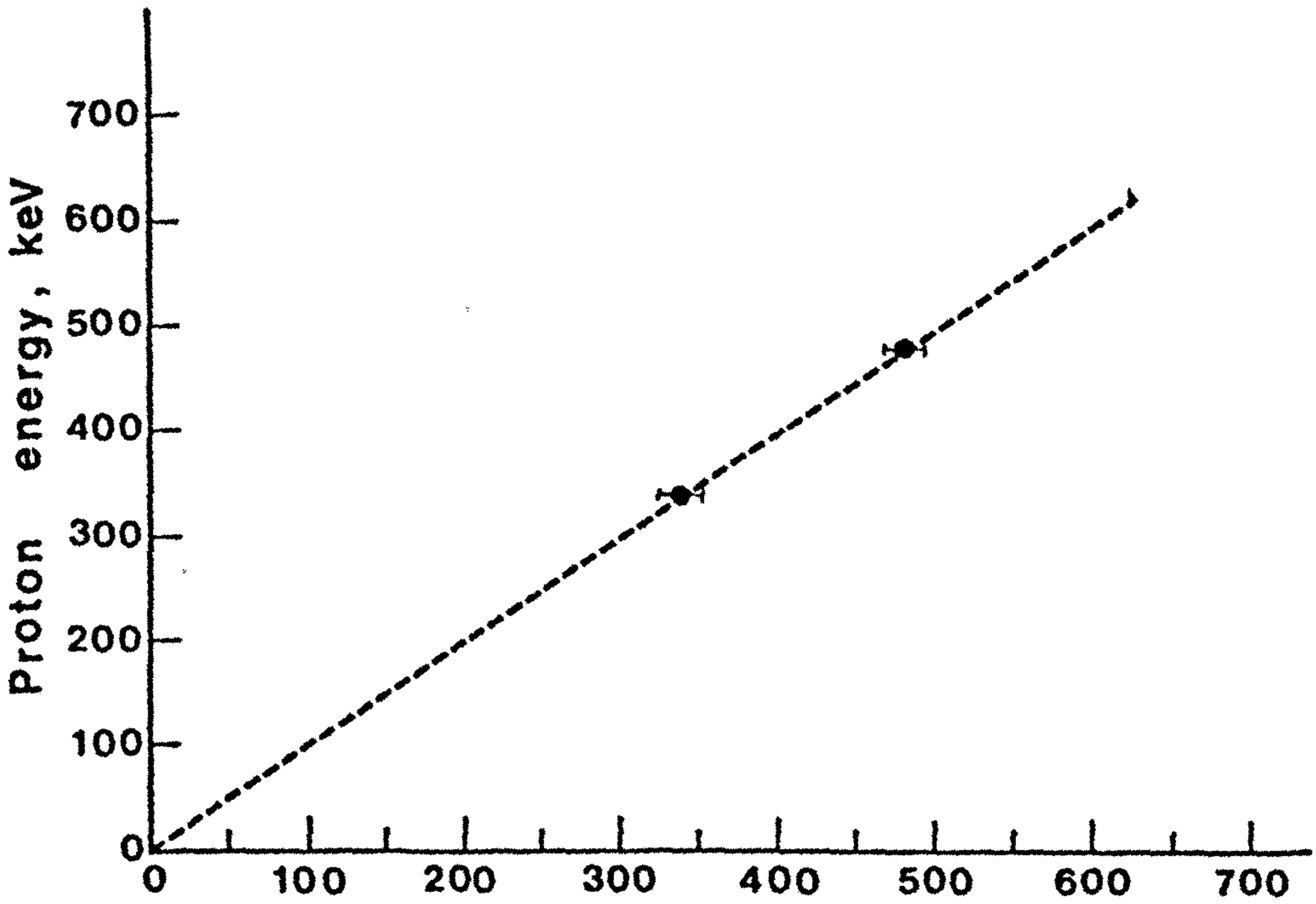

Figure 3.6 Calibration graph for the proton energy as a function of the generating voltmeter reading. The regression line is shown ($y = 0.99x + 1.59$) with a correlation coefficient, $r = 1.0$.

CHAPTER 4

DATA ANALYSIS

After recording the energy distribution spectra of the emitted ultrasoft X-rays on the GOULD mini-computer, the data were transferred to the Amdahl 470 V/8 computer at the University of London Computer Centre (U.L.C.C.). Using the Amdahl, multiparameter least-squares curve fitting was attempted using the CERN Program Library Routine called "MINUIT" (James and Roos, 1975,1985).

A large class of problems in many different fields can be reduced to the problem of finding the smallest value taken by a function of one or more variable parameters by minimising the difference (chi-square, χ^2) between the theory and the experimental data. This difference is represented by the function $F\ (X_n)$ where X_n are the unknown parameters. The function $F\ (X_n)$ need not be known analytically, but may be specified by giving its value at any point X in the space of the parameters.

MINUIT is a package of programmes that minimises a function of n variables, computes the covarience matrix and finds the true errors (James, 1978). This system of programmes incorporates three different minimisation methods, each of which may be used individually, or in combination with the others, depending on the behaviour of the function and the requirements of the user. The three minimisation subroutines available are:-

(i) 'SEEK' - a Monte-Carlo searching subroutine.

(ii) 'SIMPLX' - a subroutine employing the simplex method of Nelder and Mead (1965).

(iii) 'MIGRAD' - a minimisation subroutine based on a variable metric method (Fletcher, 1970).

MINUIT is generally used to minimise a χ^2 function or a negative log likelihood function. It is assumed that the point where the function $F\ (X)$ takes on its lowest value, *FMIN*, determines the most likely or best-fit parameter values, and that the region over which the function takes on values smaller than *(FMIN + UP)* corresponds to a confidence interval for which the confidence level is determined by the value of the positive constant *UP*. For example, if $F\ (X_n)$ is a χ^2 function of one variable parameter $(n = 1)$, a value of $UP = 1.0$ determines 'one-standard-deviation' errors corresponding to a confidence level of 68%.

For the analysis of the X-ray energy spectra, only the subroutine SIMPLX was used. This is a relatively fast method even when far from the minimum but will also converge to the exact minimum. It does not compute the covariance matrix but gives order-of-magnitude estimates of its diagonal elements - the parameter errors (James, 1972).

4.1 Subroutine SIMPLX

In the minimisation method of Nelder and Mead (1965) the information about the function $F\ (X_1, ----, X_n)$ consists of its values at $n + 1$ points, forming a simplex. A simplex is the smallest n- dimensional geometrical figure with $n + 1$ vertices : a triangle for $n = 2$, a tetrahedron for $n = 3$, *etc.* How the method works can be shown by considering a two dimensional case as in Figure 4.1.

The three starting simplex points $(P_1,\ P_2\ and\ P_3)$ are supplied by the user and the function $F\ (X_n)$ is evaluated at each point. Let the point P_H be that at which the function value is highest (worst) and P_L that at which it is lowest. Let $\overline{P}$ be the centre-of-mass of all points in the simplex except P_H , that is

$$\overline{P} = \frac{1}{n} \left\{ \sum_{i=1}^{i=n+1} P_i - P_H \right\} . \qquad 4.1$$

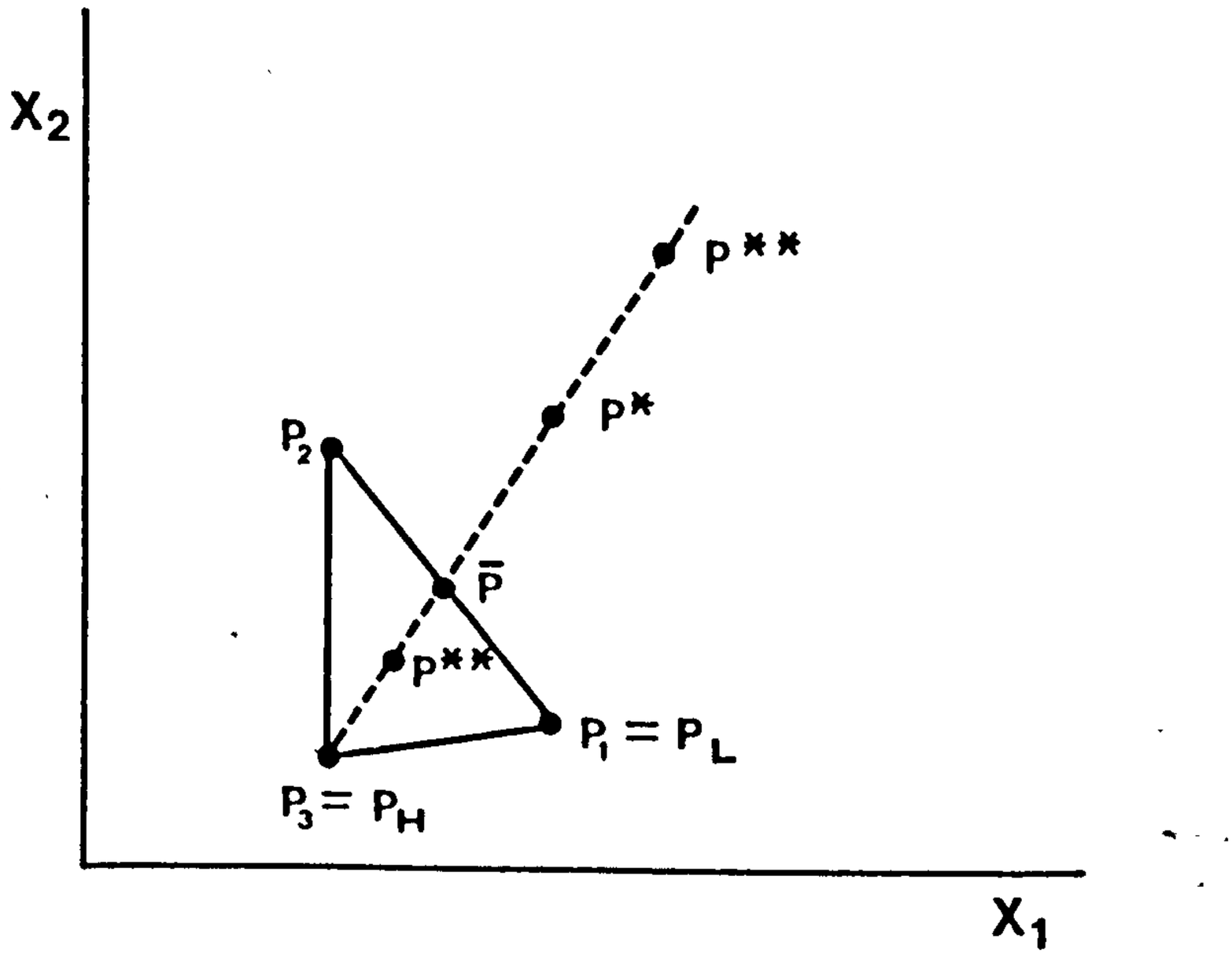

Figure 4.1 A two dimensional simplex formed from P_1, P_2 and P_3 (refer to text for detail).

From the original simplex, a new simplex is formed by replacing P_H with a better point if possible. The first attempt to find a better point is made by reflecting P_H with respect to $\overline{P}$, producing $P^* = \overline{P} + (\overline{P} - P_H)$. If $F(P^*) < F(P_L)$, a new point is tried at $P^{**} = \overline{P} + 2(\overline{P} - P_H)$, but if $F(P^*) > F(P_H)$ then a new point is tried at $P^{**} = \overline{P} - \frac{1}{2}(\overline{P} - P_H)$. The best of the new points then replaces P_H in the simplex for the next step, unless neither of them is better than P_H in which case a whole new simplex is formed around P_L, with dimensions reduced by a factor of 0.5.

A convenient convergence criterion for the simplex method is based on the difference $F(P_H) - F(P_L)$. The iterations are stopped when this difference is less than a pre-set value. As a final step, the function is evaluated at $\overline{P}$, which is often slightly better than $F(P_L)$.

MINUIT is designed to handle any function, $F(X_n)$, and hence the definition of the function to be minimised must be supplied separately. This is done through the subroutine "FCN" in which $F(X_n)$ is calculated and which is therefore supplied by the user.

4.2 Subroutine FCN (Appendix 1)

The energy distributions of the characteristic X-rays, as detected by the proportional counter, were found to be well fitted by a linear combination of Gaussian curves super-imposed on a constant background - one Gaussian curve describing the energy distribution for each target characteristic X-ray energy.

If the area under a Gaussian curve is 'A' then the distribution function is defined as:

$$P_G\ (x,\mu,\sigma,A) = \frac{A}{\sigma\sqrt{2\pi}} \cdot \exp\ \{ -\tfrac{1}{2} \left(\frac{x-\mu}{\sigma} \right)^2 \} \qquad 4.2$$

(Bevington, 1969)

where x is the value of a random observation,

μ is the mean value of the parent distribution

and σ is the standard deviation of the distribution.

The standard deviation, σ, can be defined in terms of the full-width at half-maximum (F.W.H.M.), Γ, of the curve (Bevington, 1969):

$$\Gamma = 2.354\ \sigma \qquad 4.3$$

and substituting this into Equation 4.2 gives

$$P_G\ (x,\mu,\Gamma,A) = \frac{0.94.A}{\Gamma} \cdot \exp\ \{ -2.77\ \left(\frac{x-\mu}{\Gamma} \right)^2 \} \qquad 4.4$$

The subroutine FCN was written to include a possible three Gaussian distributions with separate μ, Γ and A combined with a constant background, c. Thus the complete distribution, Y_{theor}, as described in FCN is given by:

$$\begin{aligned} Y_{theor} = & \frac{0.94.A_1}{\Gamma_1} \cdot \exp\ \{ -2.77\ \left(\frac{x-\mu_1}{\Gamma_1} \right)^2 \} \\ & + \frac{0.94.\ A_2}{\Gamma_2} \cdot \exp\ \{ -2.77\ \left(\frac{x-\mu_2}{\Gamma_2} \right)^2 \} \\ & + \frac{0.94.\ A_3}{\Gamma_3} \cdot \exp\ \{ -2.77\ \left(\frac{x-\mu_3}{\Gamma_3} \right)^2 \} + c \end{aligned} \qquad 4.5$$

where the variable parameters were c, A_i, μ_i and Γ_i (i = 1, 2, 3) with x, the MCA channel number, being directly proportional to the photon energy.

Having calculated the theoretical spectrum obtained above (Y_{theor}), FCN proceeded to calculate the χ^2 using the definition of James (1972):

$$\chi^2\ (X) = \sum_{k=1}^{K} \left(\frac{Y_k - T_k(X)}{\sigma_k} \right)^2 \qquad 4.6$$

where Y_k and σ_k are measured values and errors, and $T_k\ (X)$ are the values predicted by the model, depending on some parameter(s), X.

In the case of the X-ray energy spectra considered in this work, Equation 4.6 became:

$$\chi^2 = \sum_{x=1}^{NPTS} \left(\frac{Y_{obs}(x) - Y_{theor}(x)}{\sqrt{Y_{obs}(x)}} \right)^2 \qquad 4.7$$

where *NPTS* represented the number of channels considered on the MCA and $Y_{obs}(x)$ was the observed X-ray energy spectrum as collected on the MCA. The error in the observed values was taken to be given by the square root of the value, $(Y_{obs}(x))^{\frac{1}{2}}$.

The function $F(X_n)$ required by MINUIT for minimisation was defined in the subroutine FCN to be the χ^2 as given in Equation 4.7 with $Y_{theor}(x)$ being defined by Equation 4.5. Before starting the iterative process of minimising $F(X_n)$, MINUIT requires an initial estimate of the parameter values (c, A_i, μ_i *and* Γ_i, i = 1,2,3) to facilitate the location of the minimum. The choice of initial parameter values were based on estimates taken from the MCA as the spectra were collected.

Once MINUIT had located the minimum value of the function $F(X_n)$, and hence had calculated the best fitted curve to the experimental data, the calculated values for each parameter were returned to the user. Of particular interest were the mean energy of the photon - given by the mean value (μ) of the distribution, the width (Γ) of the distribution and the intensity (A) produced for a given proton charge onto the target.

CHAPTER 5

EXPERIMENTAL SECTION

5.1 Experimental Procedures

The characterisation of proton-induced ultrasoft X-rays in this study comprised three experimental investigations:

(i) a study of target surface contamination and the way it effects the intensity of emitted X-rays,

(ii) the angular distribution of the X-rays resulting from target absorption and attenuation effects, and

(iii) the dependence of X-ray yield on proton energy.

5.1.1 Surface contamination study

With the target and proportional counter at 45° and 90° to the beam respectively, the proton beam was run continuously onto a target with an X-ray energy distribution spectrum being recorded for each 25 μC increment of charge collected on the target as measured by the charge integrator. This was done for both the Aluminium and Carbon targets, with the proton beam energy being kept constant at 500 ± 10 keV and the current kept at 35 ± 1 nA. Each spectrum took ~ 12 min to collect and the beam was run onto the target for a total time of 8 hours in the case of Carbon and 17 hours for Aluminium. In the latter case there was an interval of about 12 hours after the first 9 hours, during which the beam was off.

For the Aluminium target, the dependence of the rate of contamination build-up on beam current was also considered. Keeping the proton beam energy at 500 ± 10 keV, spectra were collected for beam currents of 10, 40 and 70 nA. Spectra were also recorded for a beam current of 50 nA but with a reduced proton energy of 300 ± 10 keV. All the spectra were collected for a constant charge of 25 μC on the target.

5.1.2 Angular distribution study

To study the angular distribution of the emitted X-rays the proton beam was run onto the target for a total collected charge of 25 μC (taking approximately 500s). The proton beam energy was kept at 500 ± 10 keV with a beam current of ~ 50 nA. For each target angle (θ) X-ray spectra were recorded over a full range of detector angles ($40° \leq \alpha \leq 130°$), in 10° steps. Four complete sets of data were taken for each target element, with $\theta = 30°$, 45° and 60°, and the data combined to give average yields. A clean target surface was used for each complete set, cleaning being achieved using a combination of abrasion with fine emery cloth, then soaking the target in one molar solution of Hydrochloric acid and finally immersing it in an ultra-sound bath for about three hours.

The starting angle with which a given set of data was taken was varied between experiments in order to eliminate any possible effect of the order in which data were collected. In addition to the full scan of detector angles for each target angle, data were also obtained for $\alpha = 90°$ at the start and end of each target angle scan so as to provide information on any surface contamination build-up (Section 6.1).

5.1.3 Proton energy dependence of X-ray emission

Using the Aluminium and Carbon targets, the effect of varying the proton beam energy on the yield of X-rays was studied. With the target and detector at 45° and 90° to the beam respectively, spectra were collected for 25 μC of collected charge on the target. The proton beam energy was varied between 225 ± 10 keV and 700 ± 10 keV, the beam current being maintained at 35 ± 1 nA throughout.

5.2 Results

Within the text of this, and following chapters, reference is made to the characteristic X-ray energies. The values given are taken from

the X-Ray Data Booklet (1986) and, where the energies of the lines differ, the energy of the K_{α_1} line is used. However, the compilation of Storm and Israel (1970) show that the weighted average of the K-shell X-ray energies varies less than 1% from the energy of the K_{α_1} line, even for the highest atomic number element considered for this work (Titanium, Z = 22). The characteristic X-rays are denoted as 'A_s' where A represents the chemical symbol of the target element and s denotes the electron shell (K,L,M). For example, Al_K represents the K-shell characteristic X-ray of Aluminium. The characteristic energies studied in this work are given in Table 5.1 (with the Au_M X-ray energy taken from 'Table of X-ray Emission Energies').

Having collected the X-ray energy distribution spectra on the MCA the data were recorded on computer and transferred to the Amdahl 470V/8 computer at U.L.C.C. where MINUIT (Chapter 4) was used to fit Gaussian curves to the data. The output from MINUIT came in the form of a plotted spectrum with both experimental data and theoretical fit shown. Also given were the theoretical positions, F.W.H.M. and area under the peaks (with an estimate of the uncertainties), the background level and the average value of χ^2 (Equation 4.7) per channel. This latter value gave a measure of the goodness of the theoretical fit and was found to be $\leq$ 2 per channel in all cases. The error on each of the variable parameters was less than 1%.

Shown in Figure 5.1 ((i) - (vii)) are examples of the spectra obtained (both experimental and theoretical) for each target. Figure 5.1 ((i) - (vi)) were obtained with 1700V on the proportional counter anode (Section 2.4.1) whereas Figure 5.1 (vii) was obtained with an anode voltage of 1600V. Also shown is the variation between different qualities of Aluminium (Figure 5.1 (iii) A and B), where the 'pure' Aluminium spectrum gives a far better fit between theory and experimental data in the region of channels 200 - 400 than the 'Dural' Aluminium alloy. Over these 200 channels the average χ^2 value for the

Characteristic X-ray	Energy *(keV)*
B_K	0.183
C_K	0.278
N_K	0.392
Al_K	1.487
Si_K	1.740
Au_M	2.120
Ti_K	4.511

Table 5.1 The energies of the characteristic X-rays studied.

Figure 5.1 Examples of the spectra obtained from each of the targets when bombarded with 500 keV protons:

(i.) TiB_2 target, 1700 V on the counter anode wire (Peak at channel 75)
(ii.) C target, 1700 V on the counter anode wire (Peak at channel 91)
(iii.A) Dural Al target, 1700 V on the counter anode wire (Peaks at channels 90 and 585)
(iii.B) Pure Al target, 1700 V on the counter anode wire (Peaks at channels 90 and 580)
(iv.) SiC target, 1700 V on the counter anode wire (Peaks at channels 90 and 690)
(v.) Si/N target, 1700 V on the counter anode wire (Peaks at channels 90 and 690)
(vi.) Au target, 1700 V on the counter anode wire (Peaks at channels 90 and 850)
(vii.) TiB_2 target, 1600 V on the counter anode wire (Peak at channel 690).

i.

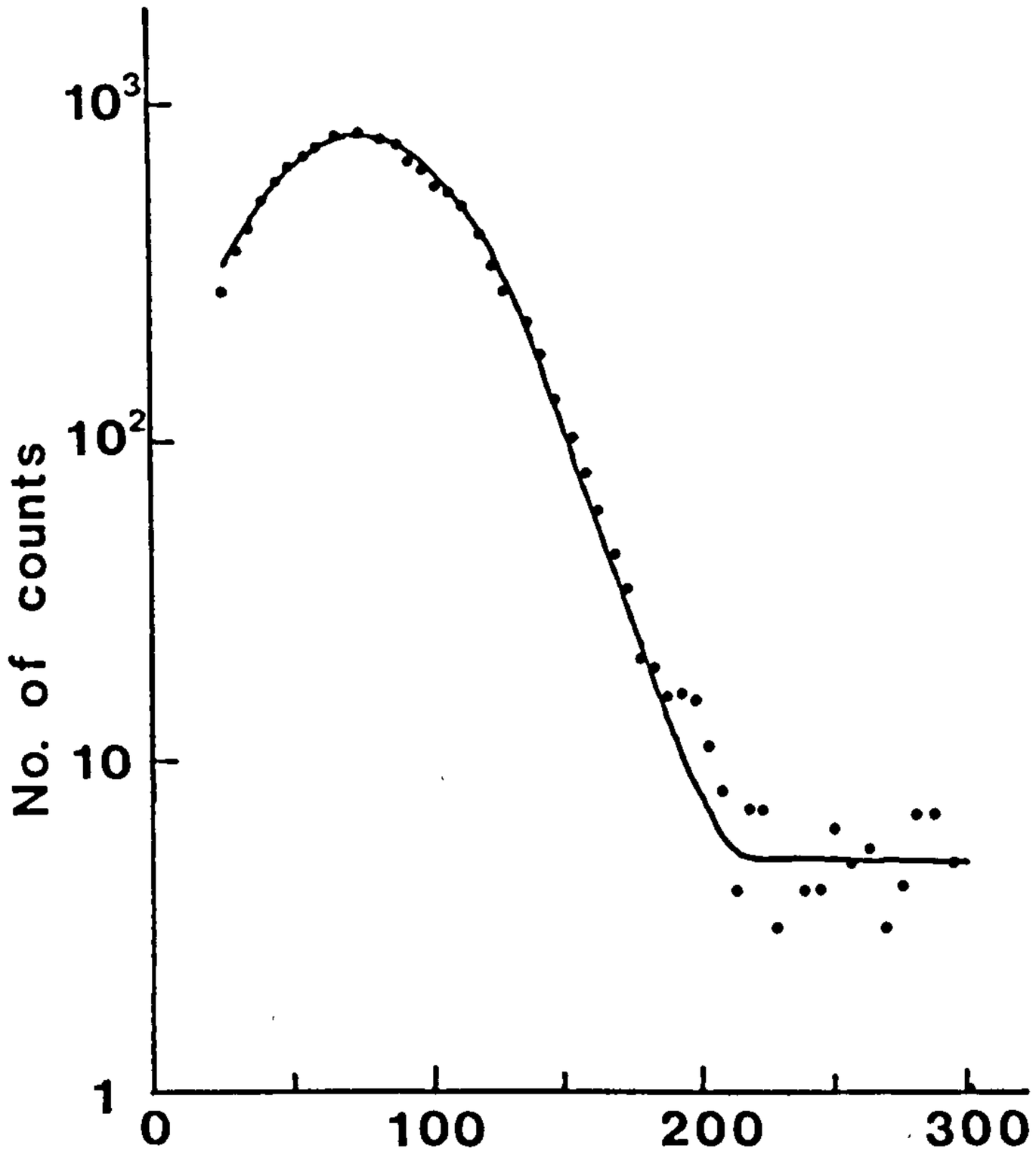
10^3
10^2
10
1
No. of counts
0
100
200
300
Channel no.

ii.

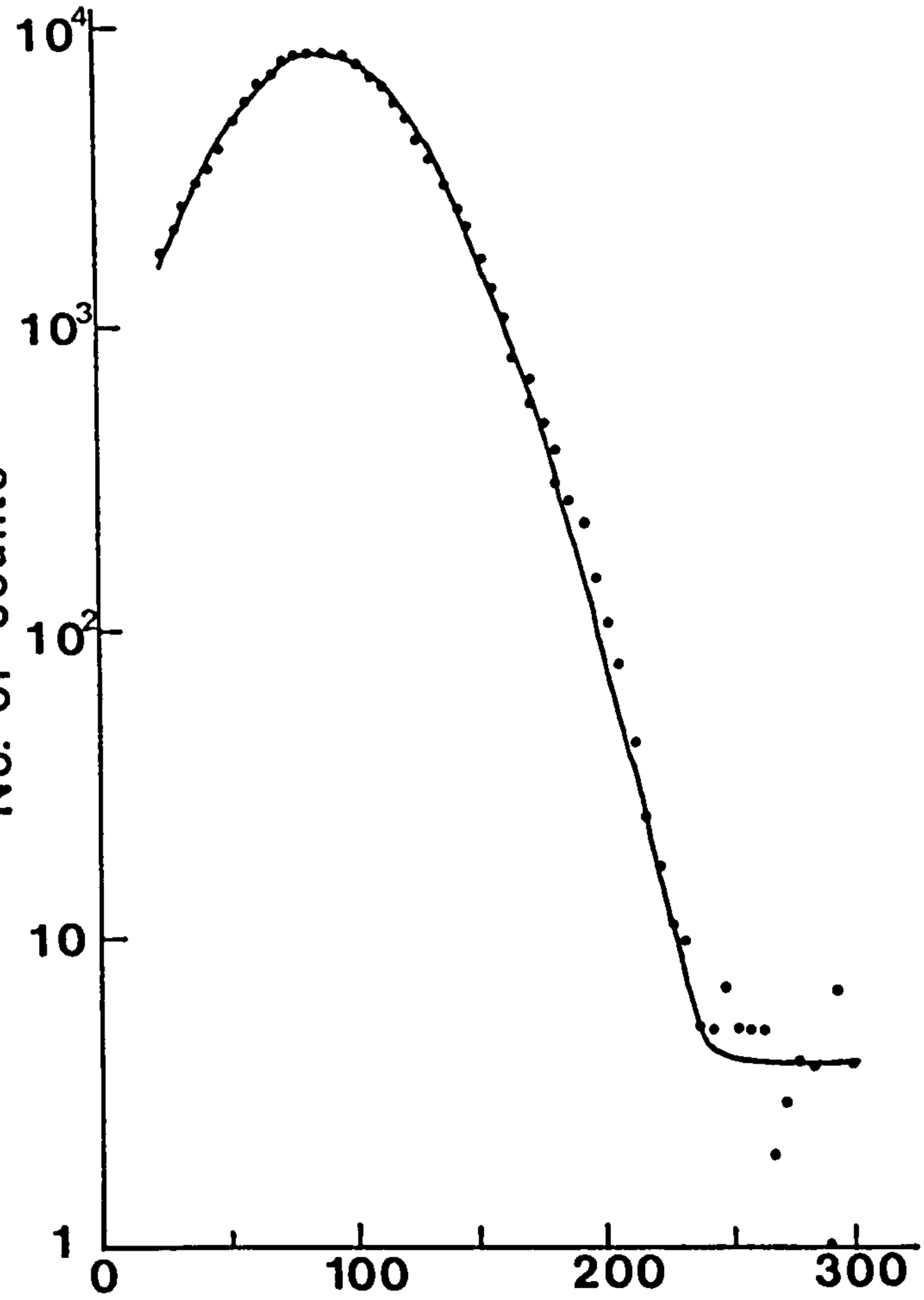
10^4
10^3
10^2
10
1
No. of counts
0
100
200
300
Channel no.

iii. A

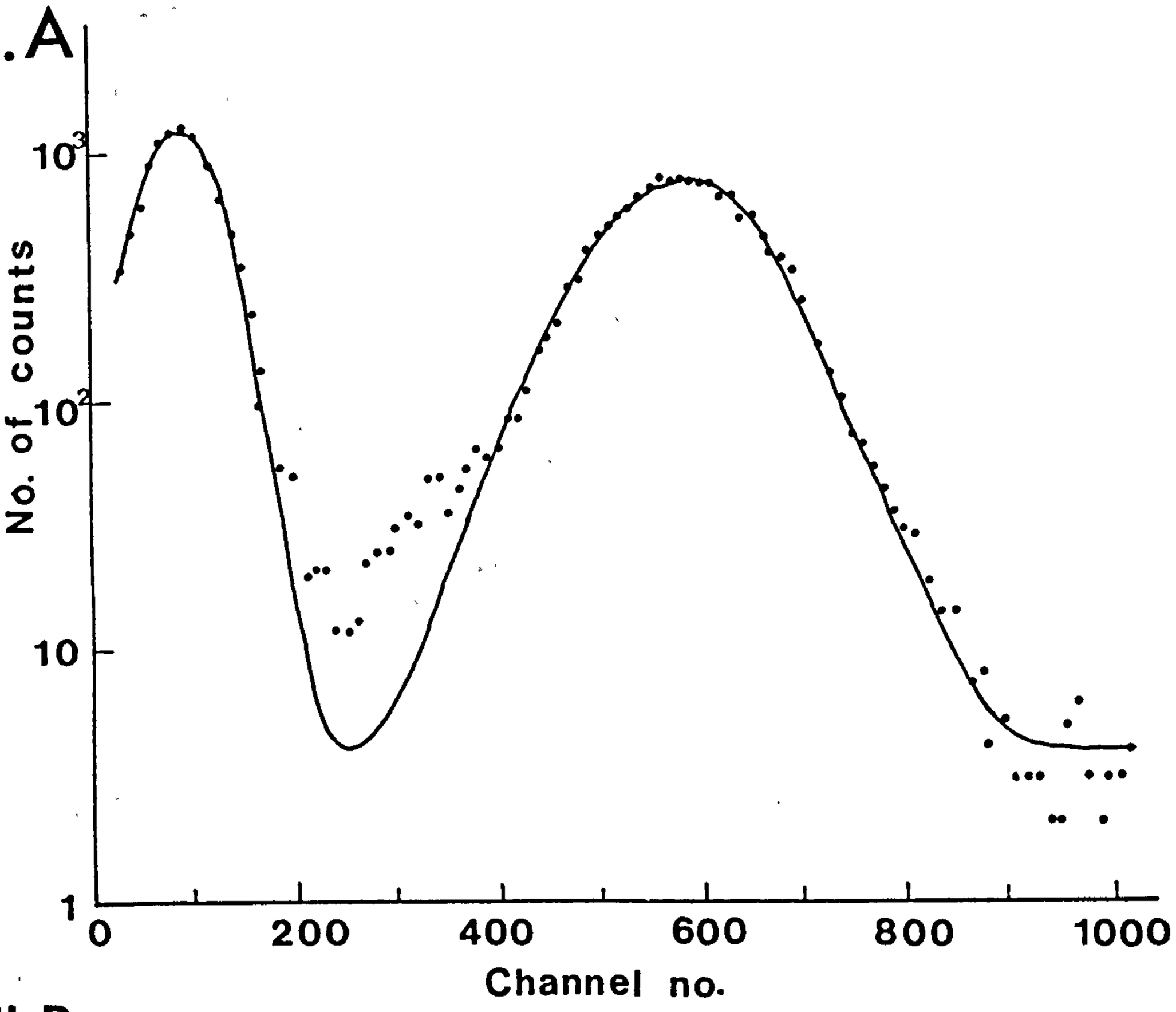
No. of counts
10³
10²
10
1
0
200
400
600
800
1000
Channel no.

iii. B

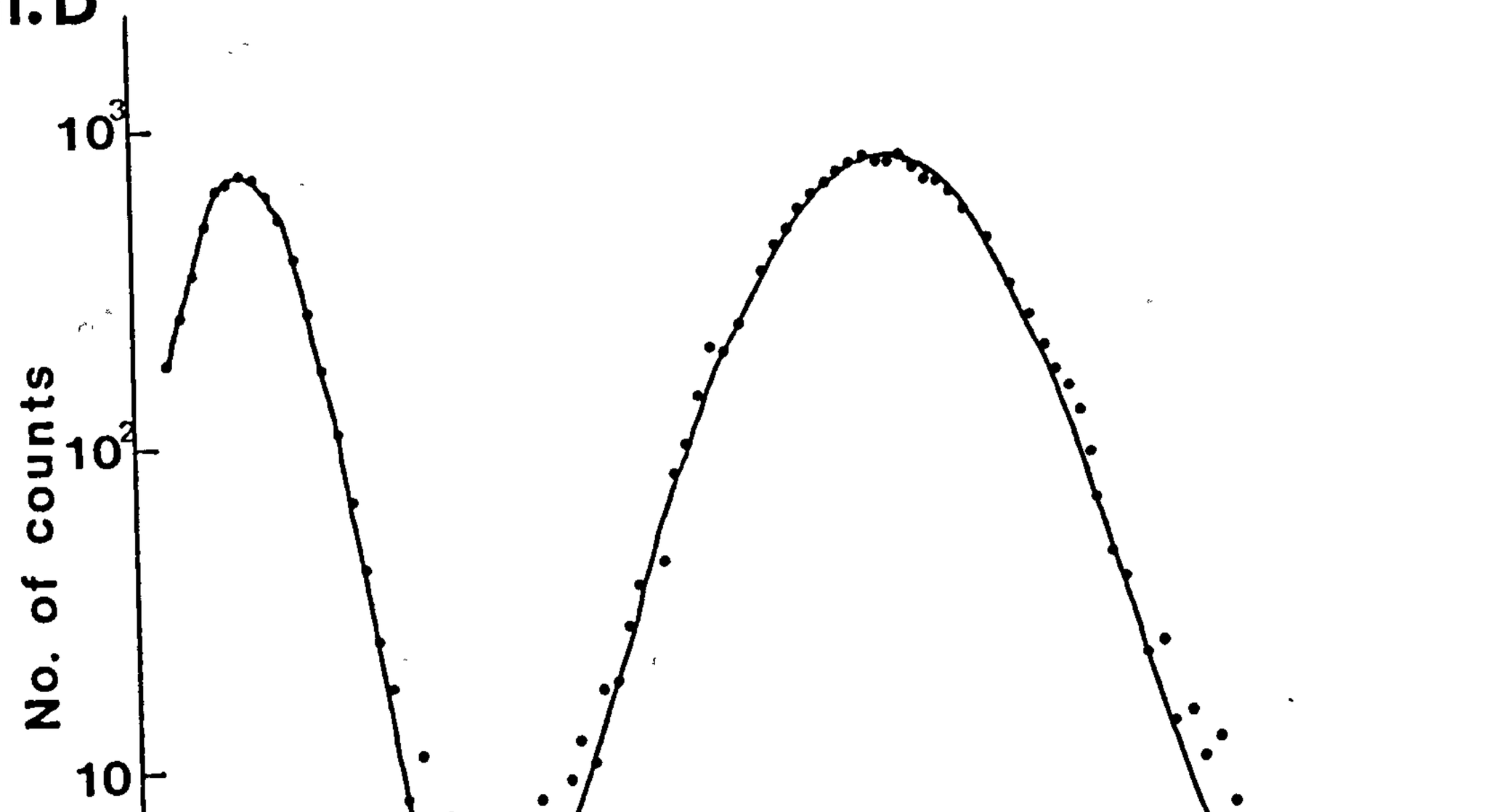
No. of counts
10³
10²
10
1
0
200
400
600
800
1000
Channel no.

iv.

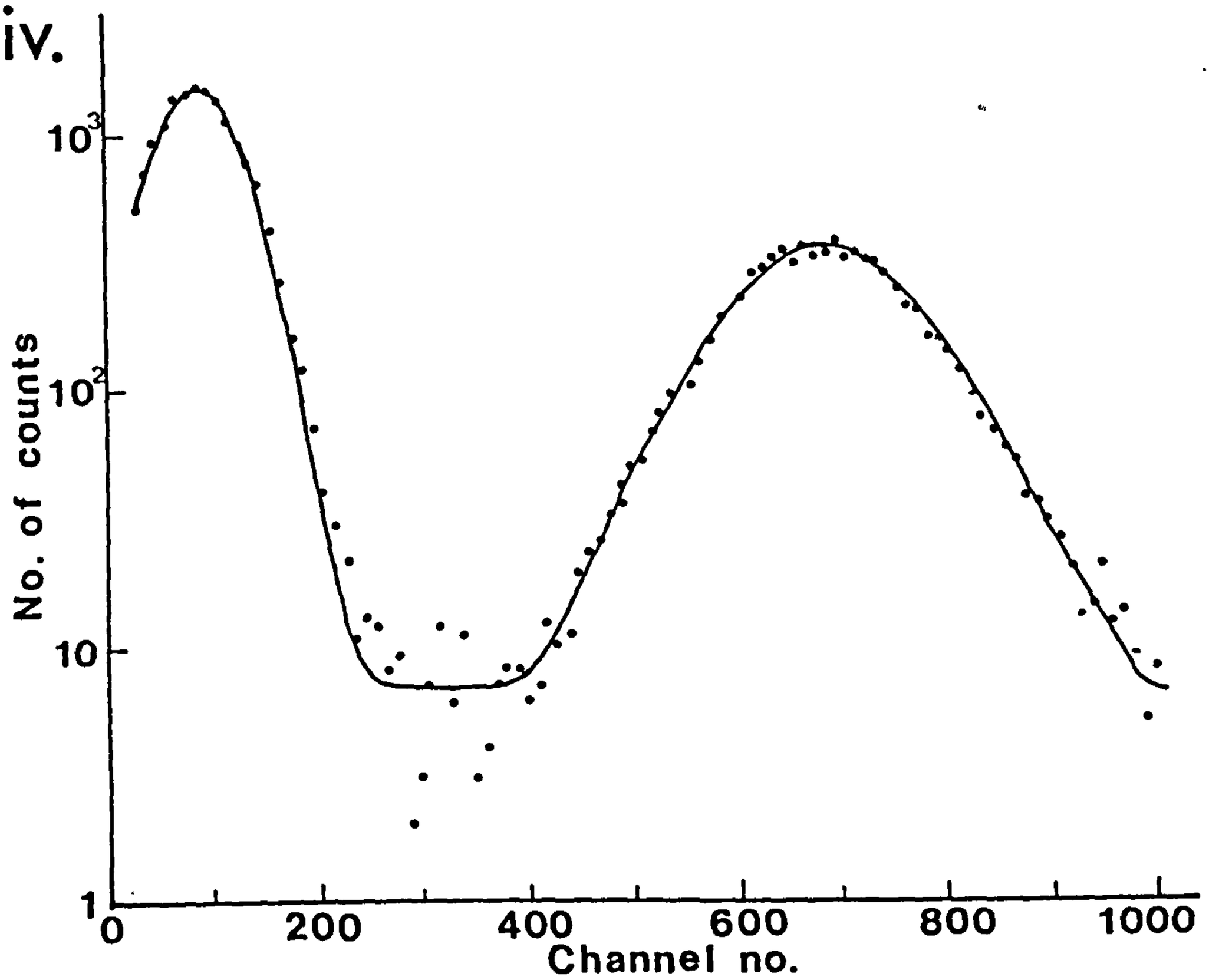
No. of counts
10³
10²
10
1
0
200
400
600
800
1000
Channel no.

V.

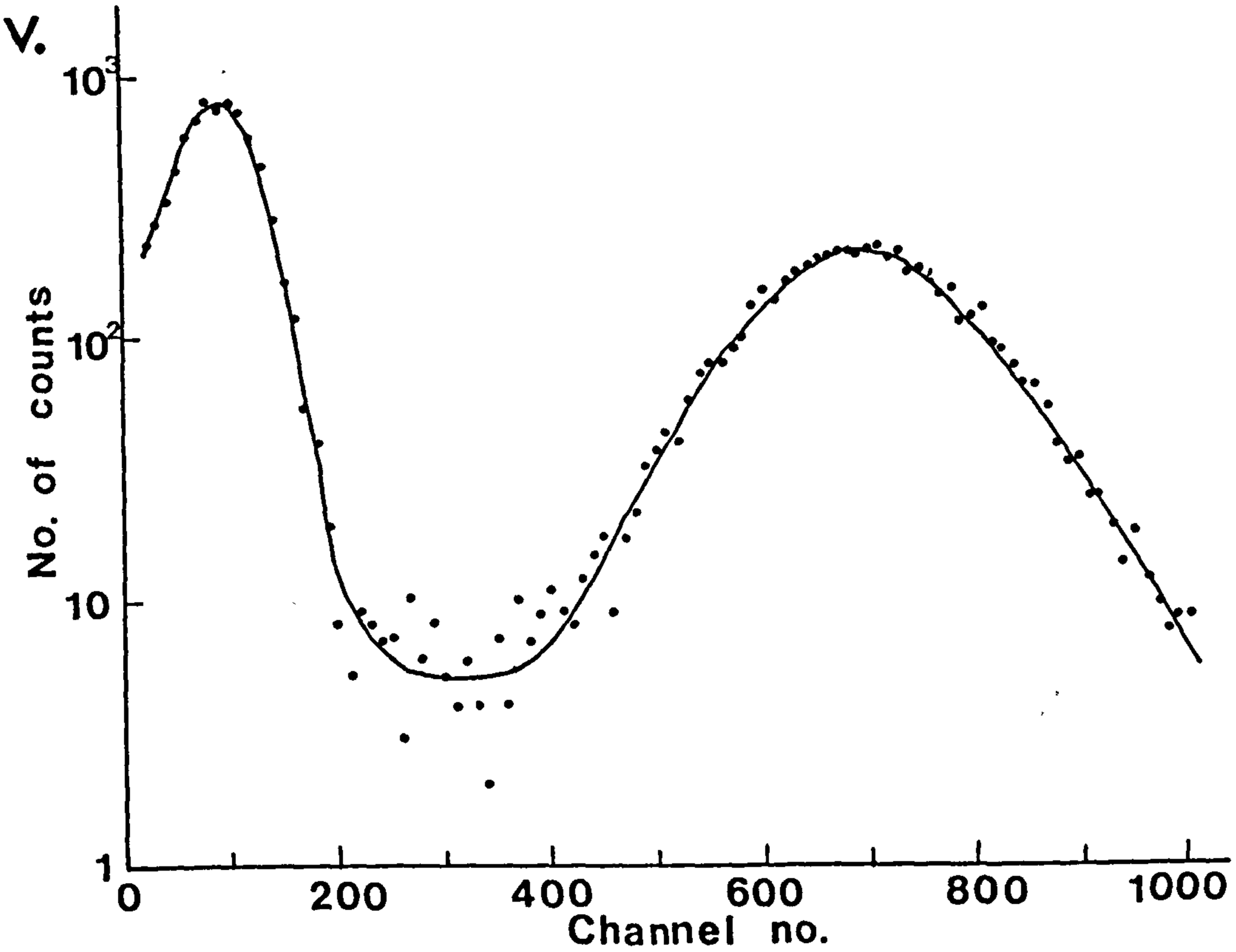
No. of counts
10³
10²
10
1
0
200
400
600
800
1000
Channel no.

vi.

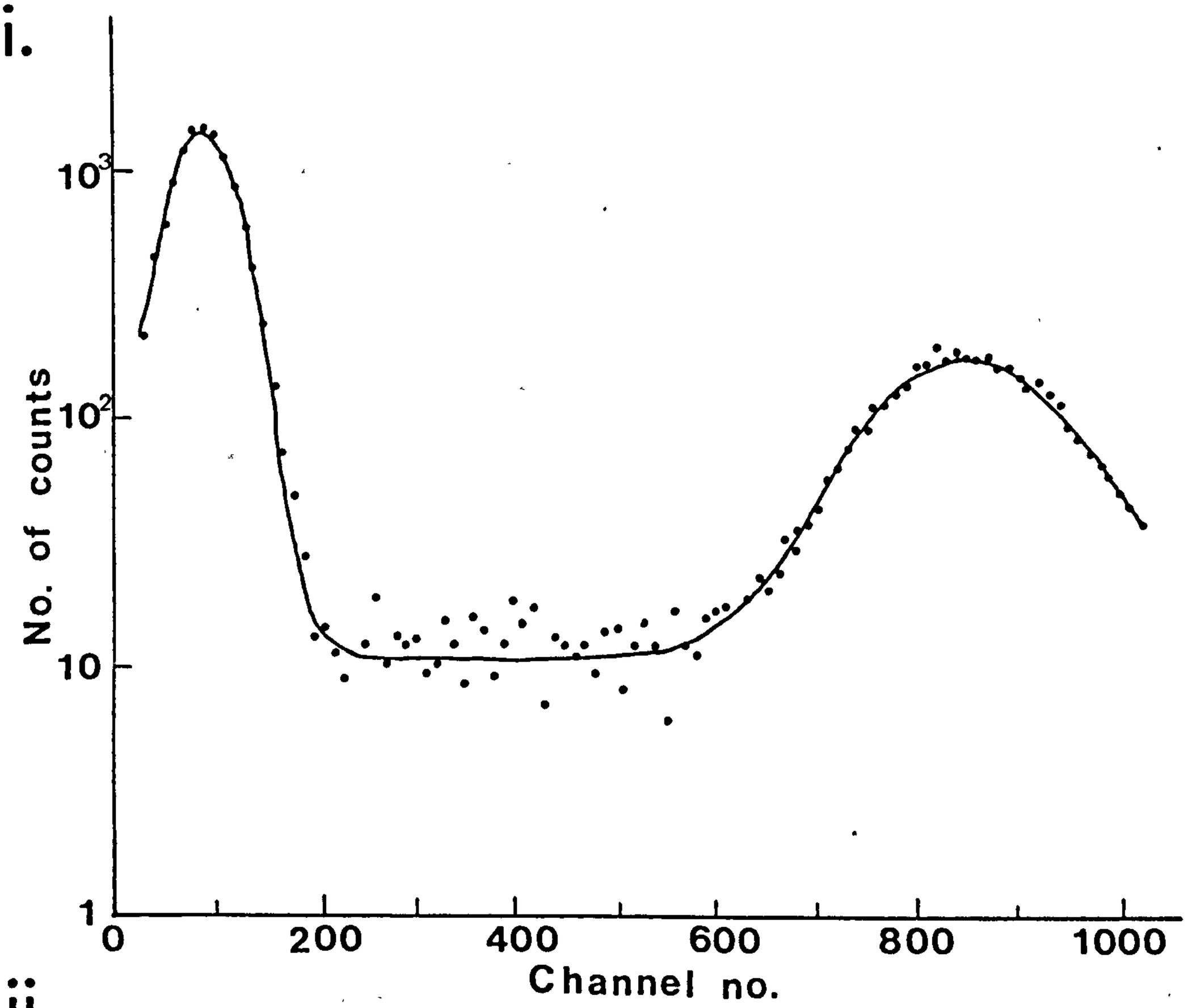
No. of counts
10³
10²
10
1
0
200
400
600
800
1000
Channel no.

vii.

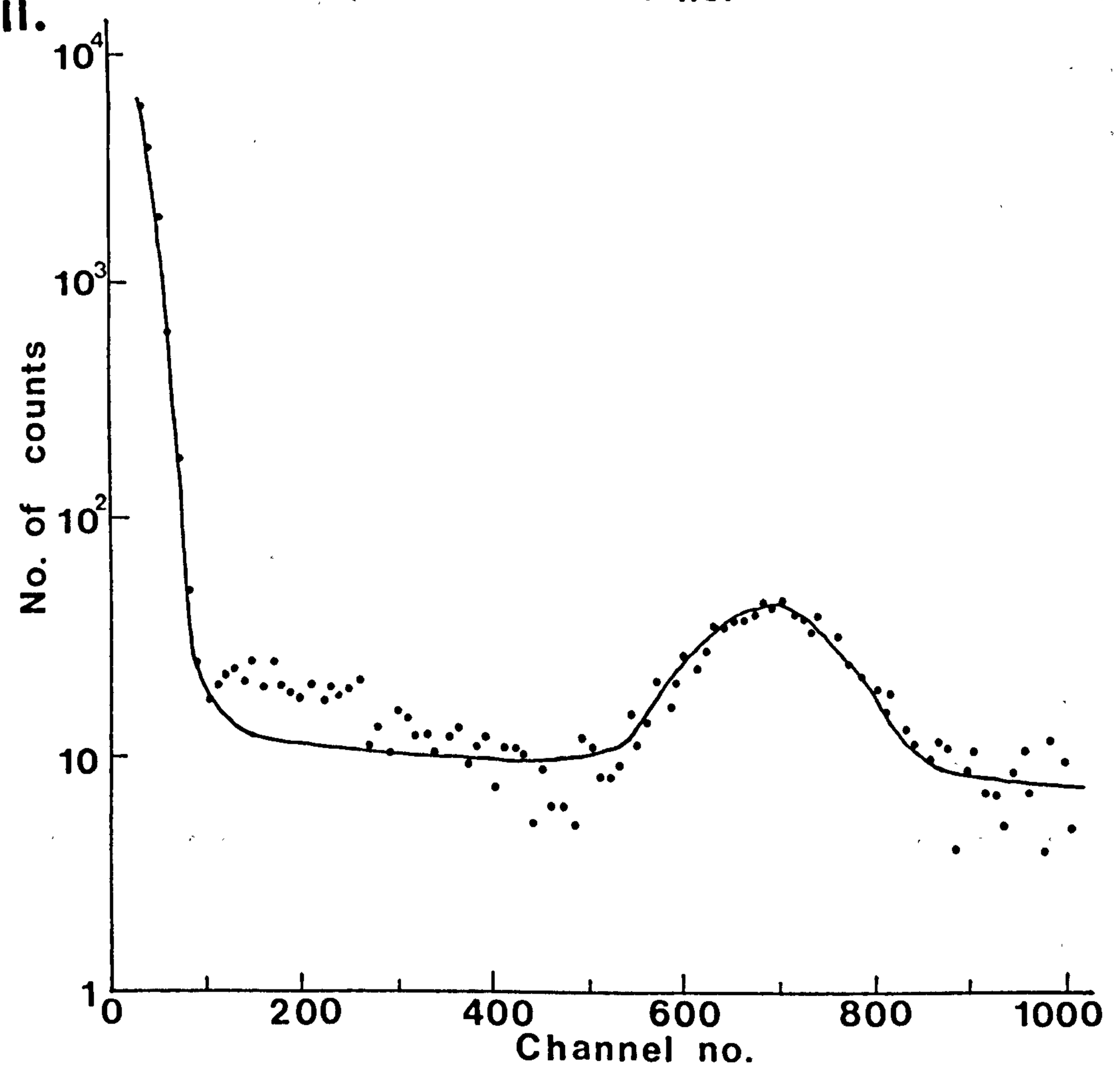
No. of counts
10⁴
10³
10²
10
1
0
200
400
600
800
1000
Channel no.

Dural spectrum is 10 per channel compared with a χ^2 of 2 per channel for the pure Aluminium spectrum. Dural Aluminium comprises 95% Al, 4% Cu and 1% Mg (Goodfellow Metals Ltd.) with both impurities having characteristic X-rays slightly lower in energy than the Al_K X-ray at 1.487 keV (Mg_K X-ray at 1.254 keV and Cu_L X-ray at 0.93 keV). It is probable that the X-rays from the impurities in the Dural are therefore responsible for the increased χ^2 in the region below the Al_K X-ray peak.

The values obtained from MINUIT for the peak position and F.W.H.M. for each target are summarised in Table 5.2. Whilst the error on each individual parameter as given by MINUIT is ~1%, the errors shown in Table 5.2 are the standard deviation (s.d.) of the averaged parameter values taken over all the collected spectra for each target (about 140 in total). The deviations from the average values arose primarily as a result of slight fluctuations in the gain of the proportional counter, particularly when spectra were taken on different days with possible small deviations around the optimal anode voltage of 1700V. The widths of the peaks, as given in Table 5.2, compare favourably with the specified performance of the proportional counter (Manson literature). For example, the F.W.H.M. is expected to be 115% of the peak energy for the B_K peak and 36% of the peak energy for a Mg_K peak (1.254 keV). There is also agreement between the width of the Aluminium peak as given in Table 5.2 with that measured for a similar proportional counter by Hoshi *et al.* (1985) where the F.W.H.M. of the Al_K peak was about 30% of the peak energy. Hoshi *et al.* (1985) showed that the spectral resolution of the proportional counter is limited almost entirely by the statistics of the small numbers of ionisations within the counter.

For the spectra taken with an anode voltage of 1700V it can be seen that a low energy peak (at about channel 90) was present in all cases. This has been shown (Section 5.2.1) to be the result of Carbon contamination of the target surface, resulting in C_K X-rays being

Target	Detector Anode Voltage (V)	PEAK NO. 1			PEAK NO. 2		
		Peak Position (channel)	F.W.H.M. (channels)	F.W.H.M. / Pk.position (%)	Peak Position (channel)	F.W.H.M. (channels)	F.W.H.M. / Pk.position %
TiB_2	1700	75 ± 7	90 ± 4	120	-	-	-
C	1700	91 ± 5	82 ± 2	90	-	-	-
Dural Al	1700	91 ± 5	82 ± 2	90	584 ± 17	184 ± 8	32
Pure Al	1700	89 ± 5	80 ± 1	90	580 ± 12	175 ± 7	30
SiC	1700	90 ± 4	82 ± 2	91	692 ± 20	219 ± 10	32
Si/N	1700	90 ± 5	79 ± 2	88	690 ± 18	222 ± 8	32
Au	1700	88 ± 6	80 ± 2	91	848 ± 21	220 ± 7	26
TiB_2	1600	25 ± 3	30 ± 6	120	692 ± 25	205 ± 17	30

Table 5.2 Summary of the average (over ≈ 140) parameter values (± s.d.) obtained from MINUIT, in terms of channel numbers.

emitted along with the characteristic X-rays of the target. The Al_K, Si_K and Au_M X-rays were well resolved from the contaminating C_K X-rays but this was not the case for the Boron- and Nitrogen-containing targets.

For the TiB_2 target, with a 1700V detector anode voltage, the low energy X-ray peak was observed at a lower position than in any of the other examples at 1700V (channel 75 ± 7 as opposed to channel 90 ± 5). Since the B_K X-ray energy is 183 eV and the C_K X-ray energy is 278 eV it was concluded that the peak observed from the TiB_2 target was a combination of Boron from the target and Carbon from the surface contamination. This conclusion is supported by the increased width of the combined peak (90 ± 4 channels rather than 81 ± 2 channels). Since the rate of Carbon build-up was found to be constant for a given current in the surface contamination study (Figure 5.8) an estimation of the B_K X-ray yield could be found by subtracting the C_K X-ray yield from the Aluminium target data (assuming that the Carbon contamination rate does not depend on target material) from the combined B_K and C_K X-ray peak of the TiB_2 target (Figure 5.2).

Whilst a similar effect might have been expected for the Si/N target (with a low energy peak slightly higher in position than channel 90, consisting of a combination of C_K and N_K (392 eV) X-rays), this was not found to be the case. As is shown in Table 5.2 there was no observable difference between the low energy peaks of the Si/N target and the SiC, Al or Au targets. Since there was no reason to suspect that the N_K X-rays were not being produced from the target it was concluded that the lack of observable N_K X-rays was the result of their increased attenuation in the Polypropylene filter (Section 2.4.1) since there was no significant difference in the attenuation of C_K and N_K X-rays in the VYNS window (Figure 2.7). Using the mass-attenuation coefficients of Hubbell (1977), the transmission characteristics of 6 μm of Polypropylene

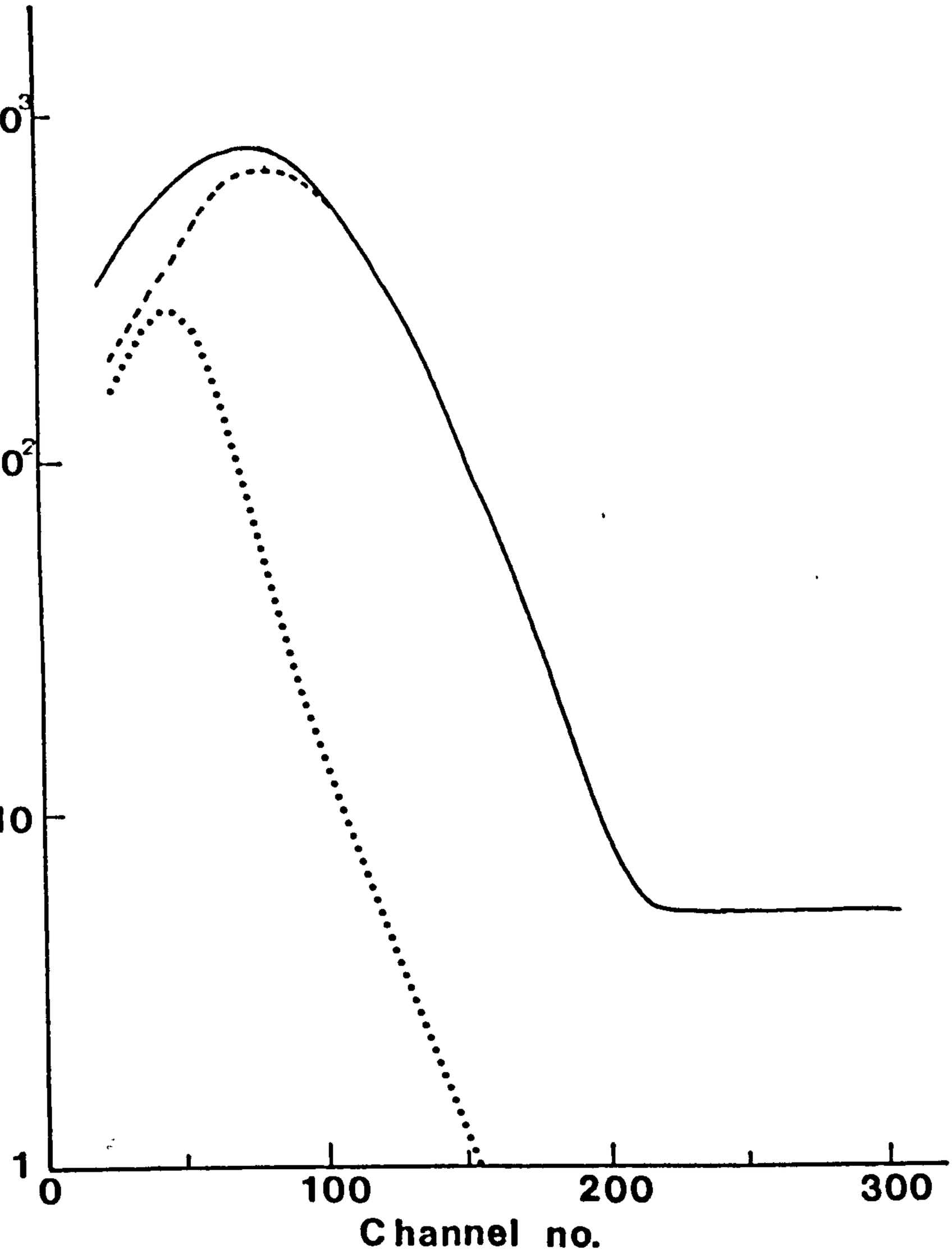

Figure 5.2 Derivation of the B_K X-ray intesity:

—— Spectrum from TiB_2 target (as fitted by MINUIT).

------- C_K X-ray peak derived from the Al target.

..... B_K X-ray peak calculated by subtracting the C_K X-ray peak away from the TiB_2 target spectrum.

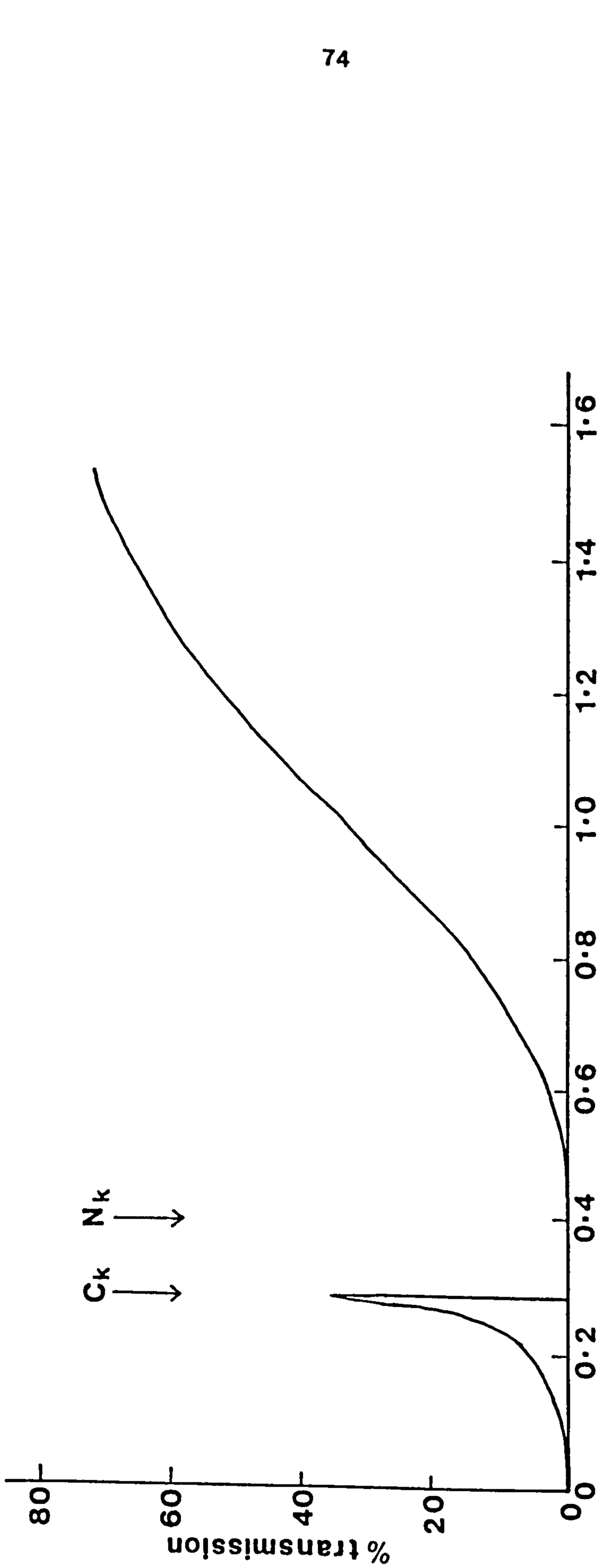

Figure 5.3 The transmission characteristics of 6 μm Polypropylene at low energies, showing the position of the C and N K-shell X-ray lines.

were calculated (Figure 5.3). It is seen that whilst Polypropylene will transmit 35% of the C_K X-rays, less than 1% of the N_K X-rays will be transmitted. It is not surprising therefore that the N_K X-rays were not seen by the proportional counter.

With an anode voltage of 1600V the Ti_K X-rays from the TiB_2 target were observed (Figure 5.1 (vii)). In this case the B_K X-rays from the target and the contaminant C_K X-rays appeared as a narrow peak, high in counts, at the low energy edge of the spectrum. Whilst the overall MINUIT fit gives $\chi^2 = 1.7$ per channel, there is a region (channels 100 - 300) where the theoretical curve underestimates the experimental data. This may be a result of the lower energy peak being calculated to be narrower than it actually is, or a result of small amounts of other X-ray energies being present, such as the L-shell Titanium X-rays (~ 0.5 keV).

All the spectra shown in Figure 5.1 ((i) - (vii)) have a constant background level ('c' of Equation 4.5) calculated to be ≤ 10. The main contribution to this background arose from electronic noise within the detection system itself - collecting a spectrum for 500s with no proton beam but with an anode voltage of 1700V on the detector gave an average of 8 ± 3 counts per channel over the 1024 channels of the MCA.

From the data summarised in Table 5.2 (columns 3,6) it was possible to draw an energy calibration graph for the proportional counter and MCA (Figure 5.4). All the data (at 1700V counter anode voltage) were found to lie on a straight line (with a linear correlation coefficient, $r = 1.0$), including the deduced B_K X-ray position.

Using the values obtained from MINUIT for the areas under the Gaussian peaks to represent the number of X-rays detected by the proportional counter, an estimate of the absolute yields of X-rays could be derived. The number of X-rays produced per steradian per proton onto the target, N^x, was calculated using (modified from Hoshi *et al.*, 1985):

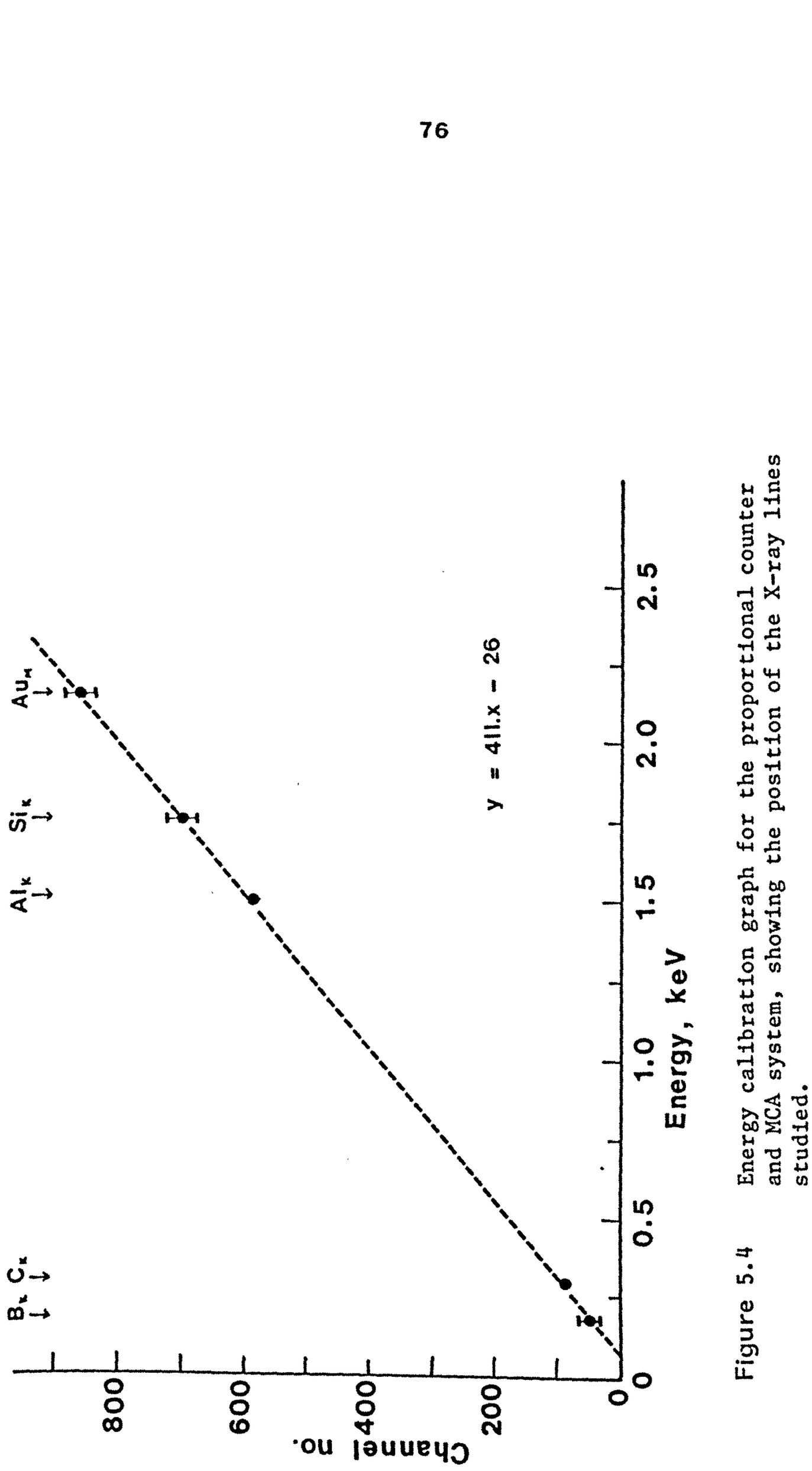

Figure 5.4 Energy calibration graph for the proportional counter and MCA system, showing the position of the X-ray lines studied.

$$N^x = \frac{1.6 \times 10^{-13}.\ C^x}{\Omega.T.\varepsilon.\ (1 - T)} \quad . \qquad 5.1$$

The number of X-rays detected per μC of charge on the target, C^x was obtained from the area under the photon peak as calculated by MINUIT, correcting for surface contamination effects (Section 5.2.1). The solid angle, Ω, subtended by the area of the pinhole aperture was given by

$$\Omega = \frac{\pi r^2}{R^2} \qquad 5.2$$

where r, the pinhole radius, = 0.5 mm and R, the target-to-pinhole distance, = 15 cm. T represents the proportion of the emitted photons transmitted through the counter window and the Polypropylene filter at the different X-ray energies and was calculated from the product of the window (Manson literature) and the filter (Hubbell, 1977) transmission coefficients, the low energy region of which are shown in Figures 2.7 and 5.3 respectively. The detection efficiency, ε, of the counter was calculated from X-ray absorption coefficients (μ/ρ) for P10 gas (Handbook of Chemistry and Physics, 1987-88) using a gas density, ρ, of 1.677 x 10^{-3}g. cm^{-3} and the maximum gas path length, x = 2.05 cm (Section 2.4.1). A combined pressure and temperature correction of 1.09 was applied to account for ambient pressure (9.87 x 10^4 Pa) and temperature (18°C), thus giving

$$\varepsilon = 1 - exp-\left(\frac{\mu}{\rho} . \rho . x . \frac{1}{1.09} \right) \quad . \qquad 5.3$$

The dead time, T, was kept at $\lesssim$ 3% of the counting time throughout.

In order to compare the calculated yields with those available in the literature, the number of X-rays detected at 90° to the beam when the target was at 45° to the beam was considered. Using Equation 5.1, the number of X-rays produced was calculated for each target element (Table 5.3).

However these calculations represent only the number of X-rays in the direction of the counter for one particular target angle since no corrections are included for target self-absorption effects. The

Target	Photon Energy (keV)	No. of photons per 25 μC on the target	N^X (± 15%) (photons per proton per steradian)
B	0.183	45404	4.5×10^{-4}
C	0.278	700491	1.2×10^{-3}
Al	1.487	155669	7.6×10^{-5}
Si	1.740	75584	3.5×10^{-5}
Au	2.120	34619	2.0×10^{-5}
Ti	4.511	6933	9.2×10^{-6}

Table 5.3 The observed yield of X-rays at 90° to the proton beam for a target angle of 45°. (The uncertainty in the value of N^X is the result of the combination of the experimental uncertainties in the parameters involved.)

absolute X-ray yield per proton would require integration over the complete sphere taking into account the variation in absorption length within the target at all angles. However an estimate may be obtained by assuming a constant yield at each angle such that the total X-ray yield is given by $4\pi N^x$, which may then be compared with the yields given in the literature (Table 5.4). For the cases where direct comparison can be drawn (that is, where the proton energies are the same) it is seen that the yields calculated in this study are approximately a factor of two less than the documented values, but there is insufficient information on these calculations to enable the identification of a possible systematic reason for this.

In calculating N^x (Equation 5.1) the anode wire of the proportional counter was assumed to be infinitely thin. In practice the 50 μm diameter central wire would be expected to reduce the detector efficiency. However, as this effect is more noticeable for small pinholes it was assumed to be negligible for the 1 mm diameter pinhole used in this study (Hoshi *et al.*, 1985 for example, calculated that the required correction when detecting Al_K X-rays was 0.89 for a 30 μm pinhole and 0.92 for a 200 μm pinhole).

In the following sections (5.2.1 - 5.2.3 and Chapter 6) reference is frequently made to the 'intensity' of the X-rays. Whilst intensity is normally used to define the rate of energy transfer per unit area normal to the direction of propagation, in the context of this work it is used to describe the integrated number of counts under the peak.

5.2.1 Surface contamination study

It has already been shown (Figure 5.1) that continuous bombardment of a target by a proton beam results in the production of not only the target's characteristic X-rays but also a low energy photon similar in energy to the C_K X-ray. This was assumed to be caused primarily by

Photon Energy *(keV)*	Observed yield $4\pi N^{X}$ (± 15%) *(photons per proton)*	Documented yield *(photons per proton)*	Reference
0.278	1.51×10^{-2}	3.43×10^{-2}	Khan, Potter and Worley, 1965
1.487	9.55×10^{-4}	2.07×10^{-3}	Khan and Potter, 1964
		2.0×10^{-3}	Sterk, 1964
		1.66×10^{-3}	Khan, Potter and Worley, 1965 (E_p = 484 keV)
4.511	1.56×10^{-4}	9.92×10^{-6}	Jopson, Mark and Swift, 1962 (E_p = 441 keV)

Table 5.4 Comparison between the observed and documented yields of proton-induced characteristic, ultrasoft X-rays. The proton energy, E_p = 500 keV unless stated otherwise.

a deposition of Carbon containing contaminant on the target surface due to the decomposition of organic vapours from the diffusion pump oil (Khan, Potter and Worley, 1965). However, work performed by Gaines (1981) has shown that hydrocarbon build-up occurs on target surfaces even at the very low pressures ($\lesssim 10^{-6}$ Pa) achieved by turbo-molecular pumps, thereby suggesting that all the contamination may not have been due to the deposition of the pump oil vapours.

Since the X-ray line observed from the contaminant was indistinguishable in energy from C_K X-rays, it would indicate that the surface contamination is Carbon being deposited on the target's surface. This assumption was borne out by the observed effect of continuous proton bombardment onto the Aluminium and Carbon targets. In the case of the Carbon target, the intensity of the C_K X-rays remained constant (± 1%) throughout 8 hours of bombardment at 35 nA (± 1 nA) beam current (Figure 5.5). However, the Al_K X-rays showed a reduction in intensity with time (Figure 5.6) accompanied by a simultaneous increase in the intensity of the low energy X-ray.

The observed effect of continuous proton bombardment on the Aluminium and Carbon targets can be explained if the contaminant was indeed Carbon. A reduction in the intensity of Al_K X-rays would then be expected as a result of absorption in the Carbon layer. However, no effect would be expected for the Carbon target since any surface deposition would only serve to increase the target thickness somewhat - the absorption of the C_K X-rays in the contamination layer would be equivalent to the self-absorption in the target itself.

The decrease in the Al_K X-ray intensity was found to be exponential with time, having a characteristic exponent of $\simeq 37$ hrs^{-1} at a beam current of 35 nA. The ratio of the intensity of Al_K X-rays to that of the surface C_K X-rays was found to fall from 15 to 0.3 over a total proton bombardment time of 17 hours (Figure 5.7).

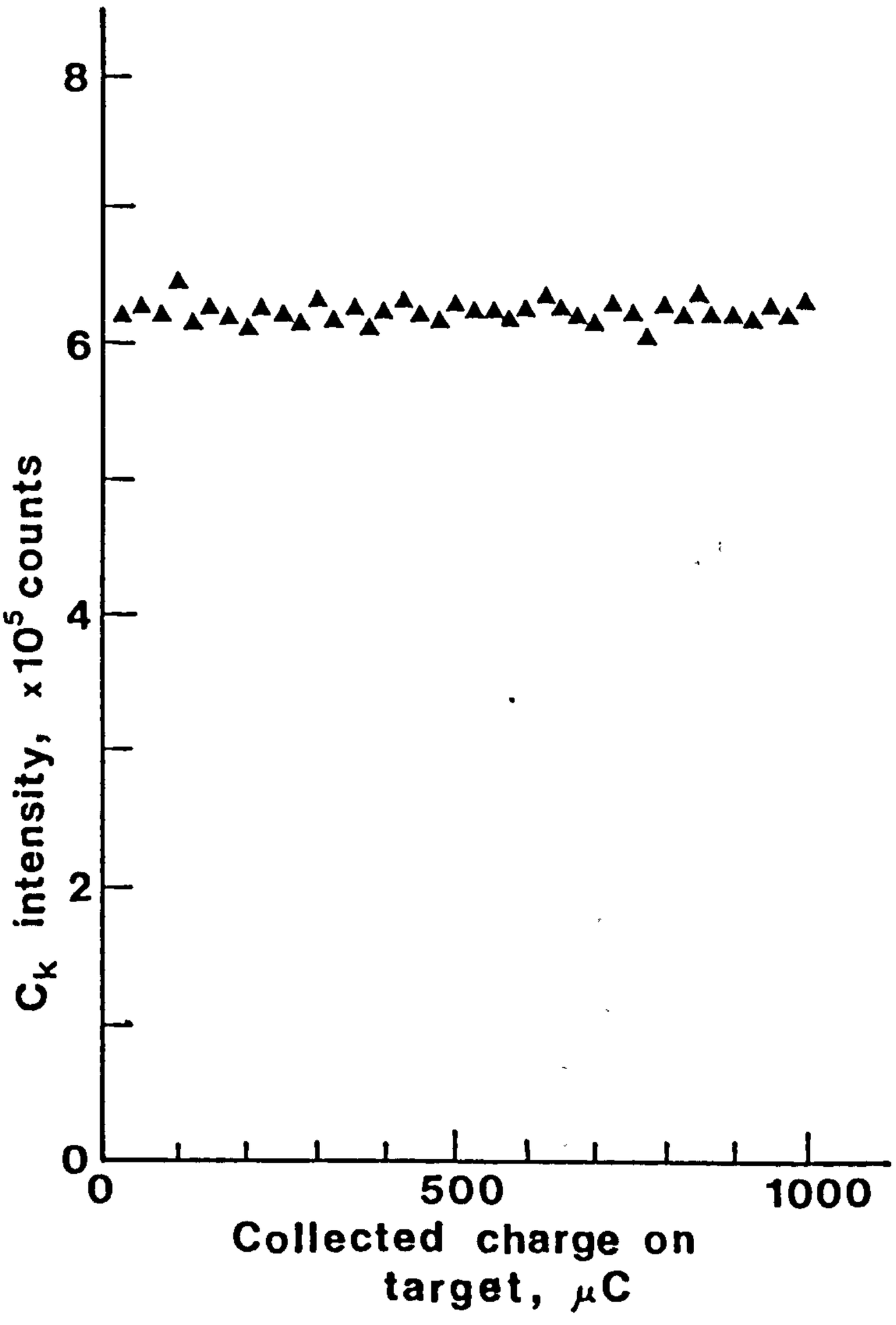

Figure 5.5 The variation of the C_K X-ray yield with collected charge on the target for 500 keV protons.

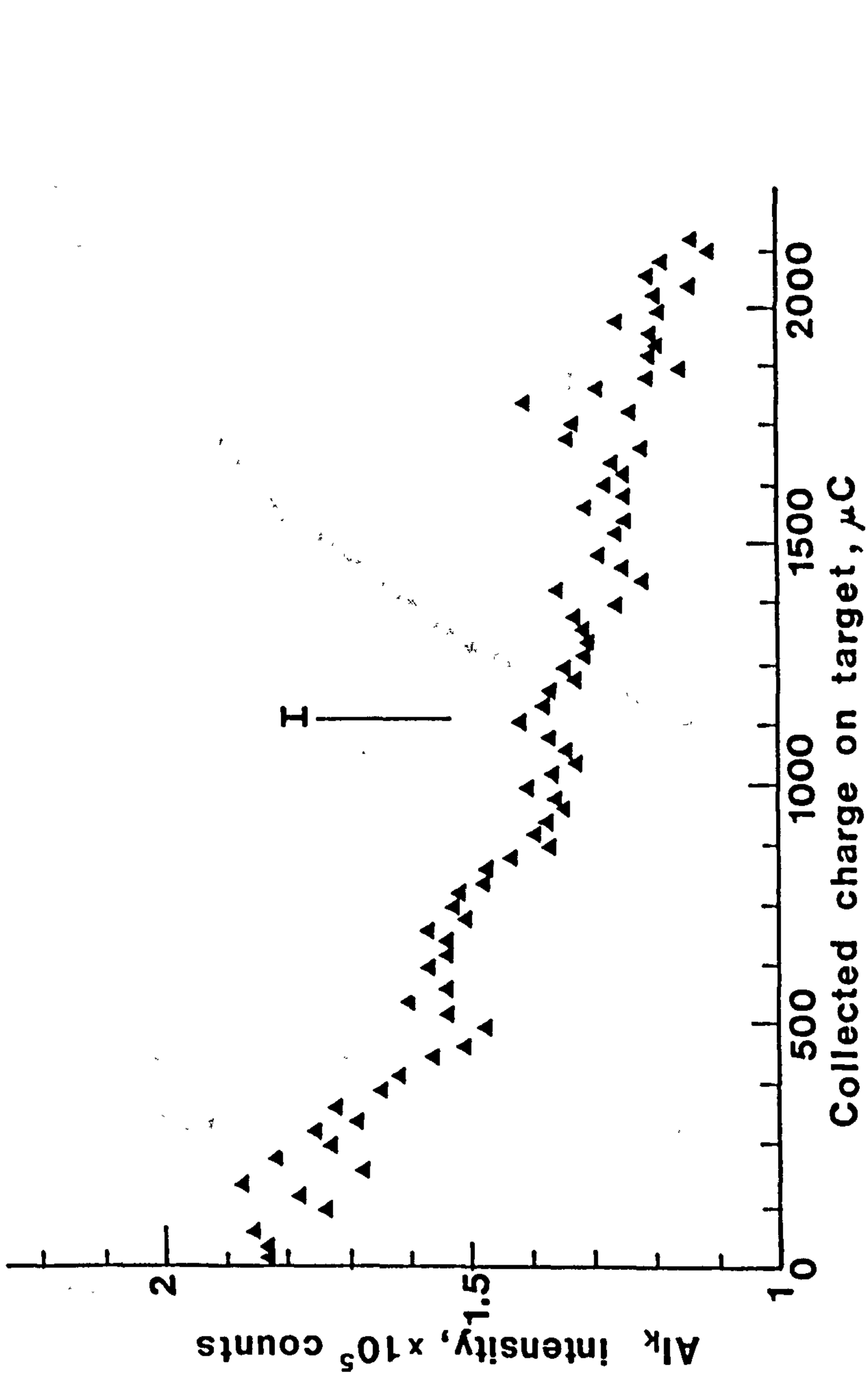

Figure 5.6 The variation of the Al_K X-ray yield with collected charge on the target for 500 keV protons. I denotes the point at which the accelerator was switched off for a time interval of ≈ 12 hours.

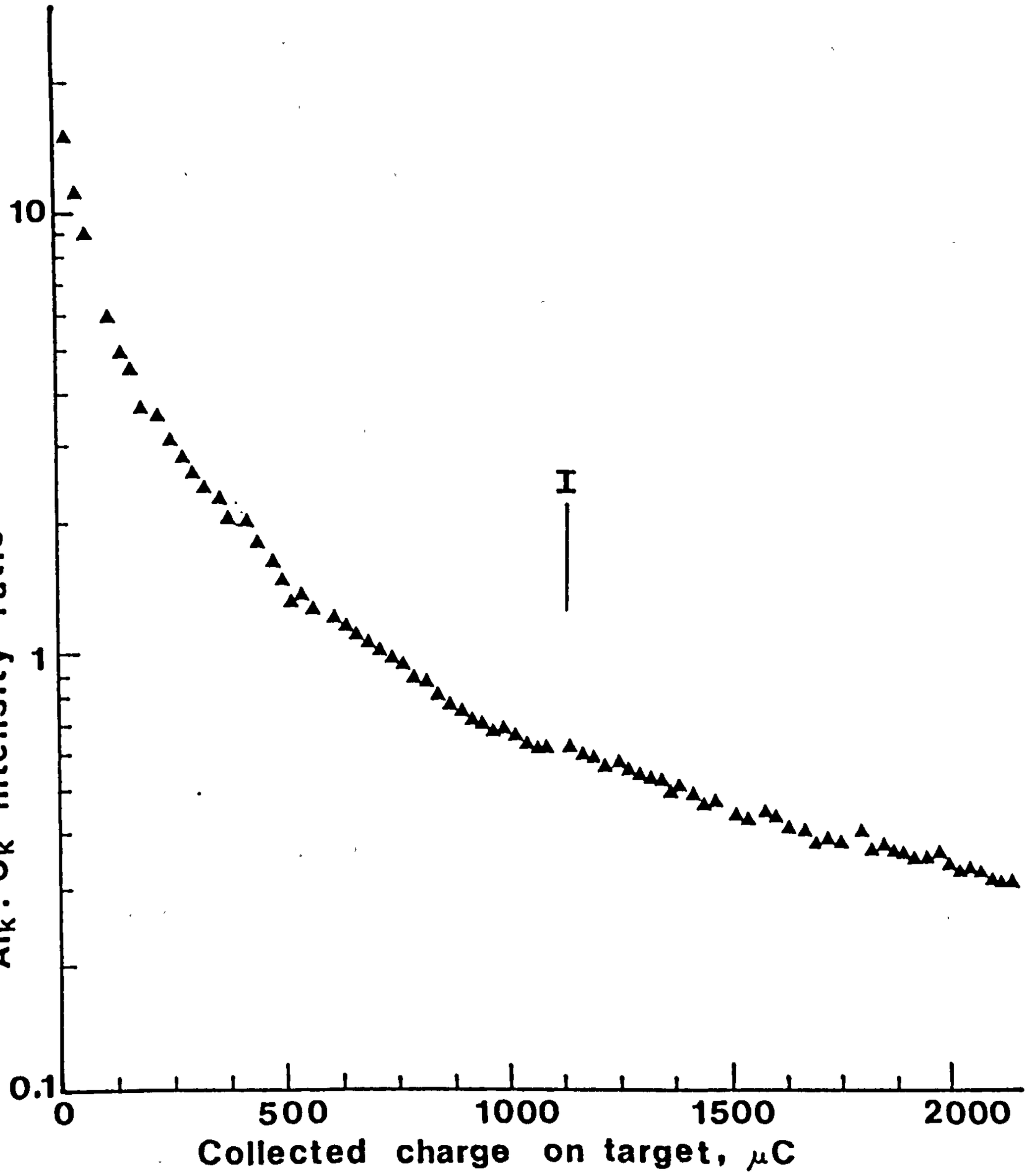

Figure 5.7 The Al_K : C_K X-ray intensity ratio as a function of the charge collected on the target for 500 keV protons bombarding an Al target. I denotes the point at which the accelerator was switched off for a time interval of ≈ 12 hours.

The effect of varying the proton current on the rate of Carbon build-up was also studied. In Figure 5.8 the intensity of the C_K X-rays emitted from an initially 'clean' Aluminium target (Section 5.1.2) is presented as a function of the collected charge on the target at varying currents. It is clear that the gradients for the three 500 keV proton beam currents (10, 40 and 70 nA) are different, implying that the surface deposition was current related. It would also appear that the highest beam currents produced the lowest rate of Carbon build-up and that varying the proton energy had very little effect on the rate of Carbon build-up (Figure 5.9). It is difficult to extrapolate this effect to large currents to find conditions under which Carbon contamination is reduced to an acceptable level. Clearly however, there is always the possibility that Carbon build-up takes place even at currents of the order of mA.

Having established that Carbon was deposited on the target surface it was possible to correct for the absorption of the target X-rays in the contaminant layer (Section 6.1). The intensities referred to in the following sections have been corrected for absorption in the Carbon layer.

5.2.2 Angular distribution study

For each target, four sets of data were taken - each set consisting of a full detector angle scan ($40° \leq \alpha \leq 130°$) at target angles, θ, of 30°, 45° and 60°. In the latter case ($\theta = 60°$), the detector angle was limited to $\alpha \leq 110°$ since at $\alpha = 120°$ the detector was in line with the target edge resulting in an intesity reduction owing to the restricted view of the target by the detector. After compensating for absorption in the surface Carbon layer the four sets of data were combined to give average values (± s.d.) of the X-ray intensity at each target/detector angle combination. In order to compare the angular

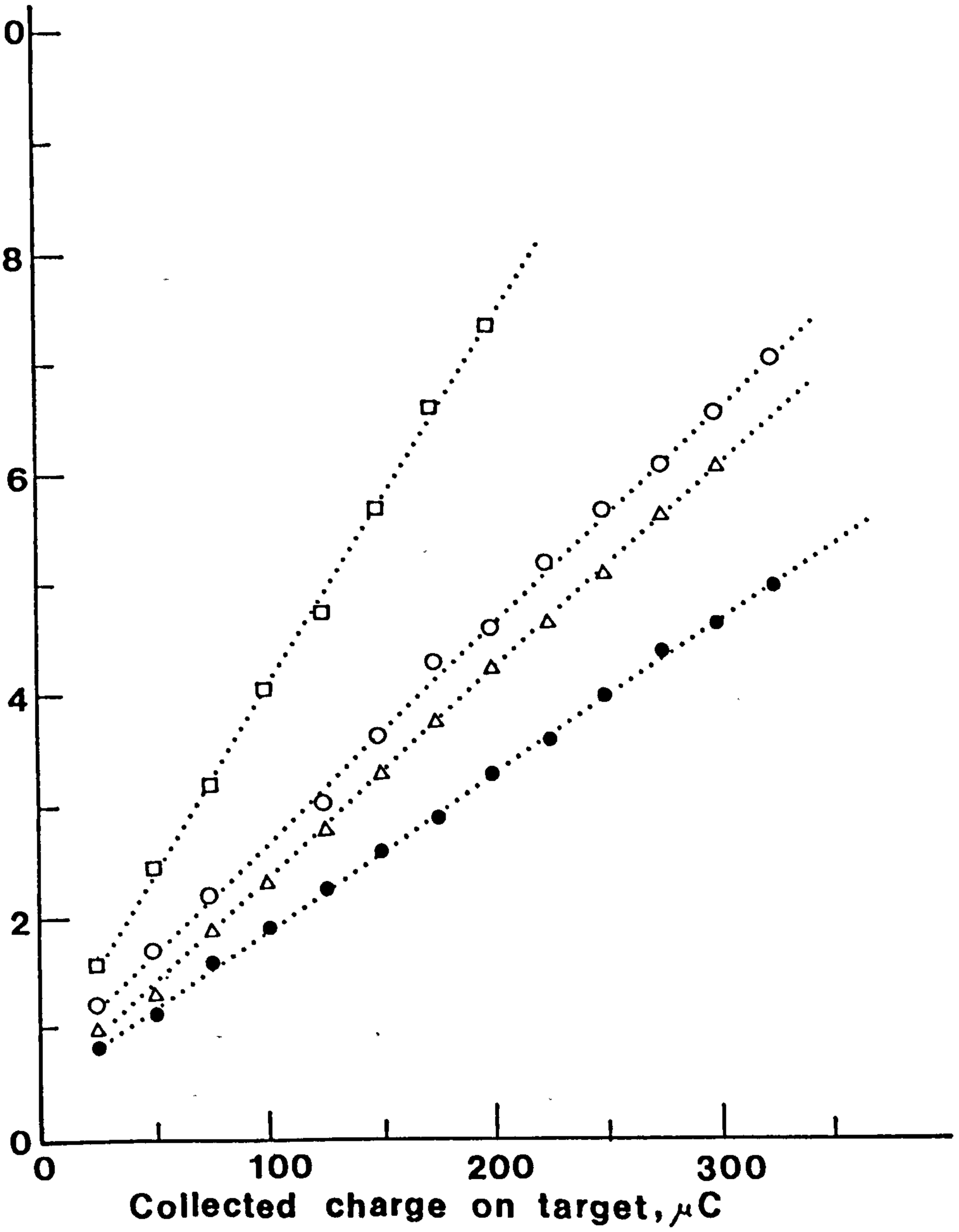

Figure 5.8 The build-up of Carbon contamination X-ray intensity with the total amount of charge collected on an Al target.

□ : 500 keV protons at 10 nA
○ : 500 keV protons at 40 nA
● : 500 keV protons at 70 nA
△ : 300 keV protons at 50 nA

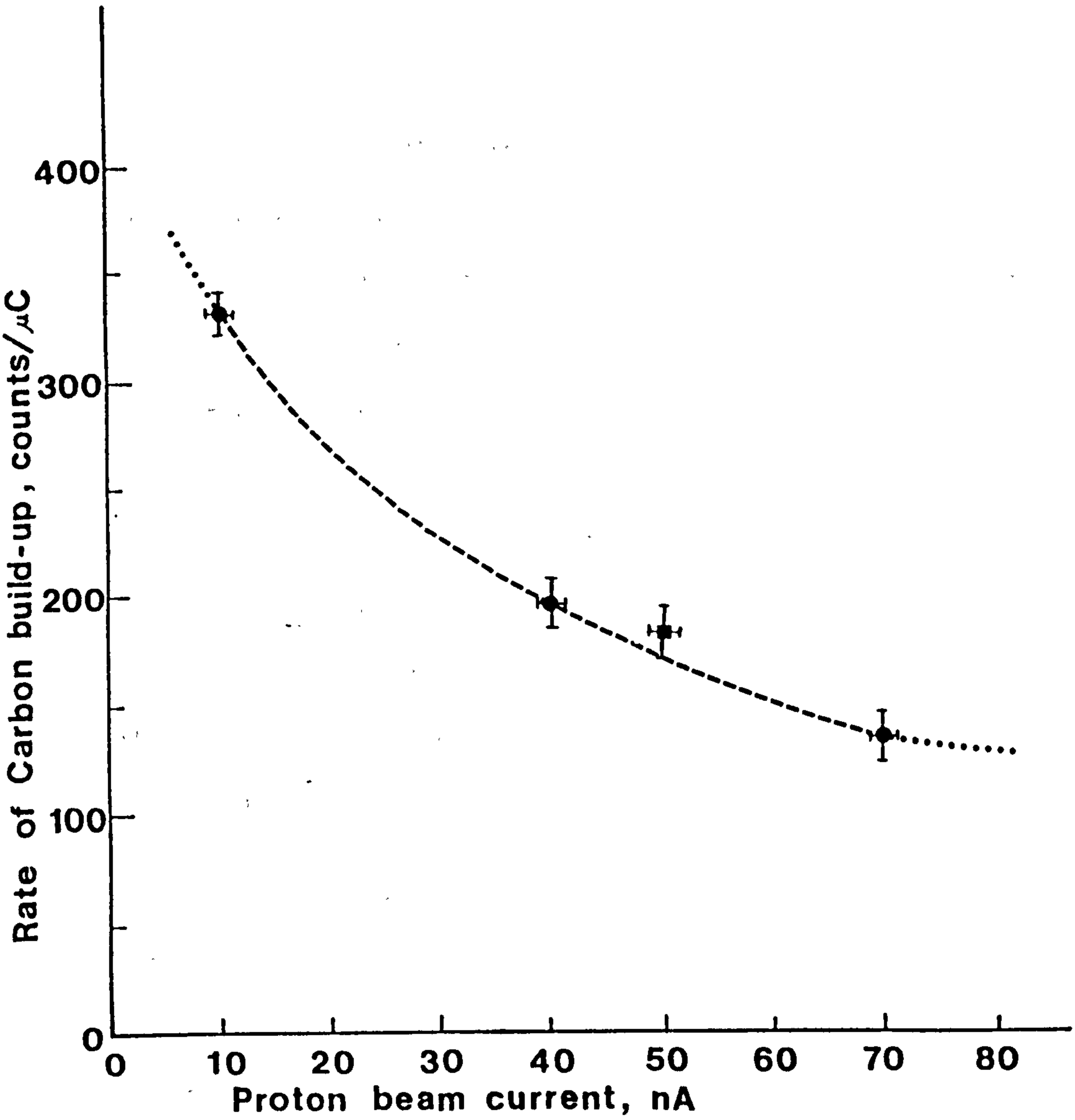

Figure 5.9 The rate of Carbon contamination build-up as a function of the proton beam current.

● 500 keV protons ■ 300 keV protons

distribution of intensities with theoretical expectations (Section 6.2) the intensities were normalised to the intensity at $\theta = 30°$, $\alpha = 60°$ - this being the maximum theoretical intensity.

The resulting distributions are shown in Figure 5.10 ((i) - (vi)) where the experimental data are given along with the theoretical calculations (details of which are given in Chapter 6). Also shown in Figure 5.10 are the calculated angular distributions assuming that the X-rays are produced only in the first 1 μm of the proton's path in the target (for example, Table 6.7). The errors on the theoretical values are encompassed within the data symbols used on the figures. In the case of Titanium (Figure 5.10 (vi)) there was insufficient difference between the calculations based on the assumption that X-rays are produced over the whole of the proton range and those based on production in the first 1 μm only, to warrant their separate plotting.

From the results shown in Figure 5.10 it was deduced that for K-shell X-rays the degree of angular variation showed an approximate inverse proportionality to the X-ray photon energy, with the X-ray intensity being constant over a far wider range of target/detector angles for the Ti_K X-rays (4.5 keV) than the C_K (278 eV) or B_K (183 eV) X-rays. It was also observed that the degree of agreement between the experimental data and the theoretical calculation improved with increasing photon energy. However, this would appear not to be the case when considering the Au_M X-rays (2.12 keV) where it might have been expected that the agreement between experimental and theoretical data for the Au_M X-rays would be similar to that of the Si_K X-rays (1.7 keV). In addition, the degree of angular dependence observed for Au_M X-rays (Figure 5.10 (v)) is larger than that for K-shell X-rays at approximately the same energy (Figure 5.10 (iii) and (iv)). This may be due to the self-attenuation coefficient of Gold for its M-shell X-rays being nearer in magnitude to the self-attenuation coefficient of low energy X-rays, such as the

Figure 5.10 The relative X-ray intensity as a function of the detector angle, α, for target angles $\theta = 30°$, 45° and 60°.

o Experimental data

▲ Theoretical calculation (X-rays produced in the total proton range)

● Theoretical calculation (X-rays produced in the first 1 μm of the proton's range only)

(A calculated point is not shown where it lies within the experimental error bars)

(i.) Boron K-shell X-rays (183 eV)
(ii.) Carbon K-shell X-rays (278 eV)
(iii.) Aluminium K-shell X-rays (1.487 keV)
(iv.) Silicon K-shell X-rays (1.740 keV)
(v.) Gold M-shell X-rays (2.120 keV)
(vi.) Titanium K-shell X-rays (4.509 keV)

i.

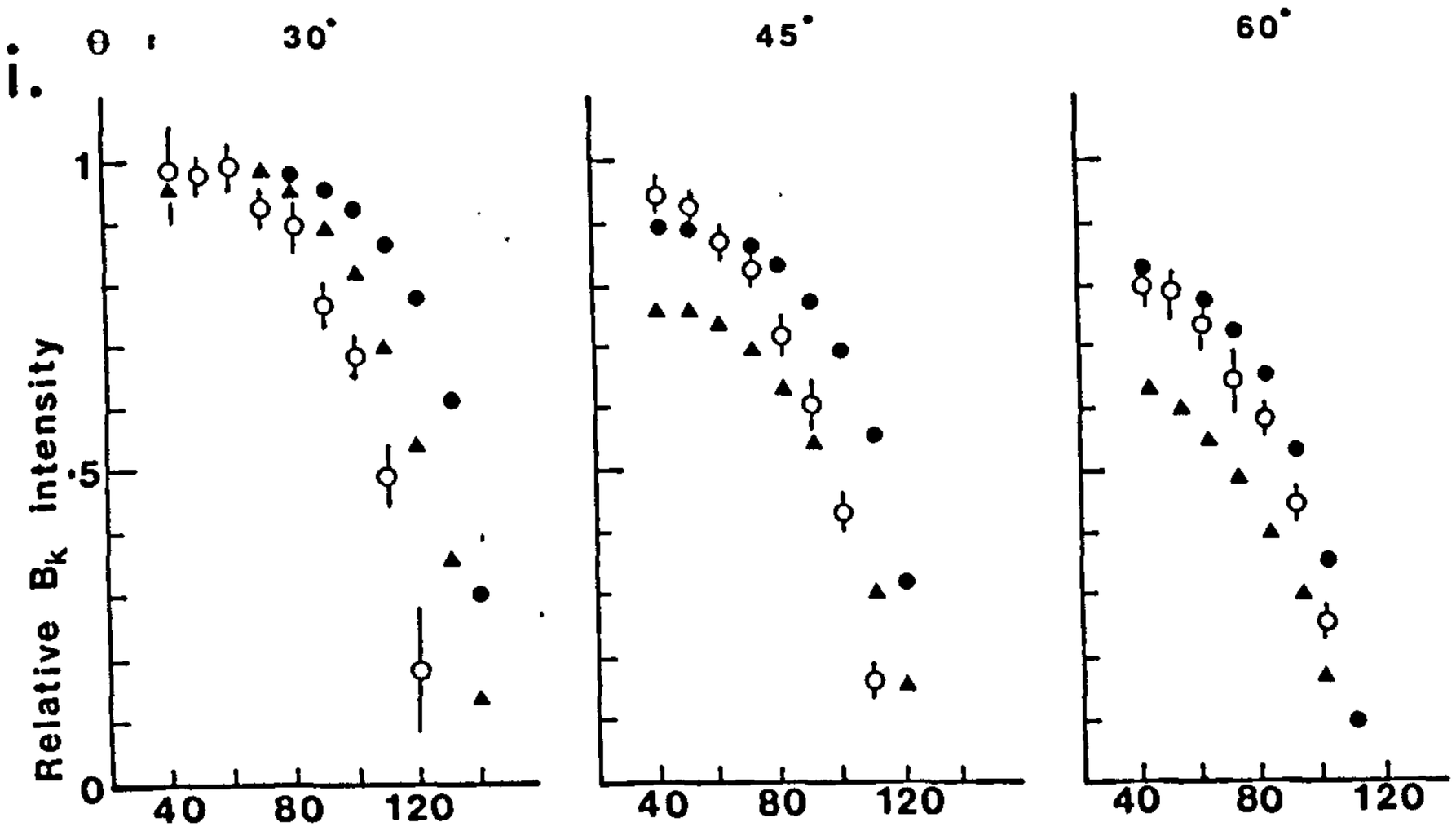
θ : 30°
45°
60°
Relative B_k
1
.5
0
40
80
120
Detector angle, α

ii.

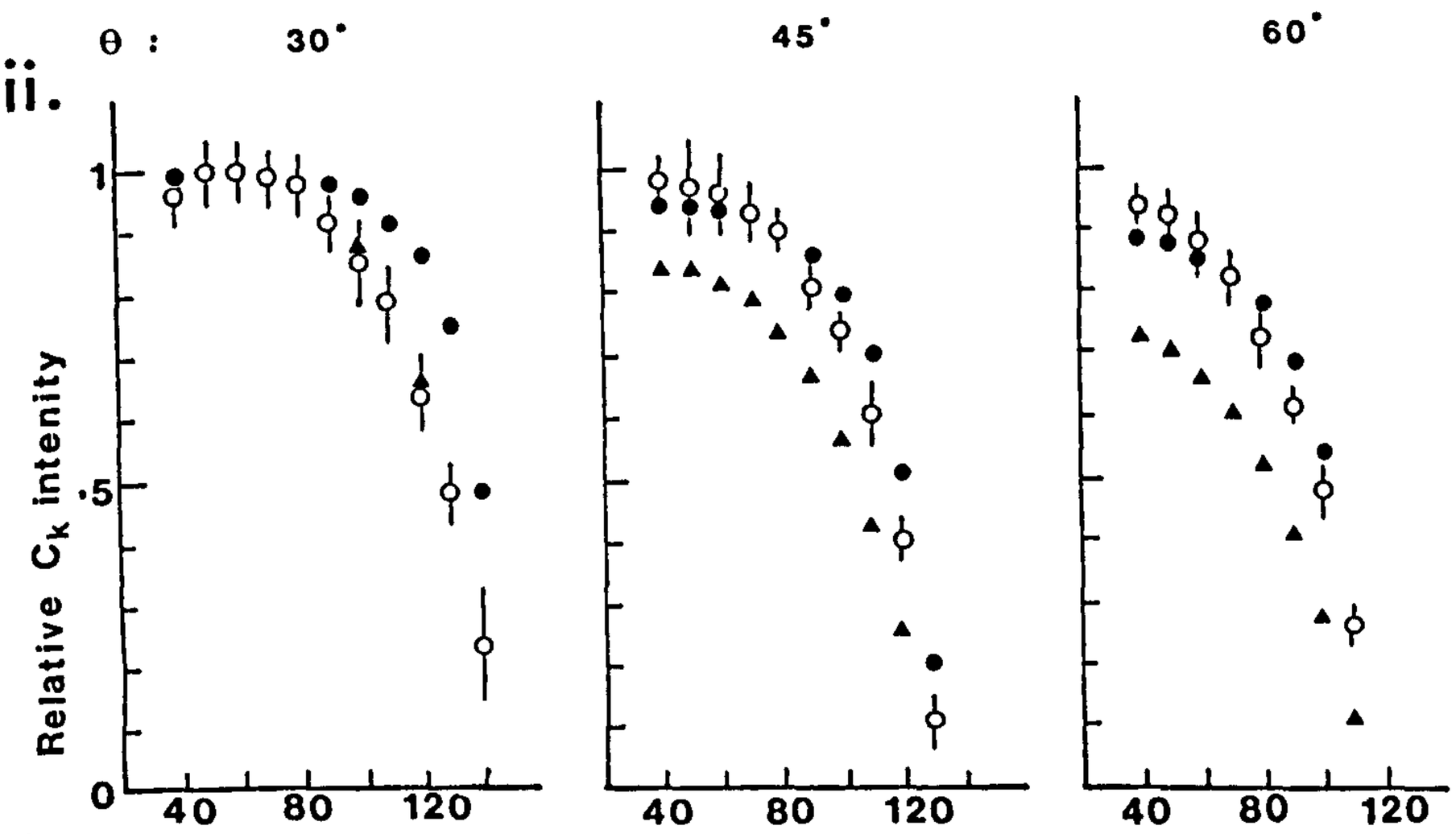
θ : 30°
45°
60°
Relative C_k intenity
1
.5
0
40
80
120
Detector angle , α

iii.

θ : 30°
45°
60°
Relative Al_k intensity
1
.5
0
40
80
120
Detector angle , α

iv.

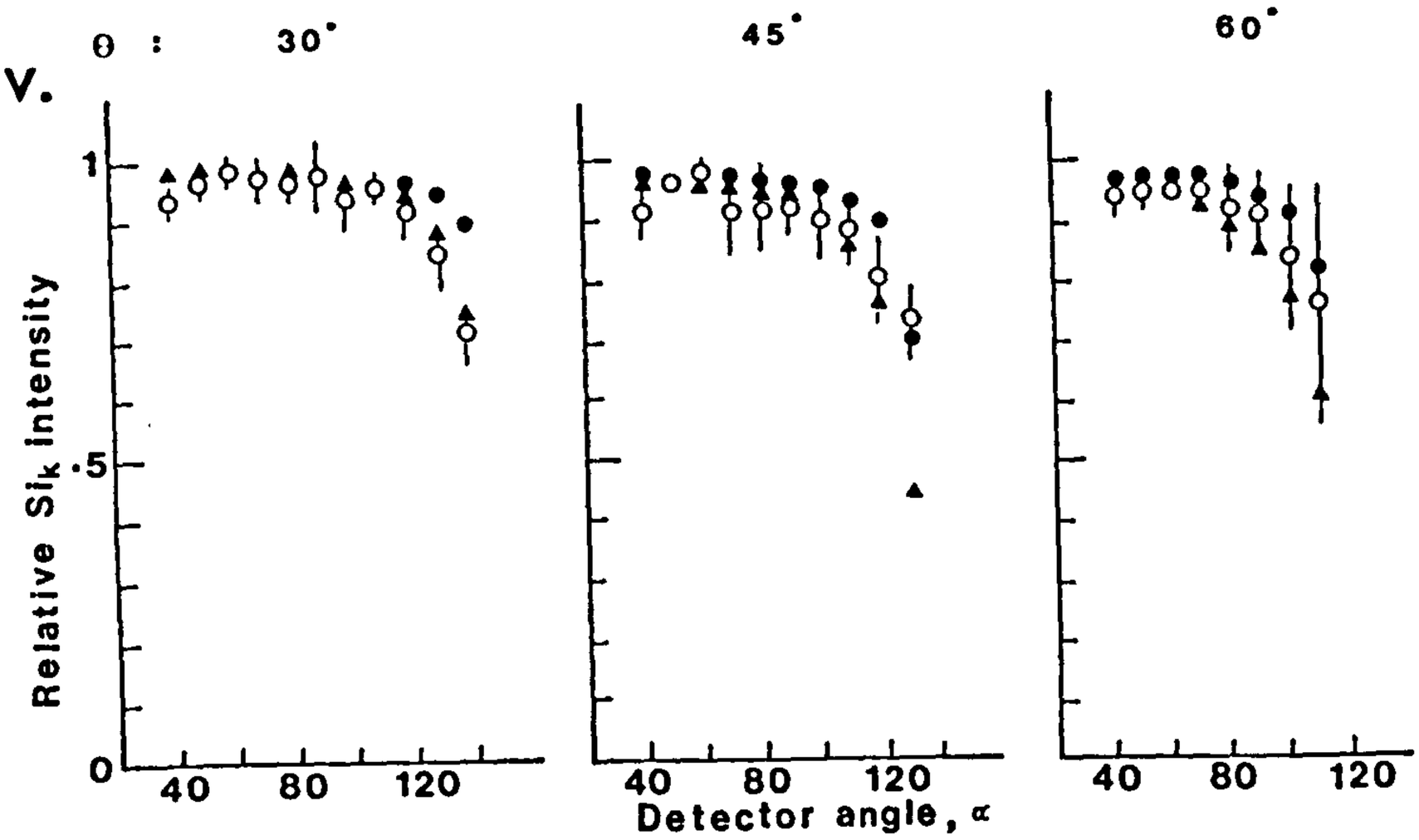
θ : 30°
45°
60°
Relative Si$_K$ intensity
1
·5
0
40
80
120
Detector angle, α

V.

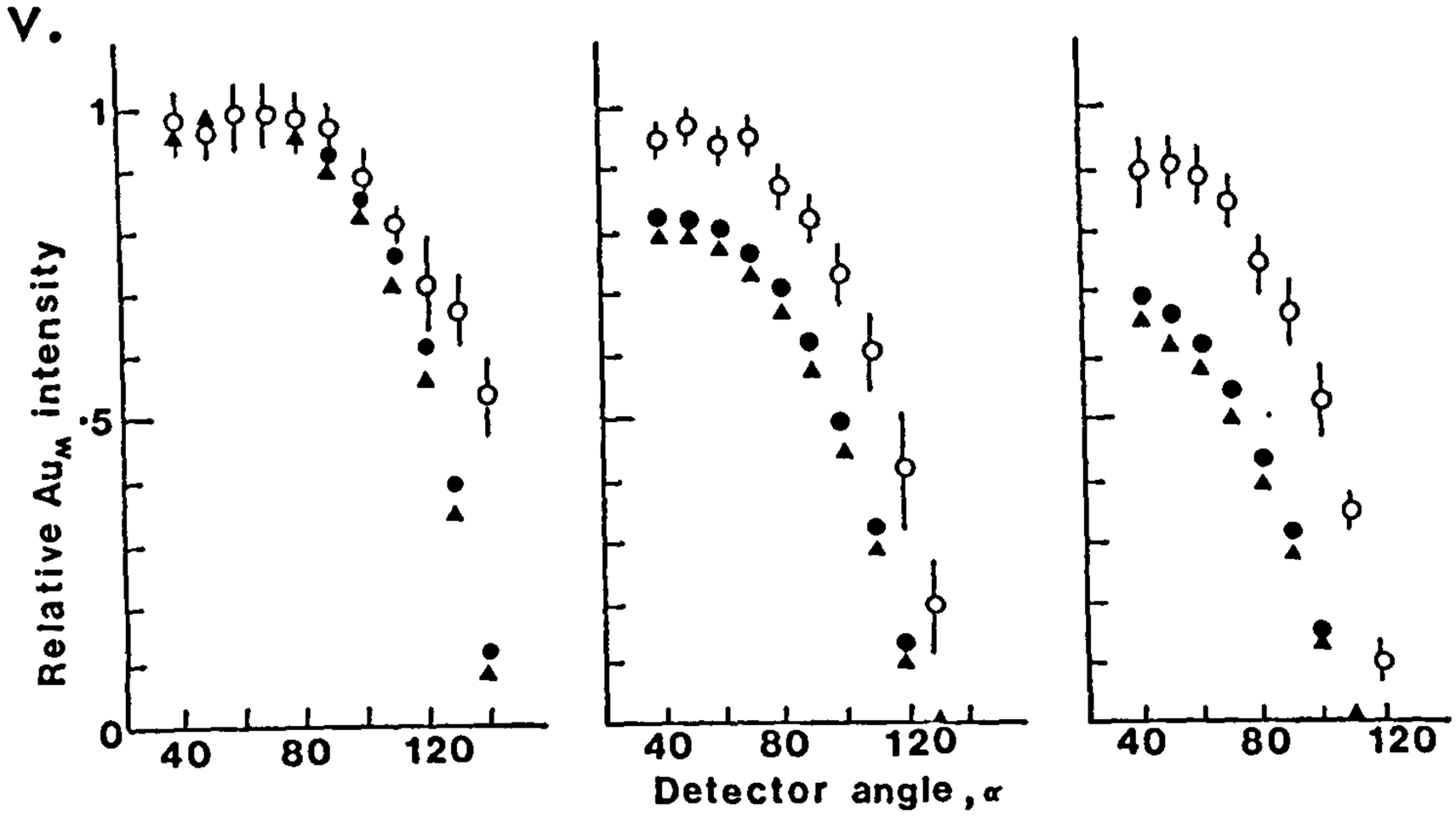
θ : 30°
45°
60°
Relative Au$_M$ intensity
1
·5
0
40
80
120
Detector angle, α

vi.

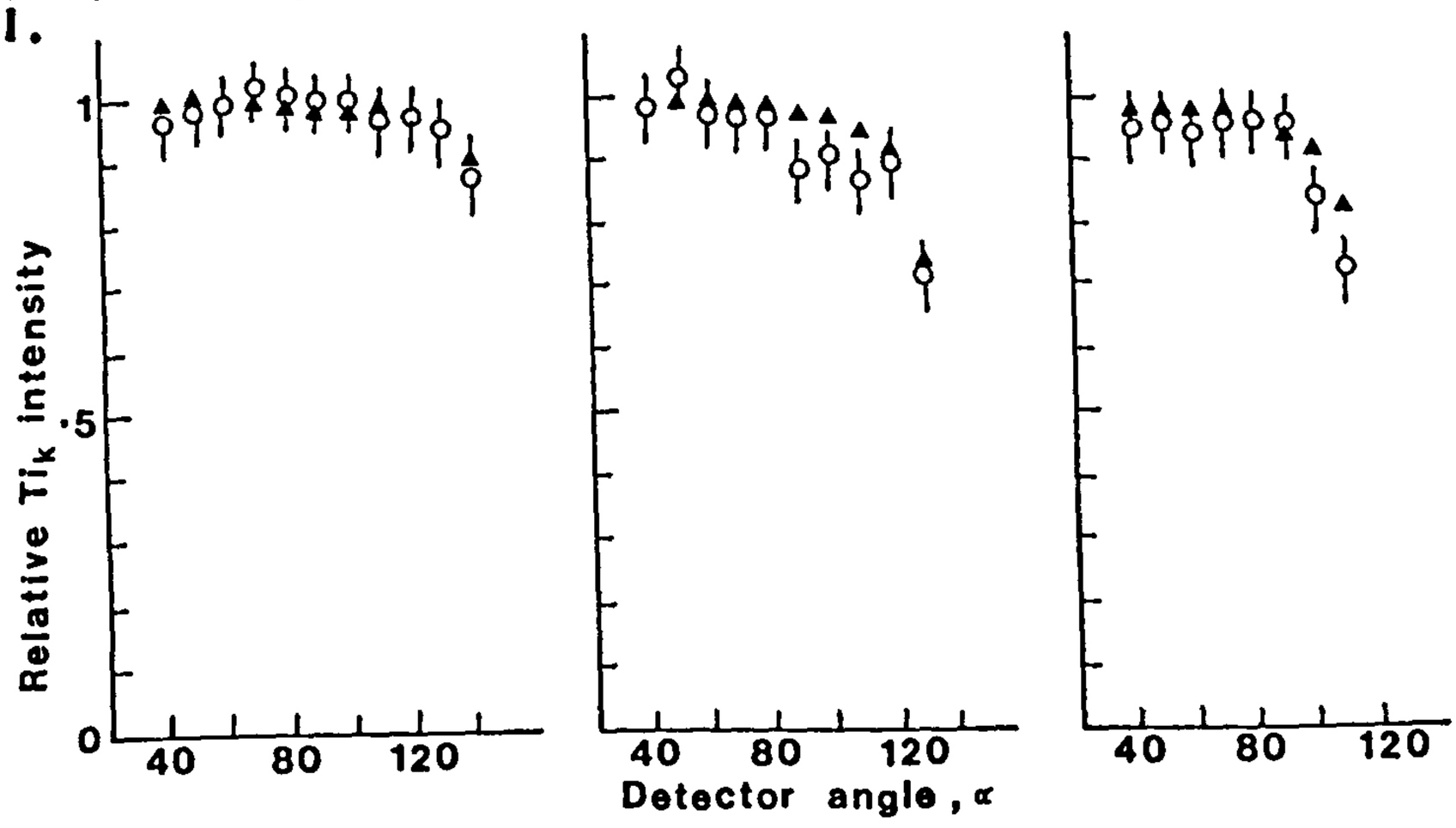
θ : 30°
45°
60°
Relative Ti$_K$ intensity
1
·5
0
40
80
120
Detector angle, α

C_K X-rays in a Carbon target, than for higher energies such as Si_K X-rays in a Silicon target (Figure 5.11). A further anisotropy in the emission of M-shell X-rays might also be expected because of the angular momenta change which occur in the system upon the emission of M X-rays.

5.2.3 Proton energy dependence of X-ray emission

The variation in X-ray intensity with proton energy (at constant current and for a fixed amount of charge onto the target) was measured for the Aluminium and Carbon targets. Three sets of data were taken for each target, the average values being shown in Figure 5.12, with the uncertainties (± s.d.) being less than the size of the plotted points.

Whilst the X-ray production cross-section for 500 keV protons onto a Carbon target is 15 times that for an Aluminium target (Figure 6.5) only a factor 4 difference was observed in practice. This may however be explained by the decreased transmission of the C_K X-rays through the VYNS window and the Polypropylene filter compared to Al_K X-rays - a factor of 2 in each case (Figures 2.7 and 5.3). It was also seen that whilst the intensity of the Al_K X-rays continued to be increasing rapidly as the proton energy approached 700 keV, the intensity of the C_K X-rays appeared to be levelling off. As a result the measured ratio of the Carbon-to-Aluminium intensity decreased with energy (Figure 5.13).

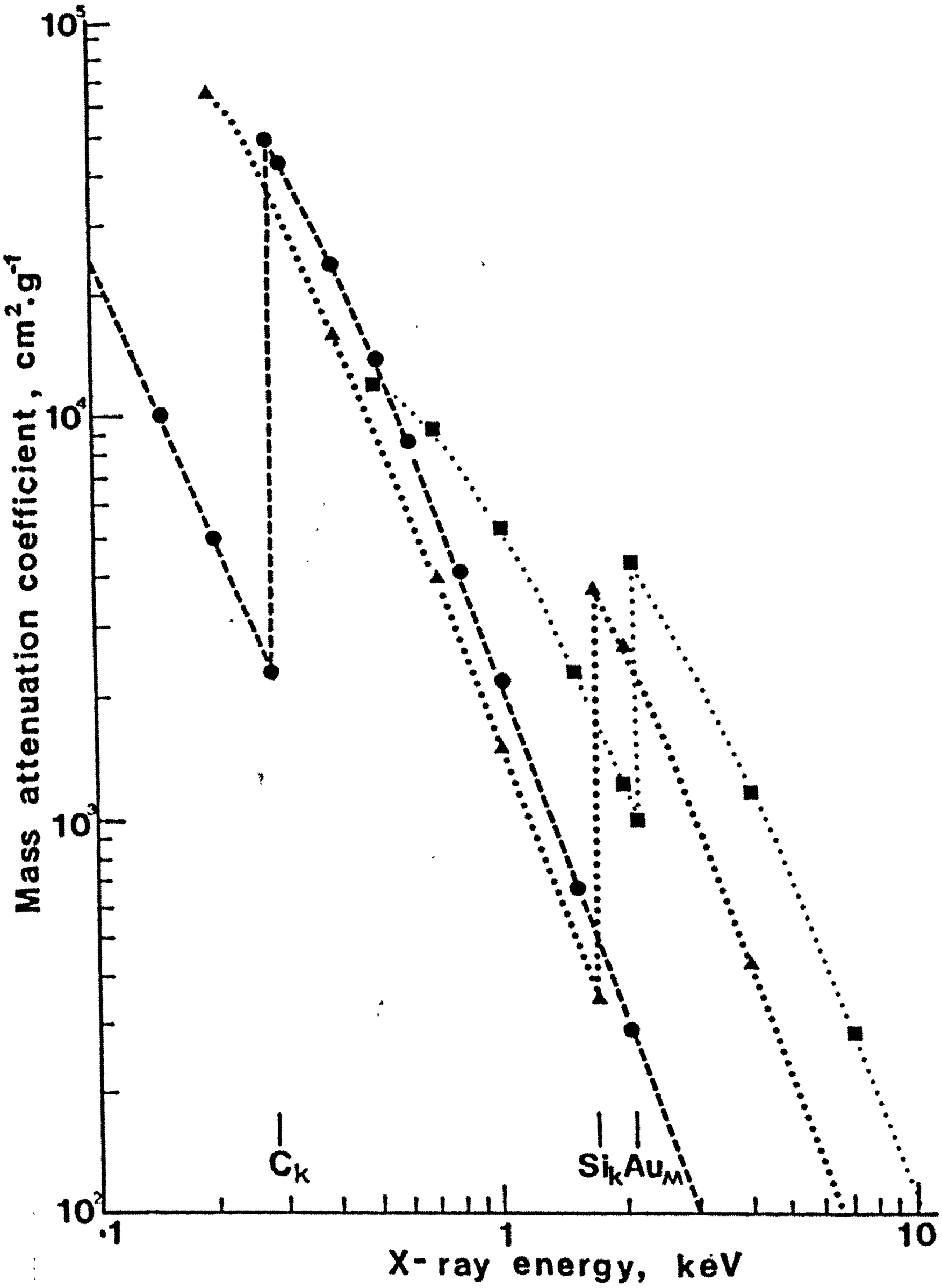

Figure 5.11 The mass attenuation coefficient of low energy X-rays in Carbon (●), Silicon (▲) and Gold (■) targets with the positions of the C_K, Si_K and Au_M X-rays indicated.

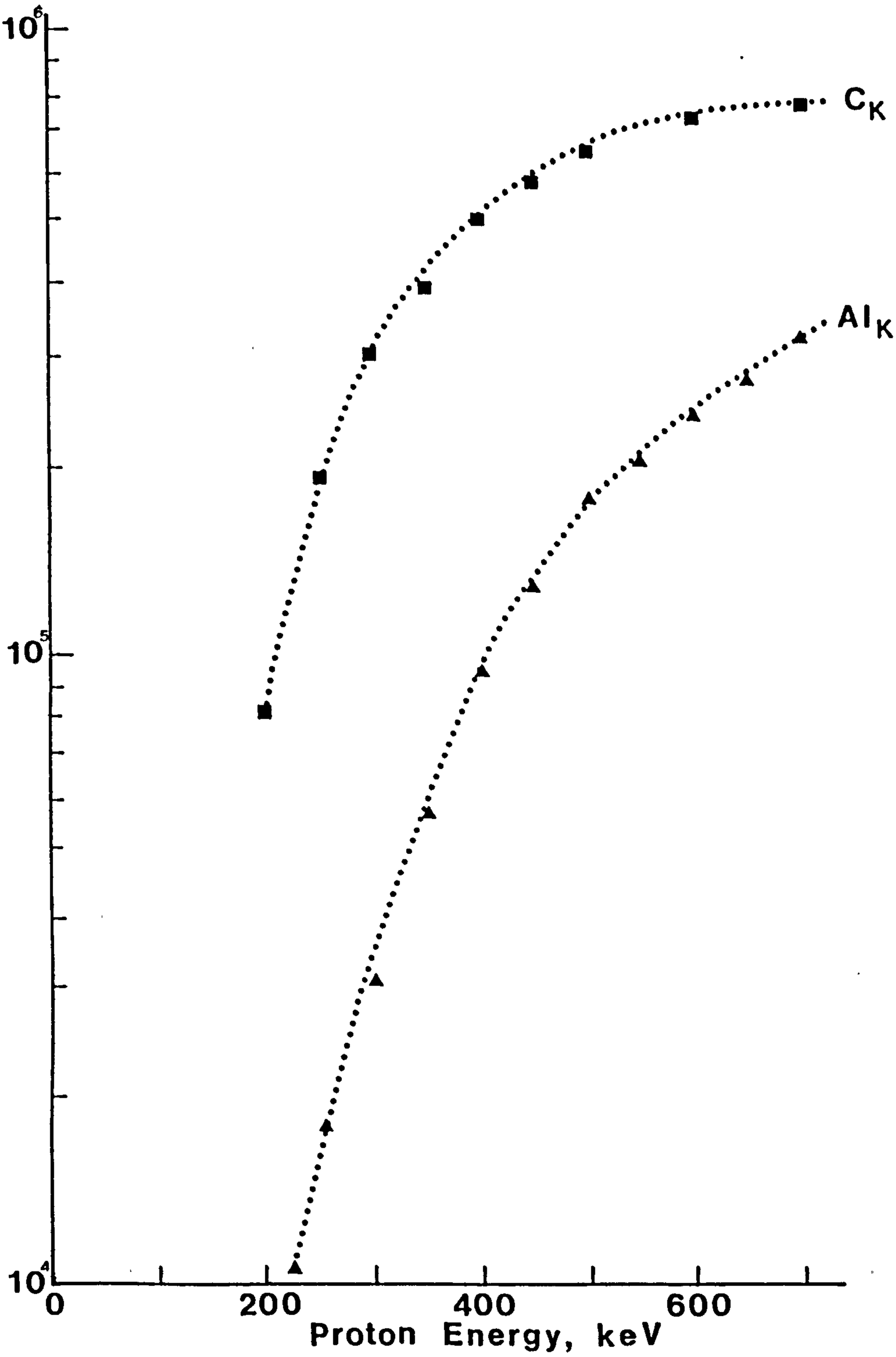

Figure 5.12 The measured X-ray intensities of C_K from a Carbon target (■) and Al_K from an Aluminium target (▲) as a function of proton energy.

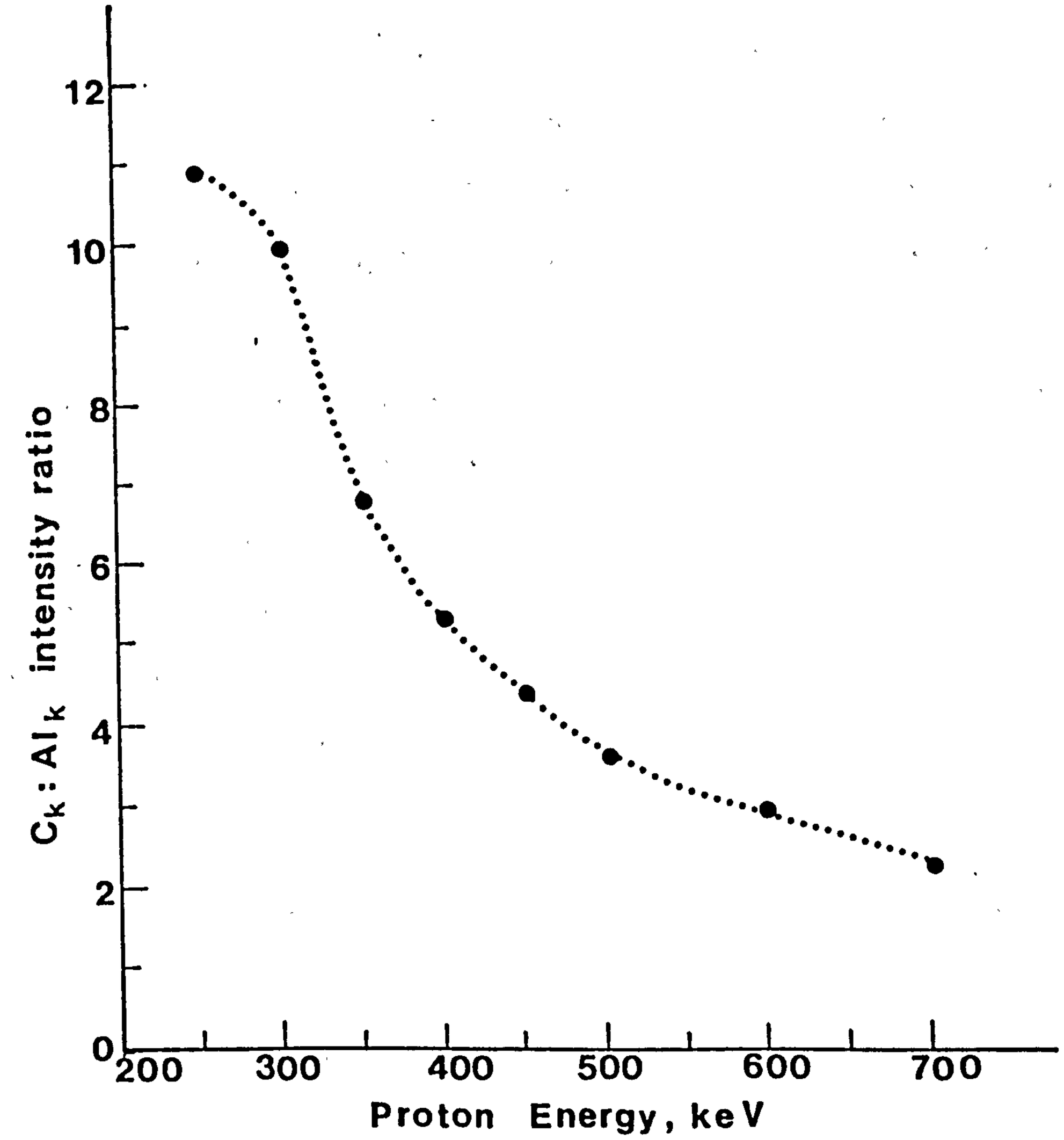

Figure 5.13 The ratio of the measured Carbon-to-Aluminium K-shell X-ray intensity (as given in Figure 5.12) as a function of proton energy.

CHAPTER 6

THEORETICAL TREATMENT OF RESULTS

6.1 Compensation for target surface contamination

The results of the surface contamination study (Section 5.2.1) showed that most, if not all, of the observed target surface contamination was Carbon. Whilst this would appear to be of no relevance for a C_K X-ray beam (Figure 5.5) it most certainly does affect the intensity of other photon energies (Figure 5.6) because of their absorption in the Carbon layer. In order to ensure that any intensity variations occurring in the angular distribution study (Section 5.2.2) was a result of changing the target and/or detector angle, and not due to the build-up of Carbon on the target surface, corrections were applied to the angular distribution data to take into account the depth of Carbon the proton beam had to traverse on leaving the target.

Using the data taken with the detector at an angle of 90° to the beam at the start and end of each target angle scan, it was possible to deduce the effective depth of Carbon on the target surface. If the initial intensity of the target's characteristic X-rays was I_1 and this falls to an intensity I_2 by the end of a scan then, using the expression for the attenuation of a homogeneous X-ray beam in traversing a thickness 'x' of matter (Harnwell and Livingood, 1933):

$$I_2 = I_1 \cdot \exp(-\mu x) \qquad 6.1$$

where μ is a constant of proportionality known as the linear attenuation coefficient.

The μ-values used were derived from the mass attenuation coefficients (μ/ρ) as given by Hubbell (1977)(Figure 6.1), taking the density, ρ, of Carbon as 2300 $kg.m^{-3}$ (Science Data Book, 1978). The linear attenuation coefficients used for the surface contamination

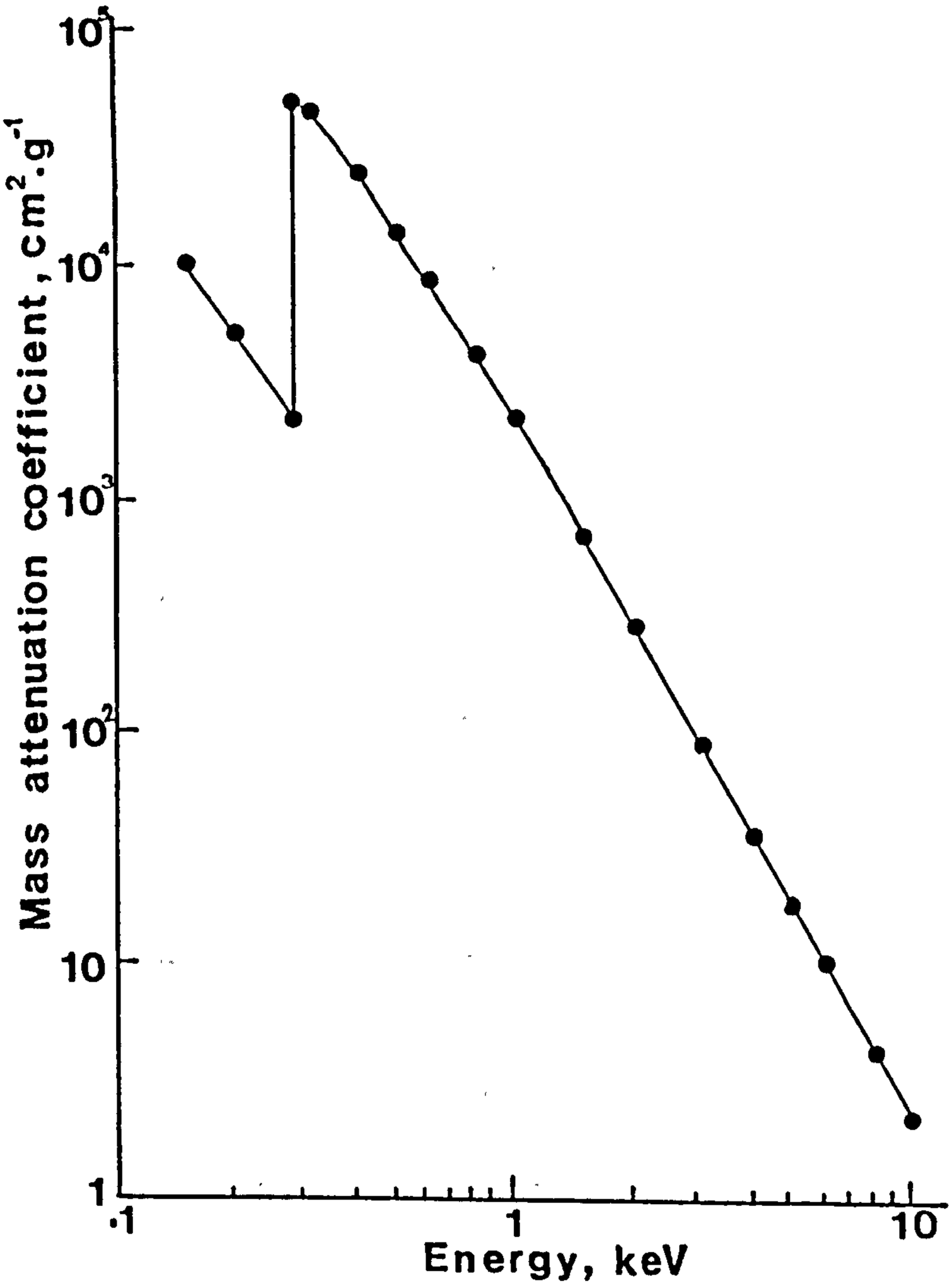

Figure 6.1 The mass attenuation coefficient of low-energy photons in Carbon.

Characteristic X-ray	Energy (keV)	μ (cm^{-1})
B_K	0.183	1.38×10^4
C_K	0.278	4.95×10^3
N_K	0.392	5.75×10^4
Al_K	1.487	1.56×10^3
Si_K	1.740	989
Au_M	2.120	575
Ti_K	4.511	57.5

Table 6.1 The linear attenuation coefficient, μ, of ultrasoft X-rays in Carbon (derived from Hubbell, 1977).

correction are given in Table 6.1. These values were then used in Equation 6.1 to give the depth, x, of Carbon laid down on the target surface between the measurements of I_1 and I_2. In doing this, it was assumed that the incoming proton energy loss in the Carbon layer was negligible. Calculations (Section 6.1.1) showed this assumption to hold within 5%.

Knowledge of the amount of charge which had been collected on the target between the measurements of I_1 and I_2 enabled the Carbon contamination to be expressed in terms of 'thickness per charge' (nm/μC). It was therefore possible to deduce the depth of Carbon on the target surface at any stage of the angular scan. However, as this calculation gave the thickness at 90° to the beam (in line with the detector position), a geometrical correction factor had to be included when the detector angle was varied before the depth of Carbon through which the X-ray photon had to traverse on leaving the target could be calculated (Figure 6.2).

Having calculated the amount of Carbon on the target surface at any particular stage of the angular scan it was possible to modify the intensities obtained for the characteristic X-ray yield to compensate for any attenuation occurring in the Carbon layer. If I_M was the measured intensity, as given by MINUIT (Chapter 4), at target angle, θ, and detector angle, α, then the real intensity, before absorption in the Carbon layer, I_X, was given by

$$I_M(\theta, \alpha) = I_X(\theta, \alpha) \cdot \exp(-\mu \cdot y_{\theta,\alpha}) \qquad 6.3$$

where μ is the linear attenuation coefficient of Carbon for the X-ray energy and $y_{\theta,\alpha}$ is the calculated Carbon thickness on the target surface as given by Equation 6.2 (Figure 6.2). The actual X-ray intensity was therefore taken as

$$I_X(\theta, \alpha) = \frac{I_M(\theta, \alpha)}{\exp(-\mu \cdot y_{\theta,\alpha})} \qquad 6.4$$

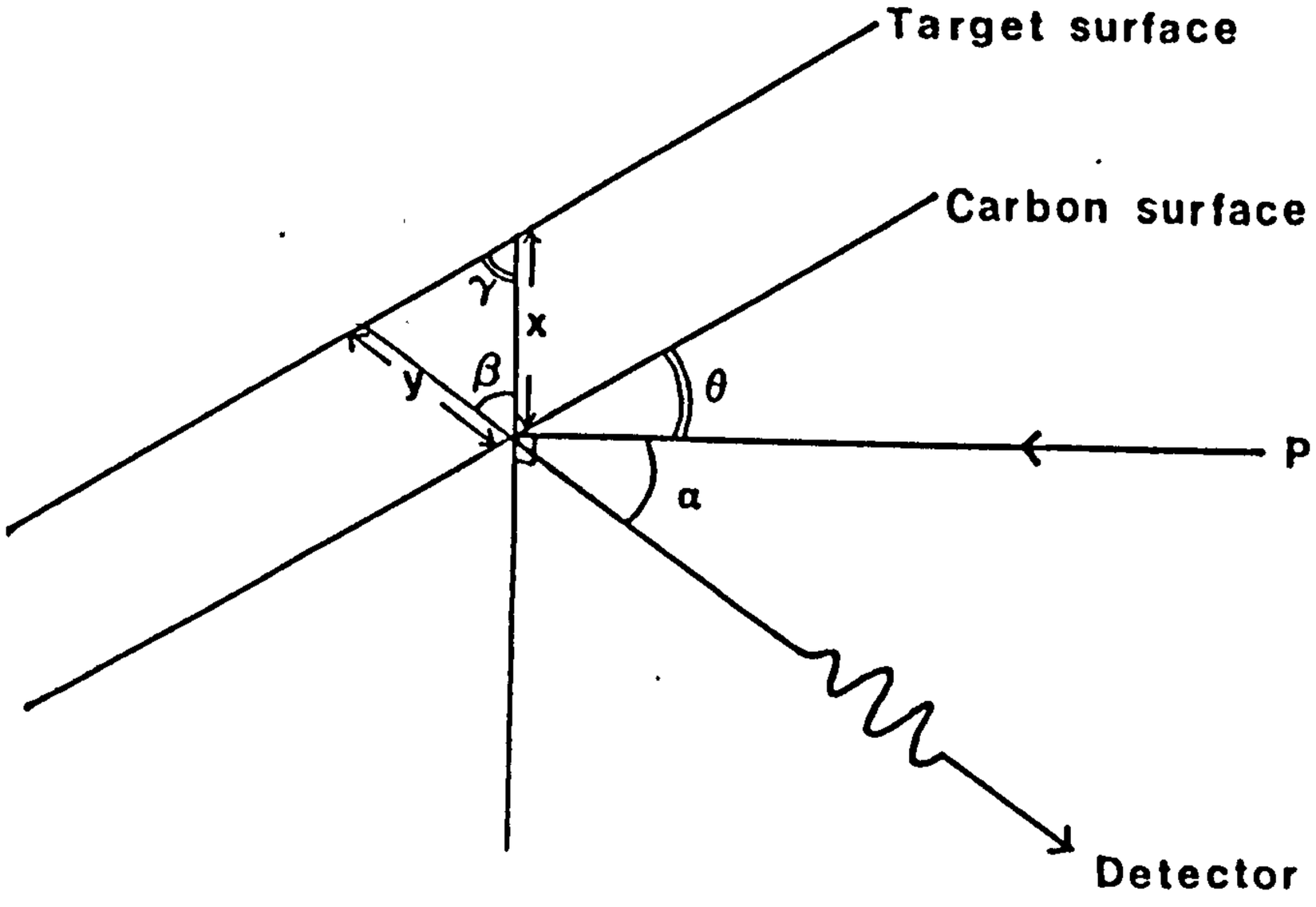

Figure 6.2 Calculation of the depth of Carbon contaminant on the target surface.

$$\beta = 90^\circ - \alpha , \quad \gamma = 90^\circ - \theta$$

Using the Sine theorem :

$$\frac{x}{\sin (180^\circ - (\beta+\gamma))} = \frac{y}{\sin \gamma}$$

$$y = \frac{x.\cos \theta}{\sin (\alpha+\theta)} = y_{\theta,\alpha} \qquad 6.2$$

6.1.1 Example of surface contamination calculation

An example of a set of data for the Aluminium target is shown in Table 6.2, with the measured Al_K X-ray intensities given in the second column. In order to calculate the thickness, x, of Carbon laid down on the target surface between the first (I_1 = 164269 counts) and last (I_2 = 159694 counts) measurements, Equation 6.1 was rearranged to give

$$x = - \frac{ln\ (I_2/I_1)}{\mu} \quad . \qquad 6.5$$

Substituting the values of I_1 and I_2 and using $\mu = 1.56 \times 10^3$ cm^{-1} (Table 6.1) gave

$$x = 1.81 \times 10^{-5} \text{ cm (181 nm)}.$$

Since all the measurements were normalised to the charge collected on the target, each spectrum being collected for 25 μC, the total charge collected between the measurements of I_1 and I_2 was 300 μC. This gave a Carbon build-up depth of 0.6 nm. μC^{-1} or, alternatively, 15 nm per 25 μC of charge collected on the target.

Taking the geometrical correction factor given in Equation 6.2 into consideration, the thickness, y, of Carbon through which the Al_K X-rays had to traverse on leaving the target was calculated for each detector angle (Table 6.2, column 6). It was then possible to use Equation 6.4 to calculate the real intensity of the Al_K X-rays having compensated for the absorption in the surface Carbon layer (Table 6.2, column 7). Finally, the intensities were normalised to the theoretical maximum flux at $\theta = 30°$ and $\alpha = 60°$ (Section 6.2) - Table 6.2, column 8.

As can be seen from Table 6.2, the total Carbon depth at the end of the scan was 195 nm at 90° to the proton beam. This corresponds to a depth of 0.3 μm in the direction of the beam ($\alpha = 0°$) which would result in the proton beam losing ~ 20 keV in the Carbon layer (Figure 6.4), with a 5% reduction in the X-ray production cross-section (Figure 6.5).

Detector Angle α°	Intensity measured I_M	Total charge collected on target (μC)	Depth of C at 90° to the beam x (nm)	$\frac{\cos\theta}{\sin(\theta+\alpha)}$	Depth of C at α° to the beam y (nm)	Emitted X-ray intensity I_X	Intensity normalised to I_X at $\theta=30^\circ, \alpha=60^\circ$
90	164269	25	15	1.00	15.0	164654	1.00
40	157269	50	30	0.92	27.6	157948	0.96
50	160694	75	45	0.88	39.6	161690	0.98
60	163203	100	60	0.87	52.2	164537	1.00
70	162470	125	75	0.88	66.0	163975	1.00
80	162295	150	90	0.92	82.8	164405	1.00
90	161951	175	105	1.00	105.0	164627	1.00
100	160150	200	120	1.13	135.6	163574	0.99
110	158105	225	135	1.35	182.3	162666	0.99
120	149410	250	150	1.73	259.5	155583	0.95
130	130623	275	165	2.53	417.5	139414	0.85
140	92209	300	180	4.99	898.2	106078	0.64
90	159694	325	195	1.00	195.0	164627	1.00

Table 6.2 The Al_K intensity for a target angle, $\theta = 30^\circ$, correcting for surface contamination.

6.2 Calculation of theoretical angular distribution

K-shell characteristic X-rays are emitted isotropically as a result of the initial state having an angular momentum of 1/2 (Folkmann, Cramon and Hertel, 1984). The only angular dependence therefore expected is a geometrical effect due to the self-absorption of the X-rays in the target.

The complete description of the effect of self-absorption in the target would require detailed information on the energy and X-ray production cross-section of the proton beam as a function of the distance travelled within the target. However, for the purpose of comparison with the experimental data a more simplified approach, outlined below, was used (Figure 6.3).

Using the 'Stopping Power' graphs of Anderson and Ziegler (1977) the energy of the proton beam, E_p, at 1 μm increments within the target was calculated, with E_p = 500 keV at the target surface (Figure 6.4). This does assume a constant stopping power within each 1 μm interval and will therefore cumulatively underestimate the energy loss in each interval. However, the range of the proton as calculated in this manner was within 3% of the range as given by Anderson and Ziegler (1977) and therefore the underestimation in the energy loss was deemed negligible. The average energy of the proton beam in each μm, E_i, was taken to be that of a proton at the centre of the increment, that is for

$$x_i = x_1 + (i - 1)\,\Delta x \qquad 6.6$$

with x_1 = 0.5 μm, Δx = 1 μm and i = 1 to 6. Using the analytical cross-section formula of Paul (1984), the K-shell X-ray production cross-section at each position, $\sigma_i(E_i)$, were calculated (Figure 6.5):

$$\sigma = \frac{S_c \times 10^f}{Z^{2.2}} \qquad 6.7$$

where f and S_c are functions of proton energy, E, and target atomic number, Z.

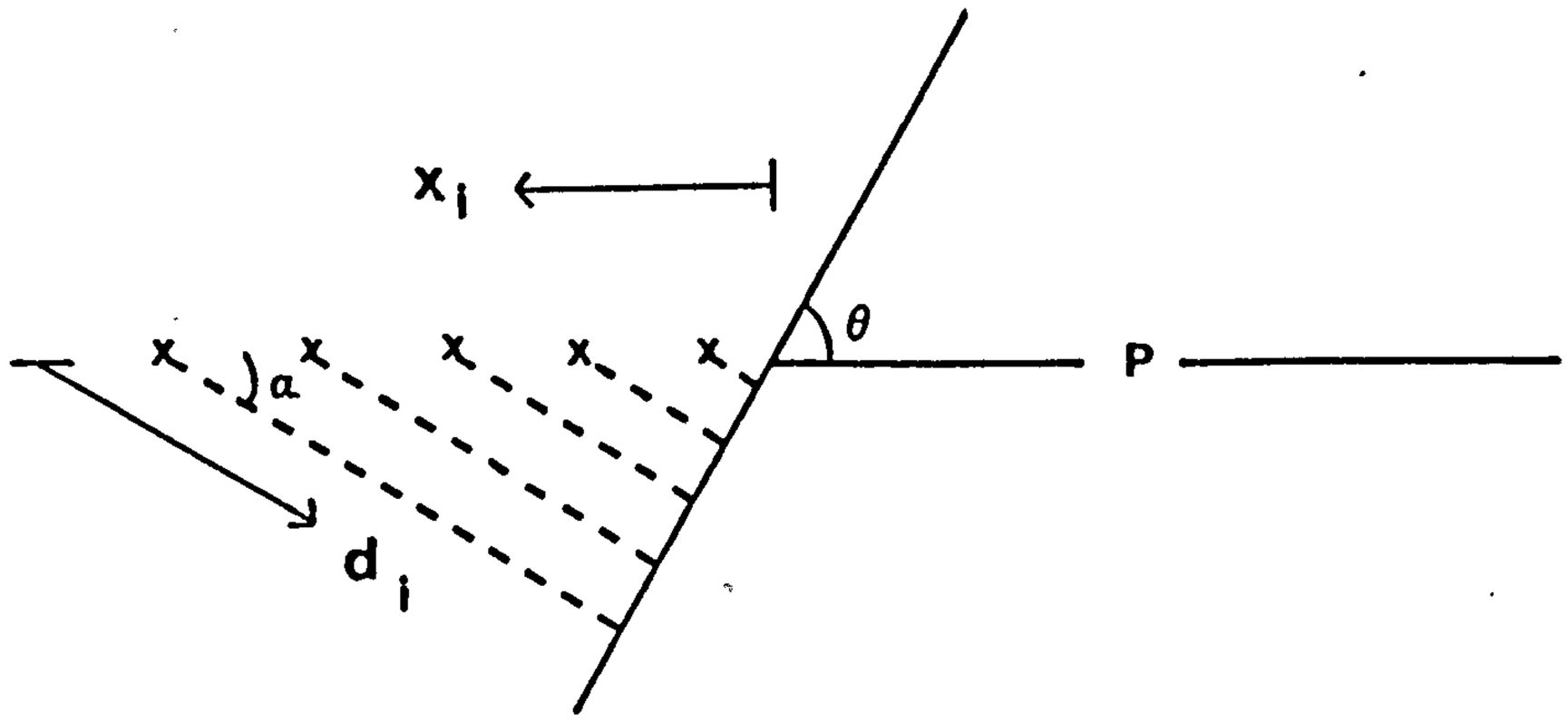

Figure 6.3 Simplifying assumptions used for the calculation of the theoretical angular dependence of the emitted X-rays from a thick target.

$$d_i = \frac{x_i \cdot \sin \theta}{\sin (\theta + \alpha)}$$

$\theta = 30°$, $45°$ and $60°$; $40° \leqslant \alpha \leqslant 130°$

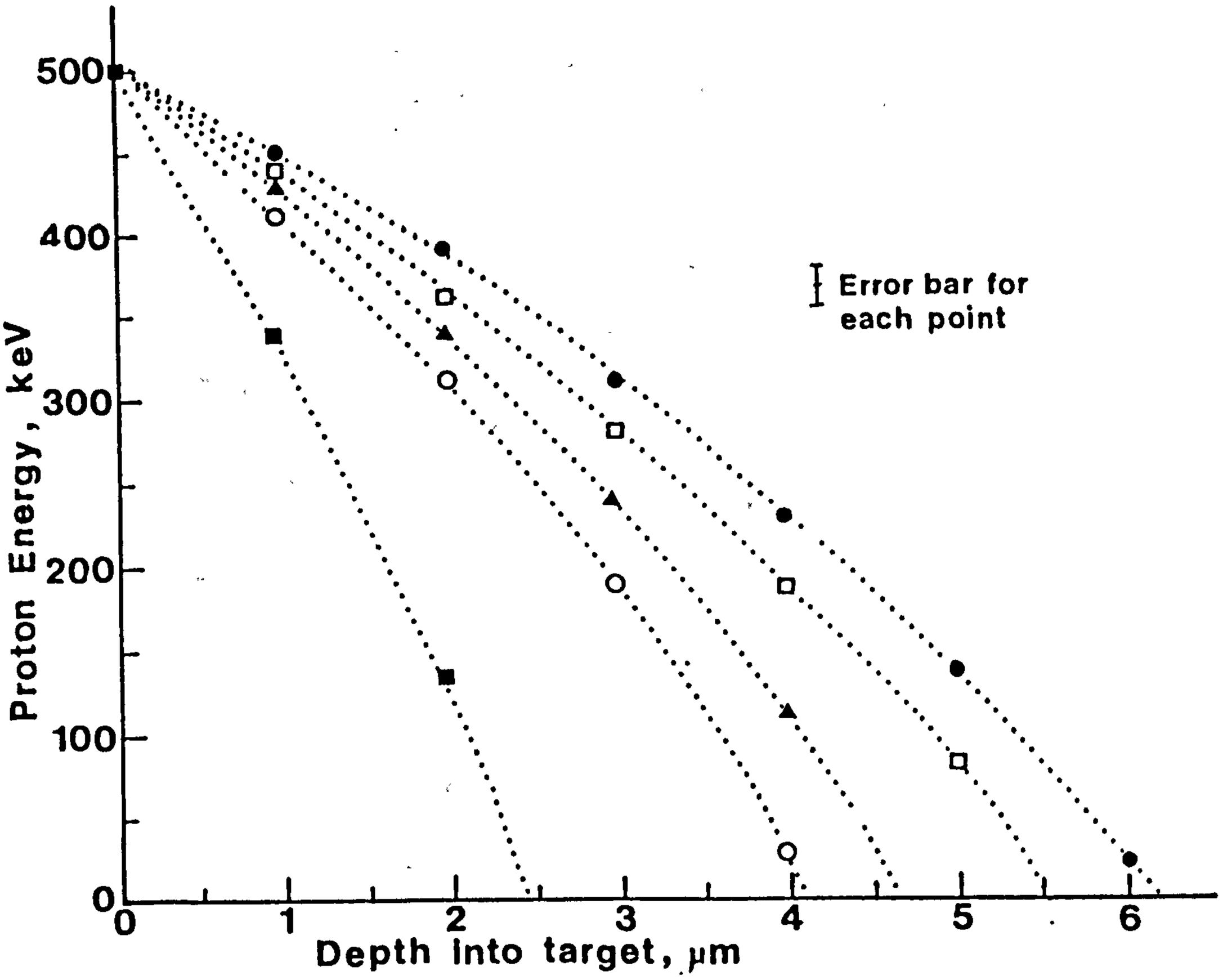

Figure 6.4 The variation of proton energy with depth into the target.

■ Gold target ○ Titanium target

▲ Carbon target (a similar curve is obtained for Boron)

□ Aluminium target ● Silicon target

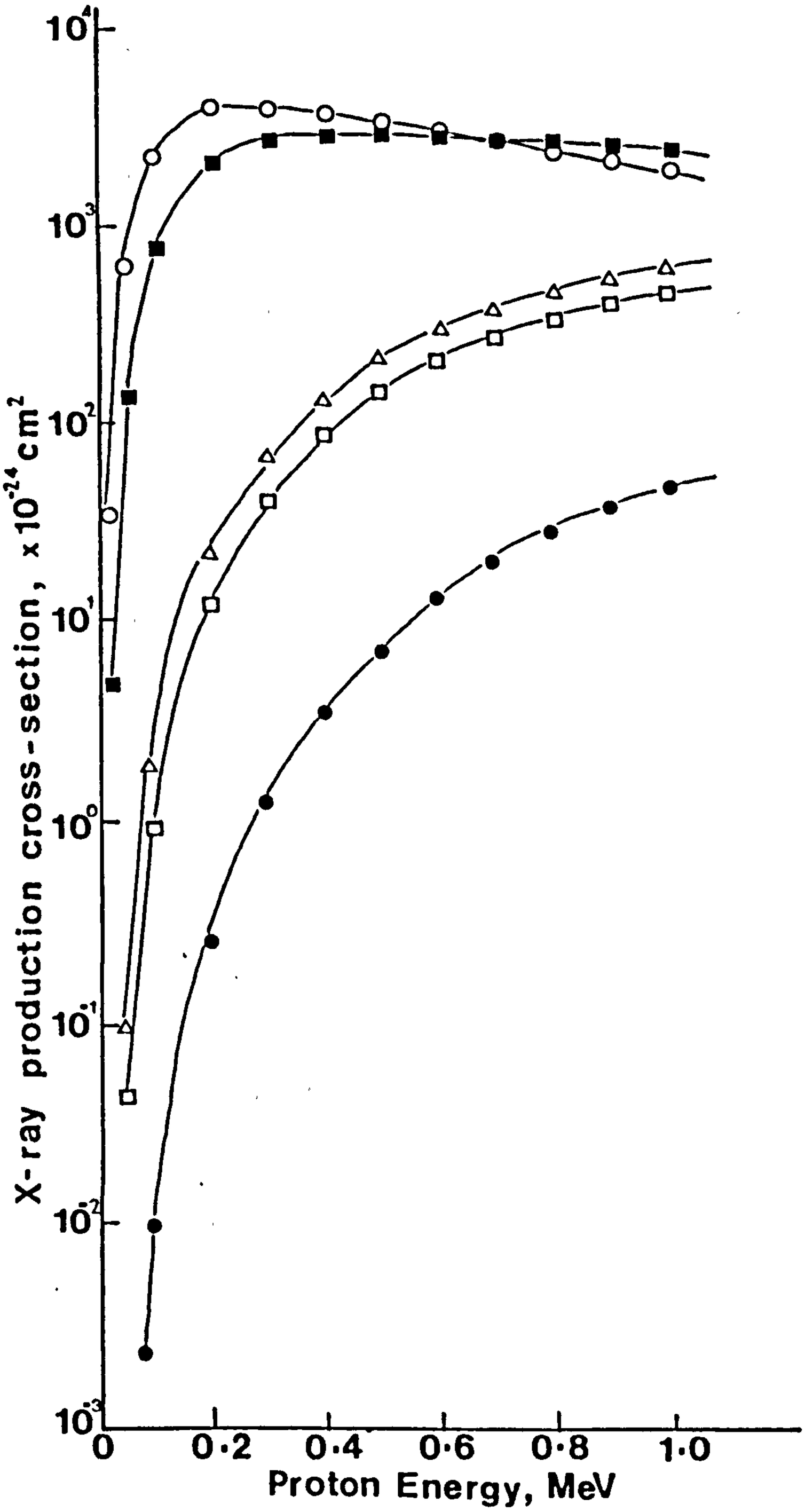

Figure 6.5 The K-shell X-ray production cross-section for proton bombardment of various low Z targets (using the method of Paul (1984))

○ Boron ■ Carbon

△ Aluminium □ Silicon

● Titanium

The proton flux was assumed to be constant over the whole of the proton range, which is generally the case provided $E_P >> I_k$, the electron ionisation energy (~1 keV). No account was taken of the divergence of the proton beam, the assumption being that this will only be of major importance towards the end of the proton range and that even if divergence is occurring it may still be assumed that on average the protons follow a central path.

The number of K-shell photons emitted from a thick target into a solid angle Ω per N incident protons of energy E and range R_o is given by (Lewis, Simmons and Merzbacher, 1953):

$$I(R_o) = \frac{\Omega}{4\pi} \cdot Nn\rho \int_o^{R_o} e^{-\mu d(x)} \cdot \sigma\{E(x)\}\, dx \qquad 6.8$$

where n represents the number of target atoms per gram, ρ represents the density of the target, μ is the absorption coefficient of the target for its own characteristic X-rays (Hubbell and Veigele, 1976; Hubbell, 1977) and d is the distance which the X-ray travels in the target. In the simplified calculation considered here, the photon flux in the direction of the detector was taken to be proportional to:

$$\phi_{\theta,\alpha} = \sum_{i=1}^{6} \sigma_i(E_i) \cdot e^{-\mu d_i} \qquad 6.9$$

where $\sigma_i(E_i)$ was calculated using Equation 6.7 and d_i (Figure 6.3) was calculated from

$$d_i = \frac{x_i \cdot \sin\theta}{\sin(\theta + \alpha)} \cdot \qquad 6.10$$

$\phi_{\theta,\alpha}$ was calculated for each target/detector angle combination and normalised to the maximum flux (found at $\theta = 30°$ and $\alpha = 60°$).

Also calculated were the normalised flux when considering only the first interval of the proton's interaction within the target, that is for the first 1 μm only. In this case the photon flux was taken to be

represented by

$$\phi^{1}_{\theta,\alpha} = \sigma_1 (E_1) \cdot e^{-\mu d_1} \qquad 6.11$$

and all values normalised to $\phi^{1}_{30,60}$.

In the case of the Gold M-shell X-rays a similar treatment was considered but with the production cross-section, $\sigma_i (E_i)$, derived from the total M-shell ionisation cross-section, σ^{I}_{M}, (Johnson, Basbas and McDaniel, 1979) combined with the M-shell average fluorescence yield, $\bar{\omega}_M$, (Bambynek *et al.*, 1972):

$$\sigma_i = \sigma^{I}_{M} \cdot \bar{\omega}_M \qquad 6.12$$

6.2.1 Example of the theoretical angular distribution calculation

For 500 keV protons penetrating an Aluminium target, the energy of the protons along their range (~ 5.5 μm) was calculated using the stopping power data of Anderson and Ziegler (1977), (Table 6.3). These values were plotted (Figure 6.4) and used to find the energy of the proton beam at the centre of each μm increment (Table 6.4, column 2). The X-ray production cross-section at each energy was then derived from Figure 6.5 (Table 6.4, column 3).

Using Equation 6.10, the distance travelled by the X-ray through the target (d_i) was calculated for a given target and detector angle combination for each of the distances travelled by the proton (x_i, $i = 1$ to 6) (Table 6.5). Taking the Aluminium self-absorption coefficient as 1.08×10^{3} cm^{-1} (Hubbell and Veigele, 1976) the product, ϕ_i, of the production cross-section (σ_i) and the attenuation in the target ($e^{-\mu d_i}$) was calculated (Table 6.6).

For each target/detector angle combination, $\phi_{\theta,\alpha}$ (Equation 6.9) was calculated from

$$\phi_{\theta,\alpha} = \sum_{i=1}^{6} \phi_i \qquad 6.13$$

Depth into target (μm)	Proton energy (keV)	Stopping Power of Aluminium (keV/μm)	Proton energy after 1 μm (keV)
0	500.0	69.3	430.7
1	430.7	74.1	356.6
2	356.6	81.3	275.3
3	275.3	90.3	185.0
4	185.0	105.4	79.6
5	79.6	125.3	-

Table 6.3 The energy loss experienced by a 500 keV proton on entering an Aluminium target, assuming a constant stopping power within each 1 μm interval.

Depth into target x_i (μm)	Proton Energy E_i (keV)	X-ray production cross-section σ_i ($\times 10^{-24}\ cm^2$)
0.5	466	190
1.5	392	130
2.5	316	75
3.5	230	32
4.5	132	6
5.5	14	$< 10^{-5}$

Table 6.4 The Al_K production cross-section for the proton as it penetrates the target.

Detector Angle	d_i (μm)					
i :	1	2	3	4	5	6
a^o x_i :	0.5	1.5	2.5	3.5	4.5	5.5
40	0.266	0.798	1.330	1.862	2.394	2.926
50	0.254	0.762	1.269	1.777	2.285	2.792
60	0.250	0.750	1.250	1.750	2.250	2.750
70	0.254	0.762	1.269	1.777	2.285	2.792
80	0.266	0.798	1.330	1.862	2.394	2.926
90	0.289	0.866	1.443	2.021	2.598	3.175
100	0.326	0.979	1.632	2.284	2.937	3.590
110	0.389	1.167	1.945	2.723	3.500	4.278
120	0.500	1.500	2.500	3.500	4.500	5.500
130	0.731	2.193	3.655	5.117	6.579	8.040
140	1.440	4.319	7.198	10.078	12.957	15.837

Table 6.5 The distance travelled by the X-ray, d_i, within the target for a target angle, $\theta = 30°$.

Detector Angle	ϕ_i						$\phi_{30,\alpha}$	
i :	1	2	3	4	5	6		
$\alpha°$ X_i :	0.5	1.5	2.5	3.5	4.5	5.5	$(=\Sigma\phi_i)$	$\frac{\phi_{30,\alpha}}{\phi_{30,60}}$
40	185	119	65	26	5	N	400	1.00
50	185	120	65	26	5	E	401	1.00
60	185	120	66	26	5	G	402	1.00
70	185	120	65	26	5	L	401	1.00
80	185	119	65	26	5	I	400	1.00
90	184	118	64	26	5	G	397	0.99
100	183	117	63	25	4	I	392	0.98
110	182	115	61	24	4	B	386	0.96
120	180	111	57	22	4	L	374	0.93
130	176	103	51	18	3	E	351	0.87
140	163	82	34	11	2	(< 1)	292	0.73

Table 6.6 The product, ϕ_i, of the Al_K X-ray production cross-section, σ_i, and the attenuation of the X-ray in the target $(exp\ [-\mu d_i\ ])$ for a target angle, $\theta = 30°$.

and the intensities normalised to the maximum flux occurring at $\theta = 30°$ and $\alpha = 60°$. Finally $\phi^1_{\theta,\alpha}$ ($= \phi_1$) was considered (Table 6.6, column 2) and normalised to $\phi^1_{30,60}$ (Table 6.7).

Detector Angle α°	$\phi_i = 1$ (= $\phi^1_{30,\alpha}$)	$\phi^1_{30,\alpha} / \phi^1_{30,60}$
40	185	1.00
50	185	1.00
60	185	1.00
70	185	1.00
80	185	1.00
90	184	0.99
100	183	0.99
110	182	0.98
120	180	0.97
130	176	0.95
140	163	0.88

Table 6.7 The contribution of the Al_K X-rays produced in the first μm of the target normalised to those produced at a target angle, $\theta = 30°$ and detector angle, $\alpha = 60°$.

CHAPTER 7

APPLICATION OF MONTE-CARLO TRACK STRUCTURE CODES

7.1 Introduction

This chapter sets out to consider the microtopography of the radiation tracks produced by the interactions of ultrasoft X-rays of varying energy in soft tissue. Significant differences in patterns of energy deposition may result in differences in biological effectiveness which are open to experimental investigation.

Whenever photons interact with matter they create secondary electrons by means of three competing interactions :

(a) the photoelectric effect, in which most of the incident photon's energy is expended in the ejection of an orbital electron;

(b) the Compton effect, in which part of the primary photon's energy is transferred to a single atomic electron and a 'Compton scattered' photon is emitted with energy and direction determined from relativistic momentum-energy conservation;

and

(c) pair production, requiring a minimum of 1.02 MeV, in which an electron-positron pair is produced. The relative importance of each interaction type shifts with increasing energy such that for photon energy, $h\upsilon \lesssim$ 30 keV the photoelectric effect is dominant (in low atomic number material) whilst for $h\upsilon \gtrsim$ 10 MeV it is pair production which is most important. Thus the energy deposition by X- or γ- ray fields on a microscopic scale is determined almost exclusively by the energy loss of their secondary electrons. The importance of the energy deposition of electrons is in fact common to all radiation fields, including heavy ions and neutrons (Paretzke, 1980). A detailed theoretical understanding of the microtopography of events occurring within the track of a charged particle is consequently important. The

availability of the necessary cross-section data (for example Opal, Beaty and Peterson, 1972) and the development of sufficiently powerful computers has contributed towards an increase in our knowledge of the energy deposition by ionising radiation by permitting the calculation of the local concentrations of activations on a nanometer scale using Monte-Carlo track structure simulation codes (Berger, 1974; Heaps and Green, 1974; Hamm *et al.*, 1976; Paretzke, 1978).

Ionising radiations can induce in cells a variety of biological changes. The cell nucleus appears to be the main region of radiosensitivity. However, a large proportion of the ionisations, excitations, and their products, produced by the radiation appear to have no permanent effect on the cell (Goodhead and Brenner, 1983a; Goodhead *et al.*, 1985). Permanent effects such as cell death (loss of proliferation capacity), mutations and chromosome aberrations appear to be caused by some rare, critical damage induced by the radiation. Differing types ('qualities') of ionising radiations have differing efficiencies in producing biological effects thus underlying the need for information on the physical properties of radiation interaction which may be correlated with the biological effect of practical radiations and assist in the understanding of the mechanisms of radiation action.

7.2 Local Energy Deposition of Radiation Tracks

Previous experiments with ultrasoft X-rays have shown that complete biological effects can be efficiently produced by small amounts of highly localised energy depositions (Goodhead, Thacker and Cox, 1979; Goodhead *et al.*, 1980; Thacker, Goodhead and Wilkinson, 1983). For example, the photo-electron produced as a result of the absorption of a C_K X-ray photon in soft tissue deposits < 280 eV in $\lesssim$ 7 nm. These studies indicate that the damage produced by ultrasoft X-rays is similar in nature to that produced by conventional low L.E.T. radiations such as hard X-rays and γ-rays (Goodhead, Cox and Thacker, 1981).

The small dimensions (down to $\lesssim$ 10 nm) involved in the energy deposition of low-energy electrons, including those produced by ultra-soft X-rays are, unfortunately, below the region of most experimental measurement techniques (~ 1 - 10 μm). However, a possible way of identifying the critical characteristics of radiation action is by the use of Monte-Carlo track structure codes. These simulate the radiation tracks in the form of complete atomic, interaction-by-interaction histories, recording all spatial and energy transfer information (Paretzke, 1980). This information can then be compared with the observed relative biological effectiveness (R.B.E.) of the different radiations.

During the late 1950s analyses of the relative effectiveness of heavy ions of different L.E.T. indicated that it might be possible to describe their mechanism of action in terms of a threshold energy deposition in small sites (~ hundreds of eV in ~ nm) (Howard-Flanders,1958). The availability of Monte-Carlo track structure calculations (Paretzke *et al.*,1974; Hamm *et al.*,1978; Terrisol, Patau and Eudaldo,1978; Wilson and Paretzke,1980) supported by low-pressure cloud chamber measurements (Budd and Marshall,1980; Kwok, Budd and Marshall,1981; Brenner,1982) has enabled the threshold energy concept to be reassessed.

Previously reported experiments (Cox, Thacker and Goodhead,1977; Goodhead *et al.*,1980; Thacker, Cox and Goodhead,1980; Virsik *et al.*,1980; Goodhead, Thacker and Cox,1981a) have shown that very low energy photons have considerably greater effectiveness per unit dose than hard X-rays or γ-rays, the lowest energy X-rays having the greater biological effect. Since the X-rays deposit energy throughout the irradiated cells only in highly localised, small quantities, complete biological lesions may be produced by these well defined energy concentrations. Goodhead and Brenner (1983b) set out to investigate the threshold energy concept in terms of a distance and an energy such that the probability of this

amount of energy (or greater) being deposited by the X-rays within a volume correlated with the observed R.B.E. of the radiation. By comparing data obtained from experiments (Goodhead and Brenner,1983b and references therein) with those calculated using the Monte-Carlo track structure codes (Brenner,1982; Brenner and Zaider,1982; Zaider, Brenner and Wilson,1983) it was concluded that, for low L.E.T. radiations at least, there was correlation for threshold energies of about 100 eV in a spherical volume of diameter ~ 3 nm. This correlation did not hold for high L.E.T. radiations.

Whilst spherical volumes are mathematically convenient, intracellular structures at the nanometer level of organisation (such as the D.N.A. double helix, nucleosome, chromatin fibre) are better modelled by cylindrical volumes. Since 1983 a method for scoring energy depositions in randomly orientated cylinders has been developed (Charlton *et al.*,1985a,1985b; Goodhead *et al.*,1985) and using a Monte-Carlo track structure code, based on that of Wilson and Paretzke (1980), an extensive calculation and tabulation of absolute frequencies of energy deposition by mono-energetic protons and α-particles has already been produced (Charlton *et al.*,1985a). The process is being extended to include mono-energetic electrons and photons (H. Nikjoo, *pers. comm.*).

7.3 Calculations using a Monte-Carlo structure code

The energy deposition in small cylindrical targets by simulated electron tracks from the absorption of Carbon, Aluminium and Titanium K-shell X-rays has already been calculated (Nikjoo, Goodhead and Charlton,1987). The Monte-Carlo technique employed has the capability of dealing with extensive input-tables on the relative photo-absorption and atomic de-excitation probabilities for a given irradiated medium, such as soft tissue. However, the construction of complete input

tables to include all modes of absorption of an ultrasoft characteristic X-ray by atoms of all elements in soft tissue, weighted to take account of the photoionisation cross-sections and the percentage by weight of each element in soft tissue, is very time consuming. It would therefore seem practical to try to reduce the time taken by considering only the most significant contribution(s). In this way a wider range of photon energies may be investigated and any discontinuities in local energy deposition as a function of photon energy observed. These may have biological consequences and therefore be open to experimental investigation with appropriate proton-induced ultrasoft X-ray beams.

Goodhead and Thacker (1977) have shown that Carbon, Nitrogen and Oxygen atoms are responsible for ~ 99% of the absorbed dose when mammalian soft tissue is irradiated by Al_K X-rays. The most significant contribution (~ 90%) is the result of absorption in the Oxygen atom's K-shell - Oxygen accounting for ~ 75% by mass of soft tissue of the same atomic composition as spleen of 'reference man' (I.C.R.P., 1975). It might therefore be expected that an input table which showed the production of electrons resulting from the absorption of characteristic X-rays in the Oxygen atoms only would approximately simulate the effects taking place in soft tissue having its full atomic composition.

7.3.1 Track Structure and Scoring Programme

Using a Norsk Data mini-computer at the M.R.C. Radiobiology Unit and the electron track simulation code 'MOCA7' contained within the charged-particle track structure code 'MOCA14' (Wilson and Paretzke, 1981) along with the scoring programme 'ESCORE' (D.E. Charlton and H. Nikjoo, *pers. comm.*) it was possible to carry out scoring for energy deposition in small cylindrical volumes for the K-shell characteristic X-rays of selected elements within the atomic number range $4 \leq Z \leq 20$.

A number of photons were considered for each X-ray energy, taking only absorption by the Oxygen atom into account. This resulted in either one or two electrons, depending on whether the photon energy was sufficiently large to cause the release of an Auger electron as well as the initial photo-electron (Coghlan and Clausing, 1973) (Figure 1.2). A minimum amount of energy required to free an electron ('residual potential energy') of 32 eV was assumed for Oxygen in soft tissue (H. Nikjoo, *pers. comm.*). The resulting input parameters for all the elements considered are given in Table 7.1.

The code MOCA7 was then used to generate the tracks of electrons in water vapour adjusted to a density of 1 $g.cm^{-3}$ (10^3 $kg.m^{-3}$), the electron histories being followed until their energies had fallen to 10 eV. Although liquid water is of greater biological relevance than water vapour (the cell consisting of ~ 80% water), there are fewer experimentally measured cross-sections on which to base a liquid water transport code. Although it is known that there are differences between macroscopic cross-sections in the liquid and vapour phases (Goodhead, 1987d) a comparison of spatial patterns of energy deposition, for electrons, between liquid water codes (Hamm *et al.*, 1976; Terrisol, Patau and Eudaldo, 1978) and those obtained from a water vapour code (Turner *et al.*, 1982, 1983a, 1983b) indicate significant differences only in energy deposition over small ($\lesssim$ 1 nm) distances (Paretzke *et al.*, 1986).

7.3.2. Results

Scoring of the energy deposition of the electrons was carried out within a gross volume defined by a virtual sphere whose radius was at least 1.1 times that of the length of the longest electron track. Chords cutting the virtual sphere were generated using 'μ-randomness' (Kellerer, 1971) and these served as the axes of the cylindrical

Element	Atomic No. Z	Photon Energy (eV)	Residual potential energy (eV)	Photo-electron energy (eV)	Auger electron energy (eV)
Be	4	109	32	77	-
B	5	183	32	151	-
C	6	278	32	246	-
N	7	392	32	360	-
O	8	525	32	493	-
F	9	677	32	140	505
Na	11	1041	32	504	505
Mg	12	1254	32	717	505
Al	13	1487	32	950	505
Si	14	1740	32	1203	505
Cl	17	2622	32	2085	505
Ca	20	3692	32	3155	505

Table 7.1 Input parameters for the electron generating code, MOCA7, considering the interaction of characteristic K-shell X-rays with Oxygen.

Although a residual potential energy of 32eV was used in all the above cases, a slightly lower value would be more appropriate for the singly ionised cases (Be - O)

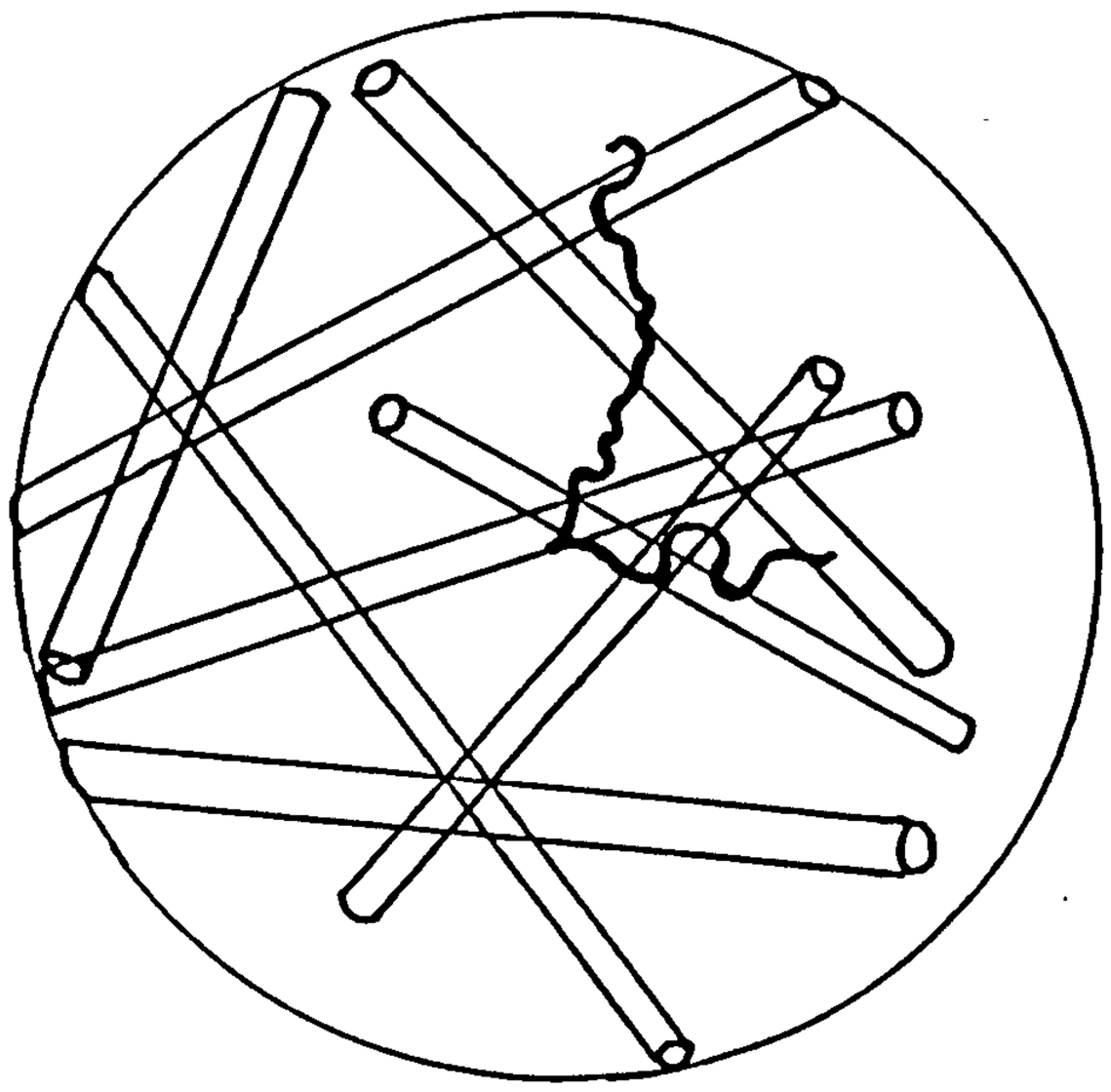

Figure 7.1 Diagram illustrating the virtual sphere enclosing the simulated electron track(s) and crossed by the scoring cylinders arranged at random.

volumes in which the energy deposition was scored (Figure 7.1). Each cylinder was then divided into small sections, beginning at a random point along its length, and the total energy deposited in each section recorded. The lengths of the sections were chosen as multiples of the radius of the cylinder. The frequency of deposition of given amounts of energy in each cylindrical section was recorded and normalised to the frequency which would have occurred had the macroscopic region containing the cylinder been subjected to an electron flux delivering one Gray (Gy). As a check on the sampling accuracy, the ratio of the volume of the virtual sphere to the volume sampled was compared with the ratio of the energy deposited in the virtual sphere to the energy deposited in the target cylinders. These two ratios were generally within 5% of each other. The diameter and length of the target cylinders could be varied and data were collected for dimensions similar to those of biological structures:

Biological Structure	Cylinder diameter (nm)
Element of DNA	2
Nucleosome	10
Element of chromatin fibre	25

In each case, energy deposition was calculated for four cylinder lengths, l, given by

$$l = n \times d \qquad 7.1$$

where d represents the cylinder diameter and n = 0.5, 1, 2 and 4.

Scoring was initially carried out for Carbon and Aluminium (Z = 6 and 13 respectively) to enable a comparison to be drawn between the data obtained from considering absorption by the Oxygen atoms only and those already obtained by H. Nikjoo (*pers. comm.*) from considering the full elemental composition of soft tissue (as given for spleen of 'reference man' (I.C.R.P., 1975)). The results obtained are shown in Figures 7.2 and 7.3. The error bars shown on these and following figures were calculated from the assumption that the statistics of the

Figure 7.2 The frequency of energy depositions greater than a given amount, E in cylinders of various sizes, per Gray of dose to the surrounding medium. Shown are the frequencies obtained when cosidering the interaction of C_K X-rays with the full elemental composition of soft tissue (□) (H. Nikjoo *(pers.comm.)*) and, where they differ by more than the size of the plotted points, considering the interaction of C_K X-rays with Oxygen atoms only (△). The error bars were calculated using Equations 7.2 and 7.3 in the text.

(i.) 2 nm diameter cylinder - A : 8 nm length
B : 4 nm length
C : 2 nm length
D : 1 nm length

(ii.) 10 nm diameter cylinder - A : 40 nm length
B : 20 nm length
C : 10 nm length
D : 5 nm length

(iii.) 25 nm diameter cylinder A : 100 nm length
B : 50 nm length
C : 25 nm length
D : 12.5 nm length

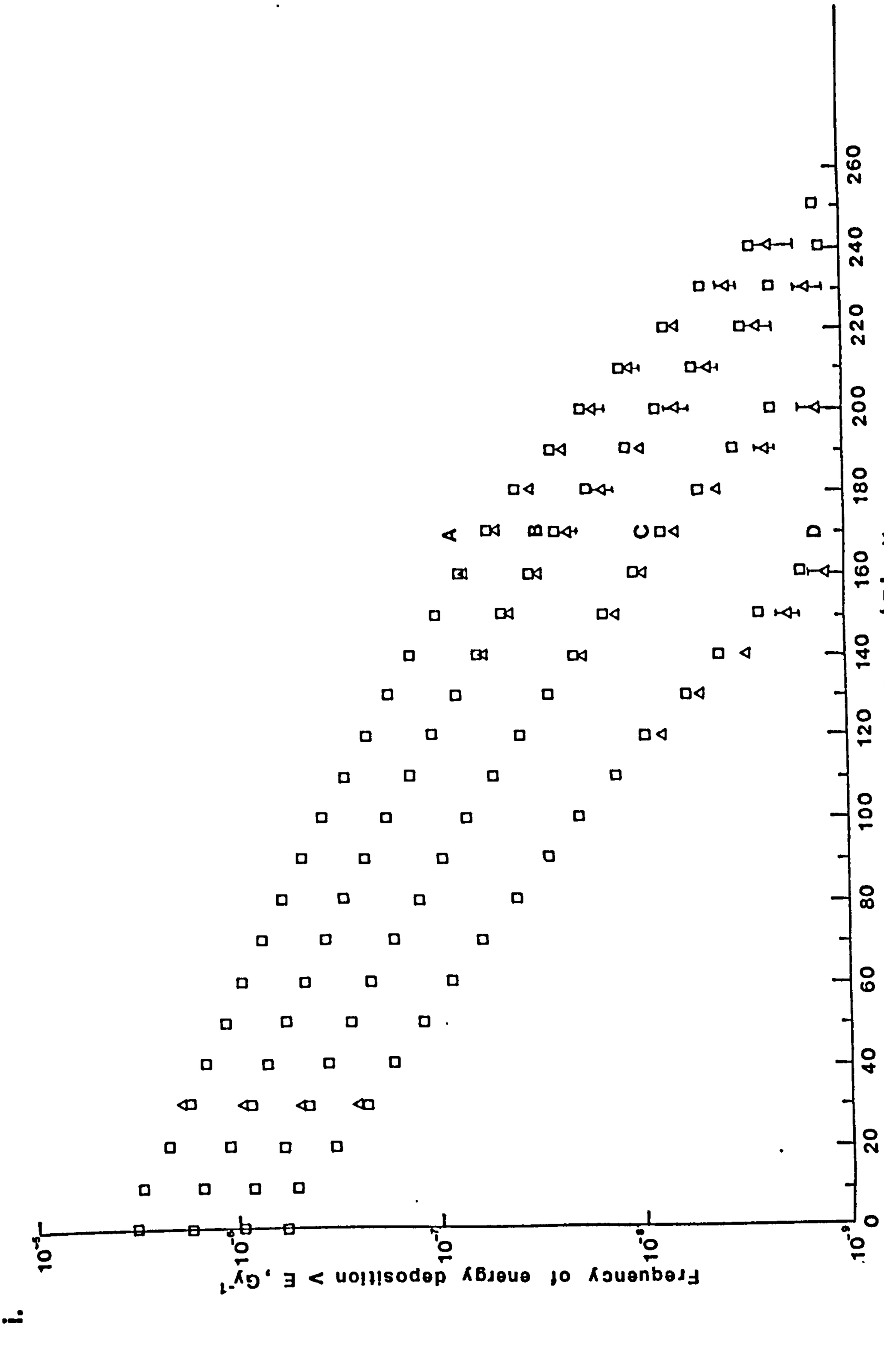
A
B
C
D
Threshold Energy 'E', eV
Frequency of energy deposition > E , Gy⁻¹
0
20
40
60
80
100
120
140
160
180
200
220
240
260
10⁻⁹
10⁻⁸
10⁻⁷
10⁻⁶
10⁻⁵

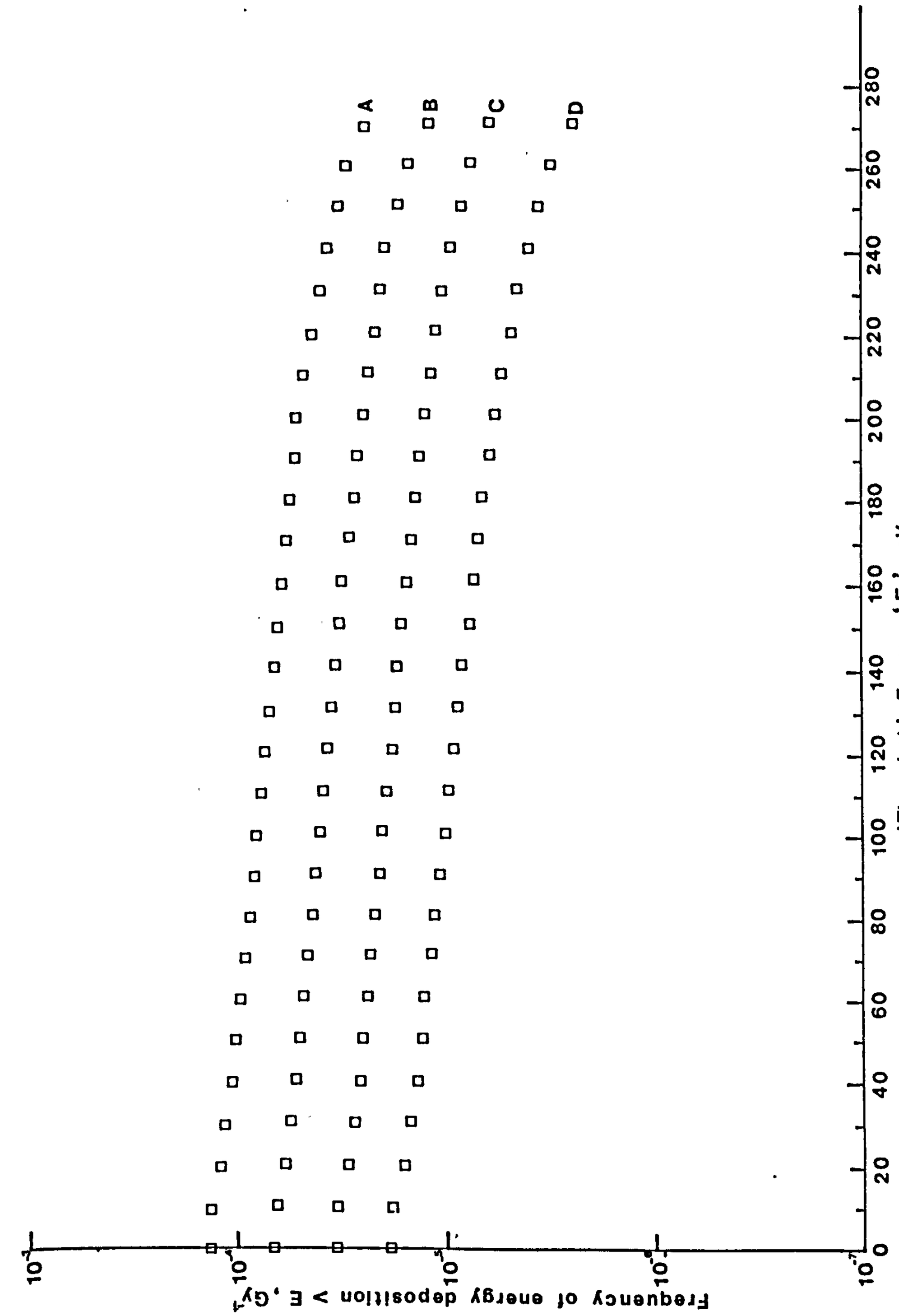
A
B
C
D
280
260
240
220
200
180
160
140
120
100
80
60
40
20
0
Threshold Energy 'E', eV
10^{-3}
10^{-4}
10^{-5}
10^{-6}
10^{-7}
Frequency of energy deposition > E, Gy^{-1}

ii.

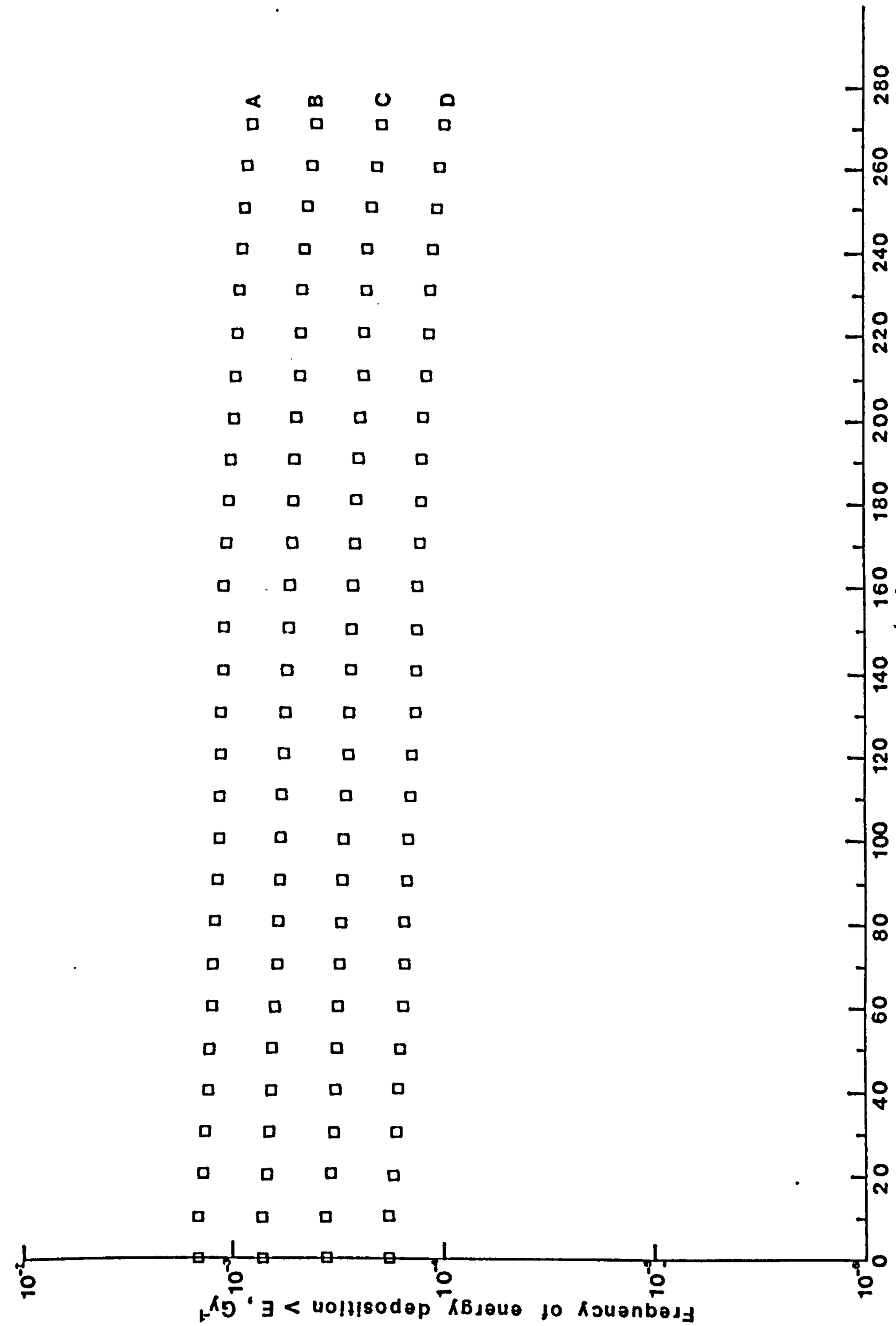
A
B
C
D
280
260
240
220
200
180
160
140
120
100
80
60
40
20
0
Threshold Energy 'E', eV
10^{-2}
10^{-3}
10^{-4}
10^{-5}
10^{-6}
Frequency of energy deposition > E, Gy^{-1}

Figure 7.3 The frequency of energy depositions greater than a given amount, E in cylinders of various sizes, per Gray of dose to the surrounding medium. Shown are the frequencies obtained when considering the interaction of Al_K X-rays with the full elemental composition of soft tissue (□) (H. Nikjoo *(pers.comm.)*) and, where they differ by more than the size of the plotted points, considering the interaction of Al_K X-rays with Oxygen atoms only (Δ). The error bars were calculated using Equations 7.2 and 7.3 in the text.

(i.) 2 nm diameter cylinder - A : 8 nm length
B : 4 nm length
C : 2 nm length
D : 1 nm length

(ii.) 10 nm diameter cylinder - A : 40 nm length
B : 20 nm length
C : 10 nm length
D : 5 nm length

(iii.) 25 nm diameter cylinder - A : 100 nm length
B : 50 nm length
C : 25 nm length
D : 12.5 nm length

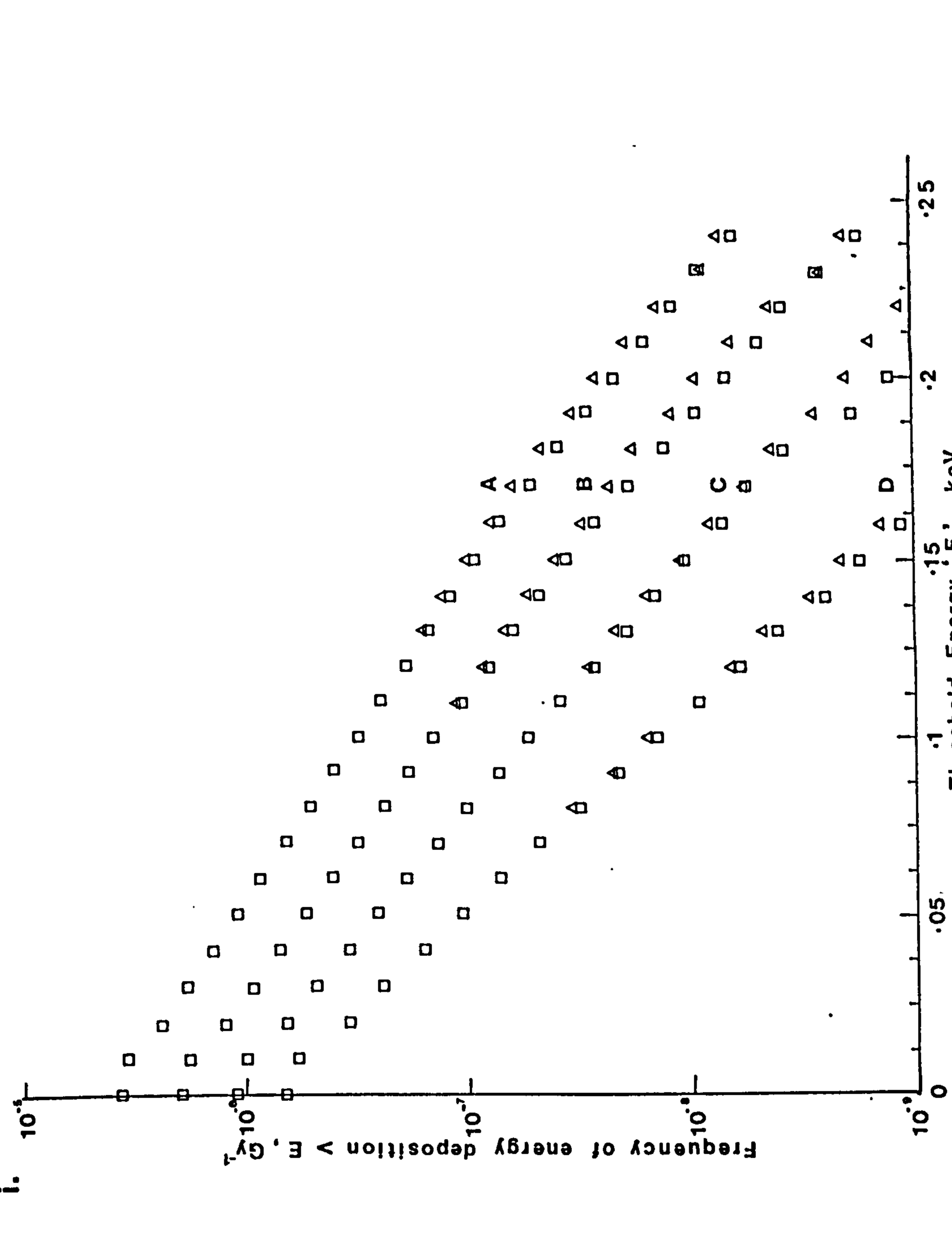
A
B
C
D
Threshold Energy 'E', keV
Frequency of energy deposition > E, Gy⁻¹
10⁻⁵
10⁻⁶
10⁻⁷
10⁻⁸
10⁻⁹
0
.05
.1
.15
.2
.25

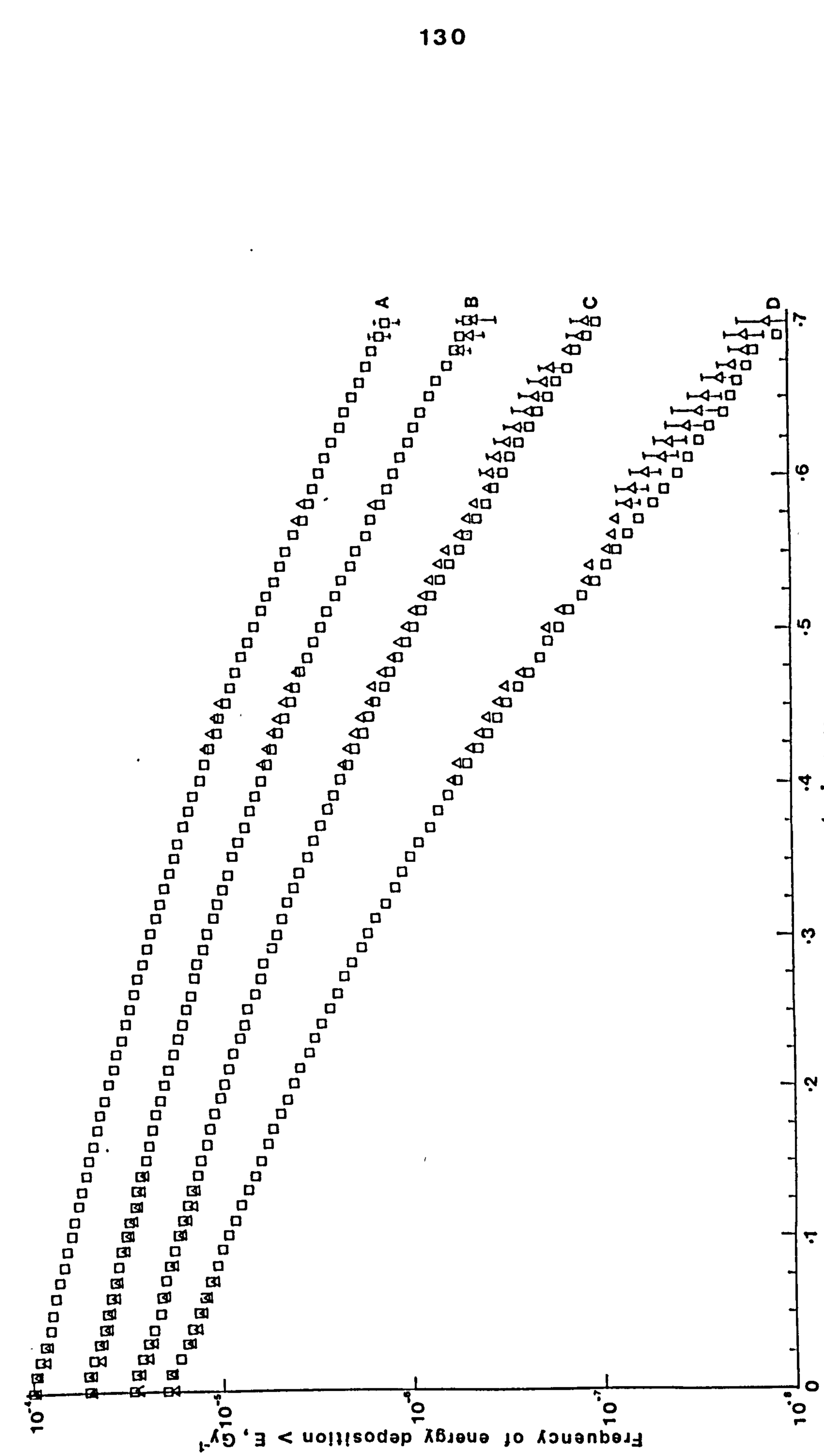
A
B
C
D
Frequency of energy deposition > E, Gy⁻¹
10⁻⁴
10⁻⁵
10⁻⁶
10⁻⁷
10⁻⁸
0
.1
.2
.3
.4
.5
.6
.7
Threshold Energy 'E', keV

ii.

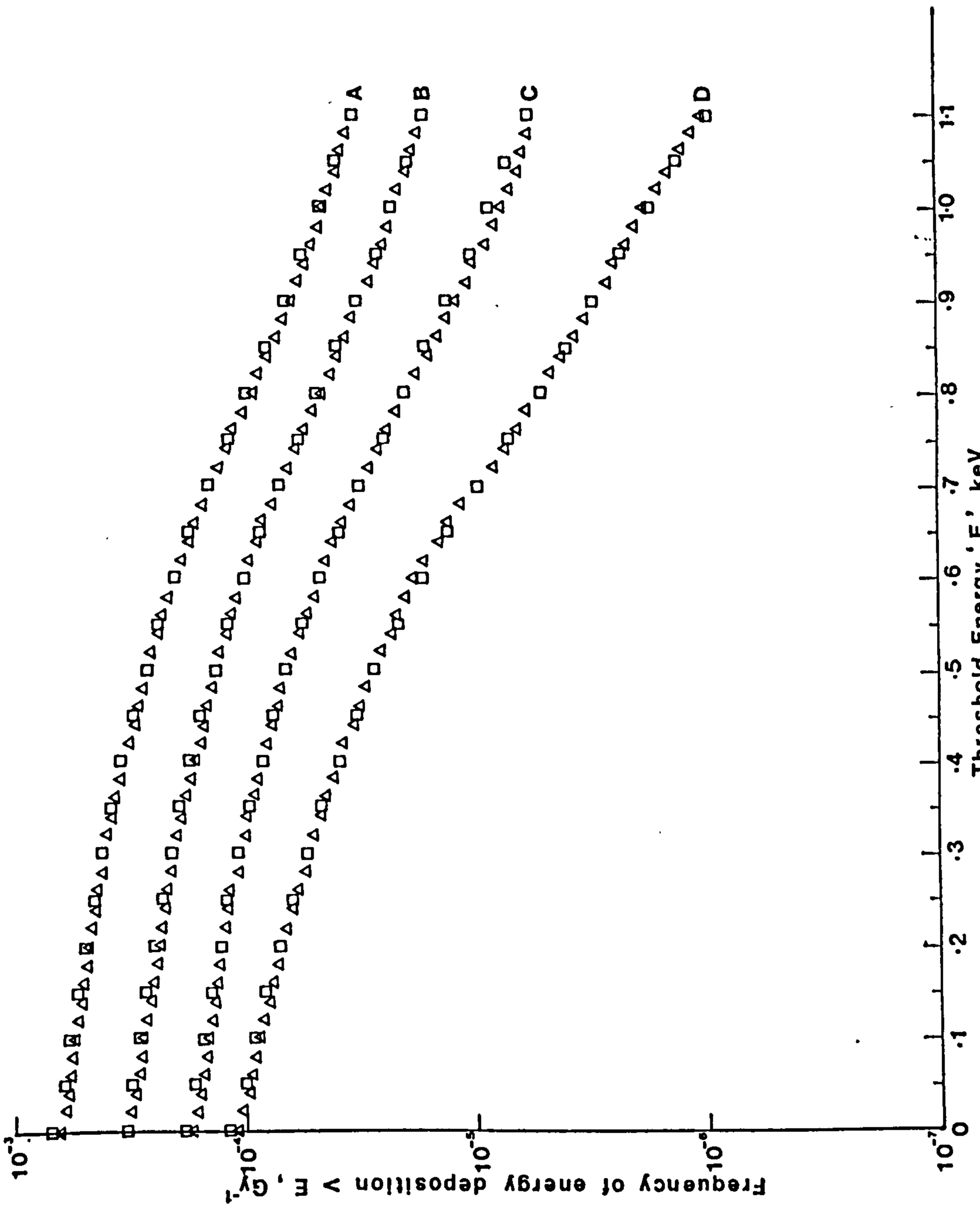
A
B
C
D
Frequency of energy deposition ν E , Gy
10⁻³
10⁻⁴
10⁻⁵
10⁻⁶
10⁻⁷
0
.1
.2
.3
.4
.5
.6
.7
.8
.9
1·0
1·1
Threshold Energy 'E', keV

data were represented by the number of hits within the target cylinders. If 'H' represents the total number of hits within the target cylinders and '$f_{>E}$' denotes the frequency of energy deposition greater than E per Gy, then the percentage error on each frequency was calculated using:

$$n_E = \frac{f_{>E}}{f_{>0}} \times H \qquad 7.2$$

$$\% \text{ error} = \frac{\sqrt{n_E}}{n_E} \times 100 = (n_E)^{-\frac{1}{2}} \times 100 \qquad 7.3$$

If the entire track of a C_K X-ray absorption in soft tissue is approximated as a highly localised ('point') event in a large scoring cylinder, then as the cylinder length increases the frequency of energy deposition greater than a given amount, E, would be expected to increase proportionally. From Figure 7.2, (ii) and (iii), it is seen that the frequency of energy deposition does double with cylinder length for the larger diameter cylinders, but for the smallest cylinder diameter (Figure 7.2, (i)) as the cylinder length is doubled the frequency increases by more than a factor 2 at high threshold energies ($E \gtrsim 50$ eV) and less than 2 at lower energies. This suggests that as the target cylinder length increases it is more likely to contain large energy depositions (large hits) and less likely to have just a small amount of energy deposited in it. Figure 7.3 shows that Al_K X-rays follow the same tendency but, because of the larger dimensions of the tracks, a larger sized target ($\gtrsim$ 25 nm diameter) is required before the approximation holds that doubling the target size doubles the chance of hitting it.

The results of scoring the C_K and Al_K X-rays showed sufficient agreement between the data considering absorption in Oxygen atoms only and the data taking the complete elemental composition of soft tissue into account to warrant the continuation of scoring using absorption by Oxygen only. Using the data of Table 7.1 as input, scoring was therefore carried out for the remaining elemental characteristic energies using the code ESCORE. A limit of $Z \leq 20$ was set because efficient scoring

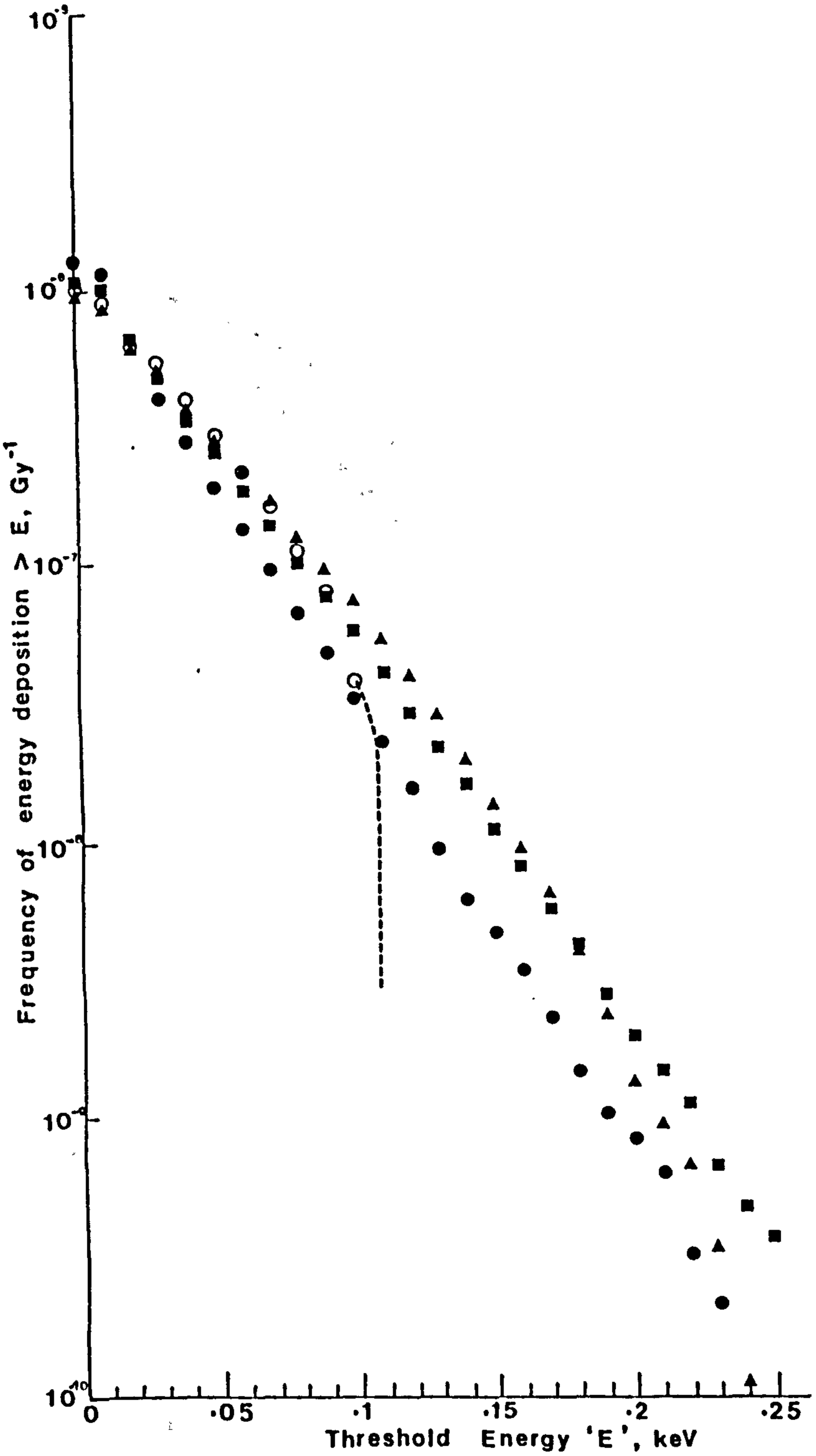

Figure 7.4 The frequency of energy depositions greater than a given amount, E in a 2 nm diameter, 2 nm long cylinder by simulated electron tracks from various low Z characteristic X-rays.

- ○ Be_K X-rays
- ▲ C_K X-rays
- ■ Al_K X-rays
- ● Ca_K X-rays

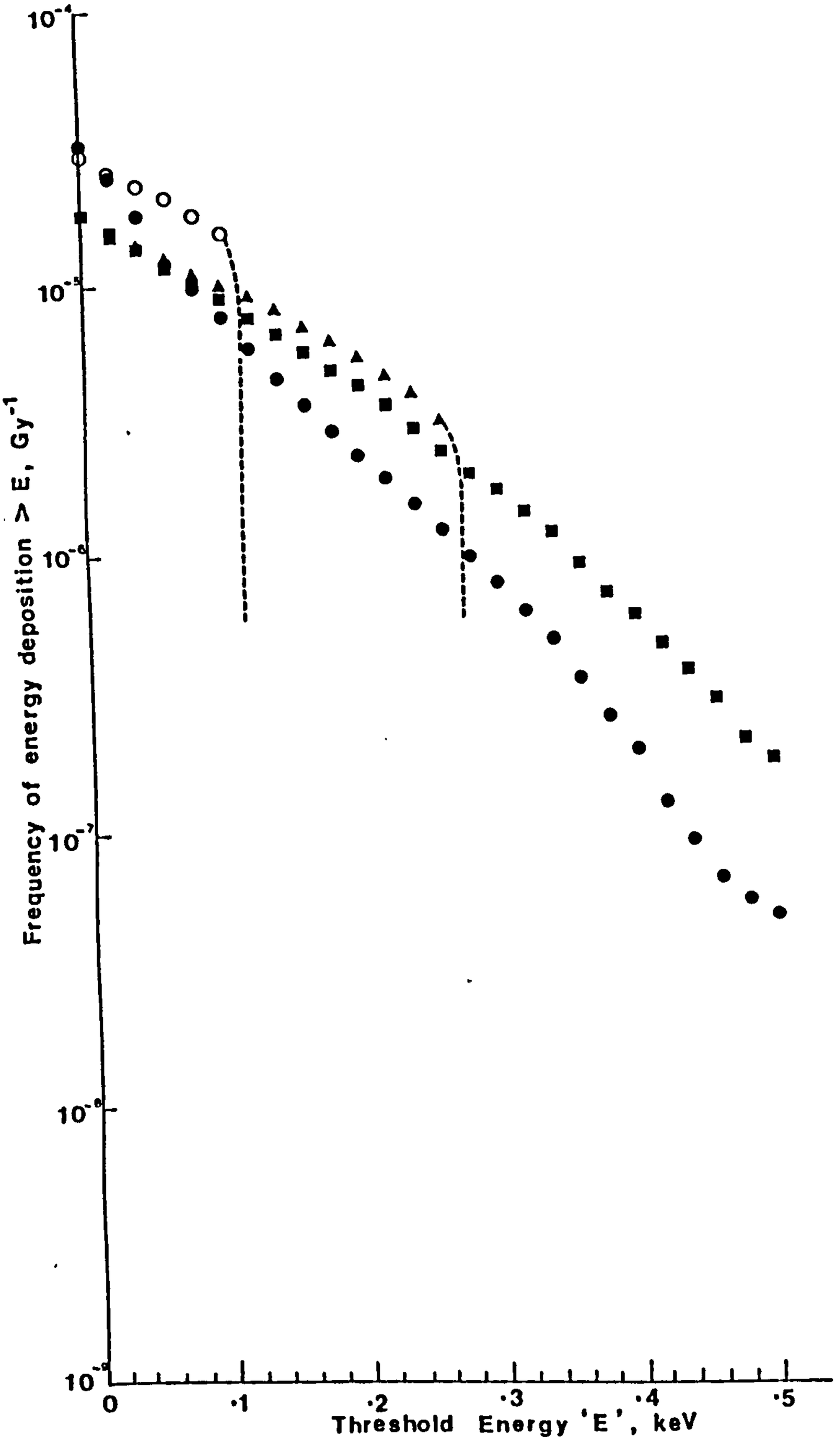

Figure 7.5 The frequency of energy depositions greater than a given amount, *E* in a 10 nm diameter, 5 nm long cylinder by simulated electron tracks from various low Z characteristic X-rays.

- ○ Be_K X-rays
- ▲ C_K X-rays
- ■ Al_K X-rays
- ● Ca_K X-rays

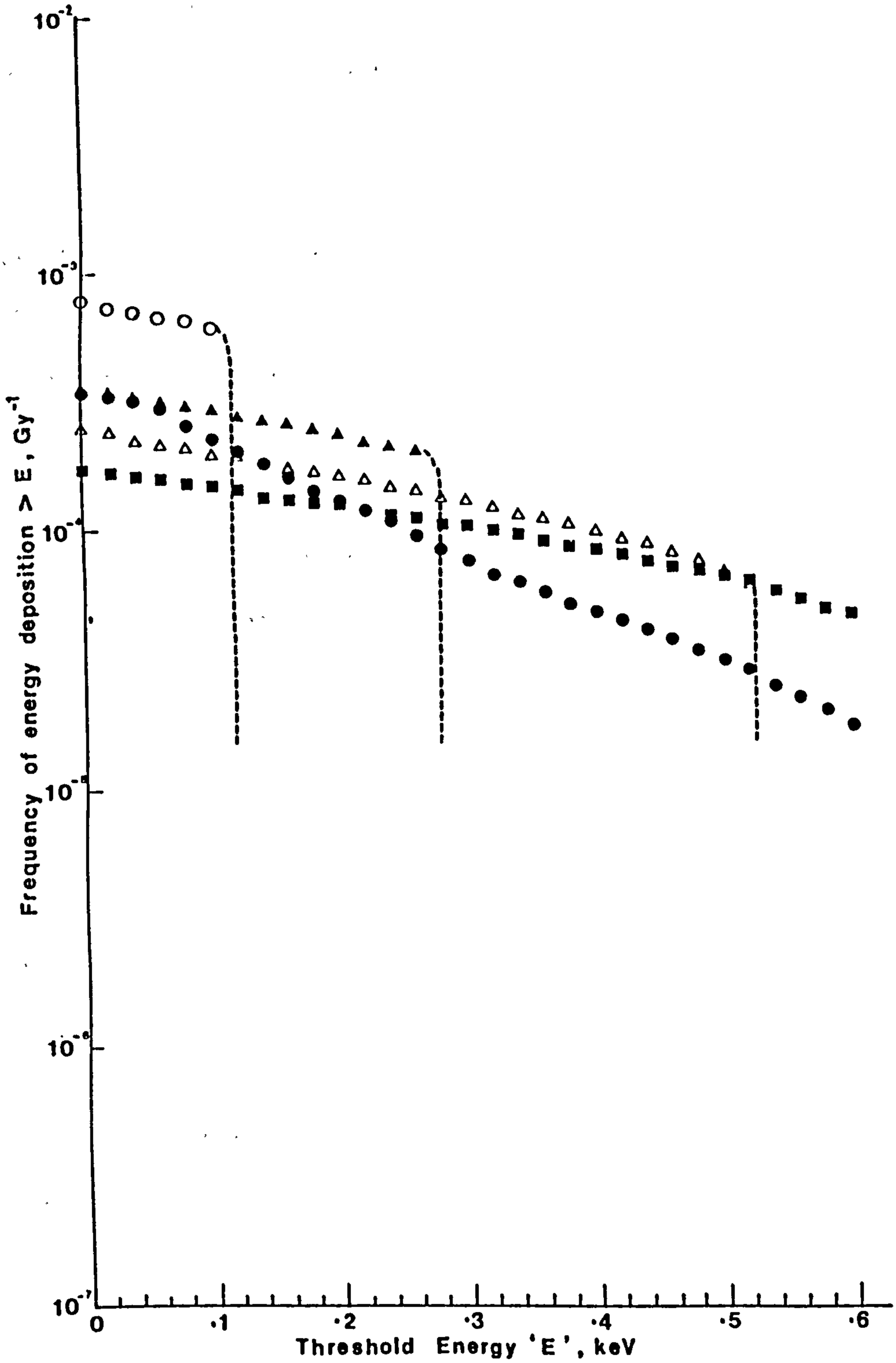

Figure 7.6 The frequency of energy depositions greater than a given amount, E in a 25 nm diameter, 25 nm long cylinder by simulated electron tracks from various low Z characteristic X-rays.

- ○ Be_K X-rays
- ▲ C_K X-rays
- △ O_K X-rays
- ■ Al_K X-rays
- ● Ca_K X-rays

can only be carried out for low-energy electrons, where the entire electron track is confined to a relatively small volume. For high-energy electrons, multi-stage sampling procedures have proved necessary to enhance the scoring efficiency (H. Nikjoo, *pers. comm.*). The complete energy deposition data are given in Appendix 2, with selected samples, including the lowest and highest (Z = 4 and 20) photon energies, plotted in Figures 7.4, 7.5 and 7.6. The target cylinder sizes were chosen to represent:

(i) element of DNA : 2nm diameter x 2nm length

(ii) nucleosome : 10nm diameter x 5nm length

(iii) element of chromatin fibre : 25nm diameter x 25nm length

The cylinder lengths chosen for the elements of DNA and chromatin fibre are arbitrary.

Having generated the basic data it was possible to draw an inter-elemental comparison by selecting a particular size of target cylinder and plotting the frequency of events depositing more than a given energy, E, in the target as a function of characteristic X-ray energy. Such data are presented in Figures 7.7, 7.8 and 7.9. Whilst comparison with existing experimental data (Goodhead and Brenner,1983b; D.T. Goodhead, *pers. comm.*) would suggest that threshold energies of the order of 100 eV within targets of ~ 2nm diameter is the important region in terms of low L.E.T. radiations such as X-rays, larger sized targets are of particular interest when considering high L.E.T. radiations such as α-particles (Goodhead *et al.*, 1985).

Figure 7.7 shows that low energy X-ray photons ($\lesssim$ 1 keV) are the most efficient in depositing small, localised amounts of energy within a target. Within this region, the data show varying degrees of structure, the more pronounced being at the higher energy of deposition (E = 200eV). The decrease observed at the lowest X-ray energies (Be_K, B_K and C_K) is probably due to the limit set by the X-ray energy

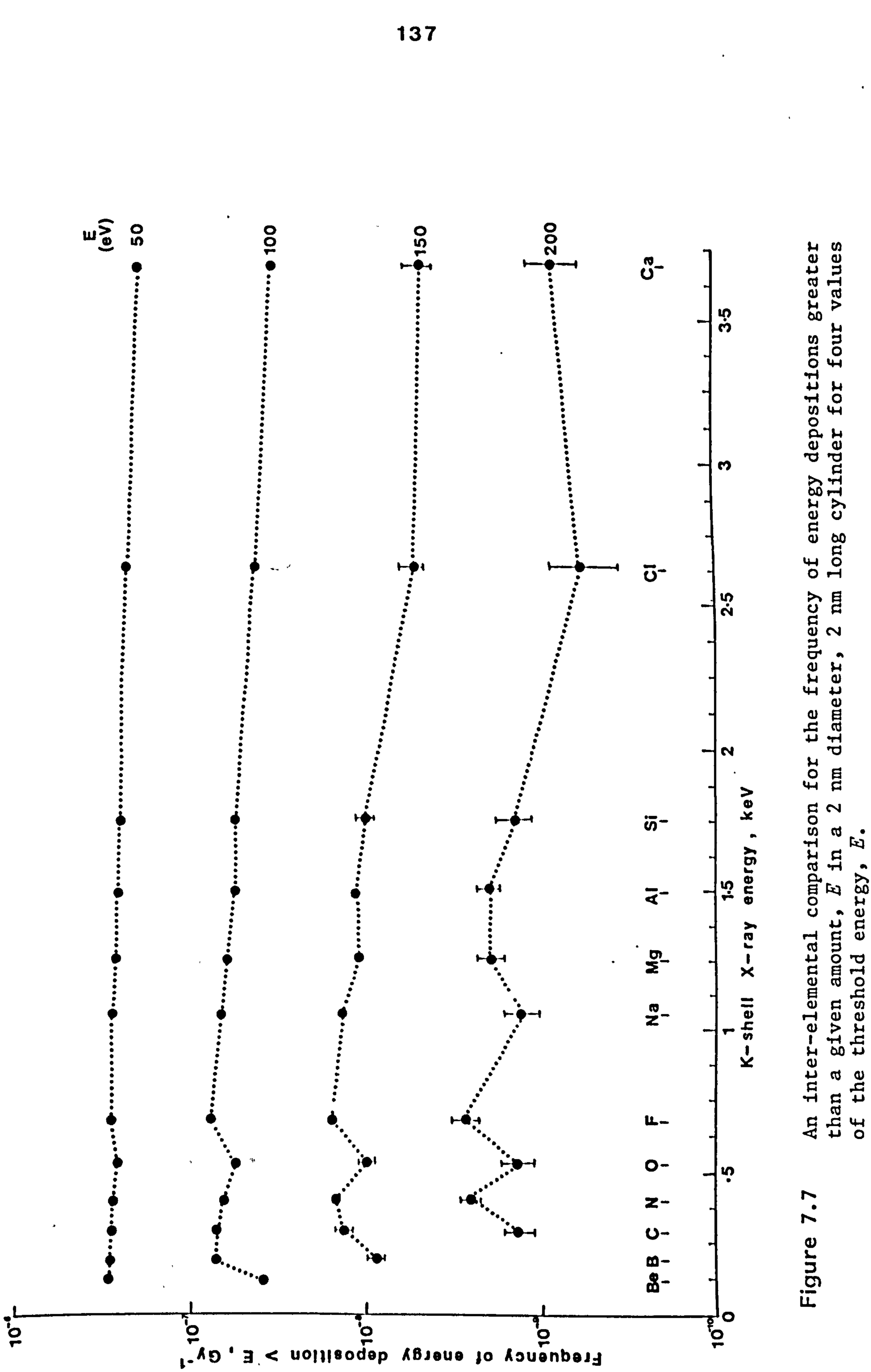

An inter-elemental comparison for the frequency of energy deposition greater than a given amount, E in a 2 nm diameter, 2 nm long cylinder for four values of the threshold energy, E.

Figure 7.7

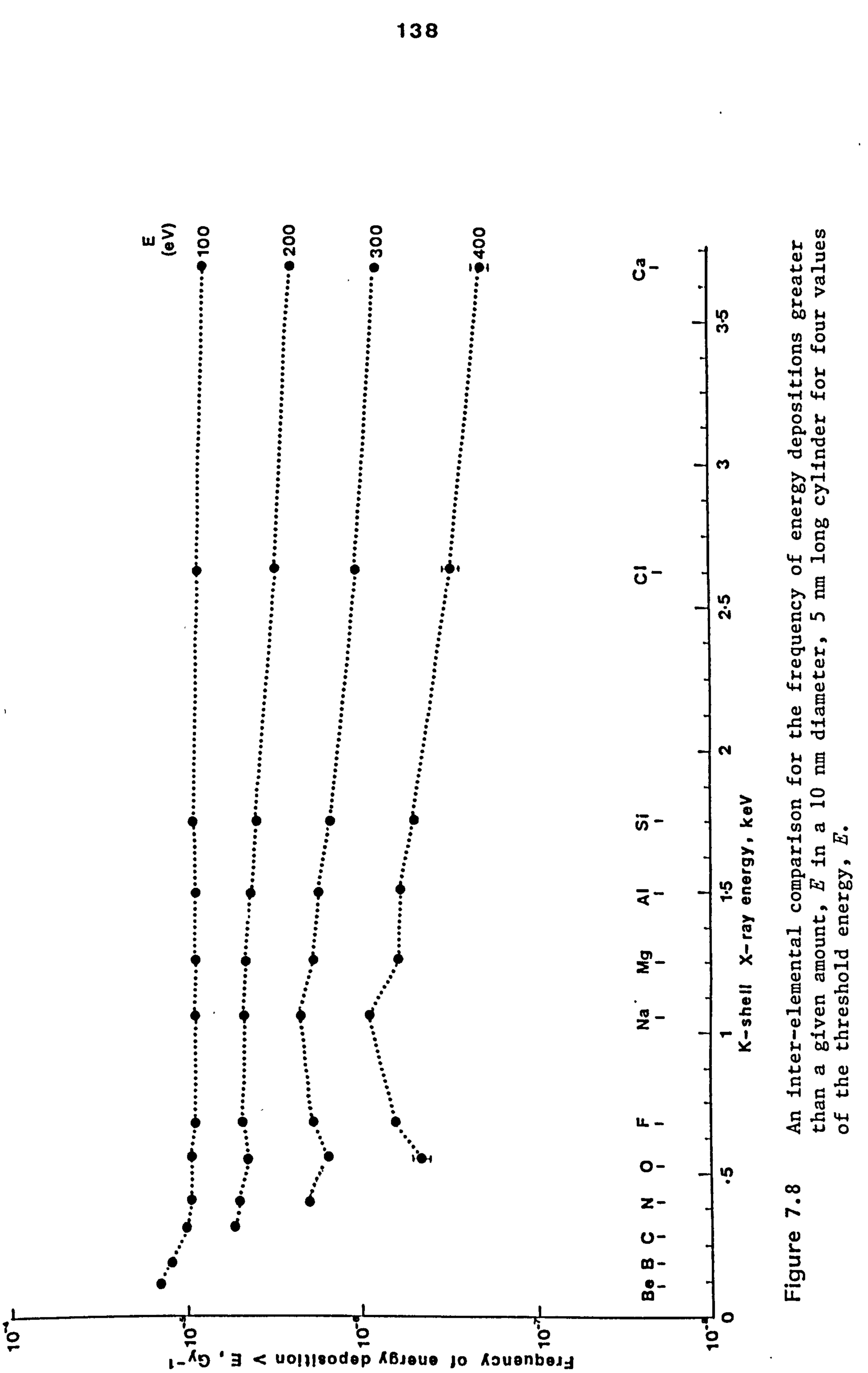

Figure 7.8 An inter-elemental comparison for the frequency of energy deposition greater than a given amount, E in a 10 nm diameter, 5 nm long cylinder for four values of the threshold energy, E.

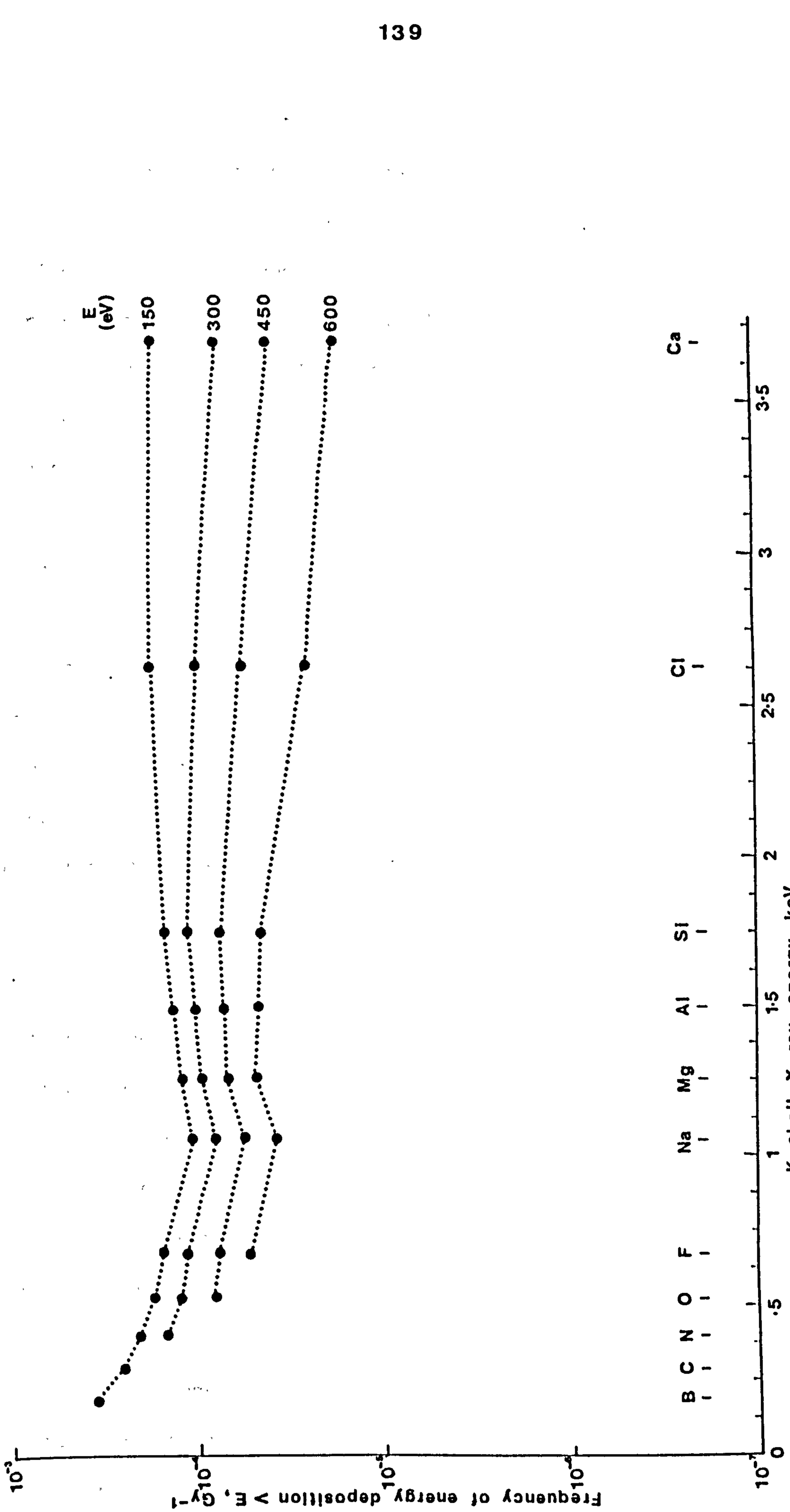

Figure 7.9 An inter-elemental comparison for the frequency of energy deposition greater than a given amount, E in a 25 nm diameter, 25 nm long cylinder for four values of the threshold energy, E.

itself; as E approaches the X-ray energy the frequency of energy deposition greater than E will obviously fall. Assuming the uncertainties are represented by Equations 7.2 and 7.3, the fluctuations in the region of the N_K, O_K and F_K X-ray energies are more than can be accounted for by scoring statistics alone. Referring to Table 7.1 it is seen that for Fluorine, an Auger electron is emitted as well as the photo-electron. Looking in particular at a threshold energy, E = 200eV, the photo-electron (at 140eV), if acting independently, should be incapable of depositing energy > 200eV within the target and hence the probability of energy deposition should be dominated by the Auger electron (505eV). The Auger electron is similar in energy to the photo-electron from the interaction of O_K X-rays with the Oxygen atoms in soft tissue, yet the probability of energy deposition > 200eV per Gy for the F_K X-rays is double that for the O_K X-rays. This would suggest that there might be a substantial combined effect resulting from the overlapping of the electrons as opposed to each electron acting independently.

Figures 7.8 and 7.9 again show that the low energy photons are the most efficient at depositing small amounts of energy within a target. With a target size of 25nm x 25nm (Figure 7.9) the electrons produced by the low energy photons are usually entirely enclosed within the targets (for example, the C_K X-ray (278eV) gives rise to an electron with a range of $\lesssim$ 7nm (I.C.R.U., 1970)). As the photon energy increases, whilst the electrons produced are still enclosed by the targets there will be fewer of them per unit dose, and hence the efficiency of depositing a threshold energy falls (from B_K to Na_K X-rays). Further increase in the photon energy ($\gtrsim$ 1 keV) leads to electrons starting to 'escape' from, or enter into, a target and so targets are more likely to be hit (from Na_K to higher energy X-rays). As the threshold energy increases (from 150eV to 600eV) the benefit of additional hits is lost because these higher energy (lower L.E.T.) electrons have a low probability of depositing large energy in a target even if they do pass through it.

CHAPTER 8

DISCUSSION

8.1 Comparison of the observed angular dependence of proton-induced ultrasoft X-rays with theoretical calculation

Both the observed and calculated angular dependence of proton-induced ultrasoft X-rays are shown in Figure 5.10 ((i) - (vi)). For K-shell X-rays the agreement between the experimental data and the theoretical estimate, based upon the consideration of X-ray production over the total proton range in the target, is best when the target is inclined at an angle of 30° to the proton beam. As the target-to-beam angle decreases the experimental data becomes more in agreement with that calculated from consideration of the X-rays produced in the first 1μm of the proton range only.

A certain amount of disagreement between experimental data and theoretical estimates might be expected because of the limited (1μm) resolution steps of the calculations and the simplifying assumption that the proton energy remained constant over each 1μm increment (Section 6.2). In fact, the proton energy (and therefore the X-ray production cross-section) would be greatest at the target edge side of each increment where self-absorption effects would be less. The effects would be expected to be more pronounced at larger target angles, θ, due to the sin θ dependence (Figure 8.1). Further reasons for disagreement might also be expected as the result of an irregular target surface profile. Studies by Gaines (1981) have shown that anisotropy additional to that produced due to self-absorption in a smooth target can be expected for surface roughness with average peak-to-valley distances greater than ~0.1μm. Methods of quantifying the effect of target roughness were considered, the most promising being the introduction of regular rulings onto a smooth target having an average

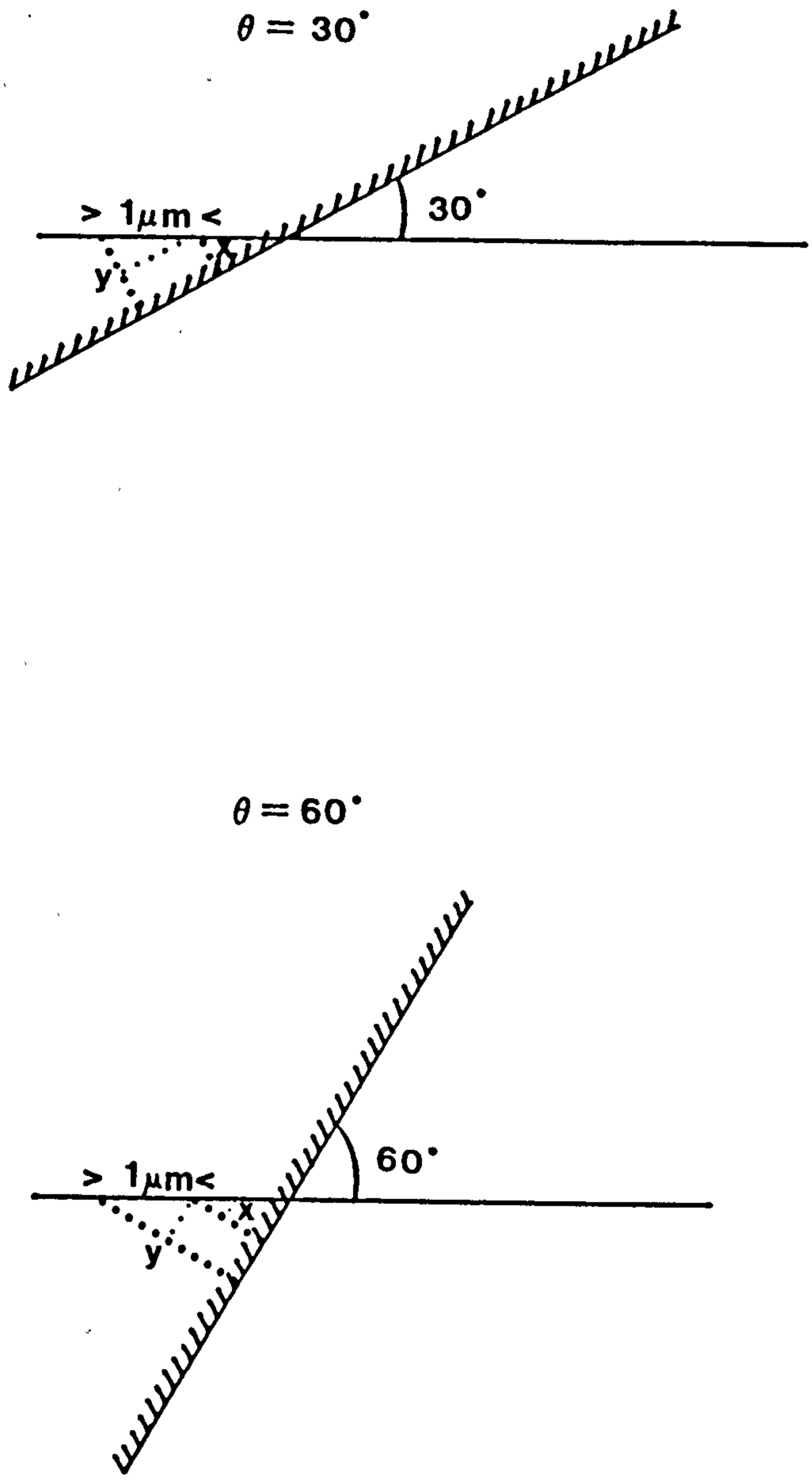

$$y - x = \frac{\sin \theta}{1}$$

Figure 8.1 The sin θ dependence of the difference in the distance travelled within the target at either end of each 1 μm increment.

peak-to-valley distance of < 0.05μm. However, the cost of producing such a high specification target meant that such a study extended beyond the scope of this work.

8.2 A practical beam line for proton-induced ultrasoft X-rays

From the results of the angular distribution study (Section 5.2.2) it is seen that for the maximum intensity of characteristic X-rays a small target-to-proton beam angle is desirable. Whilst practical limitations in this work, resulting from the need for electrical connections, have meant that the narrowest target angle studied was 30°, geometrical considerations (Equation 6.10) show that narrower angles would maximise the X-ray yield still further. For any particular target angle, the optimum detector angle, that is the irradiation position, would appear to be perpendicular to the target surface with the X-ray yield decreasing as the irradiation position moves further away from the perpendicular. With particular reference to the target angles and detector angle variations used in this work, the maximum X-ray yield occurred for a target angle of 30° and a detection angle of 60° to the beam. These effects become less important as the X-ray energy increases - a direct consequence of the reduction in the target self-absorption of the X-rays.

Whilst increased proton energy does, in general, lead to an increased X-ray production cross-section (although for the lowest Z elements such as Boron and Carbon, the cross-section does reach a plateau at proton energies of a few 100 keV (Figure 6.5) before falling as the energy increases further towards 1 MeV and greater), the advantage thus gained must be weighed against the necessity of eliminating all scattered protons from the photon beam. Since this would appear to require some form of filtration (Section 2.4.1), the higher the proton energies the greater will be the filter thickness required to stop the scattered protons. This will result in a corresponding

decrease in the transmission of the photon beam thereby offsetting the increased production at high proton energies.

Previous work (Sterk,1965; Khan, Potter and Worley,1965; Gaines, 1981) has shown that Carbon contamination of the target surface is a common problem when studying proton-induced ultrasoft X-rays. The indications are, however, (Section 5.2.1) that this may at least be reduced by making use of high ($\gtrsim$ μA) proton beam currents. Beam currents of the order of 500 μA have been used at the M.R.C. Radiobiology Unit and whilst Carbon deposition was still observed on the target surface, the rate of build-up of Carbon and the subsequent reduction in characteristic X-ray yield (from an Aluminium target) is far less pronounced (D.T. Goodhead, *pers. comm.*) than with beam currents of ~ 35 nA as used in this work. The beneficial effects of high target currents may be due to target heating.

When considering the irradiation of biological systems, and in particular, mammalian cells, additional factors have to be taken into account. Although all the measurements in this study were made within the evacuated scattering chamber (Section 2.2.3) the detection/irradiation position for mammalian cell irradiations would almost certainly need to be at atmospheric pressure in order for the cells to be able to survive. It is necessary to irradiate an attached monolayer of cells such that their position is well-defined and there is minimum attenuation across the cell layer. The subsequent removal, counting and biological assay of the cells necessitates the irradiation of a large number ($\sim 10^4 - 10^5$) of cells and hence an irradiation dish base of the order of 3cm in diameter is required. A well-defined entrance surface is required for dosimetry purposes and therefore irradiation cannot be from the air side (as opposed to the dish base side) of the cells since, even if the growing medium was poured away there would remain an unmeasurable, variable layer of liquid, and if

the dishes were dried the cells would die. As a result of these considerations the preferred system in use is to make an irradiation dish with a thin plastic base on which cells are grown, and irradiate through the dish base (First International Ultrasoft X-Ray Workshop, 1987). A typical experiment (for example, to obtain a dose-response curve) would require the irradiation of many such dishes.

Whilst cells may be grown on a variety of materials, the best combination of small, well-defined attenuation across the irradiation dish base and cell growth compatibility appears to be provided by 1.5μm Polyethylene terephthalate, $C_{10}H_8O_4$, ('Mylar' (Du Pont)) (D.T. Goodhead, *pers. comm.*). In order to achieve uniformity of dose to a large area monolayer of cells, very little distortion of the dish base can be tolerated and so to avoid a pressure differential across the dish base, atmospheric pressure is required on both sides of the irradiation dish. This leads to the requirement of a 'vacuum window' to bring the photon beam out of the vacuum chamber, in which the target is positioned, into atmospheric pressure. There will, therefore, be a 'flight-path' between the vacuum window and the dish base.

Assuming an irradiation dish base size of ~ 3cm diameter, a required uniformity of beam across the base means that the vacuum window has to be of comparable diameter. However, the vacuum window also needs to be able to tolerate the pressure differential of 10^{-3} - 10^{-4} Pa on the vacuum side and atmospheric pressure (10^5 Pa) on the other, and an unsupported window thick enough to tolerate such a pressure differential over a circular area ~ 3cm in diameter would greatly reduce the X-ray flux. A thin window (for example, 2.5μm 'Hostaphan', (Hoechst)) on a supporting grid would therefore appear to be more appropriate. There is then the additional problem resulting from the 'shadowing' of the transmitted beam by the grid wires.

The irradiation dish must not therefore be too near the vacuum window in order that the natural divergence of the photon beam from the finite-sized source will cancel out any shadowing effects.

Whilst the vacuum window and the irradiation dish base will offer some filtration of the scattered protons, additional filtration will be required in order to ensure that no protons enter the irradiation dish. The vacuum window-to-dish base separation may be used as a flight tube with low atomic number gas (Hydrogen, H_2, or Helium, He) flowing at atmospheric pressure. Whilst Helium would be preferable from the safety point of view, the increased attenuation in Helium at energies $\lesssim$ 1 keV would make Hydrogen a better choice at the lowest energies. Both H_2 and He are efficient at stopping protons (500 keV protons having a range of < 10cm in both gases) and have lower attenuation coefficients, μ, for ultrasoft X-rays than air. For example (Hubbell and Veigele,1976):

for C_K X-rays :
$\mu_{AIR} \sim 6.2\ cm^{-1}$
$\mu_{H_2} \sim 3 \times 10^{-2}\ cm^{-1}$
$\mu_{He} \sim 0.6\ cm^{-1}$

and

for Al_K X-rays :
$\mu_{AIR} \sim 1.3\ cm^{-1}$
$\mu_{H_2} \sim 1.6 \times 10^{-4}\ cm^{-1}$
$\mu_{He} \sim 3 \times 10^{-3}\ cm^{-1}$

For the X-ray beam to achieve a uniformity within 5 - 10% over the base of the irradiation dish, the photons need to be produced over a large target area. The nearer the vacuum window is to the target position, the larger the required production area since there will be less distance over which the photon beam may diverge. In terms of maximising the dose rate to the cells however, the nearer the vacuum window and the dish base are to the target, the better. One possible alternative to using a large diameter proton beam bombarding the target would be to scan the proton beam across the target surface such that the overall production surface area is larger.

Finally, consideration must be given to the Carbon contamination X-rays, the elimination of which will require additional filtration to that offered by the window, dish base and flight tube gas. Whilst it was possible in this study to deduce the B_K X-ray yield by subtracting the C_K X-ray yield (taken from the Aluminium target data) from the combined peak, for biological irradiations deduction of effectiveness by subtraction of observed effectiveness of mixed beams would introduce very large errors and would usually not be practical. The necessity of growing cells on some material, usually polymers, and the need for a vacuum window (both of which will in general have transmission characteristics dominated by the C_K edge) means that it would also be very difficult to filter out the C_K X-rays from a combined beam of Carbon and some other low Z elemental X-ray without removing the X-ray energy actually required. X-rays from targets of atomic number lower than Carbon (Z = 6) have the added disadvantage of having higher attenuation coefficients in the flight tube gases than Carbon. Hence, even if it were possible to filter out the C_K X-rays produced along with, for example, the Be_K X-rays from a Beryllium target using a Be filter (X-ray Data Booklet, 1986) it is unlikely that a sufficiently intense beam of Be_K X-rays could be obtained at a practical irradiation position.

For elements with Z near, but greater than 6, a similar problem exists. Whilst it might be possible to use a Nitride or Oxide filter to transmit the N_K or O_K X-rays respectively at the expense of the C_K X-rays, these elemental X-rays would have had to have been produced from compound targets such as Si_3N_4 or Al_2O_3, SiO_2 and MgO_2, and hence the photon beam would also consist of the higher energy characteristic X-rays which could not be filtered out efficiently whilst still leaving the lower energy X-rays. However, once the characteristic photon energies are > 1 keV it should be possible to use a filter, ideally of the same Z as the target, such that the C_K X-rays are removed

without over-reducing the yield of the required X-rays. Additional filters would also reduce the gas tube length required to ensure the removal of all scattered protons from the photon beam.

Because of the difficulty in achieving a total removal of the contaminant C_K X-rays from other characteristic low energy ($\lesssim$ 1 keV) X-rays, it would appear that, other than for Carbon targets, there is a very limited biological use for proton-induced low target Z characteristic X-rays. It may however, in a well characterised system where the Carbon build-up is kept to a minimum and in which a detailed study is made on the rate of build-up under specific operating conditions, be possible to look at the effect of a combined energy photon beam on biological systems and then, by comparison with the effectiveness of C_K X-rays alone, deduce the additional effects due to a second X-ray energy.

A schematic diagram summarising some of these practical considerations is shown in Figure 8.2. Specific distances (such as target-to-window, window-to-dish base) will vary according to particular systems. Proton beam energy, available beam diameter, supporting grid wire size and separation, and practical limitations on target and irradiation angles all have to be considered.

The beam line shown in Figure 8.2 is by no means a unique solution to the practical problems of biological irradiation with proton-induced ultrasoft X-rays. Different systems can be, and are being, used (First International Ultrasoft X-Ray Workshop, 1987). Attenuation problems are greatly reduced by actually growing the cells on the vacuum window, thus eliminating the need for a flight tube. However, in this case it would be necessary to incorporate filters into the vacuum system to ensure that scattered protons do not reach the cells and, other than for Carbon targets, to absorb the C_K X-rays. Also, assuming that an

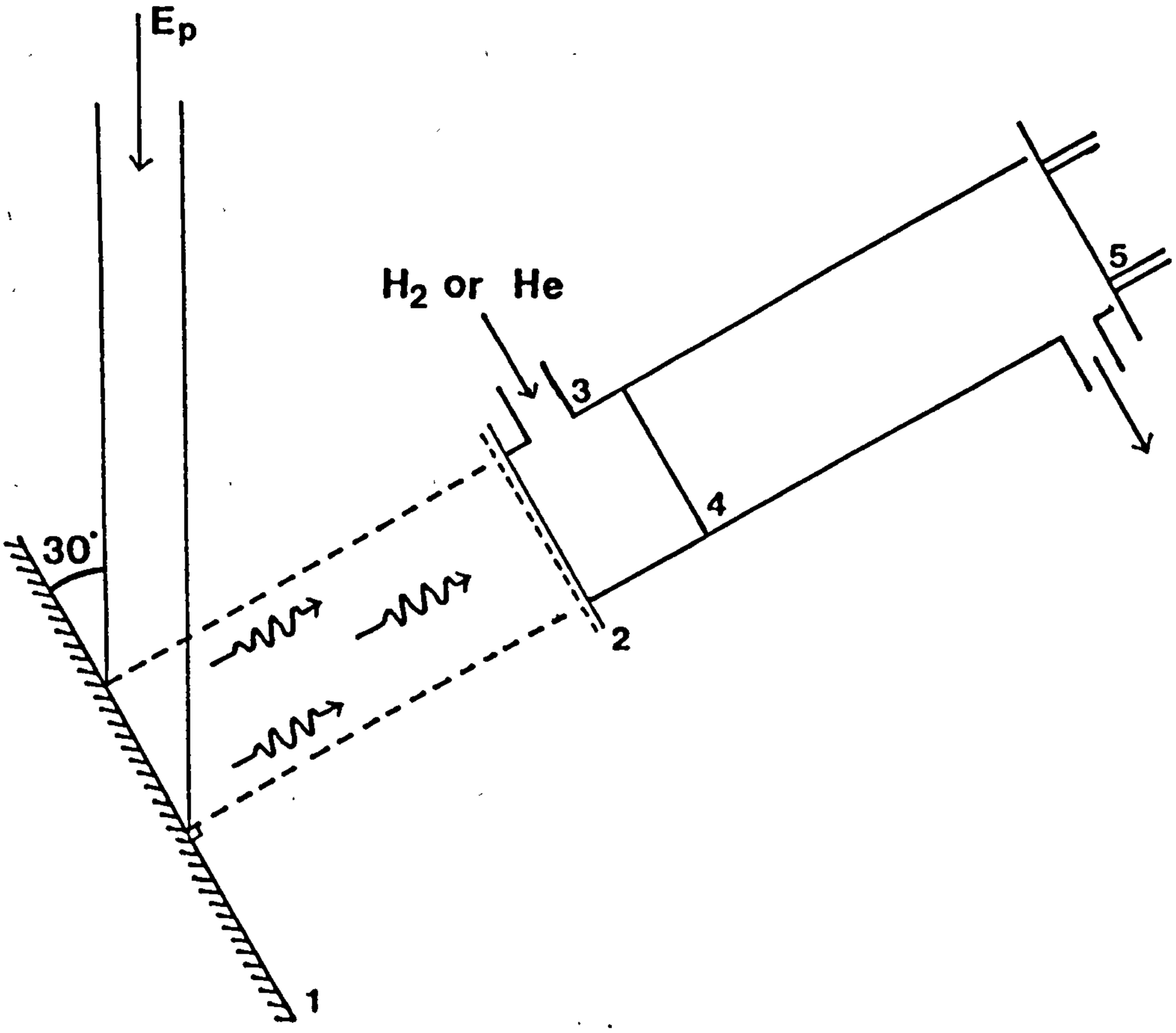

Figure 8.2 A schematic diagram summarising some of the properties of a practical beam line for biological irradiation by proton-induced ultrasoft X-rays.

1. Target
2. Window (2.5 μm Hostaphan
3. Flight Tube (≃ 10 cm in length), with H_2 or He gas flowing to prevent scattered protons from reaching the irradiation position
4. Variable filter - depending on target - to absorb C_K X-rays
5. Irradiation dish (cells grown on 1.5 μm Mylar)

irradiating beam area of ~ 3cm diameter is required, the vacuum window would still need to be supported by a grid so that the cells would have to be grown carefully in between the grid wires if they were to be uniformly irradiated. Growing the cells on the vacuum window would also mean that the area immediately inside the window would have to be let up to atmospheric pressure prior to the irradiation of each sample for the window to be changed.

The pressure differential across the vacuum window could be reduced by irradiating the cells under reduced pressure. Instead of bringing the photon beam out into atmospheric pressure the cells could be enclosed in a 'wet irradiation chamber' where saturated water vapour, at a pressure of ~ 10^4 Pa (0.1 atmospheric pressure), was admitted into an evacuated chamber. Another alternative would be to bring the photon beam out through a much smaller vacuum window, such as a narrow slit, and then scan the irradiation dish across the slit. The reduced area of the vacuum window might also eliminate the need for a support grid.

8.3 Monte-Carlo electron track structure data

Previous comparisons (Goodhead and Brenner,1983b; D.T. Goodhead, *pers. comm.*) between experimental data and the calculated frequencies of energy deposition using Monte-Carlo simulated tracks of randomly emitted photo- and Auger-electrons generated by ultrasoft X-rays seem to suggest that energy deposition of $\gtrsim$ 100 eV in small volumes (~ 2nm diameter) may be a critical property when considering the biological effectiveness of low ionisation density radiation such as X-rays. The effectiveness of various K-shell X-rays at depositing threshold energies of ~ 100 eV within small cylindrical (2nm diameter x 2nm length) targets is shown in Figure 7.7, where a certain degree of structure is observed at the low ($\lesssim$ 1 keV) photon energies. This suggests that biological irradiations with these characteristic X-rays

would be an useful indication of the validity of the threshold energy concept.

However, biological irradiations with proton-induced ultrasoft X-rays in the region of interest (C_K to F_K X-rays) are subject to a number of experimental problems. Irradiations with proton-induced C_K X-rays (278 eV) have been undertaken at, for example, the M.R.C. Radiobiology Unit. The main problem at this energy is one of attenuation within the cells, the absorbed dose being reduced by 50% over 1.2μm depth of the cell (Goodhead, Thacker and Cox,1979). This compares with an average 'flattened' cell thickness of ~ 7μm (Goodhead and Thacker, 1977). Using the data of Henke *et al.*(1982) for the mass attenuation coefficients (μ/ρ) for the various X-ray energies in Oxygen (Table 8.1) to represent the attenuation in soft tissue, the attenuation coefficient for F_K X-rays is found to be twice that for C_K X-rays. F_K X-rays would therefore be a very unsuitable choice for practical irradiations.

From Table 8.1, it is seen that in terms of attenuation, N_K and O_K X-rays would be a better choice of low energy photons, but there are further practical difficulties concerning their production. If proton bombardment is to be used as a means of producing the characteristic, ultrasoft X-rays then, as has been already discussed in Section 8.2, there are problems with scattered proton filtration and the elimination of contaminant C_K X-rays as well as the higher energy characteristic X-rays, such as Si_K, Al_K or Mg_K X-rays, which will inevitably be produced from the compound target.

It would therefore appear necessary to use an alternative method to proton bombardment of solid targets for the production of low energy photons (other than C_K X-rays) if these particular biological irradiations are to be undertaken. A strong contender would be the use of synchrotron radiation sources which are capable of producing

X-ray line	Photon energy (eV)	$\frac{\mu}{\rho}$ ($cm^2.g^{-1}$)
B_K	183	1.65×10^4
C_K	278	6.04×10^3
N_K	392	2.53×10^3
O_K	525	1.20×10^3
F_K	677	1.24×10^4

Table 8.1 The mass attenuation coefficients (μ/ρ) of low energy X-rays in Oxygen (from Henke *et al.*, 1982).

high intensities of monochromatic ultrasoft X-rays. These are not confined to producing characteristic energies and would eliminate the need for filtration of scattered protons and contaminating X-rays. There are, however, other practical difficulties such as a small beam size and the requirement for vacuum windows capable of withstanding ultra high vacuum on one side and atmospheric pressure on the other, but these problems are not insurmountable. It might, therefore, be possible, using synchrotron produced ultrasoft X-ray energies, to carry out biological irradiations at low photon energies such as N_K (392 eV) and O_K (525 eV) X-rays and compare their biological effectiveness with the frequency of threshold energy depositions within small volumes as calculated by Monte-Carlo techniques. Such information would aid the further elucidation of the critical properties of ionising radiation action.

BIBLIOGRAPHY

(Abbreviations are given according to the

World List of Scientific Periodicals.)

ANDERSON, H.H. and ZIEGLER, J.F. (1977) Hydrogen: Stopping Powers and Ranges in All Elements. In: *The Stopping and Ranges of Ions in Matter. (Vol.3)* Pergamon Press, New York and London

BAMBYNEK, W., CRASEMANN, B., FINK, R.W., FREUND, H.U., MARK, H., SWIFT, C.D., PRICE, R.E. and RAO, P.V. (1972) X-ray Fluorescence Yields, Auger, and Coster-Kronig transition probabilities. *Rev.Mod.Phys.* 44 716 - 817

BARTON, H.A. (1930) Comparison of protons and electrons in excitation of X-rays by impact. *J. Franklin Inst.* 209 1 - 19

BERGER, M.J. (1974) Some new transport calculations of the deposition of energy in biological material by low energy electrons. In: *Proc.IV.Symp.Microdosimetry (Verbania-Pallanza, Italy, 24 - 28 Sept. 1973 [EUR5122]* (eds. J.Booz, H.G.Ebert, R.Eickel and A.Waker) 695 - 711 Commission of the European Communities, Luxembourg

BEVINGTON, P.R. (1969) Distributions. In: *Data Reduction and Error Analysis for the Physical Sciences.* 27 - 53 Mc.Graw-Hill Book Company

BOTHE, W. and FRÄNZ, H. (1928) Röntgen Radiations Excited by α-particles. *Z.Phys.* 52 466 - 484

BRENNER, D.J. (1982) Calculation of ionization distributions in a tissue equivalent cloud chamber gas mixture. *Radiat.Res.* 89 194 - 202

BRENNER, D.J., BIRD, R.P., ZAIDER, M., GOLDHAGEN, P., KLIAUGA, P.J. and ROSSIE, H.H. (1987) Inactivation of Synchronized Mammalian Cells with Low-Energy X-rays - Results and Significance. *Radiat.Res.* 110 413 - 427

BRENNER, D.J. and ZAIDER, M. (1982) Proceedings of the Workshop in the interference between Radiation Chemistry and Radiation Physics. In: *Argonne National Laboratory Report. (Argonne, U.S.A.)*

BUCK, T.M., WHEATLEY, G.H. and FELDMAN, L.C. (1973) Charge states of 25 - 150 keV H and ^{4}He Backscattered from solid surfaces. *Surf.Sci.* 35 345 - 361

BUDD, T. and MARSHALL, M. (1980) Analysis of Ionization Distributions in a Low-Pressure Cloud Chamber. *Radiat.Res.* 82 225 - 234

BURCH, P.R.J. (1957) Some physical aspects of relative biological efficiency. *Br.J.Radiol.* 30 524 - 529

CHADWICK, J. (1912) γ-rays excited by the α-rays of Radium. *Lond.Edinb.Dubl.Phil.Mag.* 24 594 - 600

CHADWICK, J. (1913) Excitation of γ-rays by α-rays. *Lond.Edinb.Dubl.Phil.Mag.* 25 193 - 197

CHADWICK, J. and RUSSELL, A.S. (1913) Excitation of γ-rays by the α-rays of Ionium and Radio-thorium. *Proc.R.Soc.* A88 217 - 229

CHADWICK, J. and RUSSELL, A.S. (1914) γ-rays of Polonium, Radium, and Radio-actinium. *Lond.Edinb.Dubl.Phil.Mag.* 27 112 - 125

CHARLTON, D.E., GOODHEAD, D.T., WILSON, W.E. and PARETZKE, H.G. (1985a) Energy Deposition in Cylindrical Volumes : (a) Protons - Energy 0.3 keV - 4.0 MeV (b) α-particles - Energy 1.2 MeV - 20.0 MeV. *M.R.C. Radiobiology Unit, Monograph 85/1* (Chilton, Didcot, Oxon.)

CHARLTON, D.E., GOODHEAD, D.T., WILSON, W.E. and PARETZKE, H.G. (1985b) The deposition of energy in small cylindrical targets by high LET radiations. *Radiat.Prot.Dosim.* 13 123 - 125

COGHLAN, W.A. and CLAUSING, R.E. (1973) Auger Catalog. Calculated Transition Energies Listed by Energy and Element. *At.Data* 5 317 - 469

CORK, J.M. (1941) Production of characteristic X-rays by deuteron bombardment. *Phys.Rev.* 59 957 - 959

COX, R., THACKER, J. and GOODHEAD, D.T. (1977) Inactivation and mutation of cultured mammalian cells by aluminium characteristic ultrasoft X-rays. II. Dose-responses of Chinese hamster cells and human diploid cells to aluminium X-rays and radiations of different LET. *Int.J.Radiat.Biol.* 31 561 - 576

EVANS, H.J. (1962) Chromosome aberrations induced by ionizing radiations. *Int.Rev.Cytol.* 13 221 - 321

FIRST INTERNATIONAL ULTRASOFT X-RAY WORKSHOP (1987)
(Milton Hill House, Abingdon, Oxon., 17 - 18 July 1987)
Report in Press.

FLETCHER, R. (1970) A new approach to variable metric algorithms.
Comput.J. 13 317 - 322

FOLKMANN, F., CRAMON, K.M. and HERTEL, N. (1984)
Angular distribution of particle-induced X-ray emission.
Nucl.Instrum.Meth. B3 11 - 15

GAINES, J.L. (1981) Low Energy X-ray Calibration Sources at the Lawerence Livermore National Laboratory.
In: *A.I.P. Conference Proceedings No.75 : Low Energy X-ray Diagnostics* (eds. D.T. Attwood and B.L. Henke) 246 - 251 A.I.P.

GERTHSEN, C. and REUSSE, W. (1933) Stimulation of X-radiation by Canal-ray impacts. *Phys.Z.* 34 478 - 482

GOODHEAD, D.T. (1977) Inactivation and mutation of cultured mammalian cells by aluminium characteristic ultra-soft X-rays. III. Implications for theory of dual radiation action. *Int.J.Radiat.Biol.* 32 43 - 70

GOODHEAD, D.T. (1982) An Assessment of the Role of Microdosimetry in Radiobiology. *Radiat.Res.* 91 45 - 76

GOODHEAD, D.T. (1987a) Physical Basis for Biological Effect.
In: *Nuclear and Atomic Data for Radiotherapy and Related Radiobiology : Proc.I.A.E.A. Advisory Group Meeting (Rijswijk, 16 - 20 Sept. 1985)* 37 - 53
I.A.E.A. Vienna

GOODHEAD, D.T. (1987b) Biophysical Models of Radiation Action : Introductory Review. In: *Radiation Research : Proc.VIII.Int.Congress of Radiation Research (Edinburgh, Scotland, 19 - 24 July 1987) (Vol.2)* (eds. E.M. Fielden, J.F. Fowler, J.H. Hendry and D. Scott) 306 - 311 Taylor and Francis

GOODHEAD, D.T. (1987c) Development of radiation sources and dosimetric techniques for radiobiological studies at low and high dose-rate. In: *Radiation Protection : Progress Report [EUR10953]* 93 - 96 Commission of the European Communities, Luxembourg

GOODHEAD, D.T. (1987d) Relationship of Microdosimetric Techniques to Applications in Biological Systems. In: *The Dosimetry of Ionizing Radiations (Vol.2)* (eds. K.R. Kase, B.E. Bjärngard and F.H. Attix) 1 - 89 Academic Press

GOODHEAD, D.T. and BANCE, D.A. (1984) Proton-induced characteristic X-rays : a versatile source of ultrasoft X-rays for biological and biochemical investigations. *Physics.Med.Biol.* 29 535 - 541

GOODHEAD, D.T. and BRENNER, D.J. (1983a) The mechanism of radiation action and the physical nature of biological lesions. In: *Radiation Protection, VIII.Symp.Microdosimetry (Jülich, F.R.G., 27 Sept. - 1 Oct. 1982) [EUR8395]* (eds. J. Booz and H.G. Ebert) 597 - 609 Commission of the European Communities, Luxembourg

GOODHEAD, D.T. and BRENNER, D.J. (1983b) Estimation of a single property of low LET radiations which correlates with biological effectiveness. *Physics.Med.Biol.* 28 485 - 492

GOODHEAD, D.T., CHARLTON, D.E., WILSON, W.E. and PARETZKE, H.G. (1985) Current Biophysical approaches to the understanding of biological effects of radiation in terms of local energy deposition. In: *Radiation Protection, V.Symp.Neutron Dosimetry (Munich, Neuherberg, 17 - 21 Sept. 1984) [EUR9762]* (eds. H. Schraube, G. Burger and J. Booz) 57 - 67 Commission of the European Communities, Luxembourg

GOODHEAD, D.T., COX, R. and THACKER, J. (1981) Do ultrasoft X-rays produce lesions characteristic of high LET or low LET, or neither? In: *Proc.VII.Symp.Microdosimetry (Oxford, U.K., 8 - 12 Sept. 1980) [EUR7147]* (eds. J. Booz, H.G. Ebert and H.D. Hartfiel) 929 - 939 Harwood Academic Publishers for the C.E.C.

GOODHEAD, D.T., MUNSON, R.J., THACKER, J. and COX, R. (1980) Mutation and inactivation of cultured mammalian cells exposed to beams of accelerated heavy ions. IV. Biophysical interpretation. *Int.J.Radiat.Biol.* 37 135 - 167

GOODHEAD, D.T. and THACKER, J. (1977) Inactivation and mutation of cultured mammalian cells by aluminium characteristic ultrasoft X-rays. I. Properties of aluminium X-rays and preliminary experiments with Chinese hamster cells. *Int.J.Radiat.Biol.* 31 541 - 559

GOODHEAD, D.T., THACKER, J. and COX, R. (1978) The conflict between the biological effects of ultrasoft X-rays and microdosimetric measurements and application. In: *Proc.VI.Symp.Microdosimetry (Brussels, Belgium, 22 - 26 May 1978 [EUR6064]* (eds. J. Booz and H.G. Ebert) 829 - 843 Harwood Academic Publishers for the C.E.C.

GOODHEAD, D.T., THACKER, J. and COX, R. (1979) Effectiveness of 0.3 keV Carbon ultrasoft X-rays for the inactivation and mutation of cultured mammalian cells. *Int.J.Radiat.Biol.* 36 101 - 114

GOODHEAD, D.T., THACKER, J. and COX, R. (1981a) Is selective absorption of ultrasoft X-rays biologically important in mammalian cells? *Physics.Med.Biol.* 26 1115 - 1127

GOODHEAD, D.T., VIRSIK, R.P., HARDER, D., THACKER, J., COX, R. and BLOHM, R. (1981b) Ultrasoft X-rays as a tool to investigate radiation-induced dicentric chromosome aberrations. In: *Proc.VII.Symp.Microdosimetry (Oxford, U.K., 8 - 12 Sept. 1980) [EUR7147]* (eds. J. Booz, H.G. Ebert and H.D. Hartfiel) 1275 - 1285 Harwood Academic Publishers for the C.E.C.

HAMM, R.N., WRIGHT, H.A., RITCHIE, R.H., TURNER, J.E. and TURNER, T.P. (1976) Monte Carlo Calculation of Transport of Electrons through liquid water. In: *Proc.V.Symp.Microdosimetry (Verbania-Pallanza, Italy, 22 - 26 Sept. 1975) [EUR5452]* (eds. J. Booz, H.G. Ebert and B.G.R. Smith) 1037 - 1050 Commission of the European Communities, Luxembourg

HAMM, R.N., WRIGHT, H.A., TURNER, J.E. and RITCHIE, R.H. (1978) Spatial Correlation of Energy Deposition Events in Irradiated Liquid Water. In: *Proc.VI.Symp.Microdosimetry (Brussels, Belgium, 22 - 26 May 1978) [EUR6064]* (eds. J. Booz and H.G. Ebert) 179 - 186 Harwood Academic Publishers for the C.E.C.

HANDBOOK OF CHEMISTRY AND PHYSICS (1987 - 88) Mass attenuation coefficients. In: *Handbook of Chemistry and Physics (1987 - 88)* (eds. R.C. Weast, M.J. Astle and W.H. Beyer) E136 - E138 C.R.C. Press

HARNWELL, G.P. and LIVINGOOD, J.J. (1933) *Experimental Atomic Physics.* Mc.Graw-Hill Book Company

HEAPS, M.G. and GREEN, A.E.S. (1974) Monte Carlo approach to the spatial deposition of energy by electrons in molecular hydrogen. *J.appl.Phys.* 45 3183 - 3188

HEDDLE, J.A. and WOLFF, S. (1966) Estimation of the rejoining distance for chromosome exchanges induced in *Drosophila* sperm by combined doses of X-rays and neutrons. *Int.J.Radiat.Biol.* 10 207 - 210

HENKE, B.L., LEE, P., TANAKA, T.J., SHIMABUKURO, R.L. and FUJIKAWA, B.K. (1982) Low-energy X-ray interaction coefficients : Photoabsorption, Scattering, and Reflection. *At.Data & Nucl.Data Tables* 27 1 - 144

HORNYAK, W.F., LAURITSEN, T., MORRISON, P. and FOWLER, W.A. (1950) Energy levels of light nuclei III. *Rev.Mod.Phys.* 22 291 - 372

HOSHI, M., GOODHEAD, D.T., BRENNER, D.J., BANCE, D.A., CHMIELEWSKI, J.J., PACIOTTI, M.A. and BRADBURY, J.N. (1985) Dosimetry comparison and characterisation of an Al K ultrasoft X-ray beam from an MRC cold-cathode source. *Physics.Med.Biol.* 30 1029 - 1041

HOWARD-FLANDERS, P. (1958) Physical and Chemical mechanisms in the injury of cells by ionizing radiations. *Advances in Biological and Medical Physics* 6 553 - 603

HUBBELL, J.H. (1977) Photon Mass Attenuation and Mass Energy Absorption coefficients for H, C, N, O, Ar and seven mixtures from 0.1 keV to 20 MeV. *Radiat.Res.* 70 58 - 81

HUBBELL, J.H. and VEIGELE, Wm.J. (1976) Comparison of Theoretical and Experimental Photoeffect Data 0.1 keV to 1.5 keV. In: *N.B.S. Technical Note 901.* N.B.S.Dept.Commerce, Washington, D.C.

HUNT, S.E. and JONES, W.M. (1953) The Absolute Determination of Resonant Energies for the Radiative Capture of Protons by Boron, Carbon, Fluorine, Magnesium and Aluminium in the Energy Range below 500 keV. *Phys.Rev.* 89 1283 - 1287

ICRP (1975) Report of the Task Group on Reference Man. *ICRP Report No.23* Pergamon Press, Oxford

ICRU (1970) Linear Energy Transfer. *ICRU Report No.16* ICRU, Bethesda, Maryland

ICRU (1983) Microdosimetry. *ICRU Report No.36* ICRU, Bethesda, Maryland

JAMES, F. (1972) Function Minimization. In: *Proc.1972 CERN Computing and Data Processing School. (Pertisau, Austria, 10 - 24 Sept. 1972) [CERN 72 - 21]* CERN, Geneva, Switzerland

JAMES, F. (1978) Interpretation of the Errors on Parameters as given by MINUIT. *Supplement to Routine D506*. CERN Computing Centre Program Library, Geneva, Switzerland

JAMES, F. and ROOS, M. (1975) MINUIT - a system for function minimization and analysis of the parameter errors and correlations. *Comput.Phys.Commun.* 10 343 - 367

JAMES, F. and ROOS, M. (1985) Function Minimization and Error Analysis. *CERN Library Routine D506*. CERN Computer Centre Program Library, Geneva, Switzerland

JOHANSSON, S.A.E. and JOHANSSON, T.B. (1976) Analytical Application of Particle Induced X-ray Emission. *Nucl.Instrum.Meth.* 137 473 - 516

JOHNSON, D.E., BASBAS, G. and Mc.DANIEL, F.D. (1979) Non-relativistic plane-wave Born-approximation calculations of direct Coulomb M-subshell ionization by charged particles. *At.Data & Nucl.Data Tables* 24 1 - 11

JOPSON, R.C., MARK, H. and SWIFT, C.D. (1962) Production of Characteristic X-Rays by Low-Energy Protons. *Phys.Rev.* 127 1612 - 1618

KELLERER, A.M. (1971) Considerations on the random traversals of convex bodies and solution for general cylinders. *Radiat.Res.* 47 359 - 376

KHAN, J.M. and POTTER, D.L. (1964) Characteristic K-shell X-ray Production in Magnesium, Aluminium, and Copper by 60- to 500- keV Protons. *Phys.Rev.* 133 A890 - A894

KHAN, J.M., POTTER, D.L. and WORLEY, R.D. (1965) Studies in X-ray Production by Proton Bombardment of C, Mg, Al, Nd, Sm, Gd, Tb, Dy, and Ho. *Phys.Rev.* 139 A1735 - A1746

KWOK, C.S., BUDD, T. and MARSHALL, M. (1981) Track studies in tissue equivalent gas and water vapour with a low pressure cloud chamber. In: *Proc.VII.Symp.Microdosimetry (Oxford, U.K., 8 - 12 Sept. 1980) [EUR7147]* (eds. J. Booz, H.G. Ebert and H.D. Hartfiel) 347 - 357 Harwood Academic Publishers for the C.E.C.

LEA, D.E. (1955) *Actions of Radiations on Living Cells*. Cambridge University Press, London

LEA, D.E. and CATCHESIDE, D.G. (1942) The mechanism of induction by radiation of chromosome aberrations in *Tradescantia*. *J. Genet.* 44 216 - 245

LEWIS, H.W., SIMMONS, B.E. and MERZBACHER, E. (1953) Production of Characteristic X-rays by Protons of 1.7- to 3- MeV Energy. *Phys.Rev.* 91 943 - 946

LIVINGSTON, M.S., GENEVESE, F. and KONOPINSKI, E.J. (1937) Excitation of characteristic X-rays by protons. *Phys.Rev.* 51 835 - 839

LLOYD, D.C., PURROTT, R.J., DOLPHIN, G.W., BOLTON, D., EDWARDS, A.A. and CORP, M.J. (1975) The relationship between chromosome aberrations and low LET radiation dose to human lymphocytes. *Int.J.Radiat.Biol.* 28 75 - 90

LLOYD, D.C., PURROTT, R.J., DOLPHIN, G.W. and EDWARDS, A.A. (1976) Chromosome aberrations induced in human lymphocytes by neutron irradiation. *Int.J.Radiat.Biol.* 29 169 - 182

MEYER, M.A., VENTER, I. and REITMANN, D. (1975) Energy levels of ^{28}Si. *Nucl.Phys.* A250 235 - 256

NEARY, G.J., PRESTON, R.J. and SAVAGE, J.R.K. (1967) Chromosome aberrations and the theory of RBE. III. Evidence from experiments with soft X-rays, and a consideration of the effects of hard X-rays. *Int.J.Radiat.Biol.* 12 317 - 345

NELDER, J.A. and MEAD, R. (1965) A simplex method for function minimization. *Comput.J.* 7 308 - 313

NIKJOO, H., GOODHEAD, D.T. and CHARLTON, D.E. (1987) Energy deposition in small size targets by high and low LET radiations. In: *Radiation Research : Proc.VIII. Int.Congress of Radiation Research (Edinburgh, Scotland, 19 - 24 July 1987) (Vol.1)* (eds. E.M. Fielden, J.F. Fowler, J.H. Hendry and D. Scott) 87 Taylor and Francis

OPAL, C.B., BEATY, E.C. and PETERSON, W.K. (1972) Tables of secondary-electron-production cross-sections. *At.Data* 4 209 - 253

PARETZKE, H.G. (1978) On limitations of classical microdosimetry and advantages of track structure analysis for radiation biology. In: *Proc.VI.Symp.Microdosimetry (Brussels, Belgium, 22 - 26 May 1978) [EUR6064]* (eds. J. Booz and H.G. Ebert) 925 - 935 Harwood Academic Publishers for the C.E.C.

PARETZKE, H.G. (1980) Advances in Energy Deposition Theory. In: *Advances in Radiation Protection and Dosimetry in Medicine*. (eds. R.H. Thomas and V. Perez-Mendez) 51 - 73 Plenum Publishing Corporation

PARETZKE, H.G., LEUTHOLD, G., BURGER, G. and JACOB, W. (1974) Approaches to Physical Track Structure Calculations. In: *Proc.IV.Symp.Microdosimetry (Verbania-Pallanza, Italy, 24 - 28 Sept. 1973) [EUR5122]* (eds. J. Booz, H.G. Ebert, R. Eickel and A. Waker) 123 - 138 Commission of the European Communities, Luxembourg

PARETZKE, H.G., TURNER, J.E., HAMM, R.N., WRIGHT, H.A. and RITCHIE, R.H. (1986) Calculated yields and fluctuations for electron degradation in liquid water and water vapour. *J.chem.Phys.* 84 3182 - 3188

PAUL, H. (1984) An analytical cross-section formula for K X-ray production by protons. *Nucl.Instrum.Meth.* B3 5 - 10

RAJU, M.R., CARPENTER, S.G., CHMIELEWSKI, J.J., SCHILLACI, M.E., WILDER, M.E., FREYER, J.P., JOHNSON, N.F., SCHOR, P.L., SEBRING, R.J. (1987) Radiobiology of Ultrasoft X-rays. I. Cultured and GOODHEAD, D.T. Hamster Cells (V79). *Radiat.Res.* 110 396 - 412

REVELL, S.H. (1974) The Breakage-and-Reunion Theory and the Exchange Theory for Chromosomal Aberrations Induced by Ionizing Radiations : A Short History. In: *Advances in Radiation Biology (Vol.4)* (eds. J.T. Lett, H. Alder and M. Zelle) 367 - 416 New York Press

ROSENBLATT, J. (1968) *Particle Acceleration*. Methuen and Co. Ltd.

ROSSI, H.H. and ROSENZWEIG, W. (1955) A device for the measurement of dose as a function of specific ionizations. *Radiology* 64 404 - 411

RUTLEDGE, C.H. and WATSON, R.L. (1973) Cross-sections for K-shell ionization by ^{1}H, ^{2}H, ^{3}He and ^{4}He ion impact. *At.Data & Nucl.Data Tables* 12 195 - 216

SAVAGE, J.R.K. (1975) Radiation-induced chromosomal aberrations in the plant *Tradescantia* : Dose-response curves. I. Preliminary considerations. *Radiat.Bot.* 15 87 - 140

SAX, K. (1938) Chromosome aberrations induced by X-rays. *Genetics* 23 494 - 516

SAX, K. (1940) An analysis of X-ray induced chromosomal aberrations in *Tradescantia*. *Genetics* 25 41 - 68

SAX, K. (1957) The effect of ionizing radiation on chromosomes. *Q.Rev.Biol.* 32 15 - 26

SCIENCE DATA BOOK (1978) (edt. R.M. Tennent) Oliver and Boyd, Edinburgh

SLATER, F.P. (1921) The excitation of Y-radiation by α-particles from Radium Emanation. *Lond.Edinb.Dubl.Phil.Mag.* 42 904 - 923

STERK, A.A. (1965) X-ray Generation by Proton Bombardment. In: *Advances in X-ray Analysis (Vol.8)* 189 - 197 Plenum Press

STERK, A.A., MARKS, C.L. and SAYLOR, W.P. (1967) Production efficiencies of X-ray emission spectra by proton bombardment. In: *Advances in X-ray Analysis (Vol.10)* 399 - 408 Plenum Press

STORM, E. and ISRAEL, H.I. (1970) Photon cross-sections from 1 keV to 100 MeV for Elements Z=1 to Z=100. *Nucl.Data Tabl.* A7 565 - 681

TABLE OF ISOTOPES (1978) [7th Edition] (eds. C.M. Lederer and V.S. Shirley) John Wiley and Sons, inc.

TABLE OF X-RAY EMISSION ENERGIES Princeton Gamma-Tech, Europa.

TERRISOL, M., PATAU, J.P. and EUDALDO, T. (1978) Application à la microdosimetric et à la radiobiologie de la simulation due transport des électrons de basse énergie dans l'eau et l'etat liquide. In: *Proc.VI. Symp.Microdosimetry (Brussels, Belgium, 22 - 26 May 1978) [EUR6064]* (eds. J. Booz and H.G. Ebert) 169 - 178 Harwood Academic Publishers for the C.E.C.

THACKER, J., COX, R. and GOODHEAD, D.T. (1980) Do Carbon ultrasoft X-rays induce exchange aberrations in cultured mammalian cells? *Int.J.Radiat.Biol.* 38 469 - 472

THACKER, J., GOODHEAD, D.T. and WILKINSON, R.E. (1983) The role of localised single-track events in the formation of chromosome aberrations in cultured mammalian cells. In: *Radiation Protection, VIII. Symp.Microdosimetry (Jülich, F.R.G., 27 Sept. - 1 Oct. 1982) [EUR8395]* (eds. J. Booz and H.G. Ebert) 587 - 595 Commission of the European Communities, Luxembourg

THOMSON, J.J. (1914) Soft Röntgen Radiation produced by impact of positive and slow kathode rays. *Lond.Edinb.Dubl.Phil. Mag.* 28 620 - 625

TURNER, J.E., PARETZKE, H.G., HAMM, R.N., WRIGHT, H.A. and RITCHIE, R.H. (1982) Comparative study of electron energy deposition and yields in water in the liquid and vapour phases. *Radiat.Res.* 92 47 - 60

TURNER, J.E., PARETZKE, H.G., HAMM, R.N., WRIGHT, H.A. and RITCHIE, R.H. (1983a) Comparison of electron transport calculations for water in the liquid and vapour phases. In: *Radiation Protection, VIII.Symp.Microdosimetry (Jülich, F.R.G., 27 Sept. - 1 Oct. 1982) [EUR8395]* (eds. J. Booz and H.G. Ebert) 175 - 185 Commission of the European Communities, Luxembourg

TURNER, J.E., PARETZKE, H.G., HAMM, R.N., WRIGHT, H.A. and RITCHIE, R.H. (1983b) Calculated yields and fluctuations of electron energy losses in water in the liquid and vapour phases. In: *Proc.Int.Congr.Radiat.Res.VII., Session A (Amsterdam)* A1 - A53 Nijhoff, The Haque

VIRSIK, R.P., GOODHEAD, D.T., COX, R., THACKER, J., SCHÄFER, CH. and HARDER, D. (1980) Chromosome aberrations induced in human lymphocytes by ultrasoft Al_k and C_k X-rays. *Int.J.Radiat. Biol.* 38 545 - 557

WILSON, W.E. and PARETZKE, H.G. (1980) Calculation of ionization frequency in small sites. *Radiat.Res.* 81 326 - 335

WILSON, W.E. and PARETZKE, H.G. (1981) Calculation of distributions of energy imparted and ionisations by fast protons in nanometer sites. *Radiat.Res.* 87 521 - 537

WOLFF, S. (1959) Interpretation of induced chromosome breakage and rejoining. *Radiat.Res.Suppl.* 1 453 - 462

X-RAY DATA BOOKLET (1986) (edt. D.Vaughan) 2.13 - 2.17 Lawerence Berkeley Laboratory, Univ.California, Berkeley, California.

ZAIDER, M., BRENNER, D.J. and WILSON, W.E. (1983) The Applications of Track Calculations to Radiobiology. I. Monte-Carlo Simulation of Proton Tracks. *Radiat.Res.* 95 231 - 247

APPENDIX 1

```
      SUBROUTINE FCN(NPAR,G,F,X,IFLAG)
C
C GAUSSIAN FITTING:THREE GAUSSIANS ON A CONSTANT BACKROUND
C
      DIMENSION DESCP(40),TITLE(40)
      DIMENSION DRAW(90)
      INTEGER SPEC(1024),DRAW,BLANK,DOT,PLUS,LINE,STAR,RUB
      DOUBLE PRECISION THEO1(1024),THEO2(1024),THEO3(1024),R,R2,RR
      DOUBLE PRECISION AVX1,AVX2,AVX3,S1,S2,S3,BCK
      DOUBLE PRECISION X(15),FWHM1,FWHM2,FWHM3,AR1,AR2,AR3
      DOUBLE PRECISION SUM(1024),CHI(1024),ERR(1024)
      DOUBLE PRECISION XMAX,XMIN,P,Q,T,RM,RN,U,V
      DATA BLANK,DOT,PLUS,LINE,STAR/' ','.','+','-','*'/
C
C PARAMETER DEFINITIONS
C
      BCK=X(1)
      AVX1=X(2)
      FWHM1=X(3)
      AR1=X(4)
      AVX2=X(5)
      FWHM2=X(6)
      AR2=X(7)
      AVX3=X(8)
      FWHM3=X(9)
      AR3=X(10)
C
C READ IN RAW DATA
C
      IF (IFLAG.GT.1) GO TO 25
      READ(5,10) (TITLE(I),I=1,40)
      READ(5,10) (DESCP(I),I=1,40)
      READ(5,15) NPTS
      K=(NPTS/5)+1
      DO 30 J=1,K
      M=J*5-4
      N=J*5
      READ(5,20) RUB,ZERO,(SPEC(I),I=M,N)
   10 FORMAT(40A1)
   15 FORMAT(I4)
   20 FORMAT(/,A1,I4,1X,I6,1X,I6,1X,I6,1X,I6,1X,I6)
   30 CONTINUE
   25 CONTINUE
      DO 35 I=26,NPTS
      R=DFLOAT(SPEC(I))
      ERR(I)=DSQRT(DABS(R))
      IF (DABS(ERR(I)).LT.1.0D-03) ERR(I)=1.0D+00
   35 CONTINUE
C
C COMPUTE THEORETICAL FUNCTION
C
```

```
C
C FIRST PEAK
C
      DO 40 I=26,NPTS
      M=I-1
      IF(AVX1.EQ.0.0D+00) GO TO 50
      FAC1=AVX1-DFLOAT(M)
      IF (FWHM.LT.1.0D-03) FWHM=1.0D+00
      F1=FAC1/FWHM1
      ARG1=-2.7726D+00*F1*F1
      IF(ARG1.LT.-10) GO TO 50
      S1=0.9394/FWHM1
      THEO1(I)=AR1*S1*EXP(ARG1)
      GO TO 40
   50 THEO1(I)=0.0D+00
   40 CONTINUE
C
C SECOND PEAK
C
      DO 42 I=26,NPTS
      M=I-1
      IF(AVX2.EQ.0.0D+00) GO TO 52
      FAC2=AVX2-DFLOAT(M)
      IF(FWHM2.LT.1.0D-03) FWHM2=1.0D+00
      F2=FAC2/FWHM2
      ARG2=-2.7726D+00*F2*F2
      IF(ARG2.LT.-10) GO TO 52
      S2=0.9394/FWHM2
      THEO2(I)=AR2*S2*EXP(ARG2)
      GO TO 42
   52 THEO2(I)=0.0D+00
   42 CONTINUE
C
C THIRD PEAK
C
      DO 44 I=26,NPTS
      M=I-1
      IF(AVX3.EQ.0.0D+00) GO TO 54
      FAC3=AVX3-DFLOAT(M)
      IF(FWHM3.LT.1.0D-03) FWHM3=1.0D+00
      F3=FAC3/FWHM3
      ARG3=-2.7726D+00*F3*F3
      IF(ARG3.LT.-10) GO TO 54
      S3=0.9394/FWHM3
      THEO3(I)=AR3*S3*EXP(ARG3)
      GO TO 44
   54 THEO3(I)=0.0D+00
   44 CONTINUE
C
C CALCULATE TOTAL THEORETICAL VALUES
C
      DO 60 I=26,NPTS
      SUM(I)=THEO1(I)+THEO2(I)+THEO3(I)+BCK
   60 CONTINUE
```

```
C
C CHISQUARE OVER ALL CHANNELS
C
      F=0.0D+00
      ISTART=26
      ISTOP=NPTS
      DO 70 I=ISTART,ISTOP
      R2=DFLOAT(SPEC(I))
      SPECPT=(R2-SUM(I))/ERR(I)
      CHI(I)=SPECPT*SPECPT
      F=F+CHI(I)
   70 CONTINUE
      IF(IFLAG.NE.3) GO TO 80
      FEXP=FLOAT(ISTOP-ISTART)
      FLOLIM=FEXP-SQRT(2*FEXP)
      FUPLIM=FEXP+SQRT(2*FEXP)
      CHIPCH=F/FEXP
C
C OUTPUT RESULTS
C
      WRITE(6,100) (TITLE(I),I=1,40)
      WRITE(6,100) (DESCP(I),I=1,40)
  100 FORMAT(/,40A1)
      WRITE(6,110)F,FEXP,FLOLIM,FUPLIM
  110 FORMAT(////,20X,'CHISQUARE IS: ',D10.3,//,1X,'EXPECTED VALUE IS: ',
     1F7.1,1X,'WITH LIMITS:',F7.1,1X,'AND:',1X,F7.1)
      WRITE(6,115) CHIPCH
  115 FORMAT(//,1X,'CHISQUARE PER CHANNEL IS: ',D10.1)
      WRITE(6,120)
  120 FORMAT(///,5X,'PEAK POSITION',5X,'F.W.H.M.',10X,'AREA')
      WRITE(6,130) X(2),X(3),X(4),X(5),X(6),X(7),X(8),X(9),X(10)
  130 FORMAT(6X,F7.0,11X,F7.0,4X,F10.1)
      WRITE(6,140) X(1)
  140 FORMAT(//5X,'BACKGROUND IS:',F7.0)
C
C GRAPHICAL OUTPUT
C
      XMAX=0
      XMIN=1E08
      DO 1000 I=ISTART,ISTOP
      IF(SUM(I).LT.1) SUM(I)=1
      IF (SPEC(I).LT.1) SPEC(I)=1
      IF(SUM(I).GT.XMAX) XMAX=SUM(I)
      IF(SUM(I).LT.XMIN) XMIN=SUM(I)
      IF(SPEC(I).LT.XMIN) XMIN=SPEC(I)
      IF(SPEC(I).GT.XMAX) XMAX=SPEC(I)
 1000 CONTINUE
      WRITE(6,1020) XMIN,XMAX
 1020 FORMAT(/8X,'YMIN=',F8.1,17X,'LOGARITHMIC SCALE',23X,'YMAX=',F8.1)
      DO 1100 I=1,90
 1100 DRAW(I)=LINE
      WRITE(6,1030) DRAW
 1030 FORMAT(/4X,'CH',2X,90A1,5X,'CAL',5X,'OBS',8X,'CHI',/)
```

```
      P=DLOG10(XMAX)
      Q=DLOG10(XMIN)
      T=89./(P-Q)
      K=(NPTS/5)+1
      DO 1400 J=6,K
      I=J*5-4
      IF(I.EQ.1) I=2
      DO 1200 L=1,90
 1200 DRAW(L)=BLANK
      RR=DFLOAT(SPEC(I))
      RM=DLOG10(RR)
      RN=DLOG10(SUM(I))
      U=T*(RM-Q)
      V=T*(RN-Q)
      DRAW(U)=DOT
      DRAW(V)=PLUS
      IF(U.EQ.V) DRAW(U)=STAR
      M=I-1
      WRITE(6,1040) M,DRAW,SUM(I),SPEC(I),CHI(I)
 1040 FORMAT(2X,I4,2X,90A1,1X,F7.1,4X,I5,4X,D9.2)
 1400 CONTINUE
      WRITE(6,1060)
 1060 FORMAT(/,40X,'SYMBOL: .=OBS., +=CAL., *=OBS. AND CAL.')
   80 CONTINUE
      RETURN
      END
```

APPENDIX 2

The absolute frequency of energy depositions greater than a given amount in each elemental cylinder per Gray of absorbed dose to the medium

The tables are headed by the photon energy for the particular scoring run, and the number of interactions considered. The diameter of the target cylinder is given and also the number of infinitely long cylinders that were hit (a measure of the statistics of the run). The body of the table shows the frequency of hits of energy greater than E, and data for four different lengths of cylinders are given. The frequencies apply to a single target cylinder placed at random in water irradiated uniformly with an absorbed dose of 1 Gy. In some cases, the last values in each column are subject to very large uncertainties (Equation 7.3) resulting in the repetition of the same value, and may therefore be ignored.

The frequency averaged mean specific energy in the targets, z, is given at the base of each column. This was calculated from the full frequency distribution of hit sizes and independently of the absolute normalisation of the scoring frequencies in the Table. Let $f(E)$ be the frequency of energy depositions ('hits') of energy between E and $E + dE$. Then the frequency mean hit size, $\overline{E}$, is given by

$$\overline{E} = \frac{\int_0^\infty E.\ f(E).dE}{\int_0^\infty f(E).dE} \qquad A2.1$$

irrespective of the normalisation of the frequency distribution.

Hence, the frequency mean specific energy is

$$z = \frac{\overline{E}}{m} \qquad A2.2$$

where m is the mass of a target (I.C.R.U.,1983; Goodhead,1987d).

(In I.C.R.U. notation this frequency mean specific energy is written as $\bar{z}_F$ (I.C.R.U.,1983)). The probability of a hit of any size is given by z^{-1} and should, with ideal scoring, equal the frequency of a hit greater than 0 eV ($f_{>0}$). The difference between these values is a measure of the statistical uncertainty of the data. The 'scoring efficiency', S, is defined by:

$$S\ (\%) \quad = \quad \frac{\left| f_{>0} \ - \ z^{-1} \right|}{z^{-1}} \quad \text{x} \quad 100 \qquad \text{A2.3}$$

Finally, the number of hits from which the statistics are dervied is given at the bottom of each column.

PHOTON ENERGY : 109 eV

Number of interactions : 500
Diameter of target : 2.0 nm
Number of infinitely long cylinders hit : 6673

FREQUENCY OF ENERGY DEPOSITION GREATER THAN E PER Gy

E	Target cylinder length (nm)			
(eV)	1.0	2.0	4.0	8.0
0	5.749E-07	1.000E-06	1.924E-06	3.843E-06
10	5.017E-07	8.942E-07	1.734E-06	3.464E-06
20	3.449E-07	6.481E-07	1.280E-06	2.561E-06
30	2.782E-07	5.474E-07	1.086E-06	2.172E-06
40	1.848E-07	3.965E-07	8.008E-07	1.602E-06
50	1.309E-07	3.000E-07	6.159E-07	1.232E-06
60	9.020E-08	2.237E-07	4.665E-07	9.341E-07
70	6.306E-08	1.673E-07	3.524E-07	7.066E-07
80	4.010E-08	1.139E-07	2.453E-07	4.912E-07
90	2.620E-08	7.933E-08	1.756E-07	3.513E-07
100	1.224E-08	3.844E-08	8.667E-07	1.733E-07
110	0.000E+00	0.000E+00	0.000E+00	0.000E+00
120	-	-	-	-
z(Gy)	1.723E+06	9.903E+05	5.146E+05	2.577E+05
S(%)	0.9	1.0	1.0	1.0
Hits	7986	6946	6683	6673

PHOTON ENERGY : 109 eV

Number of interactions : 500
Diameter of target : 10.0 nm
Number of infinitely long cylinders hit : 3248

FREQUENCY OF ENERGY DEPOSITION GREATER THAN E PER Gy

E	Target cylinder length (nm)			
(eV)	5.0	10.0	20.0	40.0
0	2.941E-05	5.845E-05	1.169E-04	2.338E-04
10	2.875E-05	5.721E-05	1.144E-04	2.288E-04
20	2.616E-05	5.226E-05	1.045E-04	2.090E-04
30	2.501E-05	4.999E-05	9.999E-05	2.000E-04
40	2.353E-05	4.704E-05	9.408E-05	1.882E-04
50	2.213E-05	4.427E-05	8.854E-05	1.771E-04
60	2.100E-05	4.202E-05	8.404E-05	1.681E-04
70	1.975E-05	3.957E-05	7.915E-05	1.583E-04
80	1.837E-05	3.680E-05	7.360E-05	1.472E-04
90	1.753E-05	3.513E-05	7.026E-05	1.405E-04
100	1.545E-05	3.112E-05	6.223E-05	1.245E-04
110	0.000E+00	0.000E+00	0.000E+00	0.000E+00
120	-	-	-	-
z(Gy)	3.306E+04	1.663E+04	8.315E+03	4.158E+03
S(%)	2.8	2.8	2.8	2.8
Hits	3268	3248	3248	3248

PHOTON ENERGY : 109 eV

Number of interactions : 500
Diameter of target : 25.0 nm
Number of infinitely long cylinders hit : 2760

FREQUENCY OF ENERGY DEPOSITION GREATER THAN E PER Gy

E	Target cylinder length (nm)			
(eV)	12.5	25.0	50.0	100.0
0	3.880E-04	7.761E-04	1.552E-03	3.104E-03
10	3.827E-04	7.654E-04	1.531E-03	3.062E-03
20	3.671E-04	7.342E-04	1.468E-03	2.937E-03
30	3.615E-04	7.229E-04	1.446E-03	2.892E-03
40	3.537E-04	7.075E-04	1.415E-03	2.830E-03
50	3.450E-04	6.901E-04	1.380E-03	2.760E-03
60	3.372E-04	6.743E-04	1.349E-03	2.697E-03
70	3.290E-04	6.580E-04	1.316E-03	2.632E-03
80	3.192E-04	6.383E-04	1.277E-03	2.553E-03
90	3.130E-04	6.259E-04	1.252E-03	2.504E-03
100	2.990E-04	5.981E-04	1.196E-03	2.392E-03
110	0.000E+00	0.000E+00	0.000E+00	0.000E+00
120	-	-	-	-
z(Gy)	2.502E+03	1.251E+03	6.255E+02	3.128E+02
S(%)	2.9	2.9	2.9	2.9
Hits	2760	2760	2760	2760

PHOTON ENERGY : 183 eV

Number of interactions : 500
Diameter of target : 2.0 nm
Number of infinitely long cylinders hit : 9816

FREQUENCY OF ENERGY DEPOSITION GREATER THAN E PER Gy

E	Target cylinder length (nm)			
(eV)	1.0	2.0	4.0	8.0
0	5.579E-07	9.168E-07	1.695E-06	3.367E-06
10	4.870E-07	8.252E-07	1.544E-06	3.070E-06
20	3.306E-07	5.985E-07	1.155E-06	2.305E-06
30	2.601E-07	4.989E-07	9.704E-07	1.939E-06
40	1.780E-07	3.701E-07	7.387E-07	1.479E-06
50	1.279E-07	2.910E-07	5.951E-07	1.192E-06
60	9.403E-08	2.306E-07	4.776E-07	9.587E-07
70	6.517E-08	1.761E-07	3.759E-07	7.553E-07
80	4.626E-08	1.355E-07	3.006E-07	6.051E-07
90	3.151E-08	1.013E-07	2.317E-07	4.692E-07
100	2.088E-08	7.409E-08	1.775E-07	3.595E-07
110	1.316E-08	5.128E-08	1.305E-07	2.638E-07
120	8.447E-09	3.739E-08	9.844E-08	1.989E-07
130	4.459E-09	2.307E-08	6.603E-08	1.334E-07
140	2.658E-09	1.432E-08	4.150E-08	8.472E-08
150	1.887E-09	9.090E-09	2.573E-08	5.282E-08
160	1.029E-09	5.317E-09	1.578E-08	3.293E-08
170	3.001E-10	1.801E-09	6.689E-09	1.372E-08
180	4.288E-11	5.145E-10	2.058E-09	4.116E-09
190	0.000E+00	0.000E+00	0.000E+00	0.000E+00
200	-	-	-	-
z(Gy)	1.769E+06	1.076E+06	5.824E+05	2.931E+05
S(%)	1.3	1.4	1.3	1.3
Hits	13011	10691	9881	9816

PHOTON ENERGY : 183 eV

Number of interactions : 500
Diameter of target : 10.0 nm
Number of infinitely long cylinders hit : 3848

FREQUENCY OF ENERGY DEPOSITION GREATER THAN E PER Gy

E	Target cylinder length (nm)			
(eV)	5.0	10.0	20.0	40.0
0	2.107E-05	4.126E-05	8.249E-05	1.650E-04
10	2.039E-05	4.004E-05	8.005E-05	1.601E-04
20	1.839E-05	3.639E-05	7.276E-05	1.455E-04
30	1.756E-05	3.479E-05	6.959E-05	1.392E-04
40	1.626E-05	3.233E-05	6.466E-05	1.293E-04
50	1.543E-05	3.080E-05	6.159E-05	1.232E-04
60	1.482E-05	2.956E-05	5.913E-05	1.183E-04
70	1.414E-05	2.827E-05	5.653E-05	1.131E-04
80	1.365E-05	2.726E-05	5.452E-05	1.090E-04
90	1.294E-05	2.590E-05	5.179E-05	1.036E-04
100	1.231E-05	2.468E-05	4.935E-05	9.870E-05
110	1.162E-05	2.332E-05	4.665E-05	9.330E-05
120	1.099E-05	2.210E-05	4.421E-05	8.841E-05
130	1.032E-05	2.082E-05	4.163E-05	8.327E-05
140	9.685E-06	1.961E-05	3.921E-05	7.842E-05
150	9.133E-06	1.852E-05	3.707E-05	7.413E-05
160	8.248E-06	1.683E-05	3.368E-05	6.736E-05
170	7.450E-06	1.534E-05	3.068E-05	6.136E-05
180	6.480E-06	1.354E-05	2.708E-05	5.415E-05
190	0.000E+00	0.000E+00	0.000E+00	0.000E+00
200	-	-	-	-
z(Gy)	4.615E+04	2.356E+04	1.179E+04	5.893E+03
S(%)	2.8	2.8	2.7	2.8
Hits	3931	3849	3848	3848

PHOTON ENERGY : 183 eV

Number of interactions : 500
Diameter of target : 25.0 nm
Number of infinitely long cylinders hit : 2993

FREQUENCY OF ENERGY DEPOSITION GREATER THAN E PER Gy

E	Target cylinder length (nm)			
(eV)	12.5	25.0	50.0	100.0
0	2.506E-04	5.013E-04	1.003E-03	2.005E-03
10	2.471E-04	4.943E-04	9.885E-04	1.977E-03
20	2.357E-04	4.715E-04	9.430E-04	1.886E-03
30	2.319E-04	4.638E-04	9.275E-04	1.855E-03
40	2.248E-04	4.495E-04	8.991E-04	1.798E-03
50	2.200E-04	4.400E-04	8.800E-04	1.760E-03
60	2.162E-04	4.325E-04	8.649E-04	1.730E-03
70	2.120E-04	4.239E-04	8.478E-04	1.696E-03
80	2.085E-04	4.170E-04	8.341E-04	1.668E-03
90	2.033E-04	4.067E-04	8.133E-04	1.627E-03
100	1.996E-04	3.991E-04	7.982E-04	1.596E-03
110	1.958E-04	3.916E-04	7.832E-04	1.566E-03
120	1.924E-04	3.849E-04	7.698E-04	1.540E-03
130	1.886E-04	3.772E-04	7.544E-04	1.509E-03
140	1.842E-04	3.683E-04	7.366E-04	1.473E-03
150	1.810E-04	3.619E-04	7.239E-04	1.448E-03
160	1.754E-04	3.507E-04	7.014E-04	1.403E-03
170	1.688E-04	3.377E-04	6.753E-04	1.351E-03
180	1.625E-04	3.249E-04	6.498E-04	1.300E-03
190	0.000E+00	0.000E+00	0.000E+00	0.000E+00
200	-	-	-	-
z(Gy)	3.892E+03	1.946E+03	9.730E+02	4.865E+02
S(%)	2.5	2.4	2.4	2.5
Hits	2993	2993	2993	2993

PHOTON ENERGY : 278 eV

Number of interactions : 500
Diameter of target : 2.0 nm
Number of infinitely long cylinders hit :14503

FREQUENCY OF ENERGY DEPOSITION GREATER THAN E PER Gy

E	Target cylinder length (nm)			
(eV)	1.0	2.0	4.0	8.0
0	5.741E-07	9.340E-07	1.677E-06	3.278E-06
10	5.050E-07	8.422E-07	1.534E-06	3.009E-06
20	3.383E-07	6.070E-07	1.146E-06	2.260E-06
30	2.598E-07	4.963E-07	9.576E-07	1.896E-06
40	1.764E-07	3.652E-07	7.287E-07	1.452E-06
50	1.260E-07	2.851E-07	5.845E-07	1.172E-06
60	8.941E-08	2.209E-07	4.680E-07	9.449E-07
70	6.113E-08	1.689E-07	3.732E-07	7.618E-07
80	4.149E-08	1.258E-07	2.901E-07	5.938E-07
90	2.932E-08	9.692E-08	2.312E-07	4.762E-07
100	1.962E-08	7.225E-08	1.778E-07	3.712E-07
110	1.301E-08	5.334E-08	1.382E-07	2.886E-07
120	7.875E-09	3.895E-08	1.044E-07	2.206E-07
130	4.996E-09	2.817E-08	7.824E-08	1.673E-07
140	2.964E-09	1.953E-08	5.938E-08	1.278E-07
150	1.863E-09	1.343E-08	4.335E-08	9.461E-08
160	1.214E-09	9.653E-09	3.172E-08	7.112E-08
170	7.621E-10	6.604E-09	2.190E-08	4.990E-08
180	3.105E-10	4.121E-09	1.513E-08	3.477E-08
190	1.411E-10	2.371E-09	9.709E-09	2.371E-08
200	1.411E-10	1.355E-09	6.548E-09	1.671E-08
210	5.645E-11	9.596E-10	4.516E-09	1.084E-08
220	2.822E-11	6.774E-10	2.597E-09	6.548E-09
230	2.822E-11	3.387E-10	1.468E-09	3.613E-09
240	0.000E+00	1.129E-10	1.016E-09	2.258E-09
250	-	5.645E-11	2.258E-10	4.516E-10
260	-	0.000E+00	0.000E+00	0.000E+00
270	-	-	-	-
280	-	-	-	-
290	-	-	-	-
300	-	-	-	-
z(Gy)	1.731E+06	1.064E+06	5.925E+05	3.031E+05
S(%)	0.6	0.6	0.6	0.6
Hits	20340	16546	14853	14517

PHOTON ENERGY : 278 eV

Number of interactions : 500
Diameter of target : 10.0 nm
Number of infinitely long cylinders hit : 4697

FREQUENCY OF ENERGY DEPOSITION GREATER THAN E PER Gy

E	Target cylinder length (nm)			
(eV)	5.0	10.0	20.0	40.0
0	1.812E-05	3.323E-05	6.628E-05	1.326E-04
10	1.762E-05	3.244E-05	6.472E-05	1.294E-04
20	1.575E-05	2.951E-05	5.889E-05	1.178E-04
30	1.497E-05	2.822E-05	5.632E-05	1.126E-04
40	1.390E-05	2.642E-05	5.278E-05	1.056E-04
50	1.318E-05	2.521E-05	5.037E-05	1.007E-04
60	1.255E-05	2.405E-05	4.804E-05	9.607E-05
70	1.190E-05	2.294E-05	4.585E-05	9.170E-05
80	1.123E-05	2.185E-05	4.366E-05	8.733E-05
90	1.058E-05	2.072E-05	4.143E-05	8.287E-05
100	1.002E-05	1.976E-05	3.953E-05	7.906E-05
110	9.533E-06	1.893E-05	3.785E-05	7.570E-05
120	9.007E-06	1.801E-05	3.603E-05	7.206E-05
130	8.513E-06	1.721E-05	3.443E-05	6.887E-05
140	8.058E-06	1.643E-05	3.287E-05	6.573E-05
150	7.493E-06	1.552E-05	3.105E-05	6.209E-05
160	7.045E-06	1.477E-05	2.955E-05	5.910E-05
170	6.622E-06	1.401E-05	2.804E-05	5.608E-05
180	6.227E-06	1.331E-05	2.666E-05	5.332E-05
190	5.818E-06	1.260E-05	2.523E-05	5.046E-05
200	5.423E-06	1.188E-05	2.382E-05	4.764E-05
210	5.045E-06	1.115E-05	2.240E-05	4.479E-05
220	4.664E-06	1.044E-05	2.097E-05	4.194E-05
230	4.339E-06	9.829E-06	1.971E-05	3.943E-05
240	3.994E-06	9.145E-06	1.835E-05	3.669E-05
250	3.461E-06	8.107E-06	1.629E-05	3.257E-05
260	3.154E-06	7.522E-06	1.511E-05	3.023E-05
270	2.484E-06	6.139E-06	1.235E-05	2.470E-05
280	0.000E+00	0.000E+00	0.000E+00	0.000E+00
290	-	-	-	-
300	-	-	-	-
z(Gy)	5.448E+04	2.970E+04	1.489E+04	7.446E+03
S(%)	1.3	1.3	1.3	1.3
Hits	5136	4710	4697	4697

PHOTON ENERGY : 278 eV

Number of interactions : 500
Diameter of target : 25.0 nm
Number of infinitely long cylinders hit : 3291

FREQUENCY OF ENERGY DEPOSITION GREATER THAN E PER Gy

E	Target cylinder length (nm)			
(eV)	12.5	25.0	50.0	100.0
0	1.814E-04	3.628E-04	7.257E-04	1.451E-03
10	1.797E-04	3.593E-04	7.186E-04	1.437E-03
20	1.723E-04	3.445E-04	6.891E-04	1.378E-03
30	1.687E-04	3.374E-04	6.747E-04	1.349E-03
40	1.636E-04	3.271E-04	6.542E-04	1.308E-03
50	1.596E-04	3.192E-04	6.384E-04	1.277E-03
60	1.561E-04	3.121E-04	6.242E-04	1.248E-03
70	1.529E-04	3.057E-04	6.115E-04	1.223E-03
80	1.498E-04	2.997E-04	5.993E-04	1.199E-03
90	1.467E-04	2.934E-04	5.868E-04	1.174E-03
100	1.438E-04	2.875E-04	5.751E-04	1.150E-03
110	1.407E-04	2.814E-04	5.627E-04	1.125E-03
120	1.379E-04	2.757E-04	5.515E-04	1.103E-03
130	1.352E-04	2.703E-04	5.407E-04	1.081E-03
140	1.328E-04	2.656E-04	5.312E-04	1.062E-03
150	1.300E-04	2.600E-04	5.199E-04	1.040E-03
160	1.278E-04	2.557E-04	5.114E-04	1.023E-03
170	1.253E-04	2.506E-04	5.012E-04	1.002E-03
180	1.229E-04	2.459E-04	4.917E-04	9.835E-04
190	1.201E-04	2.401E-04	4.803E-04	9.605E-04
200	1.174E-04	2.348E-04	4.697E-04	9.393E-04
210	1.140E-04	2.280E-04	4.560E-04	9.120E-04
220	1.120E-04	2.239E-04	4.478E-04	8.957E-04
230	1.094E-04	2.187E-04	4.375E-04	8.750E-04
240	1.061E-04	2.122E-04	4.245E-04	8.489E-04
250	1.023E-04	2.045E-04	4.090E-04	8.181E-04
260	9.967E-05	1.993E-04	3.987E-04	7.973E-04
270	9.427E-05	1.885E-04	3.771E-04	7.541E-04
280	0.000E+00	0.000E+00	0.000E+00	0.000E+00
290	-	-	-	-
300	-	-	-	-
z(Gy)	5.379E+03	2.689E+03	1.345E+03	6.724E+02
S(%)	2.4	2.4	2.4	2.4
Hits	3291	3291	3291	3291

PHOTON ENERGY : 392 eV

Number of interactions : 500
Diameter of target : 2.0 nm
Number of infinitely long cylinders hit :20442

FREQUENCY OF ENERGY DEPOSITION GREATER THAN E PER Gy

E	Target cylinder length (nm)			
(eV)	1.0	2.0	4.0	8.0
0	5.919E-07	9.606E-07	1.702E-06	3.284E-06
10	5.202E-07	8.691E-07	1.565E-06	3.027E-06
20	3.417E-07	6.173E-07	1.159E-06	2.268E-06
30	2.574E-07	4.980E-07	9.602E-07	1.890E-06
40	1.697E-07	3.606E-07	7.205E-07	1.433E-06
50	1.209E-07	2.777E-07	5.729E-07	1.146E-06
60	8.480E-08	2.138E-07	4.557E-07	9.201E-07
70	5.882E-08	1.635E-07	3.627E-07	7.406E-07
80	4.017E-08	1.225E-07	2.832E-07	5.860E-07
90	2.614E-08	8.946E-08	2.192E-07	4.605E-07
100	1.815E-08	6.640E-08	1.704E-07	3.623E-07
110	1.231E-08	4.923E-08	1.328E-07	2.880E-07
120	8.586E-09	3.610E-08	1.024E-07	2.246E-07
130	5.864E-09	2.674E-08	7.805E-08	1.752E-07
140	3.843E-09	1.925E-08	5.956E-08	1.338E-07
150	2.742E-09	1.513E-08	4.763E-08	1.097E-07
160	1.961E-09	1.109E-08	3.562E-08	8.550E-08
170	1.301E-09	7.605E-09	2.674E-08	6.580E-08
180	8.405E-10	5.444E-09	2.041E-08	4.947E-08
190	5.804E-10	3.562E-09	1.425E-08	3.522E-08
200	3.802E-10	2.602E-09	1.057E-08	2.690E-08
210	2.602E-10	2.001E-09	7.685E-09	1.953E-08
220	1.801E-10	1.481E-09	5.764E-09	1.521E-08
230	8.005E-11	1.121E-09	4.083E-09	1.057E-08
240	4.003E-11	9.206E-10	3.522E-09	9.126E-09
250	2.001E-11	6.404E-10	2.642E-09	6.564E-09
260	2.001E-11	4.403E-10	2.001E-09	4.963E-09
270	0.000E+00	2.001E-10	1.921E-09	4.483E-09
280	-	8.005E-11	1.361E-09	3.042E-09
290	-	0.000E+00	5.604E-10	1.601E-09
300	-	-	4.003E-10	1.281E-09
z(Gy)	1.686E+06	1.039E+06	5.862E+05	3.039E+05
S(%)	0.2	0.2	0.2	0.2
Hits	29578	23999	21266	20511

PHOTON ENERGY : 392 eV

Number of interactions : 500
Diameter of target : 10.0 nm
Number of infinitely long cylinders hit : 5781

FREQUENCY OF ENERGY DEPOSITION GREATER THAN E PER Gy

E	Target cylinder length (nm)			
(eV)	5.0	10.0	20.0	40.0
0	1.744E-05	2.937E-05	5.787E-05	1.157E-04
10	1.705E-05	2.886E-05	5.691E-05	1.138E-04
20	1.533E-05	2.646E-05	5.230E-05	1.046E-04
30	1.456E-05	2.540E-05	5.025E-05	1.005E-05
40	1.332E-05	2.354E-05	4.665E-05	9.329E-05
50	1.257E-05	2.244E-05	4.455E-05	8.909E-05
60	1.190E-05	2.147E-05	4.262E-05	8.525E-05
70	1.131E-05	2.052E-05	4.078E-05	8.157E-05
80	1.069E-05	1.964E-05	3.908E-05	7.816E-05
90	9.996E-06	1.869E-05	3.722E-05	7.444E-05
100	9.455E-06	1.795E-05	3.575E-05	7.150E-05
110	8.910E-06	1.712E-05	3.415E-05	6.829E-05
120	8.302E-06	1.624E-05	3.243E-05	6.485E-05
130	7.846E-06	1.558E-05	3.112E-05	6.225E-05
140	7.393E-06	1.497E-05	2.990E-05	5.981E-05
150	6.926E-06	1.424E-05	2.849E-05	5.699E-05
160	6.470E-06	1.353E-05	2.712E-05	5.424E-05
170	6.077E-06	1.285E-05	2.580E-05	5.160E-05
180	5.657E-06	1.220E-05	2.457E-05	4.914E-05
190	5.289E-06	1.159E-05	2.336E-05	4.672E-05
200	4.961E-06	1.108E-05	2.233E-05	4.466E-05
210	4.646E-06	1.058E-05	2.133E-05	4.265E-05
220	4.333E-06	1.007E-05	2.033E-05	4.065E-05
230	4.006E-06	9.463E-06	1.911E-05	3.821E-05
240	3.693E-06	8.892E-06	1.796E-05	3.593E-05
250	3.395E-06	8.382E-06	1.694E-05	3.389E-05
260	3.100E-06	7.861E-06	1.593E-05	3.187E-05
270	2.830E-06	7.316E-06	1.486E-05	2.972E-05
280	2.565E-06	6.750E-06	1.374E-05	2.748E-05
290	2.329E-06	6.220E-06	1.269E-05	2.538E-05
300	2.052E-06	5.670E-06	1.154E-05	2.308E-05
310	1.834E-06	5.159E-06	1.050E-05	2.100E-05
320	1.609E-06	4.699E-06	9.578E-06	1.916E-05
330	1.426E-06	4.283E-06	8.757E-06	1.751E-05
340	1.266E-06	3.863E-06	7.946E-06	1.589E-05
350	1.078E-06	3.398E-06	7.026E-06	1.407E-05
360	9.332E-07	3.082E-06	6.395E-06	1.279E-05
370	7.631E-07	2.587E-06	5.384E-06	1.077E-05
380	5.980E-07	2.182E-06	4.534E-06	9.067E-06
390	4.829E-07	1.887E-06	3.933E-06	7.866E-06
400	0.000E+00	0.000E+00	0.000E+00	0.000E+00

Photon Energy : 392 eV ; Diameter of target : 10 nm.
(cont.)

z(Gy)	5.732E+04	3.405E+04	1.728E+04	8.641E+03
S(%)	<0.1	<0.1	<0.1	<0.1
Hits	6972	5869	5782	5781

PHOTON ENERGY : 392 eV

Number of interactions : 500
Diameter of target : 25.0 nm
Number of infinitely long cylinders hit : 3703

FREQUENCY OF ENERGY DEPOSITION GREATER THAN E PER Gy

E	Target cylinder length (nm)			
(eV)	12.5	25.0	50.0	100.0
0	1.463E-04	2.895E-04	5.791E-04	1.158E-03
10	1.446E-04	2.863E-04	5.725E-04	1.145E-03
20	1.386E-04	2.748E-04	5.495E-04	1.099E-03
30	1.357E-04	2.694E-04	5.387E-04	1.077E-03
40	1.296E-04	2.575E-04	5.150E-04	1.030E-03
50	1.264E-04	2.516E-04	5.032E-04	1.006E-03
60	1.240E-04	2.469E-04	4.938E-04	9.877E-04
70	1.215E-04	2.418E-04	4.835E-04	9.670E-04
80	1.189E-04	2.367E-04	4.734E-04	9.467E-04
90	1.168E-04	2.326E-04	4.652E-04	9.305E-04
100	1.146E-04	2.282E-04	4.563E-04	9.126E-04
110	1.125E-04	2.239E-04	4.479E-04	8.957E-04
120	1.106E-04	2.202E-04	4.404E-04	8.807E-04
130	1.085E-04	2.160E-04	4.321E-04	8.641E-04
140	1.069E-04	2.129E-04	4.258E-04	8.516E-04
150	1.046E-04	2.087E-04	4.174E-04	8.347E-04
160	1.025E-04	2.049E-04	4.097E-04	8.194E-04
170	1.006E-04	2.011E-04	4.022E-04	8.044E-04
180	9.883E-05	1.977E-04	3.955E-04	7.910E-04
190	9.699E-05	1.941E-04	3.883E-04	7.766E-04
200	9.504E-05	1.905E-04	3.809E-04	7.619E-04
210	9.340E-05	1.873E-04	3.747E-04	7.494E-04
220	9.156E-05	1.837E-04	3.673E-04	7.347E-04
230	8.949E-05	1.795E-04	3.590E-04	7.181E-04
240	8.769E-05	1.761E-04	3.522E-04	7.043E-04
250	8.562E-05	1.721E-04	3.442E-04	6.884E-04
260	8.296E-05	1.669E-04	3.337E-04	6.674E-04
270	8.108E-05	1.631E-04	3.262E-04	6.524E-04
280	7.913E-05	1.592E-04	3.184E-04	6.368E-04
290	7.666E-05	1.545E-04	3.090E-04	6.180E-04
300	7.487E-05	1.510E-04	3.020E-04	6.039E-04
310	7.291E-05	1.472E-04	2.943E-04	5.886E-04
320	7.064E-05	1.425E-04	2.851E-04	5.702E-04
330	6.853E-05	1.383E-04	2.766E-04	5.533E-04
340	6.638E-05	1.339E-04	2.677E-04	5.354E-04
350	6.357E-05	1.285E-04	2.569E-04	5.139E-04
360	6.169E-05	1.246E-04	2.493E-04	4.985E-04
370	5.852E-05	1.188E-04	2.377E-04	4.754E-04
380	5.587E-05	1.139E-04	2.278E-04	4.557E-04
390	5.395E-05	1.101E-04	2.202E-04	4.404E-04
400	0.000E+00	0.000E+00	0.000E+00	0.000E+00

Photon Energy : 392 eV ; Diameter of target : 25 nm.
(cont.)

z(Gy)	6.740E+03	3.406E+03	1.703E+03	8.516E+02
S(%)	1.4	1.4	1.4	1.4
Hits	3743	3703	3703	3703

PHOTON ENERGY : 525 eV

Number of interactions : 250
Diameter of target : 2.0 nm
Number of infinitely long cylinders hit :14165

FREQUENCY OF ENERGY DEPOSITION GREATER THAN E PER Gy

E	Target cylinder length (nm)			
(eV)	1.0	2.0	4.0	8.0
0	6.095E-07	9.989E-07	1.777E-06	3.417E-06
10	5.359E-07	9.056E-07	1.632E-06	3.150E-06
20	3.390E-07	6.246E-07	1.172E-06	2.291E-06
30	2.475E-07	4.894E-07	9.467E-07	1.864E-06
40	1.599E-07	3.458E-07	6.956E-07	1.389E-06
50	1.110E-07	2.590E-07	5.404E-07	1.087E-06
60	7.585E-08	1.952E-07	4.185E-07	8.480E-07
70	5.006E-08	1.437E-07	3.249E-07	6.622E-07
80	3.437E-08	1.069E-07	2.523E-07	5.212E-07
90	2.286E-08	7.997E-08	1.977E-07	4.124E-07
100	1.473E-08	5.720E-08	1.495E-07	3.184E-07
110	9.264E-09	3.981E-08	1.120E-07	2.451E-07
120	5.857E-09	2.737E-08	8.344E-08	1.882E-07
130	3.616E-09	1.960E-08	6.359E-08	1.449E-07
140	2.690E-09	1.393E-08	4.865E-08	1.176E-07
150	1.584E-09	9.922E-09	3.670E-08	8.941E-08
160	1.106E-09	6.515E-09	2.690E-08	7.005E-08
170	5.080E-10	4.244E-09	1.972E-08	5.355E-08
180	3.287E-10	3.168E-09	1.578E-08	4.136E-08
190	2.988E-11	2.331E-09	1.219E-08	3.251E-08
200	0.000E+00	1.315E-09	9.085E-09	2.415E-08
210	-	9.563E-10	6.694E-09	1.769E-08
220	-	5.379E-10	5.021E-09	1.387E-08
230	-	3.586E-10	3.467E-09	9.802E-09
240	-	2.391E-10	2.391E-09	6.694E-09
250	-	1.195E-10	1.076E-09	4.064E-09
260	-	0.000E+00	9.563E-10	3.586E-09
270	-	-	5.977E-10	3.108E-09
280	-	-	1.195E-10	2.391E-09
290	-	-	1.195E-10	1.913E-09
300	-	-	0.000E+00	1.434E-09
z(Gy)	1.594E+06	9.728E+05	5.469E+05	2.843E+05
S(%)	2.8	2.8	2.8	2.9
Hits	20394	16712	14863	14294

PHOTON ENERGY : 525 eV

Number of interactions : 250
Diameter of target : 10.0 nm
Number of infinitely long cylinders hit : 3713

Photon Energy : 525 eV ; Diameter of target : 10 nm.
(cont.)

PHOTON ENERGY : 525 eV

Number of interactions : 250
Diameter of target : 25.0 nm
Number of infinitely long cylinders hit : 2108

FREQUENCY OF ENERGY DEPOSITION GREATER THAN E PER Gy

E	Target cylinder length (nm)			
(eV)	5.0	10.0	20.0	40.0
0	1.812E-05	2.935E-05	5.549E-05	1.110E-04
10	1.773E-05	2.883E-05	5.470E-05	1.094E-04
20	1.592E-05	2.639E-05	5.037E-05	1.007E-04
30	1.509E-05	2.525E-05	4.839E-05	9.679E-05
40	1.377E-05	2.340E-05	4.503E-05	9.006E-05
50	1.298E-05	2.231E-05	4.294E-05	8.588E-05
60	1.223E-05	2.136E-05	4.114E-05	8.229E-05
70	1.156E-05	2.048E-05	3.956E-05	7.912E-05
80	1.084E-05	1.953E-05	3.789E-05	7.577E-05
90	1.021E-05	1.870E-05	3.629E-05	7.257E-05
100	9.617E-06	1.793E-05	3.487E-05	6.973E-05
110	8.971E-06	1.699E-05	3.319E-05	6.639E-05
120	8.369E-06	1.613E-05	3.162E-05	6.325E-05
130	7.749E-06	1.517E-05	2.986E-05	5.972E-05
140	7.192E-06	1.422E-05	2.813E-05	5.625E-05
150	6.688E-06	1.342E-05	2.660E-05	5.321E-05
160	6.154E-06	1.267E-05	2.518E-05	5.037E-05
170	5.717E-06	1.202E-05	2.397E-05	4.794E-05
180	5.354E-06	1.155E-05	2.309E-05	4.618E-05
190	4.958E-06	1.089E-05	2.184E-05	4.367E-05
200	4.547E-06	1.024E-05	2.064E-05	4.128E-05
210	4.192E-06	9.699E-06	1.964E-05	3.928E-05
220	3.841E-06	9.176E-06	1.864E-05	3.727E-05
230	3.505E-06	8.594E-06	1.752E-05	3.503E-05
240	3.109E-06	7.876E-06	1.610E-05	3.219E-05
250	2.810E-06	7.361E-06	1.517E-05	3.034E-05
260	2.511E-06	6.912E-06	1.438E-05	2.875E-05
270	2.290E-06	6.382E-06	1.342E-05	2.684E-05
280	2.033E-06	5.836E-06	1.242E-05	2.484E-05
290	1.846E-06	5.418E-06	1.170E-05	2.340E-05
300	1.629E-06	4.977E-06	1.078E-05	2.155E-05
310	1.465E-06	4.573E-06	1.001E-05	2.003E-05
320	1.326E-06	4.222E-06	9.296E-06	1.859E-05
330	1.151E-06	3.856E-06	8.683E-06	1.737E-05
340	1.039E-06	3.535E-06	8.011E-06	1.602E-05
350	9.079E-07	3.280E-06	7.517E-06	1.503E-05
360	7.884E-07	3.004E-06	7.009E-06	1.402E-05
370	6.950E-07	2.735E-06	6.352E-06	1.270E-05
380	6.090E-07	2.451E-06	5.754E-06	1.151E-05
390	5.306E-07	2.189E-06	5.216E-06	1.043E-05
400	4.596E-07	1.928E-06	4.708E-06	9.416E-06
410	4.147E-07	1.756E-06	4.364E-06	8.728E-06
420	3.624E-07	1.539E-06	3.871E-06	7.742E-06
430	2.989E-07	1.412E-06	3.602E-06	7.204E-06
440	2.578E-07	1.278E-06	3.288E-06	6.576E-06
450	2.242E-07	1.151E-06	2.974E-06	5.948E-06
460	1.868E-07	9.640E-07	2.496E-06	4.992E-06
470	1.532E-07	7.921E-07	2.152E-06	4.304E-06
480	1.233E-07	6.576E-07	1.793E-06	3.587E-06
490	1.046E-07	5.604E-07	1.524E-06	3.049E-06
z(Gy)	5.480E+04	3.383E+04	1.789E+04	8.945E+03
S(%)	0.7	0.7	0.7	0.6
Hits	4849	3927	3713	3713

FREQUENCY OF ENERGY DEPOSITION GREATER THAN E PER Gy

E	Target cylinder length (nm)			
(eV)	12.5	25.0	50.0	100.0
0	1.319E-04	2.463E-04	4.923E-04	9.845E-04
20	1.244E-04	2.340E-04	4.677E-04	9.355E-04
40	1.175E-04	2.223E-04	4.444E-04	8.888E-04
60	1.118E-04	2.132E-04	4.262E-04	8.524E-04
80	1.068E-04	2.050E-04	4.101E-04	8.201E-04
100	1.019E-04	1.965E-04	3.930E-04	7.860E-04
120	9.715E-05	1.888E-04	3.776E-04	7.552E-04
140	9.248E-05	1.809E-04	3.617E-04	7.235E-04
160	8.874E-05	1.740E-04	3.480E-04	6.959E-04
180	8.489E-05	1.670E-04	3.339E-04	6.679E-04
200	8.103E-05	1.604E-04	3.209E-04	6.417E-04
220	7.718E-05	1.533E-04	3.066E-04	6.132E-04
240	7.333E-05	1.465E-04	2.931E-04	5.861E-04
260	6.918E-05	1.391E-04	2.781E-04	5.563E-04
280	6.545E-05	1.329E-04	2.658E-04	5.315E-04
300	6.229E-05	1.273E-04	2.545E-04	5.091E-04
320	5.838E-05	1.204E-04	2.408E-04	4.815E-04
340	5.470E-05	1.138E-04	2.277E-04	4.554E-04
360	5.190E-05	1.089E-04	2.179E-04	4.358E-04
380	4.840E-05	1.026E-04	2.053E-04	4.105E-04
400	4.525E-05	9.761E-05	1.952E-04	3.905E-04
420	4.209E-05	9.166E-05	1.836E-04	3.671E-04
440	3.929E-05	8.699E-05	1.742E-04	3.484E-04
460	3.579E-05	8.057E-05	1.614E-04	3.227E-04
480	3.252E-05	7.391E-05	1.478E-04	2.956E-04
500	2.867E-05	6.632E-05	1.326E-04	2.653E-04
520	2.563E-05	6.048E-05	1.210E-04	2.419E-04
540	0.000E+00	0.000E+00	0.000E+00	0.000E+00
z(Gy)	7.430E+03	3.981E+03	1.991E+03	9.957E+02
S(%)	2.0	1.9	2.0	2.0
Hits	2260	2109	2108	2108

PHOTON ENERGY : 677 eV

Number of interactions : 150
Diameter of target : 2.0 nm
Number of infinitely long cylinders hit :10215

FREQUENCY OF ENERGY DEPOSITION GREATER THAN E PER Gy

E	Target cylinder length (nm)			
(eV)	1.0	2.0	4.0	8.0
0	6.002E-07	9.625E-07	1.676E-06	3.194E-06
10	5.252E-07	8.671E-07	1.532E-06	2.927E-06
20	3.319E-07	5.981E-07	1.111E-06	2.156E-06
30	2.413E-07	4.704E-07	9.021E-07	1.763E-06
40	1.751E-07	3.677E-07	7.241E-07	1.430E-06
50	1.256E-07	2.835E-07	5.809E-07	1.157E-06
60	8.988E-08	2.212E-07	4.746E-07	9.517E-07
70	6.454E-08	1.700E-07	3.791E-07	7.703E-07
80	4.588E-08	1.356E-07	3.118E-07	6.399E-07
90	3.171E-08	1.030E-07	2.517E-07	5.228E-07
100	2.171E-08	7.779E-08	1.967E-07	4.184E-07
110	1.487E-08	5.994E-08	1.585E-07	3.402E-07
120	1.008E-08	4.473E-08	1.270E-07	2.781E-07
130	6.141E-09	3.159E-08	9.733E-08	2.219E-07
140	4.094E-09	2.356E-08	7.416E-08	1.730E-07
150	2.704E-09	1.607E-08	5.438E-08	1.310E-07
160	1.970E-09	1.105E-08	3.893E-08	9.764E-08
170	1.545E-09	8.729E-09	2.982E-08	7.941E-08
180	1.159E-09	6.334E-09	2.379E-08	6.396E-08
190	6.566E-10	4.403E-09	1.808E-08	5.098E-08
200	3.476E-10	2.781E-09	1.313E-08	3.801E-08
210	1.545E-10	1.390E-09	8.806E-09	2.750E-08
220	3.862E-11	1.004E-09	6.798E-09	2.194E-08
230	0.000E+00	3.090E-10	4.944E-09	1.669E-08
240	-	2.317E-10	3.090E-09	1.236E-08
250	-	1.545E-10	2.008E-09	9.270E-09
260	-	0.000E+00	1.236E-09	8.034E-09
270	-	-	6.180E-10	5.871E-09
280	-	-	3.090E-10	4.635E-09
290	-	-	3.090E-10	3.708E-09
300	-	-	3.090E-10	3.090E-09
310	-	-	3.090E-10	3.090E-09
320	-	-	3.090E-10	2.472E-09
330	-	-	3.090E-10	1.854E-09
340	-	-	3.090E-10	1.545E-09
350	-	-	3.090E-10	1.545E-09
z(Gy)	1.684E+06	1.050E+06	6.028E+05	3.164E+05
S(%)	1.1	1.1	1.0	1.1
Hits	15539	12460	10851	10336

PHOTON ENERGY : 677 eV

Number of interactions : 250
Diameter of target : 10.0 nm
Number of infinitely long cylinders hit : 4015

FREQUENCY OF ENERGY DEPOSITION GREATER THAN E PER Gy

E	Target cylinder length (nm)			
(eV)	5.0	10.0	20.0	40.0
0	1.562E-05	2.483E-05	4.665E-05	9.307E-05
10	1.515E-05	2.424E-05	4.570E-05	9.117E-05
20	1.341E-05	2.194E-05	4.156E-05	8.294E-05
30	1.261E-05	2.086E-05	3.963E-05	7.907E-05
40	1.197E-05	2.003E-05	3.817E-05	7.617E-05
50	1.138E-05	1.927E-05	3.684E-05	7.353E-05
60	1.083E-05	1.860E-05	3.560E-05	7.109E-05
70	1.033E-05	1.792E-05	3.446E-05	6.882E-05
80	9.877E-06	1.743E-05	3.354E-05	6.699E-05
90	9.434E-06	1.687E-05	3.247E-05	6.488E-05
100	9.028E-06	1.636E-05	3.158E-05	6.309E-05
110	8.623E-06	1.591E-05	3.081E-05	6.156E-05
120	8.177E-06	1.532E-05	2.979E-05	5.953E-05
130	7.800E-06	1.469E-05	2.873E-05	5.742E-05
140	7.441E-06	1.423E-05	2.787E-05	5.570E-05
150	7.026E-06	1.364E-05	2.673E-05	5.341E-05
160	6.647E-06	1.309E-05	2.569E-05	5.134E-05
170	6.253E-06	1.252E-05	2.466E-05	4.930E-05
180	5.621E-06	1.158E-05	2.291E-05	4.583E-05
190	5.204E-06	1.095E-05	2.172E-05	4.344E-05
200	4.816E-06	1.037E-05	2.063E-05	4.124E-05
210	4.442E-06	9.857E-06	1.974E-05	3.945E-05
220	4.088E-06	9.243E-06	1.864E-05	3.725E-05
230	3.665E-06	8.513E-06	1.733E-05	3.465E-05
240	3.410E-06	8.101E-06	1.652E-05	3.301E-05
250	3.106E-06	7.643E-06	1.567E-05	3.134E-05
260	2.837E-06	7.174E-06	1.471E-05	2.941E-05
270	2.585E-06	6.676E-06	1.378E-05	2.756E-05
280	2.361E-06	6.270E-06	1.295E-05	2.587E-05
290	2.147E-06	5.835E-06	1.215E-05	2.427E-05
300	1.962E-06	5.540E-06	1.160E-05	2.318E-05
310	1.741E-06	5.111E-06	1.084E-05	2.165E-05
320	1.565E-06	4.682E-06	1.003E-05	2.003E-05
330	1.405E-06	4.329E-06	9.341E-06	1.866E-05
340	1.249E-06	3.998E-06	8.704E-06	1.743E-05
350	1.130E-06	3.691E-06	8.136E-06	1.634E-05
360	1.046E-06	3.494E-06	7.788E-06	1.565E-05
370	9.504E-07	3.280E-06	7.336E-06	1.474E-05
380	8.345E-07	2.950E-06	6.722E-06	1.351E-05
390	7.359E-07	2.712E-06	6.293E-06	1.266E-05
400	6.548E-07	2.486E-06	5.841E-06	1.175E-05
410	5.795E-07	2.254E-06	5.285E-06	1.064E-05
420	5.157E-07	2.057E-06	4.914E-06	9.898E-06

Photon Energy : 677 eV ; Diameter of target : 10 nm. (cont.)

FREQUENCY OF ENERGY DEPOSITION GREATER THAN E PER Gy

E	Target cylinder length (nm)			
(eV)	5.0	10.0	20.0	40.0
430	4.404E-07	1.831E-06	4.439E-06	8.924E-06
440	3.912E-07	1.681E-06	4.080E-06	8.206E-06
450	3.448E-07	1.541E-06	3.767E-06	7.580E-06
460	3.100E-07	1.397E-06	3.442E-06	6.954E-06
470	2.724E-07	1.286E-06	3.187E-06	6.444E-06
480	2.260E-07	1.165E-06	2.921E-06	5.911E-06
490	1.999E-07	1.072E-06	2.724E-06	5.517E-06
500	1.767E-07	9.504E-07	2.480E-06	5.030E-06
510	1.652E-07	8.403E-07	2.225E-06	4.520E-06
520	1.507E-07	7.765E-07	2.063E-06	4.172E-06
530	1.478E-07	7.533E-07	2.028E-06	4.103E-06
540	1.304E-07	6.490E-07	1.773E-06	3.593E-06
550	1.159E-07	6.027E-07	1.669E-06	3.384E-06
560	1.101E-07	5.621E-06	1.565E-06	3.176E-06
570	1.014E-07	5.042E-07	1.449E-06	2.944E-06
580	8.982E-08	4.752E-07	1.333E-06	2.712E-06
590	8.403E-08	4.172E-07	1.240E-06	2.527E-06
600	6.954E-08	3.651E-07	1.078E-06	2.179E-06
610	5.795E-08	3.245E-07	9.851E-07	1.993E-06
620	4.056E-08	2.839E-07	8.461E-07	1.762E-06
630	3.767E-08	2.666E-07	7.881E-07	1.646E-06
640	3.477E-08	2.202E-07	6.954E-07	1.460E-06
650	3.477E-08	1.738E-07	5.679E-07	1.205E-06
660	2.028E-08	1.101E-07	4.056E-07	9.040E-07
670	1.449E-08	6.374E-08	2.434E-07	5.331E-07
680	0.000E+00	0.000E+00	0.000E+00	0.000E+00
690	-	-	-	-
700	-	-	-	-
z(Gy)	6.163E+04	3.877E+04	2.064E+04	1.034E+04
S(%)	3.7	3.7	3.7	3.8
Hits	5391	4285	4025	4015

PHOTON ENERGY : 677 eV

Number of interactions : 250
Diameter of target : 25.0 nm
Number of infinitely long cylinders hit : 2190

Photon Energy : 677 eV ; Diameter of target : 25 nm.
(cont.)

FREQUENCY OF ENERGY DEPOSITION GREATER THAN E PER Gy

E	Target cylinder length (nm)			
(eV)	12.5	25.0	50.0	100.0
0	1.079E-04	1.987E-04	3.966E-04	7.932E-04
10	1.072E-04	1.977E-04	3.946E-04	7.892E-04
20	1.021E-04	1.895E-04	3.783E-04	7.566E-04
30	9.983E-05	1.860E-04	3.712E-04	7.425E-04
40	9.734E-05	1.821E-04	3.635E-04	7.269E-04
50	9.557E-05	1.789E-04	3.571E-04	7.142E-04
60	9.462E-05	1.773E-04	3.539E-04	7.077E-04
70	9.322E-05	1.750E-04	3.493E-04	6.987E-04
80	9.186E-05	1.728E-04	3.448E-04	6.896E-04
90	9.041E-05	1.705E-04	3.403E-04	6.805E-04
100	8.905E-05	1.681E-04	3.356E-04	6.711E-04
110	8.747E-05	1.656E-04	3.307E-04	6.614E-04
120	8.625E-05	1.636E-04	3.267E-04	6.534E-04
130	8.525E-05	1.620E-04	3.234E-04	6.469E-04
140	8.389E-05	1.598E-04	3.191E-04	6.382E-04
150	8.244E-05	1.573E-04	3.140E-04	6.280E-04
160	8.113E-05	1.554E-04	3.102E-04	6.204E-04
170	7.968E-05	1.532E-04	3.059E-04	6.117E-04
180	7.706E-05	1.491E-04	2.977E-04	5.954E-04
190	7.574E-05	1.468E-04	2.930E-04	5.860E-04
200	7.411E-05	1.441E-04	2.876E-04	5.752E-04
210	7.198E-05	1.403E-04	2.803E-04	5.607E-04
220	6.986E-05	1.366E-04	2.731E-04	5.462E-04
230	6.741E-05	1.327E-04	2.651E-04	5.302E-04
240	6.583E-05	1.297E-04	2.591E-04	5.183E-04
250	6.438E-05	1.271E-04	2.541E-04	5.081E-04
260	6.261E-05	1.242E-04	2.483E-04	4.966E-04
270	6.094E-05	1.216E-04	2.430E-04	4.861E-04
280	5.949E-05	1.192E-04	2.381E-04	4.763E-04
290	5.813E-05	1.168E-04	2.336E-04	4.672E-04
300	5.664E-05	1.145E-04	2.289E-04	4.578E-04
310	5.523E-05	1.122E-04	2.244E-04	4.487E-04
320	5.320E-05	1.086E-04	2.171E-04	4.343E-04
330	5.184E-05	1.064E-04	2.128E-04	4.256E-04
340	5.057E-05	1.042E-04	2.084E-04	4.169E-04
350	4.917E-05	1.015E-04	2.030E-04	4.060E-04
360	4.767E-05	9.906E-05	1.981E-04	3.962E-04
370	4.677E-05	9.734E-05	1.947E-04	3.894E-04
380	4.545E-05	9.535E-05	1.907E-04	3.814E-04
390	4.428E-05	9.281E-05	1.858E-04	3.716E-04
400	4.269E-05	8.991E-05	1.800E-04	3.600E-04
410	4.111E-05	8.683E-05	1.740E-04	3.481E-04
420	3.993E-05	8.466E-05	1.697E-04	3.394E-04

FREQUENCY OF ENERGY DEPOSITION GREATER THAN E PER Gy

E	Target cylinder length (nm)			
(eV)	12.5	25.0	50.0	100.0
430	3.907E-05	8.339E-05	1.671E-04	3.343E-04
440	3.817E-05	8.194E-05	1.643E-04	3.285E-04
450	3.685E-05	7.914E-05	1.586E-04	3.173E-04
460	3.531E-05	7.615E-05	1.527E-04	3.053E-04
470	3.405E-05	7.371E-05	1.480E-04	2.959E-04
480	3.246E-05	7.063E-05	1.418E-04	2.836E-04
490	3.156E-05	6.891E-05	1.384E-04	2.767E-04
500	3.024E-05	6.655E-05	1.336E-04	2.673E-04
510	2.843E-05	6.329E-05	1.271E-04	2.543E-04
520	2.775E-05	6.193E-05	1.244E-04	2.488E-04
530	2.707E-05	6.085E-05	1.222E-04	2.445E-04
540	2.648E-05	5.985E-05	1.202E-04	2.405E-04
550	2.594E-05	5.895E-05	1.184E-04	2.369E-04
560	2.540E-05	5.795E-05	1.164E-05	2.329E-04
570	2.476E-05	5.650E-05	1.135E-04	2.271E-04
580	2.399E-05	5.514E-05	1.110E-04	2.220E-04
590	2.304E-05	5.388E-05	1.085E-04	2.169E-04
600	2.241E-05	5.252E-05	1.058E-04	2.115E-04
610	2.146E-05	5.043E-05	1.014E-04	2.028E-04
620	2.055E-05	4.871E-05	9.797E-05	1.959E-04
630	1.978E-05	4.717E-05	9.489E-05	1.898E-04
640	1.906E-05	4.600E-05	9.254E-05	1.851E-04
650	1.815E-05	4.428E-05	8.910E-05	1.782E-04
660	1.725E-05	4.229E-05	8.511E-05	1.702E-04
670	1.557E-05	3.884E-05	7.823E-05	1.565E-04
680	0.000E+00	0.000E+00	0.000E+00	0.000E+00
690	-	-	-	-
700	-	-	-	-
z(Gy)	8.958E+03	4.865E+03	2.437E+03	1.218E+03
S(%)	3.3	3.3	3.3	3.4
Hits	2383	2194	2190	2190

PHOTON ENERGY : 1041 eV

Number of interactions : 100
Diameter of target : 2.0 nm
Number of infinitely long cylinders hit :10378

FREQUENCY OF ENERGY DEPOSITION GREATER THAN E PER Gy

E	Target cylinder length (nm)			
(eV)	1.0	2.0	4.0	8.0
0	6.100E-07	9.827E-07	1.713E-06	3.211E-06
10	5.346E-07	8.875E-07	1.570E-06	2.960E-06
20	3.341E-07	6.070E-07	1.130E-06	2.176E-06
30	2.423E-07	4.729E-07	9.100E-07	1.769E-06
40	1.671E-07	3.588E-07	7.142E-07	1.410E-06
50	1.187E-07	2.790E-07	5.719E-07	1.143E-06
60	8.052E-08	2.082E-07	4.467E-07	9.094E-07
70	5.572E-08	1.576E-07	3.599E-07	7.466E-07
80	3.809E-08	1.182E-07	2.833E-07	5.974E-07
90	2.664E-08	8.816E-08	2.223E-07	4.759E-07
100	1.929E-08	6.676E-08	1.762E-07	3.819E-07
110	1.285E-08	5.019E-08	1.396E-07	3.123E-07
120	8.515E-09	3.805E-08	1.099E-07	2.523E-07
130	5.539E-09	2.833E-08	8.379E-08	1.953E-07
140	3.504E-09	2.133E-08	6.526E-08	1.564E-07
150	2.148E-09	1.387E-08	4.687E-08	1.191E-07
160	1.206E-09	9.118E-09	3.451E-08	9.374E-08
170	8.666E-10	6.104E-09	2.668E-08	7.566E-08
180	4.898E-10	4.220E-09	1.929E-08	5.817E-08
190	3.768E-10	2.562E-09	1.402E-08	4.401E-08
200	1.884E-10	1.281E-09	9.344E-09	3.255E-08
210	1.130E-10	1.055E-09	6.933E-09	2.592E-08
220	1.130E-10	8.289E-10	5.878E-09	2.050E-08
230	1.130E-10	6.028E-10	4.672E-09	1.658E-08
240	3.768E-11	5.275E-10	3.617E-09	1.417E-08
250	0.000E+00	3.014E-10	2.863E-09	1.115E-08
260	-	7.535E-11	1.507E-09	6.631E-09
270	-	0.000E+00	1.055E-09	5.124E-09
280	-	-	1.055E-09	4.220E-09
290	-	-	1.055E-09	3.014E-09
300	-	-	7.535E-10	2.411E-09
310	-	-	6.028E-10	1.809E-09
320	-	-	1.507E-10	1.507E-09
330	-	-	0.000E+00	6.028E-10
340	-	-	-	0.000E+00
350	-	-	-	-
z(Gy)	1.627E+06	1.010E+06	5.794E+05	3.091E+05
S(%)	0.8	0.7	0.7	0.7
Hits	16189	13041	11366	10653

PHOTON ENERGY : 1041 eV

Number of interactions : 200
Diameter of target : 10.0 nm
Number of infinitely long cylinders hit : 4343

FREQUENCY OF ENERGY DEPOSITION GREATER THAN E PER Gy

E	Target cylinder length (nm)			
(eV)	5.0	10.0	20.0	40.0
0	1.574E-05	2.329E-05	4.110E-05	8.169E-05
10	1.530E-05	2.281E-05	4.040E-05	8.035E-05
20	1.369E-05	2.088E-05	3.730E-05	7.424E-05
30	1.297E-05	2.003E-05	3.580E-05	7.128E-05
40	1.220E-05	1.913E-05	3.429E-05	6.827E-05
50	1.159E-05	1.843E-05	3.314E-05	6.597E-05
60	1.109E-05	1.784E-05	3.223E-05	6.418E-05
70	1.051E-05	1.717E-05	3.114E-05	6.201E-05
80	9.940E-06	1.656E-05	3.014E-05	6.005E-05
90	9.419E-06	1.598E-05	2.923E-05	5.824E-05
100	8.915E-06	1.536E-05	2.813E-05	5.610E-05
110	8.397E-06	1.475E-05	2.713E-05	5.412E-05
120	7.931E-06	1.423E-05	2.631E-05	5.246E-05
130	7.445E-06	1.364E-05	2.531E-05	5.048E-05
140	7.012E-06	1.314E-05	2.453E-05	4.897E-05
150	6.635E-06	1.264E-05	2.372E-05	4.735E-05
160	6.211E-06	1.214E-05	2.286E-05	4.566E-05
170	5.825E-06	1.161E-05	2.197E-05	4.389E-05
180	5.453E-06	1.112E-05	2.124E-05	4.243E-05
190	5.092E-06	1.062E-05	2.050E-05	4.095E-05
200	4.774E-06	1.015E-05	1.977E-05	3.948E-05
210	4.463E-06	9.733E-06	1.914E-05	3.823E-05
220	4.127E-06	9.299E-06	1.844E-05	3.686E-05
230	3.853E-06	8.899E-06	1.777E-05	3.554E-05
240	3.568E-06	8.484E-06	1.706E-05	3.413E-05
250	3.309E-06	8.079E-06	1.643E-05	3.286E-05
260	3.076E-06	7.735E-06	1.577E-05	3.154E-05
270	2.878E-06	7.481E-06	1.537E-05	3.075E-05
280	2.652E-06	7.151E-06	1.483E-05	2.968E-05
290	2.412E-06	6.718E-06	1.405E-05	2.813E-05
300	2.256E-06	6.378E-06	1.346E-05	2.698E-05
310	2.092E-06	6.016E-06	1.288E-05	2.580E-05
320	1.906E-06	5.648E-06	1.226E-05	2.457E-05
330	1.748E-06	5.309E-06	1.168E-05	2.340E-05
340	1.606E-06	4.923E-06	1.108E-05	2.222E-05
350	1.467E-06	4.598E-06	1.048E-05	2.095E-05
360	1.345E-06	4.287E-06	9.977E-06	1.995E-05
370	1.199E-06	3.990E-06	9.412E-06	1.884E-05
380	1.098E-06	3.764E-06	9.007E-06	1.801E-05
390	1.008E-06	3.547E-06	8.621E-06	1.724E-05
400	9.045E-07	3.293E-06	8.084E-06	1.617E-05
410	8.126E-07	3.057E-06	7.584E-06	1.517E-05
420	7.537E-07	2.836E-06	7.113E-06	1.425E-05

Photon Energy : 1041 eV ; Diameter of target : 10 nm.
(cont.)

FREQUENCY OF ENERGY DEPOSITION GREATER THAN E PER Gy

E	Target cylinder length (nm)			
(eV)	5.0	10.0	20.0	40.0
430	6.901E-07	2.680E-06	6.727E-06	1.345E-05
440	6.195E-07	2.483E-06	6.331E-06	1.268E-05
450	5.559E-07	2.341E-06	6.039E-06	1.210E-05
460	5.205E-07	2.195E-06	5.785E-06	1.159E-05
470	4.569E-07	2.044E-06	5.427E-06	1.085E-05
480	4.169E-07	1.913E-06	5.107E-06	1.025E-05
490	3.886E-07	1.767E-06	4.767E-06	9.572E-06
500	3.368E-07	1.597E-06	4.372E-06	8.781E-06
510	3.062E-07	1.484E-06	4.136E-06	8.310E-06
520	2.921E-07	1.409E-06	3.919E-06	7.876E-06
530	2.662E-07	1.338E-06	3.693E-06	7.424E-06
540	2.426E-07	1.215E-06	3.429E-06	6.859E-06
550	2.308E-07	1.126E-06	3.232E-06	6.463E-06
560	2.073E-07	1.065E-06	3.053E-06	6.143E-06
570	1.884E-07	9.940E-07	2.883E-06	5.785E-06
580	1.696E-07	9.280E-07	2.742E-06	5.483E-06
590	1.531E-07	8.527E-07	2.600E-06	5.201E-06
600	1.437E-07	8.103E-07	2.412E-06	4.824E-06
610	1.343E-07	7.490E-07	2.214E-06	4.447E-06
620	1.178E-07	6.689E-07	2.026E-06	4.051E-06
630	1.060E-07	6.171E-07	1.903E-06	3.806E-06
640	1.036E-07	5.700E-07	1.818E-06	3.637E-06
650	9.422E-08	5.512E-07	1.696E-06	3.392E-06
660	8.244E-08	4.899E-07	1.555E-06	3.109E-06
670	7.537E-08	4.758E-07	1.498E-06	2.996E-06
680	7.066E-08	4.098E-07	1.338E-06	2.657E-06
690	6.360E-08	3.863E-07	1.234E-06	2.468E-06
700	6.360E-08	3.486E-07	1.121E-06	2.242E-06
710	5.653E-08	3.298E-07	1.046E-06	2.092E-06
720	5.182E-08	3.062E-07	9.704E-07	1.922E-06
730	4.240E-08	2.874E-07	8.951E-07	1.771E-06
740	4.240E-08	2.685E-07	8.668E-07	1.715E-06
750	3.769E-08	2.544E-07	8.103E-07	1.602E-06
z(Gy)	6.330E+04	4.277E+04	2.420E+04	1.217E+04
S(%)	0.4	0.4	0.5	0.6
Hits	6681	4944	4368	4343

PHOTON ENERGY : 1041 eV

Number of interactions : 200
Diameter of target : 25.0 mm
Number of infinitely long cylinders hit : 2170

FREQUENCY OF ENERGY DEPOSITION GREATER THAN E PER Gy

E	Target cylinder length (mm)			
(eV)	12.5	25.0	50.0	100.0
0	9.160E-05	1.428E-04	2.840E-04	5.680E-04
10	9.068E-05	1.415E-04	2.813E-04	5.627E-04
20	8.590E-05	1.353E-04	2.690E-04	5.379E-04
30	8.377E-05	1.320E-04	2.623E-04	5.247E-04
40	8.115E-05	1.285E-04	2.554E-04	5.108E-04
50	7.931E-05	1.260E-04	2.504E-04	5.008E-04
60	7.740E-05	1.240E-04	2.467E-04	4.935E-04
70	7.593E-05	1.223E-04	2.432E-04	4.864E-04
80	7.479E-05	1.209E-04	2.405E-04	4.811E-04
90	7.361E-05	1.190E-04	2.369E-04	4.737E-04
100	7.210E-05	1.169E-04	2.326E-04	4.652E-04
110	7.059E-05	1.150E-04	2.289E-04	4.578E-04
120	6.938E-05	1.134E-04	2.260E-04	4.519E-04
130	6.772E-05	1.109E-04	2.210E-04	4.419E-04
140	6.673E-05	1.093E-04	2.177E-04	4.355E-04
150	6.533E-05	1.073E-04	2.138E-04	4.275E-04
160	6.367E-05	1.050E-04	2.092E-04	4.184E-04
170	6.231E-05	1.029E-04	2.049E-04	4.098E-04
180	6.139E-05	1.012E-04	2.015E-04	4.031E-04
190	5.995E-05	9.937E-05	1.979E-04	3.957E-04
200	5.885E-05	9.812E-05	1.954E-04	3.907E-04
210	5.716E-05	9.613E-05	1.915E-04	3.831E-04
220	5.579E-05	9.429E-05	1.878E-04	3.757E-04
230	5.458E-05	9.267E-05	1.846E-04	3.692E-04
240	5.362E-05	9.127E-05	1.818E-04	3.636E-04
250	5.237E-05	8.929E-05	1.778E-04	3.557E-04
260	5.145E-05	8.774E-05	1.749E-04	3.498E-04
270	5.024E-05	8.619E-05	1.718E-04	3.436E-04
280	4.928E-05	8.480E-05	1.690E-04	3.380E-04
290	4.840E-05	8.332E-05	1.661E-04	3.321E-04
300	4.704E-05	8.148E-05	1.624E-04	3.248E-04
310	4.600E-05	7.986E-05	1.591E-04	3.183E-04
320	4.468E-05	7.817E-05	1.558E-04	3.115E-04
330	4.317E-05	7.655E-05	1.525E-04	3.050E-04
340	4.177E-05	7.427E-05	1.480E-04	2.959E-04
350	4.096E-05	7.309E-05	1.456E-04	2.912E-04
360	3.971E-05	7.147E-05	1.424E-04	2.847E-04
370	3.842E-05	6.941E-05	1.382E-04	2.765E-04
380	3.747E-05	6.779E-05	1.350E-04	2.700E-04
390	3.666E-05	6.691E-05	1.332E-04	2.665E-04
400	3.544E-05	6.485E-05	1.291E-04	2.582E-04
410	3.460E-05	6.316E-05	1.257E-04	2.514E-04
420	3.360E-05	6.168E-05	1.228E-04	2.456E-04

FREQUENCY OF ENERGY DEPOSITION GREATER THAN E PER Gy

E	Target cylinder length (mm)			
(eV)	12.5	25.0	50.0	100.0
430	3.283E-05	6.051E-05	1.204E-04	2.408E-04
440	3.206E-05	5.933E-05	1.181E-04	2.361E-04
450	3.106E-05	5.771E-05	1.148E-04	2.297E-04
460	3.014E-05	5.602E-05	1.114E-04	2.229E-04
470	2.930E-05	5.447E-05	1.084E-04	2.167E-04
480	2.856E-05	5.300E-05	1.054E-04	2.108E-04
490	2.742E-05	5.108E-05	1.016E-04	2.032E-04
500	2.679E-05	4.969E-05	9.878E-05	1.976E-04
510	2.562E-05	4.792E-05	9.525E-05	1.905E-04
520	2.506E-05	4.674E-05	9.289E-05	1.858E-04
530	2.444E-05	4.600E-05	9.142E-05	1.828E-04
540	2.337E-05	4.387E-05	8.715E-05	1.743E-04
550	2.249E-05	4.291E-05	8.524E-05	1.705E-04
560	2.190E-05	4.196E-05	8.332E-05	1.666E-04
570	2.124E-05	4.063E-05	8.067E-05	1.613E-04
580	2.043E-05	3.923E-05	7.788E-05	1.558E-04
590	1.973E-05	3.857E-05	7.655E-05	1.531E-04
600	1.929E-05	3.798E-05	7.537E-05	1.507E-04
610	1.859E-05	3.695E-05	7.331E-05	1.466E-04
620	1.803E-05	3.614E-05	7.169E-05	1.434E-04
630	1.744E-05	3.489E-05	6.934E-05	1.387E-04
640	1.675E-05	3.379E-05	6.713E-05	1.343E-04
650	1.612E-05	3.231E-05	6.419E-05	1.284E-04
660	1.546E-05	3.150E-05	6.257E-05	1.251E-04
670	1.450E-05	2.974E-05	5.903E-05	1.181E-04
680	1.376E-05	2.863E-05	5.682E-05	1.136E-04
690	1.325E-05	2.753E-05	5.462E-05	1.092E-04
700	1.237E-05	2.635E-05	5.226E-05	1.045E-04
710	1.211E-05	2.598E-05	5.153E-05	1.031E-04
720	1.163E-05	2.473E-05	4.902E-05	9.805E-05
730	1.111E-05	2.341E-05	4.637E-05	9.275E-05
740	1.038E-05	2.260E-05	4.475E-05	8.951E-05
750	9.974E-06	2.164E-05	4.284E-05	8.568E-05
760	9.459E-06	2.054E-05	4.063E-05	8.126E-05
770	8.980E-06	1.929E-05	3.828E-05	7.655E-05
780	8.722E-06	1.862E-05	3.710E-05	7.420E-05
790	8.060E-06	1.693E-05	3.371E-05	6.742E-05
800	7.729E-06	1.605E-05	3.195E-05	6.389E-05
810	7.140E-06	1.494E-05	2.974E-05	5.947E-05
820	6.735E-06	1.421E-05	2.827E-05	5.653E-05
830	6.109E-06	1.310E-05	2.606E-05	5.211E-05
840	5.521E-06	1.222E-05	2.429E-05	4.858E-05
850	5.153E-06	1.148E-05	2.282E-05	4.564E-05

FREQUENCY OF ENERGY DEPOSITION GREATER THAN E PER Gy

E	Target cylinder length (mm)			
(eV)	12.5	25.0	50.0	100.0
860	4.637E-06	1.067E-05	2.120E-05	4.240E-05
870	4.343E-06	9.937E-06	1.973E-05	3.945E-05
880	4.012E-06	9.054E-06	1.781E-05	3.563E-05
890	3.460E-06	8.170E-06	1.605E-05	3.209E-05
900	3.276E-06	7.729E-06	1.516E-05	3.033E-05
910	2.834E-06	6.551E-06	1.266E-05	2.532E-05
920	2.539E-06	5.889E-06	1.134E-05	2.267E-05
930	2.245E-06	5.226E-06	1.016E-05	2.032E-05
940	1.803E-06	4.564E-06	8.833E-06	1.767E-05
950	1.693E-06	4.048E-06	7.802E-06	1.560E-05
960	1.435E-06	3.460E-06	6.625E-06	1.325E-05
970	9.937E-07	2.797E-06	5.300E-06	1.060E-05
980	5.521E-07	2.135E-06	3.975E-06	7.950E-06
990	2.576E-07	8.833E-07	1.767E-06	3.533E-06

z(Gy)	1.051E+04	6.738E+03	3.383E+03	1.689E+03
S(%)	3.7	3.8	3.9	4.0
Hits	2616	2177	2170	2170

PHOTON ENERGY : 1254 eV

Number of interactions : 100
Diameter of target : 2.0 nm
Number of infinitely long cylinders hit : 13346

FREQUENCY OF ENERGY DEPOSITION GREATER THAN E PER Gy

E	Target cylinder length (nm)			
(eV)	1.0	2.0	4.0	8.0
0	6.388E-07	1.041E-06	1.825E-06	3.438E-06
10	5.538E-07	9.266E-07	1.651E-06	3.129E-06
20	3.433E-07	6.299E-07	1.177E-06	2.279E-06
30	2.379E-07	4.711E-07	9.147E-07	1.791E-06
40	1.612E-07	3.494E-07	7.100E-07	1.409E-06
50	1.134E-07	2.659E-07	5.631E-07	1.137E-06
60	7.757E-08	2.017E-07	4.420E-07	9.083E-07
70	5.167E-08	1.496E-07	3.449E-07	7.224E-07
80	3.519E-08	1.105E-07	2.635E-07	5.642E-07
90	2.440E-08	8.320E-08	2.071E-07	4.486E-07
100	1.573E-08	6.224E-08	1.616E-07	3.533E-07
110	9.852E-09	4.523E-08	1.232E-07	2.747E-07
120	6.068E-09	3.084E-08	9.146E-08	2.102E-07
130	4.473E-09	2.239E-08	7.006E-08	1.664E-07
140	2.846E-09	1.520E-08	5.142E-08	1.239E-07
150	2.064E-09	1.088E-08	3.803E-08	9.583E-08
160	1.314E-09	7.319E-09	2.865E-08	7.507E-08
170	9.071E-10	4.754E-09	2.177E-08	5.755E-08
180	5.630E-10	3.628E-09	1.651E-08	4.429E-08
190	2.815E-10	2.752E-09	1.339E-08	3.628E-08
200	1.251E-10	1.939E-09	1.013E-08	2.878E-08
210	9.383E-11	1.439E-09	6.631E-09	2.177E-08
220	6.256E-11	1.001E-09	5.004E-09	1.777E-08
230	6.256E-11	6.256E-10	3.628E-09	1.376E-08
240	3.128E-11	6.256E-10	3.253E-09	1.051E-08
250	3.128E-11	3.753E-10	2.127E-09	7.256E-09
260	0.000E+00	1.251E-10	1.501E-09	6.256E-09
270	-	6.256E-11	1.001E-09	4.254E-09
280	-	6.256E-11	2.502E-10	3.003E-09
290	-	6.256E-11	1.251E-10	2.002E-09
300	-	6.256E-11	1.251E-10	1.752E-09
310	-	6.256E-11	1.251E-10	1.251E-09
320	-	0.000E+00	0.000E+00	7.507E-10
330	-	-	-	5.004E-10
340	-	-	-	5.004E-10
350	-	-	-	5.004E-10
z(Gy)	1.557E+06	9.550E+05	5.447E+05	2.893E+05
S(%)	0.5	0.6	0.6	0.5
Hits	20422	16644	14591	13738

PHOTON ENERGY : 1254 eV

Number of interactions : 150
Diameter of target : 10.0 nm
Number of infinitely long cylinders hit : 4021

FREQUENCY OF ENERGY DEPOSITION GREATER THAN E PER Gy

E	Target cylinder length (nm)			
(eV)	5.0	10.0	20.0	40.0
0	1.640E-05	2.432E-05	4.274E-05	8.393E-05
10	1.600E-05	2.384E-05	4.205E-05	8.257E-05
20	1.434E-05	2.182E-05	3.890E-05	7.659E-05
30	1.347E-05	2.084E-05	3.744E-05	7.381E-05
40	1.268E-05	2.000E-05	3.601E-05	7.100E-05
50	1.194E-05	1.913E-05	3.467E-05	6.839E-05
60	1.123E-05	1.841E-05	3.347E-05	6.605E-05
70	1.059E-05	1.768E-05	3.220E-05	6.355E-05
80	9.993E-06	1.698E-05	3.112E-05	6.142E-05
90	9.445E-06	1.635E-05	3.009E-05	5.942E-05
100	8.953E-06	1.574E-05	2.914E-05	5.756E-05
110	8.397E-06	1.505E-05	2.806E-05	5.548E-05
120	7.912E-06	1.450E-05	2.719E-05	5.375E-05
130	7.430E-06	1.390E-05	2.620E-05	5.179E-05
140	6.922E-06	1.327E-05	2.509E-05	4.968E-05
150	6.476E-06	1.264E-05	2.404E-05	4.757E-05
160	6.056E-06	1.204E-05	2.303E-05	4.555E-05
170	5.592E-06	1.145E-05	2.204E-05	4.359E-05
180	5.287E-06	1.097E-05	2.120E-05	4.198E-05
190	4.909E-06	1.043E-05	2.035E-05	4.032E-05
200	4.599E-06	9.959E-06	1.955E-05	3.879E-05
210	4.263E-06	9.448E-06	1.874E-05	3.717E-05
220	3.981E-06	9.120E-06	1.823E-05	3.617E-05
230	3.655E-06	8.676E-06	1.759E-05	3.485E-05
240	3.371E-06	8.264E-06	1.691E-05	3.364E-05
250	3.139E-06	7.847E-06	1.620E-05	3.227E-05
260	2.805E-06	7.357E-06	1.531E-05	3.049E-05
270	2.581E-06	6.888E-06	1.451E-05	2.891E-05
280	2.323E-06	6.512E-06	1.389E-05	2.768E-05
290	2.093E-06	6.106E-06	1.314E-05	2.622E-05
300	1.911E-06	5.777E-06	1.257E-05	2.509E-05
310	1.742E-06	5.318E-06	1.178E-05	2.365E-05
320	1.567E-06	4.974E-06	1.112E-05	2.238E-05
330	1.421E-06	4.693E-06	1.067E-05	2.152E-05
340	1.249E-06	4.354E-06	1.008E-05	2.042E-05
350	1.118E-06	4.119E-06	9.636E-06	1.952E-05
360	1.019E-06	3.817E-06	9.052E-06	1.846E-05
370	9.177E-07	3.577E-06	8.583E-06	1.752E-05
380	8.160E-07	3.306E-06	8.040E-06	1.646E-05
390	6.987E-07	3.035E-06	7.529E-06	1.548E-05
400	6.022E-07	2.821E-06	7.050E-06	1.452E-05
410	5.240E-07	2.618E-06	6.632E-06	1.368E-05
420	4.641E-07	2.367E-06	6.101E-06	1.262E-05

Photon Energy : 1254 eV ; Diameter of target : 10 nm.
(cont.)

FREQUENCY OF ENERGY DEPOSITION GREATER THAN E PER Gy

E	Target cylinder length (nm)			
(eV)	5.0	10.0	20.0	40.0
430	4.276E-07	2.153E-06	5.652E-06	1.174E-05
440	3.754E-07	2.007E-06	5.329E-06	1.105E-05
450	3.546E-07	1.841E-06	5.037E-06	1.047E-05
460	3.102E-07	1.726E-06	4.766E-06	9.907E-06
470	2.868E-07	1.590E-06	4.380E-06	9.114E-06
480	2.633E-07	1.444E-06	4.067E-06	8.510E-06
490	2.372E-07	1.330E-06	3.775E-06	7.926E-06
500	2.268E-07	1.210E-06	3.483E-06	7.342E-06
510	1.955E-07	1.064E-06	3.212E-06	6.799E-06
520	1.747E-07	9.855E-07	3.003E-06	6.403E-06
530	1.590E-07	9.333E-07	2.743E-06	5.861E-06
540	1.356E-07	8.656E-07	2.638E-06	5.652E-06
550	1.199E-07	7.978E-07	2.461E-06	5.298E-06
560	1.043E-07	7.352E-07	2.305E-06	4.943E-06
570	8.864E-08	6.674E-07	2.148E-06	4.609E-06
580	7.300E-08	6.101E-07	2.002E-06	4.317E-06
590	5.996E-08	5.318E-07	1.835E-06	3.942E-06
600	4.953E-08	4.745E-07	1.669E-06	3.629E-06
610	4.171E-08	4.223E-07	1.575E-06	3.441E-06
620	3.650E-08	3.963E-07	1.481E-06	3.212E-06
630	3.128E-08	3.702E-07	1.387E-06	3.045E-06
640	2.868E-08	3.128E-07	1.210E-06	2.732E-06
650	2.086E-08	2.607E-07	1.126E-06	2.545E-06
660	1.825E-08	2.294E-07	1.064E-06	2.419E-06
670	1.825E-08	2.190E-07	9.594E-07	2.190E-06
680	1.564E-08	1.825E-07	8.864E-07	2.065E-06
690	1.564E-08	1.825E-07	8.238E-07	1.961E-06
700	1.564E-08	1.669E-07	7.404E-07	1.773E-06
710	1.304E-08	1.460E-07	6.883E-07	1.648E-06
720	1.043E-08	1.356E-07	6.674E-07	1.606E-06
730	5.214E-09	1.251E-07	6.361E-07	1.481E-06
740	2.607E-09	1.043E-07	5.527E-07	1.314E-06
750	2.607E-09	9.385E-08	5.318E-07	1.293E-06
z(Gy)	5.883E+04	3.966E+04	2.257E+04	1.149E+04
S(%)	3.5	3.5	3.5	3.6
Hits	6290	4665	4098	4024

PHOTON ENERGY : 1254 eV

Number of interactions : 150
Diameter of target : 25.0 nm
Number of infinitely long cylinders hit : 1850

FREQUENCY OF ENERGY DEPOSITION GREATER THAN E PER Gy

E	Target cylinder length (nm)			
(eV)	12.5	25.0	50.0	100.0
0	9.532E-05	1.546E-04	3.015E-04	6.029E-04
10	9.374E-05	1.529E-04	2.985E-04	5.970E-04
20	8.909E-05	1.463E-04	2.860E-04	5.719E-04
30	8.726E-05	1.438E-04	2.811E-04	5.622E-04
40	8.559E-05	1.416E-04	2.770E-04	5.540E-04
50	8.412E-05	1.396E-04	2.734E-04	5.469E-04
60	8.278E-05	1.382E-04	2.708E-04	5.416E-04
70	8.107E-05	1.360E-04	2.664E-04	5.328E-04
80	7.940E-05	1.338E-04	2.622E-04	5.244E-04
90	7.858E-05	1.328E-04	2.604E-04	5.208E-04
100	7.707E-05	1.305E-04	2.563E-04	5.126E-04
110	7.618E-05	1.293E-04	2.540E-04	5.081E-04
120	7.447E-05	1.271E-04	2.496E-04	4.993E-04
130	7.316E-05	1.251E-04	2.456E-04	4.911E-04
140	7.219E-05	1.238E-04	2.431E-04	4.862E-04
150	7.072E-05	1.221E-04	2.399E-04	4.797E-04
160	6.966E-05	1.208E-04	2.374E-04	4.748E-04
170	6.799E-05	1.184E-04	2.327E-04	4.654E-04
180	6.665E-05	1.166E-04	2.291E-04	4.582E-04
190	6.518E-05	1.144E-04	2.254E-04	4.507E-04
200	6.400E-05	1.132E-04	2.231E-04	4.462E-04
210	6.204E-05	1.107E-04	2.185E-04	4.370E-04
220	6.054E-05	1.085E-04	2.148E-04	4.295E-04
230	5.956E-05	1.074E-04	2.125E-04	4.250E-04
240	5.846E-05	1.056E-04	2.091E-04	4.181E-04
250	5.719E-05	1.037E-04	2.053E-04	4.106E-04
260	5.614E-05	1.025E-04	2.030E-04	4.061E-04
270	5.467E-05	1.002E-04	1.985E-04	3.969E-04
280	5.308E-05	9.834E-05	1.949E-04	3.898E-04
290	5.165E-05	9.647E-05	1.913E-04	3.826E-04
300	5.043E-05	9.459E-05	1.879E-04	3.758E-04
310	4.966E-05	9.321E-05	1.853E-04	3.705E-04
320	4.844E-05	9.125E-05	1.815E-04	3.630E-04
330	4.746E-05	9.035E-05	1.797E-04	3.595E-04
340	4.624E-05	8.848E-05	1.760E-04	3.520E-04
350	4.501E-05	8.661E-05	1.724E-04	3.448E-04
360	4.408E-05	8.522E-05	1.700E-04	3.399E-04
370	4.277E-05	8.376E-05	1.670E-04	3.340E-04
380	4.139E-05	8.213E-05	1.636E-04	3.272E-04
390	4.033E-05	8.058E-05	1.608E-04	3.217E-04
400	3.923E-05	7.887E-05	1.574E-04	3.148E-04
410	3.756E-05	7.675E-05	1.532E-04	3.063E-04
420	3.658E-05	7.479E-05	1.493E-04	2.985E-04

Photon Energy : 1254 eV ; Diameter of target : 25 nm. (cont.)

FREQUENCY OF ENERGY DEPOSITION GREATER THAN E PER Gy

E	Target cylinder length (nm)			
(eV)	12.5	25.0	50.0	100.0
430	3.552E-05	7.308E-05	1.460E-04	2.920E-04
440	3.446E-05	7.129E-05	1.424E-04	2.848E-04
450	3.349E-05	6.982E-05	1.396E-04	2.793E-04
460	3.194E-05	6.771E-05	1.356E-04	2.711E-04
470	3.080E-05	6.616E-05	1.325E-04	2.650E-04
480	2.990E-05	6.502E-05	1.302E-04	2.604E-04
490	2.884E-05	6.331E-05	1.271E-04	2.542E-04
500	2.807E-05	6.216E-05	1.248E-04	2.496E-04
510	2.717E-05	6.062E-05	1.219E-04	2.438E-04
520	2.636E-05	5.948E-05	1.199E-04	2.399E-04
530	2.534E-05	5.842E-05	1.176E-04	2.353E-04
540	2.444E-05	5.630E-05	1.134E-04	2.268E-04
550	2.387E-05	5.548E-05	1.121E-04	2.242E-04
560	2.322E-05	5.442E-05	1.100E-04	2.200E-04
570	2.249E-05	5.337E-05	1.080E-04	2.161E-04
580	2.188E-05	5.214E-05	1.056E-04	2.112E-04
590	2.074E-05	5.019E-05	1.017E-04	2.034E-04
600	1.996E-05	4.864E-05	9.875E-05	1.975E-04
610	1.919E-05	4.750E-05	9.630E-05	1.926E-04
620	1.866E-05	4.668E-05	9.467E-05	1.893E-04
630	1.821E-05	4.579E-05	9.288E-05	1.858E-04
640	1.727E-05	4.424E-05	8.978E-05	1.796E-04
650	1.691E-05	4.343E-05	8.832E-05	1.766E-04
660	1.629E-05	4.245E-05	8.620E-05	1.724E-04
670	1.585E-05	4.139E-05	8.424E-05	1.685E-04
680	1.511E-05	4.049E-05	8.229E-05	1.646E-04
690	1.450E-05	3.951E-05	8.050E-05	1.610E-04
700	1.369E-05	3.797E-05	7.756E-05	1.551E-04
710	1.300E-05	3.626E-05	7.430E-05	1.486E-04
720	1.247E-05	3.495E-05	7.170E-05	1.434E-04
730	1.210E-05	3.397E-05	6.974E-05	1.395E-04
740	1.185E-05	3.332E-05	6.828E-05	1.366E-04
750	1.145E-05	3.226E-05	6.616E-05	1.323E-04
760	1.108E-05	3.145E-05	6.453E-05	1.291E-04
770	1.043E-05	3.039E-05	6.257E-05	1.251E-04
780	1.002E-05	2.974E-05	6.127E-05	1.225E-04
790	9.492E-06	2.876E-05	5.948E-05	1.190E-04
800	9.207E-06	2.786E-05	5.785E-05	1.157E-04
810	8.881E-06	2.746E-05	5.687E-05	1.137E-04
820	8.433E-06	2.664E-05	5.524E-05	1.105E-04
830	8.107E-06	2.583E-05	5.377E-05	1.075E-04
840	7.577E-06	2.526E-05	5.263E-05	1.053E-04
850	7.170E-06	2.420E-05	5.051E-05	1.010E-04

Photon Energy : 1254 eV ; Diameter of target : 25 nm. (cont.)

FREQUENCY OF ENERGY DEPOSITION GREATER THAN E PER Gy

E	Target cylinder length (nm)			
(eV)	12.5	25.0	50.0	100.0
860	6.925E-06	2.355E-05	4.937E-05	9.875E-05
870	6.559E-06	2.216E-05	4.644E-05	9.288E-05
880	6.314E-06	2.159E-05	4.497E-05	8.995E-05
890	6.151E-06	2.086E-05	4.367E-05	8.734E-05
900	5.988E-06	2.029E-05	4.237E-05	8.473E-05
910	5.825E-06	1.980E-05	4.139E-05	8.278E-05
920	5.703E-06	1.923E-05	4.041E-05	8.082E-05
930	5.622E-06	1.866E-05	3.960E-05	7.919E-05
940	5.500E-06	1.825E-05	3.894E-05	7.789E-05
950	5.255E-06	1.760E-05	3.764E-05	7.528E-05
960	5.011E-06	1.719E-05	3.666E-05	7.333E-05
970	4.848E-06	1.695E-05	3.601E-05	7.202E-05
980	4.685E-06	1.646E-05	3.471E-05	6.942E-05
990	4.522E-06	1.597E-05	3.389E-05	6.779E-05
1000	4.400E-06	1.564E-05	3.324E-05	6.648E-05
z(Gy)	9.918E+03	6.114E+03	3.136E+03	1.568E+03
S(%)	5.5	5.5	5.5	5.5
Hits	2340	1898	1850	1850

PHOTON ENERGY : 1487 eV

Number of interactions : 100
Diameter of target : 2.0 nm
Number of infinitely long cylinders hit :17151

FREQUENCY OF ENERGY DEPOSITION GREATER THAN E PER Gy

E	Target cylinder length (nm)			
(eV)	1.0	2.0	4.0	8.0
0	6.701E-07	1.110E-06	1.964E-06	3.715E-06
10	5.839E-07	9.974E-07	1.791E-06	3.408E-06
20	3.472E-07	6.476E-07	1.226E-06	2.382E-06
30	2.394E-07	4.806E-07	9.399E-07	1.848E-06
40	1.573E-07	3.422E-07	6.968E-07	1.393E-06
50	1.057E-07	2.542E-07	5.346E-07	1.084E-06
60	7.209E-08	1.867E-07	4.107E-07	8.478E-07
70	4.943E-08	1.383E-07	3.206E-07	6.725E-07
80	3.368E-08	1.016E-07	2.443E-07	5.187E-07
90	2.255E-08	7.480E-08	1.871E-07	4.083E-07
100	1.548E-08	5.560E-08	1.470E-07	3.233E-07
110	9.601E-09	3.972E-08	1.117E-07	2.498E-07
120	6.594E-09	2.896E-08	8.683E-08	1.973E-07
130	4.669E-09	2.158E-08	6.816E-08	1.604E-07
140	2.928E-09	1.593E-08	5.265E-08	1.264E-07
150	2.110E-09	1.113E-08	3.914E-08	9.854E-08
160	1.424E-09	8.282E-09	3.007E-08	7.744E-08
170	9.232E-10	5.856E-09	2.289E-08	6.077E-08
180	6.858E-10	4.326E-09	1.667E-08	4.600E-08
190	3.693E-10	2.796E-09	1.192E-08	3.292E-08
200	2.374E-10	2.005E-09	9.284E-09	2.553E-08
210	1.319E-10	1.530E-09	6.541E-09	1.920E-08
220	5.275E-11	1.161E-09	4.431E-09	1.372E-08
230	0.000E+00	6.858E-10	2.532E-09	8.862E-09
240	-	4.748E-10	2.110E-09	7.596E-09
250	-	3.693E-10	1.794E-09	6.541E-09
260	-	3.165E-10	1.477E-09	5.064E-09
270	-	2.110E-10	1.161E-09	4.220E-09
280	-	1.583E-10	9.495E-10	3.587E-09
290	-	1.055E-10	7.385E-10	2.954E-09
300	-	5.275E-11	4.220E-10	1.899E-09
310	-	5.275E-11	3.165E-10	1.688E-09
320	-	0.000E+00	3.165E-10	1.688E-09
330	-	-	3.165E-10	1.477E-09
340	-	-	1.055E-10	8.440E-10
350	-	-	1.055E-10	4.220E-10
z(Gy)	1.506E+06	9.085E+05	5.136E+05	2.715E+05
S(%)	0.9	0.8	0.9	0.9
Hits	25404	21050	18617	17608

PHOTON ENERGY : 1487 eV

Number of interactions : 100
Diameter of target : 10.0 nm
Number of infinitely long cylinders hit : 3568

FREQUENCY OF ENERGY DEPOSITION GREATER THAN E PER Gy

E	Target cylinder length (nm)			
(eV)	5.0	10.0	20.0	40.0
0	1.818E-05	2.744E-05	4.858E-05	9.445E-05
10	1.772E-05	2.696E-05	4.782E-05	9.311E-05
20	1.571E-05	2.456E-05	4.401E-05	8.580E-05
30	1.461E-05	2.326E-05	4.203E-05	8.200E-05
40	1.354E-05	2.197E-05	3.986E-05	7.794E-05
50	1.260E-05	2.069E-05	3.787E-05	7.406E-05
60	1.169E-05	1.968E-05	3.621E-05	7.087E-05
70	1.089E-05	1.874E-05	3.465E-05	6.786E-05
80	1.013E-05	1.776E-05	3.304E-05	6.477E-05
90	9.448E-06	1.696E-05	3.169E-05	6.208E-05
100	8.789E-06	1.610E-05	3.020E-05	5.920E-05
110	8.106E-06	1.509E-05	2.851E-05	5.599E-05
120	7.447E-06	1.419E-05	2.719E-05	5.337E-05
130	6.906E-06	1.349E-05	2.608E-05	5.121E-05
140	6.490E-06	1.292E-05	2.516E-05	4.942E-05
150	6.078E-06	1.232E-05	2.407E-05	4.741E-05
160	5.659E-06	1.175E-05	2.314E-05	4.570E-05
170	5.250E-06	1.119E-05	2.221E-05	4.395E-05
180	4.845E-06	1.059E-05	2.113E-05	4.184E-05
190	4.498E-06	1.003E-05	2.012E-05	3.986E-05
200	4.188E-06	9.505E-06	1.925E-05	3.810E-05
210	3.812E-06	8.858E-06	1.806E-05	3.580E-05
220	3.555E-06	8.482E-06	1.744E-05	3.467E-05
230	3.275E-06	8.027E-06	1.667E-05	3.319E-05
240	2.965E-06	7.466E-06	1.563E-05	3.118E-05
250	2.717E-06	7.005E-06	1.487E-05	2.968E-05
260	2.447E-06	6.451E-06	1.384E-05	2.781E-05
270	2.206E-06	6.068E-06	1.320E-05	2.654E-05
280	2.022E-06	5.758E-06	1.268E-05	2.551E-05
290	1.913E-06	5.422E-06	1.208E-05	2.435E-05
300	1.745E-06	5.151E-06	1.157E-05	2.338E-05
310	1.590E-06	4.887E-06	1.101E-05	2.224E-05
320	1.458E-06	4.531E-06	1.037E-05	2.095E-05
330	1.322E-06	4.221E-06	9.722E-06	1.968E-05
340	1.210E-06	3.924E-06	9.102E-06	1.855E-05
350	1.062E-06	3.614E-06	8.548E-06	1.739E-05
360	9.267E-07	3.337E-06	8.100E-06	1.657E-05
370	8.014E-07	3.027E-06	7.427E-06	1.528E-05
380	7.255E-07	2.757E-06	6.926E-06	1.435E-05
390	6.530E-07	2.566E-06	6.503E-06	1.353E-05
400	5.969E-07	2.388E-06	6.108E-06	1.274E-05
410	5.507E-07	2.243E-06	5.804E-06	1.214E-05
420	4.683E-07	2.091E-06	5.422E-06	1.142E-05

Photon Energy : 1487 eV ; Diameter of target : 10 nm.
(cont.)

FREQUENCY OF ENERGY DEPOSITION GREATER THAN E PER Gy

E	Target cylinder length (nm)			
(eV)	5.0	10.0	20.0	40.0
430	4.254E-07	1.939E-06	5.118E-06	1.079E-05
440	3.859E-07	1.814E-06	4.762E-06	1.010E-05
450	3.298E-07	1.629E-06	4.393E-06	9.366E-06
460	3.067E-07	1.550E-06	4.116E-06	8.838E-06
470	2.572E-07	1.352E-06	3.760E-06	8.100E-06
480	2.144E-07	1.200E-06	3.430E-06	7.466E-06
490	1.979E-07	1.108E-06	3.232E-06	7.071E-06
500	1.847E-07	9.960E-07	2.968E-06	6.490E-06
510	1.616E-07	9.234E-07	2.691E-06	5.936E-06
520	1.319E-07	8.245E-07	2.414E-06	5.435E-06
530	1.187E-07	7.519E-07	2.190E-06	5.039E-06
540	1.121E-07	6.662E-07	2.032E-06	4.696E-06
550	8.904E-08	6.068E-07	1.873E-06	4.327E-06
560	8.575E-08	5.145E-07	1.728E-06	3.984E-06
570	8.245E-08	4.749E-07	1.636E-06	3.826E-06
580	6.926E-08	4.353E-07	1.517E-06	3.509E-06
590	6.596E-08	3.694E-07	1.280E-06	3.087E-06
600	5.606E-08	3.628E-07	1.187E-06	2.929E-06
610	4.617E-08	3.298E-07	1.069E-06	2.638E-06
620	4.287E-08	2.968E-07	9.498E-07	2.374E-06
630	3.298E-08	2.572E-07	8.443E-07	2.190E-06
640	2.968E-08	2.243E-07	7.783E-07	2.084E-06
650	2.968E-08	2.111E-07	7.387E-07	2.005E-06
660	2.638E-08	1.847E-07	6.596E-07	1.768E-06
670	2.309E-08	1.451E-07	5.804E-07	1.583E-06
680	2.309E-08	1.319E-07	4.881E-07	1.425E-06
690	1.979E-08	1.253E-07	4.353E-07	1.293E-06
700	1.979E-08	1.121E-07	4.089E-07	1.214E-06
710	1.649E-08	1.055E-07	3.826E-07	1.161E-06
720	1.649E-08	9.234E-08	3.298E-07	1.055E-06
730	1.649E-08	7.915E-08	3.034E-07	1.003E-06
740	1.319E-08	7.255E-08	3.034E-07	9.762E-07
750	1.319E-08	6.596E-08	2.770E-07	8.970E-07
z(Gy)	5.281E+04	3.500E+04	1.976E+04	1.017E+04
S(%)	4.0	4.0	4.0	4.0
Hits	5514	4160	3683	3580

PHOTON ENERGY : 1487 eV

Number of interactions : 100
Diameter of target : 25.0 nm
Number of infinitely long cylinders hit : 1561

Photon Energy : 1487 eV ; Diameter of target : 25 nm.

FREQUENCY OF ENERGY DEPOSITION GREATER THAN E PER Gy

E	Target cylinder length (nm)			
(eV)	12.5	25.0	50.0	100.0
0	1.090E-04	1.731E-04	3.226E-04	6.435E-04
10	1.076E-04	1.715E-04	3.199E-04	6.382E-04
20	1.024E-04	1.642E-04	3.069E-04	6.126E-04
30	9.971E-05	1.605E-04	3.001E-04	5.990E-04
40	9.739E-05	1.579E-04	2.952E-04	5.891E-04
50	9.538E-05	1.549E-04	2.908E-04	5.804E-04
60	9.358E-05	1.529E-04	2.873E-04	5.738E-04
70	9.162E-05	1.508E-04	2.834E-04	5.660E-04
80	8.992E-05	1.483E-04	2.791E-04	5.574E-04
90	8.843E-05	1.471E-04	2.766E-04	5.524E-04
100	8.631E-05	1.448E-04	2.729E-04	5.450E-04
110	8.379E-05	1.414E-04	2.665E-04	5.322E-04
120	8.219E-05	1.398E-04	2.640E-04	5.273E-04
130	8.049E-05	1.383E-04	2.612E-04	5.215E-04
140	7.848E-05	1.357E-04	2.562E-04	5.116E-04
150	7.673E-05	1.335E-04	2.523E-04	5.038E-04
160	7.472E-05	1.316E-04	2.492E-04	4.976E-04
170	7.328E-05	1.300E-04	2.467E-04	4.926E-04
180	7.173E-05	1.277E-04	2.422E-04	4.836E-04
190	7.018E-05	1.261E-04	2.393E-04	4.778E-04
200	6.879E-05	1.244E-04	2.366E-04	4.728E-04
210	6.709E-05	1.222E-04	2.327E-04	4.650E-04
220	6.519E-05	1.202E-04	2.288E-04	4.572E-04
230	6.354E-05	1.182E-04	2.249E-04	4.493E-04
240	6.225E-05	1.168E-04	2.224E-04	4.444E-04
250	6.019E-05	1.144E-04	2.187E-04	4.370E-04
260	5.911E-05	1.127E-04	2.156E-04	4.308E-04
270	5.730E-05	1.099E-04	2.107E-04	4.209E-04
280	5.519E-05	1.069E-04	2.053E-04	4.102E-04
290	5.431E-05	1.057E-04	2.032E-04	4.061E-04
300	5.266E-05	1.030E-04	1.991E-04	3.982E-04
310	5.127E-05	1.007E-04	1.950E-04	3.900E-04
320	4.968E-05	9.842E-05	1.905E-04	3.809E-04
330	4.823E-05	9.626E-05	1.867E-04	3.735E-04
340	4.664E-05	9.379E-05	1.824E-04	3.648E-04
350	4.524E-05	9.162E-05	1.781E-04	3.562E-04
360	4.396E-05	8.946E-05	1.744E-04	3.488E-04
370	4.236E-05	8.771E-05	1.719E-04	3.438E-04
380	4.092E-05	8.575E-05	1.686E-04	3.372E-04
390	4.019E-05	8.451E-05	1.663E-04	3.327E-04
400	3.927E-05	8.255E-05	1.626E-04	3.257E-04
410	3.782E-05	7.987E-05	1.575E-04	3.154E-04
420	3.654E-05	7.822E-05	1.544E-04	3.092E-04

Photon Energy : 1487 eV ; Diameter of target : 25 nm. (cont.)

FREQUENCY OF ENERGY DEPOSITION GREATER THAN E PER Gy

E	Target cylinder length (nm)			
(eV)	12.5	25.0	50.0	100.0
430	3.530E-05	7.657E-05	1.515E-04	3.034E-04
440	3.344E-05	7.389E-05	1.468E-04	2.939E-04
450	3.226E-05	7.235E-05	1.443E-04	2.890E-04
460	3.112E-05	7.060E-05	1.414E-04	2.828E-04
470	3.040E-05	6.977E-05	1.400E-04	2.799E-04
480	2.953E-05	6.812E-05	1.367E-04	2.733E-04
490	2.844E-05	6.658E-05	1.342E-04	2.684E-04
500	2.716E-05	6.441E-05	1.303E-04	2.605E-04
510	2.669E-05	6.266E-05	1.274E-04	2.548E-04
520	2.561E-05	6.112E-05	1.247E-04	2.494E-04
530	2.468E-05	5.895E-05	1.208E-04	2.416E-04
540	2.319E-05	5.607E-05	1.156E-04	2.313E-04
550	2.231E-05	5.503E-05	1.138E-04	2.276E-04
560	2.144E-05	5.308E-05	1.103E-04	2.206E-04
570	2.087E-05	5.153E-05	1.078E-04	2.156E-04
580	1.974E-05	4.926E-05	1.041E-04	2.082E-04
590	1.907E-05	4.844E-05	1.022E-04	2.045E-04
600	1.850E-05	4.710E-05	9.914E-05	1.983E-04
610	1.757E-05	4.566E-05	9.626E-05	1.925E-04
620	1.654E-05	4.370E-05	9.193E-05	1.839E-04
630	1.592E-05	4.215E-05	8.884E-05	1.777E-04
640	1.438E-05	4.050E-05	8.595E-05	1.719E-04
650	1.366E-05	3.906E-05	8.327E-05	1.665E-04
660	1.288E-05	3.731E-05	8.018E-05	1.604E-04
670	1.185E-05	3.576E-05	7.688E-05	1.538E-04
680	1.129E-05	3.432E-05	7.420E-05	1.484E-04
690	1.036E-05	3.267E-05	7.070E-05	1.414E-04
700	9.739E-06	3.102E-05	6.781E-05	1.356E-04
710	8.915E-06	2.989E-05	6.555E-05	1.311E-04
720	8.142E-06	2.814E-05	6.225E-05	1.245E-04
730	7.678E-06	2.690E-05	5.998E-05	1.200E-04
740	7.266E-06	2.597E-05	5.813E-05	1.163E-04
750	6.647E-06	2.443E-05	5.503E-05	1.101E-04
760	6.441E-06	2.350E-05	5.359E-05	1.072E-04
770	6.184E-06	2.267E-05	5.153E-05	1.031E-04
780	5.874E-06	2.164E-05	4.926E-05	9.853E-05
790	5.359E-06	2.030E-05	4.679E-05	9.358E-05
800	4.947E-06	1.886E-05	4.411E-05	8.822E-05
810	4.844E-06	1.834E-05	4.287E-05	8.575E-05
820	4.638E-06	1.762E-05	4.184E-05	8.369E-05
830	4.174E-06	1.618E-05	3.937E-05	7.874E-05
840	4.071E-06	1.556E-05	3.772E-05	7.544E-05
850	3.762E-06	1.484E-05	3.669E-05	7.338E-05

Photon Energy : 1487 eV ; Diameter of target : 25 nm. (cont.)

FREQUENCY OF ENERGY DEPOSITION GREATER THAN E PER Gy

E	Target cylinder length (nm)			
(eV)	12.5	25.0	50.0	100.0
860	3.607E-06	1.412E-05	3.525E-05	7.049E-05
870	3.401E-06	1.360E-05	3.422E-05	6.843E-05
880	3.246E-06	1.309E-05	3.277E-05	6.555E-05
890	3.092E-06	1.226E-05	3.112E-05	6.225E-05
900	2.937E-06	1.134E-05	2.989E-05	5.978E-05
910	2.834E-06	1.092E-05	2.927E-05	5.854E-05
920	2.628E-06	1.051E-05	2.824E-05	5.648E-05
930	2.577E-06	1.020E-05	2.741E-05	5.483E-05
940	2.422E-06	9.791E-06	2.618E-05	5.236E-05
950	2.216E-06	9.172E-06	2.535E-05	5.071E-05
960	2.164E-06	8.451E-06	2.453E-05	4.906E-05
970	2.164E-06	8.245E-06	2.412E-05	4.823E-05
980	2.010E-06	7.730E-06	2.309E-05	4.617E-05
990	2.010E-06	7.523E-06	2.288E-05	4.576E-05
1000	1.855E-06	7.214E-06	2.206E-05	4.411E-05
z(Gy)	8.741E+03	5.505E+03	2.955E+03	1.481E+03
S(%)	4.7	4.7	4.7	4.7
Hits	2116	1680	1565	1561

PHOTON ENERGY : 1740 eV

Number of interactions : 50
Diameter of target : 2.0 nm
Number of infinitely long cylinders hit :10361

FREQUENCY OF ENERGY DEPOSITION GREATER THAN E PER Gy

E	Target cylinder length (nm)			
(eV)	1.0	2.0	4.0	8.0
0	6.660E-07	1.118E-06	2.003E-06	3.823E-06
10	5.839E-07	1.008E-06	1.830E-06	3.506E-06
20	3.462E-07	6.486E-07	1.235E-06	2.399E-06
30	2.351E-07	4.707E-07	9.247E-07	1.820E-06
40	1.563E-07	3.354E-07	6.836E-07	1.360E-06
50	1.060E-07	2.465E-07	5.235E-07	1.050E-06
60	7.218E-08	1.846E-07	4.029E-07	8.237E-07
70	4.932E-08	1.370E-07	3.073E-07	6.412E-07
80	3.422E-08	9.900E-08	2.324E-07	4.973E-07
90	2.358E-08	7.466E-08	1.823E-07	3.996E-07
100	1.515E-08	5.500E-08	1.394E-07	3.109E-07
110	9.738E-09	4.003E-08	1.087E-07	2.442E-07
120	6.266E-09	2.957E-08	8.169E-08	1.868E-07
130	3.877E-09	2.128E-08	6.149E-08	1.471E-07
140	2.209E-09	1.515E-08	4.652E-08	1.150E-07
150	1.172E-09	1.028E-08	3.570E-08	8.728E-08
160	7.213E-10	7.303E-09	2.723E-08	6.888E-08
170	4.057E-10	5.410E-09	2.074E-08	5.446E-08
180	2.254E-10	3.697E-09	1.515E-08	4.148E-08
190	1.352E-10	2.164E-09	1.190E-08	3.246E-08
200	4.508E-11	1.443E-09	8.295E-09	2.380E-08
210	4.508E-11	9.016E-10	5.951E-09	1.695E-08
220	0.000E+00	5.410E-10	4.328E-09	1.190E-08
230	-	3.607E-10	3.066E-09	9.016E-09
240	-	1.803E-10	2.525E-09	7.213E-09
250	-	1.803E-10	2.164E-09	5.770E-09
260	-	9.016E-11	1.443E-09	5.049E-09
270	-	9.016E-11	9.016E-10	4.328E-09
280	-	0.000E+00	5.410E-10	3.246E-09
290	-	-	5.410E-10	1.803E-09
300	-	-	5.410E-10	1.803E-09
310	-	-	3.607E-10	1.082E-09
320	-	-	3.607E-10	1.082E-09
330	-	-	0.000E+00	0.000E+00
340	-	-	-	-
350	-	-	-	-
z(Gy)	1.500E+06	8.935E+05	4.988E+05	2.614E+05
S(%)	0.1	0.1	0.1	0.1
Hits	14773	12402	11108	10600

PHOTON ENERGY : 1740 eV

Number of interactions : 100
Diameter of target : 10.0 nm
Number of infinitely long cylinders hit : 4819

FREQUENCY OF ENERGY DEPOSITION GREATER THAN E PER Gy

E	Target cylinder length (nm)			
(eV)	5.0	10.0	20.0	40.0
0	2.111E-05	3.213E-05	5.649E-05	1.092E-04
10	2.060E-05	3.159E-05	5.566E-05	1.077E-04
20	1.803E-05	2.850E-05	5.104E-05	9.900E-05
30	1.651E-05	2.664E-05	4.804E-05	9.334E-05
40	1.505E-05	2.483E-05	4.512E-05	8.775E-05
50	1.386E-05	2.332E-05	4.277E-05	8.339E-05
60	1.277E-05	2.200E-05	4.075E-05	7.954E-05
70	1.175E-05	2.066E-05	3.853E-05	7.521E-05
80	1.087E-05	1.947E-05	3.635E-05	7.102E-05
90	9.990E-06	1.825E-05	3.430E-05	6.709E-05
100	9.142E-06	1.708E-05	3.240E-05	6.344E-05
110	8.392E-06	1.611E-05	3.072E-05	6.024E-05
120	7.727E-06	1.513E-05	2.906E-05	5.711E-05
130	7.127E-06	1.423E-05	2.757E-05	5.427E-05
140	6.563E-06	1.343E-05	2.620E-05	5.163E-05
150	5.980E-06	1.256E-05	2.471E-05	4.877E-05
160	5.515E-06	1.186E-05	2.344E-05	4.644E-05
170	5.067E-06	1.112E-05	2.220E-05	4.405E-05
180	4.647E-06	1.047E-05	2.099E-05	4.166E-05
190	4.275E-06	9.875E-06	1.991E-05	3.959E-05
200	3.926E-06	9.260E-06	1.892E-05	3.763E-05
210	3.599E-06	8.663E-06	1.786E-05	3.560E-05
220	3.263E-06	8.116E-06	1.693E-05	3.386E-05
230	2.959E-06	7.586E-06	1.591E-05	3.204E-05
240	2.705E-06	7.136E-06	1.509E-05	3.050E-05
250	2.455E-06	6.634E-06	1.435E-05	2.897E-05
260	2.294E-06	6.284E-06	1.372E-05	2.778E-05
270	2.021E-06	5.862E-06	1.291E-05	2.618E-05
280	1.852E-06	5.495E-06	1.217E-05	2.469E-05
290	1.688E-06	5.084E-06	1.153E-05	2.340E-05
300	1.513E-06	4.718E-06	1.090E-05	2.216E-05
310	1.381E-06	4.385E-06	1.024E-05	2.097E-05
320	1.243E-06	4.030E-06	9.570E-06	1.973E-05
330	1.082E-06	3.748E-06	9.041E-06	1.869E-05
340	9.300E-07	3.433E-06	8.421E-06	1.740E-05
350	8.567E-07	3.151E-06	7.913E-06	1.646E-05
360	7.637E-07	2.880E-06	7.305E-06	1.535E-05
370	6.848E-07	2.694E-06	6.741E-06	1.427E-05
380	6.087E-07	2.480E-06	6.313E-06	1.344E-05
390	5.664E-07	2.311E-06	5.941E-06	1.267E-05
400	5.016E-07	2.080E-06	5.501E-06	1.175E-05
410	4.622E-07	1.911E-06	5.061E-06	1.091E-05
420	4.199E-07	1.759E-06	4.701E-06	1.026E-05

Photon Energy : 1740 eV ; Diameter of target : 10 nm.
(cont.)

FREQUENCY OF ENERGY DEPOSITION GREATER THAN E PER Gy

E	Target cylinder length (nm)			
(eV)	5.0	10.0	20.0	40.0
430	3.748E-07	1.629E-06	4.385E-06	9.492E-06
440	3.410E-07	1.522E-06	4.148E-06	8.905E-06
450	3.100E-07	1.420E-06	3.867E-06	8.387E-06
460	2.818E-07	1.302E-06	3.607E-06	7.801E-06
470	2.508E-07	1.184E-06	3.337E-06	7.282E-06
480	2.255E-07	1.082E-06	3.100E-06	6.786E-06
490	1.888E-07	9.582E-07	2.863E-06	6.313E-06
500	1.719E-07	8.905E-07	2.672E-06	5.974E-06
510	1.437E-07	8.060E-07	2.435E-06	5.478E-06
520	1.155E-07	7.271E-07	2.209E-06	5.050E-06
530	1.043E-07	6.876E-07	2.040E-06	4.712E-06
540	9.018E-08	6.031E-07	1.826E-06	4.306E-06
550	7.891E-08	5.411E-07	1.702E-06	4.013E-06
560	6.482E-08	5.016E-07	1.589E-06	3.788E-06
570	5.073E-08	4.340E-07	1.432E-06	3.472E-06
580	4.227E-08	4.002E-07	1.319E-06	3.269E-06
590	4.227E-08	3.776E-07	1.206E-06	2.999E-06
600	3.664E-08	3.213E-07	1.082E-06	2.705E-06
610	3.100E-08	2.818E-07	1.015E-06	2.503E-06
620	1.973E-08	2.311E-07	9.244E-07	2.300E-06
630	1.973E-08	1.916E-07	8.229E-07	2.074E-06
640	1.973E-08	1.578E-07	6.651E-07	1.804E-06
650	1.409E-08	1.353E-07	5.636E-07	1.578E-06
660	1.409E-08	1.296E-07	5.411E-07	1.511E-06
670	1.127E-08	1.184E-07	5.298E-07	1.420E-06
680	1.127E-08	1.015E-07	4.960E-07	1.330E-06
690	8.454E-09	6.764E-08	4.509E-07	1.263E-06
700	8.454E-09	6.764E-08	4.284E-07	1.172E-06
710	8.454E-09	5.073E-08	3.833E-07	1.060E-06
720	5.636E-09	4.509E-08	3.495E-07	9.694E-07
730	5.636E-09	3.945E-08	3.156E-07	9.018E-07
740	5.636E-09	3.945E-08	2.818E-07	8.342E-07
750	5.636E-09	3.945E-08	2.593E-07	7.214E-07
z(Gy)	4.735E+04	3.111E+04	1.770E+04	9.152E+03
S(%)	<0.1	<0.1	<0.1	<0.1
Hits	7491	5701	5011	4845

PHOTON ENERGY : 1740 eV

Number of interactions : 100
Diameter of target : 25.0 nm
Number of infinitely long cylinders hit : 2086

FREQUENCY OF ENERGY DEPOSITION GREATER THAN E PER Gy

E	Target cylinder length (nm)			
(eV)	12.5	25.0	50.0	100.0
0	1.287E-04	2.006E-04	3.701E-04	7.349E-04
10	1.276E-04	1.996E-04	3.680E-04	7.307E-04
20	1.211E-04	1.908E-04	3.537E-04	7.021E-04
30	1.179E-04	1.872E-04	3.477E-04	6.905E-04
40	1.150E-04	1.841E-04	3.426E-04	6.803E-04
50	1.117E-04	1.801E-04	3.361E-04	6.676E-04
60	1.085E-04	1.756E-04	3.283E-04	6.521E-04
70	1.056E-04	1.722E-04	3.224E-04	6.401E-04
80	1.031E-04	1.696E-04	3.176E-04	6.310E-04
90	1.001E-04	1.666E-04	3.121E-04	6.201E-04
100	9.750E-05	1.632E-04	3.058E-04	6.077E-04
110	9.530E-05	1.604E-04	3.010E-04	5.986E-04
120	9.292E-05	1.578E-04	2.968E-04	5.901E-04
130	9.028E-05	1.553E-04	2.922E-04	5.813E-04
140	8.786E-05	1.524E-04	2.880E-04	5.728E-04
150	8.552E-05	1.488E-04	2.815E-04	5.598E-04
160	8.288E-05	1.459E-04	2.760E-04	5.489E-04
170	8.033E-05	1.426E-04	2.699E-04	5.366E-04
180	7.817E-05	1.401E-04	2.655E-04	5.278E-04
190	7.632E-05	1.377E-04	2.612E-04	5.193E-04
200	7.412E-05	1.347E-04	2.561E-04	5.091E-04
210	7.156E-05	1.320E-04	2.519E-04	5.010E-04
220	6.976E-05	1.302E-04	2.487E-04	4.946E-04
230	6.777E-05	1.278E-04	2.443E-04	4.858E-04
240	6.588E-05	1.251E-04	2.397E-04	4.770E-04
250	6.372E-05	1.226E-04	2.355E-04	4.686E-04
260	6.196E-05	1.200E-04	2.311E-04	4.598E-04
270	6.016E-05	1.176E-04	2.276E-04	4.527E-04
280	5.813E-05	1.154E-04	2.235E-04	4.446E-04
290	5.628E-05	1.128E-04	2.191E-04	4.358E-04
300	5.487E-05	1.112E-04	2.163E-04	4.302E-04
310	5.311E-05	1.072E-04	2.093E-04	4.161E-04
320	5.196E-05	1.056E-04	2.063E-04	4.101E-04
330	5.025E-05	1.033E-04	2.026E-04	4.027E-04
340	4.849E-05	9.997E-05	1.968E-04	3.911E-04
350	4.664E-05	9.688E-05	1.909E-04	3.794E-04
360	4.448E-05	9.433E-05	1.864E-04	3.703E-04
370	4.280E-05	9.213E-05	1.825E-04	3.625E-04
380	4.122E-05	8.975E-05	1.783E-04	3.541E-04
390	3.897E-05	8.693E-05	1.733E-04	3.449E-04
400	3.796E-05	8.464E-05	1.700E-04	3.386E-04
410	3.686E-05	8.323E-05	1.675E-04	3.336E-04
420	3.567E-05	8.156E-05	1.645E-04	3.280E-04

FREQUENCY OF ENERGY DEPOSITION GREATER THAN E PER Gy

E	Target cylinder length (nm)			
(eV)	12.5	25.0	50.0	100.0
430	3.417E-05	7.909E-05	1.603E-04	3.199E-04
440	3.246E-05	7.619E-05	1.554E-04	3.100E-04
450	3.158E-05	7.442E-05	1.520E-04	3.033E-04
460	3.030E-05	7.108E-05	1.464E-04	2.924E-04
470	2.911E-05	6.879E-05	1.422E-04	2.840E-04
480	2.752E-05	6.632E-05	1.370E-04	2.741E-04
490	2.647E-05	6.482E-05	1.335E-04	2.670E-04
500	2.506E-05	6.192E-05	1.281E-04	2.561E-04
510	2.365E-05	5.963E-05	1.240E-04	2.480E-04
520	2.299E-05	5.848E-05	1.219E-04	2.441E-04
530	2.189E-05	5.672E-05	1.194E-04	2.389E-04
540	2.052E-05	5.443E-05	1.143E-04	2.290E-04
550	1.920E-05	5.205E-05	1.094E-04	2.195E-04
560	1.845E-05	5.064E-05	1.069E-04	2.146E-04
570	1.744E-05	4.897E-05	1.036E-04	2.079E-04
580	1.656E-05	4.738E-05	1.004E-04	2.019E-04
590	1.568E-05	4.536E-05	9.635E-05	1.938E-04
600	1.506E-05	4.465E-05	9.495E-05	1.909E-04
610	1.431E-05	4.316E-05	9.178E-05	1.846E-04
620	1.383E-05	4.140E-05	8.896E-05	1.793E-04
630	1.286E-05	3.937E-05	8.473E-05	1.709E-04
640	1.202E-05	3.796E-05	8.121E-05	1.638E-04
650	1.136E-05	3.655E-05	7.786E-05	1.575E-04
660	1.044E-05	3.470E-05	7.434E-05	1.508E-04
670	1.004E-05	3.312E-05	7.187E-05	1.455E-04
680	9.644E-06	3.135E-05	6.993E-05	1.416E-04
690	8.896E-06	2.951E-05	6.606E-05	1.339E-04
700	8.499E-06	2.854E-05	6.359E-05	1.289E-04
710	7.619E-06	2.678E-05	6.060E-05	1.226E-04
720	7.310E-06	2.572E-05	5.848E-05	1.184E-04
730	6.650E-06	2.431E-05	5.602E-05	1.134E-04
740	6.297E-06	2.316E-05	5.373E-05	1.089E-04
750	5.769E-06	2.211E-05	5.179E-05	1.050E-04
760	5.461E-06	2.096E-05	4.950E-05	1.004E-04
770	5.152E-06	2.043E-05	4.844E-05	9.829E-05
780	4.888E-06	1.911E-05	4.562E-05	9.336E-05
790	4.448E-06	1.797E-05	4.333E-05	8.878E-05
800	4.051E-06	1.656E-05	4.034E-05	8.279E-05
810	3.875E-06	1.594E-05	3.858E-05	7.962E-05
820	3.699E-06	1.515E-05	3.752E-05	7.751E-05
830	3.479E-06	1.418E-05	3.576E-05	7.398E-05
840	3.171E-06	1.304E-05	3.382E-05	7.011E-05
850	3.039E-06	1.233E-05	3.241E-05	6.729E-05

FREQUENCY OF ENERGY DEPOSITION GREATER THAN E PER Gy

E	Target cylinder length (nm)			
(eV)	12.5	25.0	50.0	100.0
860	2.907E-06	1.154E-05	3.100E-05	6.412E-05
870	2.774E-06	1.101E-05	2.942E-05	6.060E-05
880	2.642E-06	1.066E-05	2.871E-05	5.919E-05
890	2.290E-06	9.864E-06	2.713E-05	5.602E-05
900	2.070E-06	9.336E-06	2.572E-05	5.320E-05
910	1.894E-06	8.720E-06	2.449E-05	5.108E-05
920	1.806E-06	7.927E-06	2.272E-05	4.756E-05
930	1.762E-06	7.839E-06	2.237E-05	4.650E-05
940	1.629E-06	7.486E-06	2.149E-05	4.474E-05
950	1.497E-06	7.046E-06	2.026E-05	4.228E-05
960	1.409E-06	6.870E-06	1.955E-05	4.087E-05
970	1.277E-06	6.606E-06	1.885E-05	3.946E-05
980	1.233E-06	6.430E-06	1.850E-05	3.875E-05
990	1.233E-06	6.077E-06	1.797E-05	3.770E-05
1000	1.145E-06	5.637E-06	1.709E-05	3.593E-05

z(Gy)	7.781E+03	4.992E+03	2.706E+03	1.363E+03
S(%)	0.1	0.1	0.1	0.2
Hits	2923	2278	2101	2086

PHOTON ENERGY : 2622 eV

Number of interactions : 25
Diameter of target : 2.0 mm
Number of infinitely long cylinders hit : 9040

FREQUENCY OF ENERGY DEPOSITION GREATER THAN E PER Gy

E	Target cylinder length (mm)			
(eV)	1.0	2.0	4.0	8.0
0	7.257E-07	1.250E-06	2.288E-06	4.416E-06
10	6.342E-07	1.119E-06	2.069E-06	4.008E-06
20	3.514E-07	6.683E-07	1.287E-06	2.532E-06
30	2.269E-07	4.607E-07	9.145E-07	1.817E-06
40	1.452E-07	3.199E-07	6.570E-07	1.316E-06
50	9.274E-08	2.257E-07	4.775E-07	9.612E-07
60	6.157E-08	1.621E-07	3.568E-07	7.300E-07
70	3.955E-08	1.161E-07	2.647E-07	5.495E-07
80	2.597E-08	8.149E-08	1.953E-07	4.174E-07
90	1.639E-08	5.876E-08	1.458E-07	3.169E-07
100	9.633E-09	4.105E-08	1.118E-07	2.441E-07
110	5.325E-09	2.752E-08	8.257E-08	1.852E-07
120	3.770E-09	1.831E-08	6.079E-08	1.388E-07
130	2.274E-09	1.221E-08	4.452E-08	1.024E-07
140	1.316E-09	8.736E-09	3.255E-08	7.707E-08
150	8.975E-10	5.265E-09	2.250E-08	5.888E-08
160	4.188E-10	3.231E-09	1.388E-08	3.877E-08
170	1.795E-10	2.034E-09	8.616E-09	2.824E-08
180	1.795E-10	1.316E-09	6.223E-09	2.058E-08
190	1.795E-10	1.197E-09	5.744E-09	1.771E-08
200	1.197E-10	5.983E-10	4.069E-09	1.149E-08
210	1.197E-10	5.983E-10	3.351E-09	1.005E-08
220	5.983E-11	3.590E-10	2.393E-09	8.616E-09
230	0.000E+00	2.393E-10	1.915E-09	6.701E-09
240	-	1.197E-10	9.573E-10	3.829E-09
250	-	1.197E-10	7.180E-10	2.393E-09
260	-	0.000E+00	2.393E-10	1.436E-09
270	-	-	2.393E-10	9.573E-10
280	-	-	2.393E-10	9.573E-10
290	-	-	0.000E+00	4.787E-10
300	-	-	-	4.787E-10
310	-	-	-	4.787E-10
320	-	-	-	4.787E-10
330	-	-	-	0.000E+00
340	-	-	-	-
350	-	-	-	-
z(Gy)	1.380E+06	8.016E+05	4.379E+05	2.268E+05
S(%)	0.1	0.2	0.2	0.2
Hits	12129	10442	9558	9225

PHOTON ENERGY : 2622 eV

Number of interactions : 50
Diameter of target : 10.0 mm
Number of infinitely long cylinders hit : 4859

FREQUENCY OF ENERGY DEPOSITION GREATER THAN E PER Gy

E	Target cylinder length (mm)			
(eV)	5.0	10.0	20.0	40.0
0	2.625E-05	4.211E-05	7.604E-05	1.471E-04
10	2.539E-05	4.100E-05	7.424E-05	1.438E-04
20	2.135E-05	3.565E-05	6.557E-05	1.273E-04
30	1.862E-05	3.209E-05	5.957E-05	1.160E-04
40	1.652E-05	2.905E-05	5.450E-05	1.065E-04
50	1.456E-05	2.633E-05	4.972E-05	9.744E-05
60	1.275E-05	2.364E-05	4.477E-05	8.790E-05
70	1.144E-05	2.150E-05	4.129E-05	8.153E-05
80	1.018E-05	1.964E-05	3.779E-05	7.503E-05
90	9.215E-06	1.809E-05	3.518E-05	7.001E-05
100	8.313E-06	1.664E-05	3.276E-05	6.516E-05
110	7.502E-06	1.530E-05	3.022E-05	6.026E-05
120	6.855E-06	1.413E-05	2.796E-05	5.586E-05
130	6.152E-06	1.295E-05	2.582E-05	5.167E-05
140	5.520E-06	1.184E-05	2.378E-05	4.748E-05
150	5.011E-06	1.096E-05	2.205E-05	4.434E-05
160	4.536E-06	1.013E-05	2.058E-05	4.141E-05
170	4.151E-06	9.319E-06	1.915E-05	3.856E-05
180	3.691E-06	8.527E-06	1.777E-05	3.581E-05
190	3.340E-06	7.839E-06	1.657E-05	3.351E-05
200	3.025E-06	7.233E-06	1.544E-05	3.117E-05
210	2.666E-06	6.612E-06	1.424E-05	2.884E-05
220	2.423E-06	6.148E-06	1.336E-05	2.714E-05
230	2.180E-06	5.669E-06	1.240E-05	2.537E-05
240	1.982E-06	5.228E-06	1.159E-05	2.375E-05
250	1.814E-06	4.877E-06	1.074E-05	2.196E-05
260	1.608E-06	4.555E-06	1.005E-05	2.052E-05
270	1.444E-06	4.174E-06	9.349E-06	1.915E-05
280	1.290E-06	3.807E-06	8.661E-06	1.786E-05
290	1.148E-06	3.471E-06	8.093E-06	1.675E-05
300	1.047E-06	3.261E-06	7.719E-06	1.598E-05
310	9.349E-07	3.059E-06	7.225E-06	1.496E-05
320	8.714E-07	2.842E-06	6.732E-06	1.397E-05
330	7.741E-07	2.595E-06	6.208E-06	1.295E-05
340	7.031E-07	2.423E-06	5.819E-06	1.221E-05
350	6.283E-07	2.229E-06	5.460E-06	1.143E-05
360	5.684E-07	2.064E-06	5.116E-06	1.068E-05
370	5.011E-07	1.870E-06	4.682E-06	9.873E-06
380	3.927E-07	1.660E-06	4.233E-06	9.035E-06
390	3.216E-07	1.473E-06	3.889E-06	8.287E-06
400	3.029E-07	1.391E-06	3.695E-06	7.928E-06
410	2.468E-07	1.242E-06	3.366E-06	7.270E-06
420	2.019E-07	1.070E-06	3.052E-06	6.582E-06

Photon Energy : 2622 eV ; Diameter of target : 10 mm.
(cont.)

FREQUENCY OF ENERGY DEPOSITION GREATER THAN E PER Gy

E	Target cylinder length (mm)			
(eV)	5.0	10.0	20.0	40.0
430	1.758E-07	9.349E-07	2.738E-06	5.894E-06
440	1.421E-07	8.302E-07	2.483E-06	5.415E-06
450	1.122E-07	7.704E-07	2.274E-06	4.996E-06
460	9.723E-08	6.507E-07	2.005E-06	4.518E-06
470	8.601E-08	5.834E-07	1.840E-06	4.218E-06
480	8.227E-08	5.385E-07	1.705E-06	3.919E-06
490	7.854E-08	4.787E-07	1.556E-06	3.530E-06
500	5.984E-08	3.964E-07	1.361E-06	3.141E-06
510	4.862E-08	3.740E-07	1.301E-06	3.052E-06
520	4.114E-08	3.216E-07	1.107E-06	2.693E-06
530	2.992E-08	2.693E-07	9.424E-07	2.364E-06
540	1.870E-08	2.319E-07	8.377E-07	2.064E-06
550	1.496E-08	1.795E-07	6.732E-07	1.705E-06
560	1.496E-08	1.645E-07	6.283E-07	1.586E-06
570	7.480E-09	1.197E-07	5.535E-07	1.436E-06
580	3.740E-09	8.975E-08	4.637E-07	1.197E-06
590	0.000E+00	8.227E-08	3.740E-07	1.017E-06
600	-	6.732E-08	3.291E-07	9.275E-07
610	-	5.984E-08	3.141E-07	8.975E-07
620	-	2.992E-08	2.094E-07	6.582E-07
630	-	2.992E-08	1.795E-07	5.984E-07
640	-	2.992E-08	1.795E-07	5.984E-07
650	-	2.244E-08	1.496E-07	5.385E-07
660	-	2.244E-08	1.346E-07	4.787E-07
670	-	2.244E-08	1.346E-07	4.189E-07
680	-	2.244E-08	1.346E-07	4.189E-07
690	-	2.244E-08	1.197E-07	3.590E-07
700	-	1.496E-08	1.197E-07	3.291E-07
710	-	1.496E-08	1.047E-07	2.992E-07
720	-	1.496E-08	8.975E-08	2.693E-07
730	-	7.480E-09	4.488E-08	1.795E-07
740	-	7.480E-09	2.992E-08	1.197E-07
750	-	7.480E-09	2.992E-08	1.197E-07
z(Gy)	3.663E+04	2.284E+04	1.265E+04	6.537E+03
S(%)	3.8	3.8	3.8	3.8
Hits	7020	5630	5083	4917

PHOTON ENERGY : 2622 eV

Number of interactions : 50
Diameter of target : 25.0 mm
Number of infinitely long cylinders hit : 2133

Photon Energy : 2622 eV ; Diameter of target : 25 mm.

FREQUENCY OF ENERGY DEPOSITION GREATER THAN E PER Gy

E	Target cylinder length (mm)			
(eV)	12.5	25.0	50.0	100.0
0	1.793E-04	2.821E-04	5.141E-04	1.000E-03
10	1.776E-04	2.797E-04	5.104E-04	9.927E-04
20	1.657E-04	2.659E-04	4.870E-04	9.492E-04
30	1.595E-04	2.585E-04	4.739E-04	9.235E-04
40	1.513E-04	2.495E-04	4.585E-04	8.940E-04
50	1.451E-04	2.423E-04	4.459E-04	8.702E-04
60	1.376E-04	2.330E-04	4.309E-04	8.421E-04
70	1.320E-04	2.260E-04	4.199E-04	8.206E-04
80	1.260E-04	2.192E-04	4.084E-04	7.987E-04
90	1.209E-04	2.135E-04	3.996E-04	7.814E-04
100	1.154E-04	2.057E-04	3.869E-04	7.570E-04
110	1.102E-04	1.994E-04	3.766E-04	7.365E-04
120	1.058E-04	1.938E-04	3.675E-04	7.187E-04
130	1.009E-04	1.869E-04	3.558E-04	6.967E-04
140	9.609E-05	1.804E-04	3.451E-04	6.752E-04
150	9.007E-05	1.734E-04	3.322E-04	6.504E-04
160	8.545E-05	1.662E-04	3.201E-04	6.261E-04
170	8.183E-05	1.593E-04	3.084E-04	6.041E-04
180	7.809E-05	1.530E-04	2.974E-04	5.831E-04
190	7.493E-05	1.482E-04	2.892E-04	5.667E-04
200	7.090E-05	1.417E-04	2.780E-04	5.462E-04
210	6.728E-05	1.357E-04	2.668E-04	5.246E-04
220	6.459E-05	1.313E-04	2.588E-04	5.083E-04
230	6.149E-05	1.259E-04	2.499E-04	4.910E-04
240	5.927E-05	1.219E-04	2.431E-04	4.793E-04
250	5.693E-05	1.176E-04	2.364E-04	4.662E-04
260	5.418E-05	1.133E-04	2.291E-04	4.517E-04
270	5.120E-05	1.093E-04	2.209E-04	4.363E-04
280	4.840E-05	1.050E-04	2.132E-04	4.208E-04
290	4.647E-05	1.022E-04	2.069E-04	4.101E-04
300	4.430E-05	9.843E-05	2.006E-04	3.975E-04
310	4.243E-05	9.516E-05	1.945E-04	3.858E-04
320	4.097E-05	9.258E-05	1.889E-04	3.755E-04
330	3.916E-05	8.943E-05	1.817E-04	3.624E-04
340	3.758E-05	8.697E-05	1.772E-04	3.530E-04
350	3.624E-05	8.428E-05	1.714E-04	3.418E-04
360	3.402E-05	8.148E-05	1.669E-04	3.329E-04
370	3.250E-05	7.832E-05	1.609E-04	3.212E-04
380	3.145E-05	7.552E-05	1.559E-04	3.119E-04
390	2.975E-05	7.248E-05	1.499E-04	3.002E-04
400	2.823E-05	6.920E-05	1.436E-04	2.876E-04
410	2.712E-05	6.675E-05	1.386E-04	2.782E-04
420	2.566E-05	6.348E-05	1.316E-04	2.670E-04

Photon Energy : 2622 eV ; Diameter of target : 25 mm. (cont.)

FREQUENCY OF ENERGY DEPOSITION GREATER THAN E PER Gy

E	Target cylinder length (mm)			
(eV)	12.5	25.0	50.0	100.0
430	2.472E-05	6.137E-05	1.286E-04	2.605E-04
440	2.350E-05	5.915E-05	1.244E-04	2.516E-04
450	2.198E-05	5.646E-05	1.192E-04	2.417E-04
460	2.028E-05	5.284E-05	1.132E-04	2.291E-04
470	1.946E-05	5.155E-05	1.099E-04	2.235E-04
480	1.847E-05	5.003E-05	1.071E-04	2.170E-04
490	1.718E-05	4.664E-05	1.015E-04	2.053E-04
500	1.613E-05	4.454E-05	9.796E-05	1.973E-04
510	1.520E-05	4.278E-05	9.445E-05	1.894E-04
520	1.485E-05	4.127E-05	9.212E-05	1.852E-04
530	1.420E-05	3.998E-05	8.884E-05	1.791E-04
540	1.268E-05	3.694E-05	8.323E-05	1.683E-04
550	1.187E-05	3.484E-05	7.949E-05	1.609E-04
560	1.046E-05	3.145E-05	7.318E-05	1.478E-04
570	9.878E-06	2.969E-05	6.944E-05	1.407E-04
580	9.586E-06	2.876E-05	6.710E-05	1.361E-04
590	8.767E-06	2.677E-05	6.313E-05	1.286E-04
600	7.832E-06	2.513E-05	5.962E-05	1.211E-04
610	7.306E-06	2.408E-05	5.705E-05	1.164E-04
620	6.663E-06	2.268E-05	5.354E-05	1.094E-04
630	6.079E-06	2.116E-05	5.073E-05	1.043E-04
640	5.728E-06	2.022E-05	4.840E-05	1.005E-04
650	5.553E-06	1.941E-05	4.629E-05	9.586E-05
660	5.202E-06	1.859E-05	4.466E-05	9.305E-05
670	4.734E-06	1.765E-05	4.255E-05	8.931E-05
680	4.267E-06	1.625E-05	4.068E-05	8.510E-05
690	3.858E-06	1.508E-05	3.858E-05	8.136E-05
700	3.858E-06	1.450E-05	3.671E-05	7.809E-05
710	3.682E-06	1.368E-05	3.530E-05	7.482E-05
720	3.098E-06	1.263E-05	3.320E-05	7.107E-05
730	2.806E-06	1.169E-05	3.133E-05	6.780E-05
740	2.572E-06	1.122E-05	3.016E-05	6.546E-05
750	2.455E-06	1.017E-05	2.806E-05	6.125E-05
760	2.163E-06	9.001E-06	2.572E-05	5.611E-05
770	1.987E-06	7.832E-06	2.408E-05	5.284E-05
780	1.520E-06	7.248E-06	2.221E-05	4.910E-05
790	1.227E-06	6.313E-06	2.011E-05	4.582E-05
800	9.936E-07	5.962E-06	1.800E-05	4.255E-05
810	8.767E-07	5.962E-06	1.800E-05	4.255E-05
820	7.598E-07	5.494E-06	1.707E-05	4.068E-05
830	7.014E-07	5.494E-06	1.683E-05	4.021E-05
840	6.429E-07	4.910E-06	1.543E-05	3.741E-05
850	5.260E-07	4.559E-06	1.450E-05	3.554E-05

Photon Energy : 2622 eV ; Diameter of target : 25 mm. (cont.)

FREQUENCY OF ENERGY DEPOSITION GREATER THAN E PER Gy

E	Target cylinder length (mm)			
(eV)	12.5	25.0	50.0	100.0
860	5.260E-07	3.858E-06	1.309E-05	3.226E-05
870	5.260E-07	3.858E-06	1.263E-05	3.180E-05
880	4.676E-07	3.624E-06	1.216E-05	3.039E-05
890	4.091E-07	3.390E-06	1.075E-05	2.759E-05
900	3.507E-07	3.156E-06	1.005E-05	2.572E-05
910	2.922E-07	3.039E-06	9.586E-06	2.478E-05
920	2.922E-07	2.572E-06	8.183E-06	2.198E-05
930	2.338E-07	2.338E-06	7.715E-06	2.057E-05
940	2.338E-07	2.338E-06	7.715E-06	2.057E-05
950	2.338E-07	2.338E-06	7.248E-06	1.964E-05
960	2.338E-07	2.104E-06	6.780E-06	1.870E-05
970	1.169E-07	1.637E-06	6.079E-06	1.730E-05
980	1.169E-07	1.637E-06	6.079E-06	1.683E-05
990	1.169E-07	1.403E-06	5.611E-06	1.590E-05
1000	1.169E-07	1.286E-06	5.377E-06	1.496E-05
z(Gy)	5.440E+03	3.457E+03	1.897E+03	9.750E+02
S(%)	2.5	2.5	2.5	2.5
Hits	3067	2413	2199	2139

PHOTON ENERGY : 3692 eV

Number of interactions : 20
Diameter of target : 2.0 mm
Number of infinitely long cylinders hit :10681

FREQUENCY OF ENERGY DEPOSITION GREATER THAN E PER Gy

E	Target cylinder length (mm)			
(eV)	1.0	2.0	4.0	8.0
0	7.286E-07	1.276E-06	2.381E-06	4.620E-06
10	6.317E-07	1.131E-06	2.128E-06	4.141E-06
20	3.312E-07	6.388E-07	1.244E-06	2.445E-06
30	2.026E-07	4.139E-07	8.201E-07	1.628E-06
40	1.241E-07	2.772E-07	5.692E-07	1.145E-06
50	7.750E-08	1.902E-07	4.030E-07	8.210E-07
60	5.131E-08	1.339E-07	2.928E-07	6.055E-07
70	3.182E-08	9.433E-08	2.161E-07	4.513E-07
80	2.066E-08	6.629E-08	1.627E-07	3.459E-07
90	1.269E-08	4.738E-08	1.196E-07	2.592E-07
100	7.596E-09	3.283E-08	9.072E-08	1.963E-07
110	5.418E-09	2.241E-08	6.756E-08	1.475E-07
120	3.346E-09	1.551E-08	4.972E-08	1.135E-07
130	1.912E-09	9.667E-09	3.272E-08	8.074E-08
140	1.328E-09	6.268E-09	2.125E-08	5.652E-08
150	7.436E-10	4.780E-09	1.487E-08	4.249E-08
160	4.780E-10	3.506E-09	1.254E-08	3.442E-08
170	3.187E-10	2.337E-09	8.924E-09	2.507E-08
180	1.593E-10	1.487E-09	6.161E-09	1.742E-08
190	1.062E-10	1.062E-09	3.824E-09	1.360E-08
200	1.062E-10	8.499E-10	2.974E-09	1.105E-08
210	1.062E-10	6.374E-10	2.337E-09	8.499E-09
220	1.062E-10	3.187E-10	1.700E-09	5.949E-09
230	1.062E-10	2.125E-10	1.062E-09	3.399E-09
240	1.062E-10	2.125E-10	6.374E-10	2.125E-09
250	1.062E-10	2.125E-10	6.374E-10	2.125E-09
260	1.062E-10	2.125E-10	4.249E-10	1.700E-09
270	5.312E-11	2.125E-10	4.249E-10	1.700E-09
280	5.312E-11	2.125E-10	4.249E-10	1.275E-09
290	0.000E+00	1.062E-10	2.125E-10	4.249E-10
300	-	1.062E-10	2.125E-10	4.249E-10
310	-	1.062E-10	2.125E-10	4.249E-10
320	-	1.062E-10	2.125E-10	4.249E-10
330	-	0.000E+00	0.000E+00	0.000E+00
340	-	-	-	-
350	-	-	-	-
z(Gy)	1.295E+06	7.391E+05	3.962E+05	2.042E+05
S(%)	5.6	5.7	5.7	5.7
Hits	13718	12016	11208	10872

PHOTON ENERGY : 3692 eV

Number of interactions : 50
Diameter of target : 10.0 mm
Number of infinitely long cylinders hit : 8832

FREQUENCY OF ENERGY DEPOSITION GREATER THAN E PER Gy

E	Target cylinder length (mm)			
(eV)	5.0	10.0	20.0	40.0
0	3.212E-05	5.362E-05	9.838E-05	1.908E-04
10	3.077E-05	5.175E-05	9.502E-05	1.845E-04
20	2.485E-05	4.333E-05	8.053E-05	1.568E-04
30	2.047E-05	3.675E-05	6.922E-05	1.350E-04
40	1.738E-05	3.201E-05	6.089E-05	1.188E-04
50	1.479E-05	2.817E-05	5.412E-05	1.057E-04
60	1.269E-05	2.473E-05	4.791E-05	9.368E-05
70	1.099E-05	2.175E-05	4.272E-05	8.382E-05
80	9.604E-06	1.923E-05	3.815E-05	7.504E-05
90	8.459E-06	1.709E-05	3.431E-05	6.765E-05
100	7.466E-06	1.522E-05	3.088E-05	6.138E-05
110	6.613E-06	1.369E-05	2.789E-05	5.567E-05
120	5.811E-06	1.219E-05	2.504E-05	5.036E-05
130	5.115E-06	1.096E-05	2.263E-05	4.566E-05
140	4.552E-06	9.944E-06	2.067E-05	4.194E-05
150	4.050E-06	9.051E-06	1.895E-05	3.867E-05
160	3.625E-06	8.244E-06	1.734E-05	3.542E-05
170	3.315E-06	7.606E-06	1.613E-05	3.302E-05
180	2.959E-06	6.980E-06	1.497E-05	3.066E-05
190	2.627E-06	6.273E-06	1.361E-05	2.792E-05
200	2.417E-06	5.800E-06	1.265E-05	2.603E-05
210	2.191E-06	5.333E-06	1.166E-05	2.420E-05
220	1.960E-06	4.834E-06	1.059E-05	2.199E-05
230	1.734E-06	4.382E-06	9.710E-06	2.031E-05
240	1.548E-06	4.042E-06	8.892E-06	1.857E-05
250	1.376E-06	3.708E-06	8.127E-06	1.696E-05
260	1.243E-06	3.336E-06	7.341E-06	1.551E-05
270	1.115E-06	3.086E-06	6.767E-06	1.426E-05
280	1.001E-06	2.762E-06	6.130E-06	1.296E-05
290	9.189E-07	2.619E-06	5.864E-06	1.241E-05
300	7.968E-07	2.385E-06	5.344E-06	1.143E-05
310	6.879E-07	2.167E-06	4.876E-06	1.045E-05
320	6.241E-07	1.997E-06	4.547E-06	9.710E-06
330	5.551E-07	1.817E-06	4.186E-06	9.030E-06
340	4.940E-07	1.684E-06	3.909E-06	8.393E-06
350	4.382E-07	1.583E-06	3.708E-06	8.010E-06
360	3.639E-07	1.376E-06	3.346E-06	7.203E-06
370	3.028E-07	1.206E-06	2.985E-06	6.480E-06
380	2.629E-07	1.094E-06	2.741E-06	5.907E-06
390	2.284E-07	9.986E-07	2.624E-06	5.588E-06
400	2.018E-07	9.296E-07	2.454E-06	5.269E-06
410	1.620E-07	8.233E-07	2.178E-06	4.738E-06
420	1.328E-07	7.543E-07	2.040E-06	4.419E-06

Photon Energy : 3692 eV ; Diameter of target : 10 mm.
(cont.)

FREQUENCY OF ENERGY DEPOSITION GREATER THAN E PER Gy

E	Target cylinder length (mm)			
(eV)	5.0	10.0	20.0	40.0
430	1.115E-07	6.905E-07	1.902E-06	4.143E-06
440	9.561E-08	6.268E-07	1.732E-06	3.803E-06
450	7.702E-08	5.418E-07	1.562E-06	3.442E-06
460	6.905E-08	4.515E-07	1.339E-06	3.017E-06
470	6.374E-08	4.196E-07	1.264E-06	2.868E-06
480	5.843E-08	3.771E-07	1.169E-06	2.635E-06
490	5.577E-08	3.453E-07	1.062E-06	2.443E-06
500	5.046E-08	3.081E-07	9.986E-07	2.316E-06
510	3.984E-08	2.656E-07	8.605E-07	1.997E-06
520	3.718E-08	2.443E-07	7.755E-07	1.848E-06
530	3.187E-08	2.231E-07	7.224E-07	1.700E-06
540	2.921E-08	2.018E-07	6.799E-07	1.636E-06
550	2.656E-08	1.912E-07	6.268E-07	1.509E-06
560	2.125E-08	1.700E-07	5.843E-07	1.381E-06
570	2.125E-08	1.647E-07	5.312E-07	1.296E-06
580	2.125E-08	1.487E-07	4.887E-07	1.211E-06
590	1.594E-08	1.222E-07	4.143E-07	1.105E-06
600	1.594E-08	1.169E-07	3.824E-07	1.020E-06
610	1.594E-08	1.115E-07	3.506E-07	9.561E-07
620	1.062E-08	9.561E-08	3.187E-07	8.711E-07
630	7.968E-09	8.499E-08	2.868E-07	8.074E-07
640	7.968E-09	7.968E-08	2.762E-07	7.436E-07
650	7.968E-09	6.905E-08	2.443E-07	6.799E-07
660	7.968E-09	6.905E-08	2.337E-07	6.799E-07
670	7.968E-09	6.374E-08	2.018E-07	5.737E-07
680	5.312E-09	6.374E-08	2.018E-07	5.524E-07
690	0.000E+00	5.843E-08	1.912E-07	5.312E-07
700	-	5.312E-08	1.806E-07	5.099E-07
710	-	5.312E-08	1.806E-07	4.887E-07
720	-	4.781E-08	1.594E-07	4.462E-07
730	-	4.781E-08	1.381E-07	4.037E-07
740	-	4.781E-08	1.381E-07	3.824E-07
750	-	4.781E-08	1.381E-07	3.824E-07
z(Gy)	2.966E+04	1.777E+04	9.685E+03	4.995E+03
S(%)	4.7	4.7	4.7	4.7
Hits	12095	10095	9261	8979

PHOTON ENERGY : 3692 eV

Number of interactions : 50
Diameter of target : 25.0 mm
Number of infinitely long cylinders hit : 3978

FREQUENCY OF ENERGY DEPOSITION GREATER THAN E PER Gy

E	Target cylinder length (mm)			
(eV)	12.5	25.0	50.0	100.0
0	2.402E-04	3.797E-04	6.883E-04	1.333E-03
10	2.366E-04	3.758E-04	6.824E-04	1.322E-03
20	2.169E-04	3.524E-04	6.438E-04	1.249E-03
30	1.992E-04	3.309E-04	6.070E-04	1.178E-03
40	1.863E-04	3.152E-04	5.803E-04	1.127E-03
50	1.753E-04	3.018E-04	5.578E-04	1.085E-03
60	1.630E-04	2.872E-04	5.334E-04	1.039E-03
70	1.519E-04	2.714E-04	5.064E-04	9.869E-04
80	1.404E-04	2.563E-04	4.811E-04	9.397E-04
90	1.300E-04	2.411E-04	4.556E-04	8.902E-04
100	1.214E-04	2.277E-04	4.318E-04	8.454E-04
110	1.124E-04	2.143E-04	4.084E-04	7.996E-04
120	1.049E-04	2.035E-04	3.900E-04	7.647E-04
130	9.766E-05	1.933E-04	3.729E-04	7.322E-04
140	9.119E-05	1.832E-04	3.558E-04	6.996E-04
150	8.393E-05	1.713E-04	3.359E-04	6.614E-04
160	7.832E-05	1.621E-04	3.203E-04	6.319E-04
170	7.367E-05	1.544E-04	3.071E-04	6.063E-04
180	6.820E-05	1.443E-04	2.881E-04	5.708E-04
190	6.413E-05	1.378E-04	2.761E-04	5.469E-04
200	6.085E-05	1.306E-04	2.627E-04	5.200E-04
210	5.724E-05	1.248E-04	2.512E-04	4.991E-04
220	5.342E-05	1.186E-04	2.389E-04	4.768E-04
230	4.993E-05	1.129E-04	2.278E-04	4.552E-04
240	4.682E-05	1.070E-04	2.170E-04	4.333E-04
250	4.350E-05	1.000E-04	2.044E-04	4.068E-04
260	4.063E-05	9.455E-05	1.941E-04	3.872E-04
270	3.810E-05	8.891E-05	1.845E-04	3.692E-04
280	3.590E-05	8.393E-05	1.752E-04	3.520E-04
290	3.391E-05	7.845E-05	1.664E-04	3.340E-04
300	3.229E-05	7.562E-05	1.597E-04	3.218E-04
310	3.080E-05	7.189E-05	1.529E-04	3.085E-04
320	2.955E-05	6.849E-05	1.469E-04	2.975E-04
330	2.831E-05	6.558E-05	1.405E-04	2.859E-04
340	2.673E-05	6.267E-05	1.346E-04	2.749E-04
350	2.486E-05	5.960E-05	1.297E-04	2.656E-04
360	2.353E-05	5.686E-05	1.240E-04	2.537E-04
370	2.250E-05	5.462E-05	1.197E-04	2.447E-04
380	2.113E-05	5.180E-05	1.141E-04	2.331E-04
390	2.021E-05	5.039E-05	1.112E-04	2.275E-04
400	1.947E-05	4.831E-05	1.073E-04	2.192E-04
410	1.872E-05	4.682E-05	1.039E-04	2.122E-04
420	1.756E-05	4.433E-05	9.829E-05	2.009E-04

FREQUENCY OF ENERGY DEPOSITION GREATER THAN E PER Gy

E	Target cylinder length (mm)			
(eV)	12.5	25.0	50.0	100.0
430	1.693E-05	4.242E-05	9.347E-05	1.909E-04
440	1.635E-05	4.084E-05	9.098E-05	1.856E-04
450	1.569E-05	3.927E-05	8.766E-05	1.793E-04
460	1.490E-05	3.727E-05	8.384E-05	1.727E-04
470	1.420E-05	3.561E-05	8.069E-05	1.664E-04
480	1.328E-05	3.462E-05	7.803E-05	1.617E-04
490	1.253E-05	3.321E-05	7.471E-05	1.551E-04
500	1.170E-05	3.138E-05	7.073E-05	1.464E-04
510	1.100E-05	2.972E-05	6.757E-05	1.401E-04
520	1.038E-05	2.872E-05	6.558E-05	1.361E-04
530	9.920E-06	2.789E-05	6.259E-05	1.298E-04
540	8.467E-06	2.449E-05	5.562E-05	1.162E-04
550	7.886E-06	2.366E-05	5.429E-05	1.132E-04
560	7.347E-06	2.200E-05	5.064E-05	1.053E-04
570	7.056E-06	2.150E-05	4.948E-05	1.033E-04
580	6.267E-06	1.976E-05	4.599E-05	9.630E-05
590	5.603E-06	1.835E-05	4.333E-05	9.065E-05
600	5.271E-06	1.752E-05	4.151E-05	8.766E-05
610	4.773E-06	1.635E-05	3.902E-05	8.268E-05
620	4.441E-06	1.536E-05	3.636E-05	7.770E-05
630	3.736E-06	1.361E-05	3.254E-05	7.040E-05
640	3.570E-06	1.320E-05	3.188E-05	6.907E-05
650	3.321E-06	1.220E-05	3.005E-05	6.541E-05
660	3.113E-06	1.170E-05	2.922E-05	6.309E-05
670	2.947E-06	1.079E-05	2.806E-05	6.043E-05
680	2.864E-06	1.054E-05	2.756E-05	5.944E-05
690	2.573E-06	9.796E-06	2.573E-05	5.578E-05
700	2.366E-06	8.633E-06	2.341E-05	5.180E-05
710	2.283E-06	8.135E-06	2.225E-05	4.981E-05
720	2.075E-06	7.803E-06	2.109E-05	4.748E-05
730	1.909E-06	7.305E-06	1.976E-05	4.483E-05
740	1.743E-06	6.724E-06	1.843E-05	4.217E-05
750	1.619E-06	5.977E-06	1.710E-05	3.918E-05
760	1.619E-06	5.977E-06	1.677E-05	3.885E-05
770	1.494E-06	5.645E-06	1.627E-05	3.785E-05
780	1.411E-06	5.479E-06	1.544E-05	3.653E-05
790	1.370E-06	4.815E-06	1.461E-05	3.453E-05
800	1.328E-06	4.815E-06	1.444E-05	3.420E-05
810	1.162E-06	4.566E-06	1.411E-05	3.354E-05
820	1.079E-06	3.985E-06	1.245E-05	3.055E-05
830	9.962E-07	3.653E-06	1.146E-05	2.856E-05
840	9.962E-07	3.653E-06	1.146E-05	2.789E-05
850	9.131E-07	3.570E-06	1.112E-05	2.756E-05

FREQUENCY OF ENERGY DEPOSITION GREATER THAN E PER Gy

E	Target cylinder length (mm)			
(eV)	12.5	25.0	50.0	100.0
860	8.716E-07	3.487E-06	1.079E-05	2.690E-05
870	7.886E-07	3.321E-06	1.029E-05	2.590E-05
880	7.056E-07	3.238E-06	1.013E-05	2.524E-05
890	7.056E-07	3.071E-06	9.796E-06	2.424E-05
900	7.056E-07	3.071E-06	9.796E-06	2.424E-05
910	7.056E-07	2.988E-06	9.463E-06	2.324E-05
920	6.641E-07	2.573E-06	8.633E-06	2.158E-05
930	6.226E-07	2.490E-06	8.633E-06	2.158E-05
940	5.396E-07	2.158E-06	8.135E-06	1.992E-05
950	5.396E-07	2.075E-06	7.803E-06	1.926E-05
960	5.396E-07	2.075E-06	7.803E-06	1.859E-05
970	4.981E-07	2.075E-06	7.637E-06	1.826E-05
980	4.981E-07	1.992E-06	7.139E-06	1.760E-05
990	3.321E-07	1.660E-06	5.977E-06	1.527E-05
1000	3.321E-07	1.577E-06	5.645E-06	1.494E-05
z(Gy)	3.975E+03	2.514E+03	1.387E+03	7.161E+02
S(%)	4.5	4.5	4.5	4.5
Hits	5786	4574	4146	4015